Investigating Carbon Nanotube – Polymer Blends for Organic Solar Cell Applications

Samuel D Stranks

St John's College, Oxford

Thesis submitted in fulfilment of the requirements for the degree of Doctor of Philosophy at the University of Oxford

Michaelmas Term, 2011

Investigating Carbon Nanotube – Polymer Blends for Organic Solar Cell Applications

Samuel D Stranks, St John's College, Oxford

Thesis submitted in fulfilment of the requirements for the degree of Doctor of Philosophy at the University of Oxford. Michaelmas Term, 2011

Abstract

This thesis describes studies on nanohybrid systems consisting of single-walled carbon nanotubes (SWNTs) with monolayer coatings of semiconducting polymers. Steady-state and time-resolved optical and high-resolution microscopy experiments were used to investigate the blends. These materials show promise for use in organic photovoltaics (OPVs) owing to the high carrier mobilities and large aspect ratios of SWNTs, the controllable solubilisation of tubes with various polymers and the broad light-harvesting abilities of organic polymers.

Chapters 1 and 2 introduce the theory and background behind the work and present a literature review of previous work utilising carbon nanotubes in OPV devices, revealing poor performances to date. The experimental methods used during the thesis are detailed in Chapter 3 and the solution processing techniques used to prepare the polymer–nanotube blend samples are described in Chapter 4.

Chapter 5 describes a study on a nanotube blend with a thiophene polymer, a system previously unsuccessfully implemented into OPV devices. Ultrafast spectroscopic measurements showed that electrons can transfer on a 400 fs time scale from the polymer to nanotubes and the conditions to allow long-lived free charges to be produced were found. The study is extended in Chapter 6 to show that nanostructures consisting of a nanotube coated in one polymer can then be coated by a second polymer and that these nano-engineered structures could be implemented into OPV devices. The use of a competition binding process to isolate purely semiconducting nanotubes dispersed with any desired polymer is then described in Chapter 7. Finally, Chapter 8 introduces systems consisting of chains of porphyrin units, nature's light-harvesting systems, bound to nanotubes and the blends were found to exhibit the required electronic alignment for use in OPVs.

The work described in this thesis provides an explanation for the poor device behaviour of nanotube–polymer blends to date and, in particular, demonstrates several nanohybrid systems that show particular promise for improved OPV applications.

"If I have seen further it is only by standing on the shoulders of giants."

Sir Isaac Newton

Acknowledgements

I would like to thank my supervisors, Prof. Robin J. Nicholas and Dr Michael B. Johnston, for their unwavering patience, guidance and support. I would also like to thank Prof. Laura M. Herz for invaluable discussions. This work could have not have been completed without their enthusiasm and support, which began even before I arrived in Oxford.

I would like to thank everyone in the RJN, MBJ and LMH groups for enjoyable tea time discussions, pub lunches and for making the Clarendon an even more enjoyable place to work in. There are too many to name individually but I would like to particularly thank those who directly helped with work presented in this thesis – Torben Schüttfort, Dr Patrick Parkinson, Christian Weisspfennig, Chaw Keong Yong, Jack Alexander-Webber and Anton Baker. Thank you also to Dr Henry J. Snaith and his group for help with device-related work and particularly to Dr Agnese Abrusci for her useful comments on this thesis.

I have also enjoyed working with several collaborators within the University. Thank you to Dr Johannes K. Sprafke and Prof. Harry L. Anderson (Department of Chemistry), Dr Jamie H. Warner (Department of Materials), and Prof. Robert A. Taylor and Dr Xu Wang (Department of Physics) for enjoyable and fruitful collaborations.

I would not have been able to come to Oxford without the wonderful opportunity provided by the Rhodes Trust and it is an honour and a privilege to be among such brilliant people in the Rhodes Community. A special thank you to the Warden, Dr Donald Markwell, and staff at Rhodes House for the many amazing opportunities I would otherwise never have been able to experience.

Many thanks also to St John's College, the Condensed Matter Physics Sub-Department, and the Institute of Physics for additional funding to allow me to present my work at

international conferences. Also, to the University for the Vice Chancellors' Fund to see me through the final few months of my DPhil. Finally, to Dr Johnston and Prof. Hans Kraus at Corpus Christi College for giving me many teaching opportunities during my DPhil.

Last, and certainly not least, thank you to my friends and family for their unwavering support, both in Oxford and from abroad. I have met so many wonderful people during my time in Oxford and you have certainly made my experience amongst the Spires unforgettable. Thank you to my parents, Geoff and Gerry, for their support and encouraging me to live my dream. Finally, to my wonderful wife, Amanda – you are my guiding star and my world and I can never thank you enough for supporting and putting up with me every step of the way.

Contents

Publications

S. D. Stranks, C. Weisspfennig, P. Parkinson, M. B. Johnston, L. M. Herz and R. J. Nicholas. Ultrafast charge separation at a polymer–single-walled carbon nanotube molecular junction. *Nano Letters*, **11**:66–72, 2011.

S. D. Stranks, C. Weisspfennig, P. Parkinson, M. B. Johnston, L. M. Herz and R. J. Nicholas. Ultrafast charge separation at a single-walled carbon nanotube-polymer interface. *MRS Proceedings*, **1286**:mrsf10-1286-e02-07, 2011.

S. D. Stranks, J. K. Sprafke, H. L. Anderson and R. J. Nicholas. Electronic and mechanical modification of single-walled carbon nanotubes by binding to porphyrin oligomers. *ACS Nano*, **5**:2307-2315, 2011.

J. K. Sprafke, S. D. Stranks, J. H. Warner, R. J. Nicholas and H. L. Anderson. Noncovalent binding of carbon nanotubes by porphyrin oligomers. *Angewandte Chemie International Edition*, **50**:2313–2316, 2011.

Manuscripts in preparation/submitted

S. D. Stranks, C. Yong, J. A. Alexander-Webber, C. Weisspfennig, M. B. Johnston, L. M. Herz and R. J. Nicholas. Nano-engineering coaxial carbon nanotube–dual polymer heterostructures. *Submitted for publication.*

S. D. Stranks, A. M. R. Baker, J. A. Alexander-Webber and R. J. Nicholas. Production of high purity single chirality carbon nanotube hybrids by selective polymer exchange. *Submitted for publication.*

J. A. Alexander-Webber, X. Wang, S. D. Stranks, C. Faugeras, P. Kossacki, M. Potemski, R. A. Taylor and R. J. Nicholas. Photoluminescence spectroscopy of individual single-walled carbon nanotubes at low temperatures and high magnetic fields. *Manuscript in preparation.*

J. A. Alexander-Webber, X. Wang, S. D. Stranks, W. Jia, M. J. Holmes, C. C. S. Chan, B. P. L. Reid, H. D. Kim, R. A. Taylor and R. J. Nicholas. Localization and charge transfer of quantum dots confined in single-walled carbon nanotubes. *Manuscript in preparation.*

Oral Presentations

Investigating Charge Transfer in Carbon Nanotube Blends for Use in Organic Solar Cells. *Advances in Photovoltaics International Meeting, Institute of Physics, London, UK, 2011.*

Promising Carbon Nanotube Blend Materials for Organic Photovoltaics. *JUDO-PV International Dye-Sensitised and Organic Photovoltaics Workshop, Oxford, UK, 2011.*

Electronic and Mechanical Modification of Single-Walled Carbon Nanotubes by Binding to Porphyrin Oligomers. *WONTON International Nanotube Spectroscopy Workshop, Bordeaux, France, 2011.*

Harvesting the Sun's Energy Using Carbon Nanotubes – How Tubes So Small Can Help Solve a Problem So Big. *St John's College Research Lecture Supper, Oxford, UK, 2011.*

Ultrafast Charge Separation at a Single-Walled Carbon Nanotube-Polymer Interface. *Materials Research Society (MRS) Fall Meeting, Boston, USA, 2010.*

Prizes

Nicholas Kurti Prize for Distinguished Work as a Third Year Postgraduate Student
Condensed Matter Physics, University of Oxford, 2011.

Academic Poster Prize
Carbon Nanotechnology Symposium, University of Cambridge, 2012.

Chapter 1

Introduction

1.1 Introduction and Motivation

The limited supply of the world's main energy resources, together with the growing concerns about climate change, have prioritised the development of renewable energy sources such as solar energy. The International Energy Agency estimates that the total primary energy supply, the sum of all of the world's power sources, averaged over the year, will be between 20 and 24 TW by 2035 [1]. In comparison, the power from the sun intercepted by the earth is estimated to be 180,000 TW [2], meaning that the world's power demands could be comfortably met by covering just 0.3 % of the earth's surface with solar photovoltaics operating at a conversion efficiency of 10 %.

However, current solar cell technologies require highly purified silicon, resulting in high costs of production, energy-intensive fabrication processes, and long pay-back periods [3]. Recently, organic photovoltaics (OPVs) have been demonstrated as low-cost alternatives to silicon-based cells, with the possibility of low temperature "reel-to-reel" fabrication, necessary for large scale power generation [4]. The current barrier to commercial viability for organic photovoltaic cells is their low power conversion efficiencies and short lifetimes, which would need to be raised to around 10% and 10 years, respectively, to compete with current silicon cells [5].

Nanotechnology broadly encompasses the study of materials with at least one dimension

on the molecular to nanoscale (nanometer to submicron scale) [6]. It is currently an area of intense research; it was found that the total number of published nanotechnology papers increased from 8000 in 1991 to 87,000 in 2009 [7]. The field is highly interdisciplinary, bridging the subjects of physics, chemistry, materials science and biology, and applications are revolutionising industries ranging from automotive to medical to energy.

One rapidly growing area of nanotechnology includes carbon nanomaterials such as carbon nanotubes. Following the seminal paper by Iijima in 1991 [8], carbon nanotubes have received huge interest from the scientific community, and rapid discoveries of their remarkable electronic and mechanical properties have been made in the ensuing years. This is demonstrated by the plot in Fig. 1.1, which shows the rapid growth in the number of carbon nanotube papers published annually since 1990.

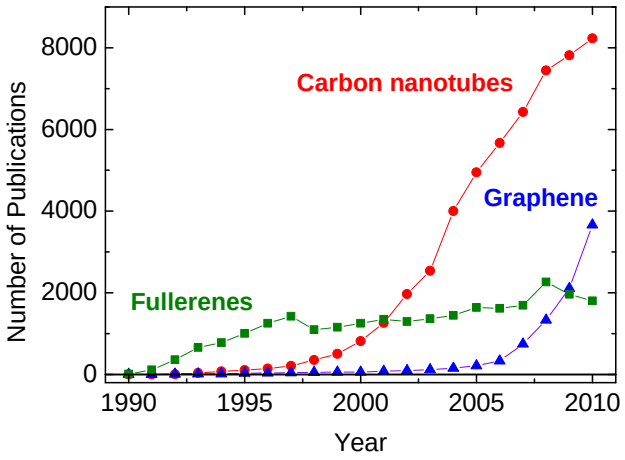

Figure 1.1: Plot showing the number of papers published each year since 1990 relating to carbon nanotubes, graphene or fullerenes. The data were extracted from the Scopus database [9].

Carbon nanotubes have been proposed as primary components in OPV devices, with the aim of achieving more efficient devices with high stabilities. However, devices based on carbon nanotubes have to date shown poor performances. The research described in this thesis addresses the issue of why carbon nanotubes have not been successfully incorporated into OPV devices and, in particular, investigates blends with semiconducting polymers that show particular promise for use in OPVs.

1.2 Carbon: The Element and its Allotropes

Carbon is a remarkable element that appears naturally in many different forms, ranging from molecules that comprise the building blocks of life to the hardest naturally occurring substance to recently discovered nanomaterials such as fullerenes, carbon nanotubes and graphene. Most of the materials presented in this thesis are carbon-based molecules and hence are classed as "organic" compounds.

To understand how the many carbon-based materials are formed, we must first consider the element's electronic configuration. An isolated carbon atom has six electrons which sequentially fill the atomic orbitals to give a configuration of $1s^2 2s^2 2p_x^1 2p_y^1$. The spherically symmetyric s- and the three dumbbell-shaped p-orbitals are illustrated in Fig. 1.2, where the p_x-, p_y- and p_z-orbitals are aligned along the (arbitrary) x, y and z axes, respectively [10].

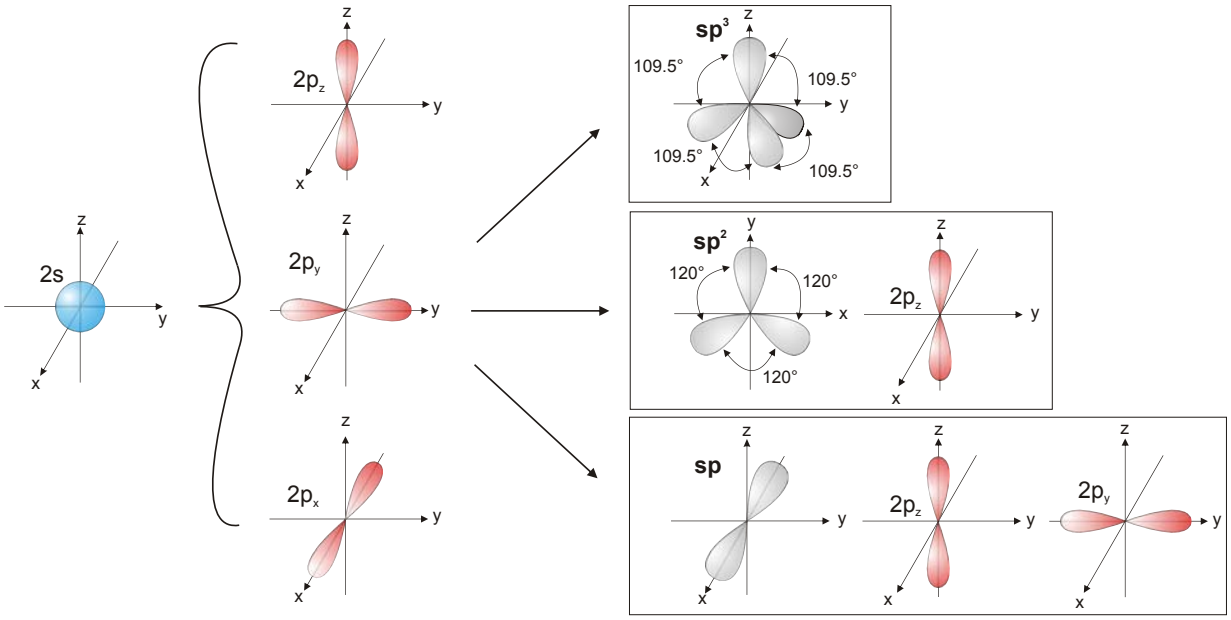

Figure 1.2: Linear combinations of the outer orbitals of carbon (2s, $2p_x$, $2p_y$ and $2p_z$) can be taken to give the hybridised sp^3-, sp^2- or sp-orbitals, which form σ-bonds with other atoms. The remaining unhybridised p-orbitals form π-bonds with neighbouring atoms.

Non-metallic atoms such as carbon form covalent bonds with other non-metals by the sharing of electrons between the atoms. A covalent bond between atoms can be described by considering the overlap of hybridised atomic orbitals. For carbon, this is achieved by first

promoting one of the 2s electrons to the empty p_z-orbital. Linear combinations of the s- and three p-orbitals, each containing a single electron, can be taken to form spatially directed hybrid orbitals [10]. The resulting orbitals [11] are illustrated in Fig. 1.2 and can take one of the following three hybridisations:

- All three p-orbitals are hybridised with the s-orbital to give four **sp^3-orbitals**, or
- the p_x- and p_y-orbitals are hybridised with the s-orbital to form three **sp^2-orbitals** but the p_z-orbital remains unhybridised, or
- only the p_x-orbital is hybridised with the s-orbital to form two **sp-orbitals**, leaving both the p_y- and p_z-orbitals unperturbed.

Covalent bonds are then formed by overlapping the directed hybridised orbitals with those from the other bonding atoms. For sp^3-hybridised carbon, the four sp^3-orbitals will overlap with an orbital from each of the four other atoms in a tetrahedral arrangement about the carbon to form four σ-(single) bonds. For sp^2-hybridised carbon, the three sp^2-orbitals will overlap with orbitals from each of the three other atoms to form three σ-bonds in a trigonal planar arrangement (*i.e.* bonds at 120° to each other) in the x-y plane. In addition, the remaining p_z-orbital, oriented orthogonally to the plane of the σ-bonds, will form a π-bond by overlapping with a p_z-orbital of one of the atoms, effectively forming a double bond. Finally, for sp-hybridised carbon, the two sp-orbitals will overlap with the orbitals of two other co-linear atoms to form two σ-bonds. The remaining p_y- and p_z-orbitals will be oriented orthogonally to the σ-bond and to each other and overlap with the corresponding p_y- and p_z-orbitals of one of the other atoms to form two π-bonds, making a triple bond overall [11].

The resulting linear combinations of the original atomic s- and p-orbitals can also be considered as 'molecular orbitals'. The σ- and π-bonds are represented by the lower energy bonding molecular orbitals (σ and π) if the orbital wavefunctions overlap constructively and the higher energy anti-bonding molecular orbitals (σ^* and π^*) in the case of destructive overlap [10].

Following this model, carbon can bond with itself and other atoms to form a vast array of molecules. The bonding can be in an sp^3-, sp^2- or sp-configuration about each C-atom, forming, for example, the backbones and side-chains of the long-chain polymer molecules that were used in this thesis and described in Chapter 2. Atomic carbon can also form large networks with itself to produce several different allotropes depending on the bonding (hybridisation) type. These allotropes are summarised in Fig. 1.3 and will be discussed below. Until the discovery of the carbon nanomaterials, namely fullerenes (1985), carbon nanotubes (1991) and graphene (2004), the carbon allotropes were widely thought to be limited to the naturally occurring diamond, graphite and amorphous carbon soot [9].

Diamond

In the sp^3-hybridised form, each carbon atom can bond to four other carbons in a tetrahedral geometry to give the 3-dimensional network constituting diamond, shown in Fig. 1.3 (a). Due to the strongly bonded and rigid network structure, diamond is the hardest naturally occurring substance known. It has the highest thermal conductivity of any bulk material [11] and is industrially used as a cutting tool. Such a rigid lattice only allows a small number of doping defects which lead to diamond's remarkable optical properties [11] and make it one of the most sought after gemstones.

Graphite

In the sp^2-hybridised form, carbon can form stable hexagonal arrangements in which each atom bonds to three others, one bond of which is a π-bond. This lattice can extend in all directions in the plane to give a sheet of hexagonal sp^2-carbons. The π-bonds form a large network on either side of the plane along which these π-electrons are delocalised. The π-electrons lead to strong intermolecular forces between sheets, allowing them to stack together and form a material known as graphite with an interlayer distance of 0.34 nm [12], as shown in Fig. 1.3 (b). The delocalised electrons lead to graphite being a very good electrical and thermal conductor within each sheet [11]. Graphite is also used as a lubricant, such as in

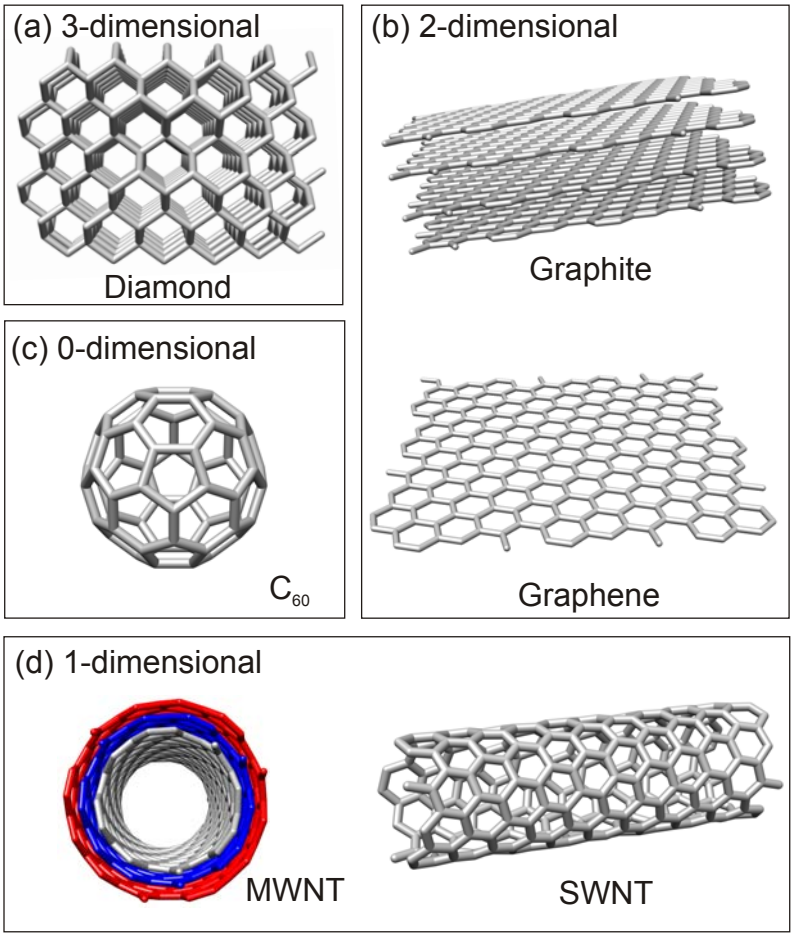

Figure 1.3: The allotropes of carbon. (a) The 3-dimensional sp^3-hybridised carbon tetrahedral network that constitutes diamond. (b) Sheets of sp^2-hybridised carbon in a hexagonal lattice that can stack to form graphite (top) or remain as a single atomic layer called graphene (bottom). (c) A spherical sp^2-hybridised carbon hexagonal structure called buckinsterfullerene (C_{60}). (d) Graphene sheets roll up to form fullerene cylinders called single-walled carbon nanotubes (right). If multiple shells are present it is a multi-walled carbon nanotube (left).

its everyday use as a "lead" pencil, because the weaker intermolecular forces between sheets (relative to the strong covalent bonding network within the sheets) mean they are able to easily slide over one another.

Graphene

A single sheet of hexagonal sp^2-hybridised carbon, one atom thick, is called graphene (Fig. 1.3 (b)). Graphene is a zero-bandgap semiconductor with very high electron mobilities and strong mechanical properties [13]. The isolation of single layers of graphene by

exfoliation of graphite was first demonstrated by Andre Geim and Konstantin Novoselov in 2004 at the University of Manchester [13] and, for this discovery and subsequent ground-breaking experiments, they were awarded the Nobel Prize for Physics in 2010. Since the electron delocalisation is in the plane of these materials, graphene and graphite are referred to as 2-dimensional semiconductors. Graphene has many potential applications, the most promising being in electronic applications such as touchscreen displays and transparent conducting electrodes in OPV devices.

Fullerenes

In 1985, chemists at Rice University discovered a closed spherical structure consisting of 60 carbon atoms in the hexagonal sp^2-hybridised arrangement. The structure was called buckminsterfullerene (otherwise bucky ball or C_{60}) and it is shown in Fig. 1.3 (c). This discovery gave rise to the fullerene family, which contains molecules comprised entirely of carbon in spherical, ellipsoidal or tubular shapes [11]. Many fullerenes have been discovered both naturally and synthetically in the years following the initial discovery by Robert Curl, Harold Kroto and Richard Smalley, leading to them being awarded the 1996 Nobel Prize in Chemistry. The strained geometry of the hexagonal lattice leads to enhanced chemical reactivity for fullerenes over other carbon allotropes [11]. The confinement of the electron density to the finite structure means C_{60} is a 0-dimensional semiconductor and often referred to as a carbon quantum dot [14]. Modified fullerenes are the electron accepting components in the current benchmark OPV devices.

Carbon Nanotubes

A single graphene sheet can be rolled up into a cylinder to form a fullerene called a single-walled carbon nanotube (SWNT), shown in Fig. 1.3 (d). Since the electron delocalisation is confined in the circumferential direction but not along the length of the tube, carbon nanotubes are 1-dimensional semiconductors. Carbon nanotubes can also be comprised of several concentric shells nested about the inner wall, called multi-walled carbon nanotubes

(MWNTs), with an intertube spacing the same as that of graphite (0.34 nm) [12]. The work in this thesis concentrates solely on SWNTs and will be the only type discussed herein.

There is controversy over who should receive credit for the discovery of carbon nanotubes. The first TEM images of nano-sized tubular carbon filaments appeared in the Journal of Physical Chemistry of Russia in 1952 [15] and it has been argued that the authors, Radushkevich and Lukyanovich, should be credited with the discovery of carbon nanotubes [16]. Over the following 40 years, many papers emerged describing nanotube-like objects and gradual improvements in TEM resolution allowed finer details to be resolved [16]. However, despite such earlier reports, Iijima is commonly credited for the discovery of carbon nanotubes as a result of his 1991 paper [8] that describes nanotubes on the cathode of a carbon arc used to produce fullerenes. It has been speculated that it was because the timing of Iijima's paper was just right – the scientific world was starting to embrace the "nano" revolution and it was the first time that the work was published in a journal widely accessible to many scientists across many fields [16]. The discovery of single-walled carbon nanotubes is less ambiguous and is attributed jointly to Iijima and Ichihashi (NEC) [17] and Bethune *et al.* (IBM) [18], who published two independent papers in 1993.

Carbon nanotubes are nanometre-sized in diameter but can be up to centimetres long, giving aspect ratios over 10^7. They are almost chemically inert, are two orders of magnitude stronger than steel under strain but $1/6^{\text{th}}$ of the weight and are stable in air up to 750 °C [19, 20]. Depending on the tube structure, they can exhibit ballistic electron conduction or semiconducting behaviour and have thermal conductances matching the record values of diamond [21, 22]. This remarkable collection of properties renders nanotubes ideal for a variety of current and future applications, including optoelectronic devices such as organic photovoltaics (discussed in this thesis), structural reinforcement, as well as other electronic, mechanical, chemical and biological applications.

Chapter 2

Theory and Background

2.1 Single-Walled Carbon Nanotubes (SWNTs)

2.1.1 Carbon Nanotube Synthesis

Carbon nanotubes are always produced with a distribution of different diameters and electronic structures depending on the synthetic method and subsequent purification and processing steps [19].

The earliest methods to produce SWNTs in large amounts were arc discharge and laser ablation, both involving the condensation of hot gaseous carbon atoms generated from the evaporation of solid carbon. However, this is very energetically inefficient and only powdered, bundled nanotube samples can be produced [19].

HiPCO (High-Pressure Catalytic Decomposition of Carbon Monoxide) is a method for the preparation of intermediate-diameter SWNTs using high-pressure CO as the carbon source [23]. A volatile organometallic catalyst species is introduced into the reactor which decomposes and forms metal clusters on which SWNTs nucleate and grow. It is a continuous-flow process and is currently the only method capable of producing SWNTs on a kilogram-per-day scale [12].

The development of the CoMoCAT process [24], where high selectivities for specific SWNT formation using a silica-supported Co-Mo catalyst are achieved [25], represented an important advance in the CO-method. The resultant nanotube distribution depends on the Co:Mo ratio and the catalyst treatments that precede nanotube growth [26], with the CoMoCAT process product containing a much narrower and smaller average diameter distribution than the HiPCO method [25].

Following synthesis, further purification is carried out to remove various impurities such as amorphous carbon, catalysts, and unwanted carbon species such as MWNTs [19]. Purification methods typically include oxidative methods, chemical functionalisation protocols, filtration and chromatography techniques, and microwave heating methods [27].

2.1.2 Characterising Carbon Nanotubes

A carbon nanotube is theoretically constructed by rolling up a flat graphene sheet. As such, nanotubes are labelled in terms of the graphene lattice vectors, $\mathbf{a_1}$ and $\mathbf{a_2}$ [12]. These vectors span the space defined by the plane of the hexagonal graphene lattice, as shown in Fig. 2.1, and have length $a_0 = |\mathbf{a_1}| = |\mathbf{a_2}| = 0.2461\,\text{nm}$ and are at an angle of $60\,^\circ$ to each other. The unit cell of the graphene lattice contains two carbon atoms at the positions $\frac{1}{3}(\mathbf{a_1} + \mathbf{a_2})$ and $\frac{2}{3}(\mathbf{a_1} + \mathbf{a_2})$, making the carbon-carbon bond distance $a_{\text{C}-\text{C}} = \frac{1}{\sqrt{3}}a_0 = 0.142\,\text{nm}$.

To form a nanotube, the graphene sheet is rolled up by joining two points defined by the vector $\mathbf{c} = n\mathbf{a_1} + m\mathbf{a_2}$. This vector is often referred to as the circumferential, "roll-up" or chiral vector and uniquely defines a particular nanotube with the chiral indices (n, m). This is illustrated in Fig. 2.1 for the construction of a (10,5) nanotube, as an example.

The chiral angle is defined as the angle θ between $\mathbf{c}$ and $\mathbf{a_1}$ and is given by:

$$\cos\theta = \frac{\mathbf{a_1} \cdot \mathbf{c}}{|\mathbf{a_1}|\,|\mathbf{c}|} = \frac{n + m/2}{\sqrt{n^2 + nm + m^2}}. \tag{2.1}$$

The six-fold rotational symmetry of the graphene lattice means that, for any chiral vector,

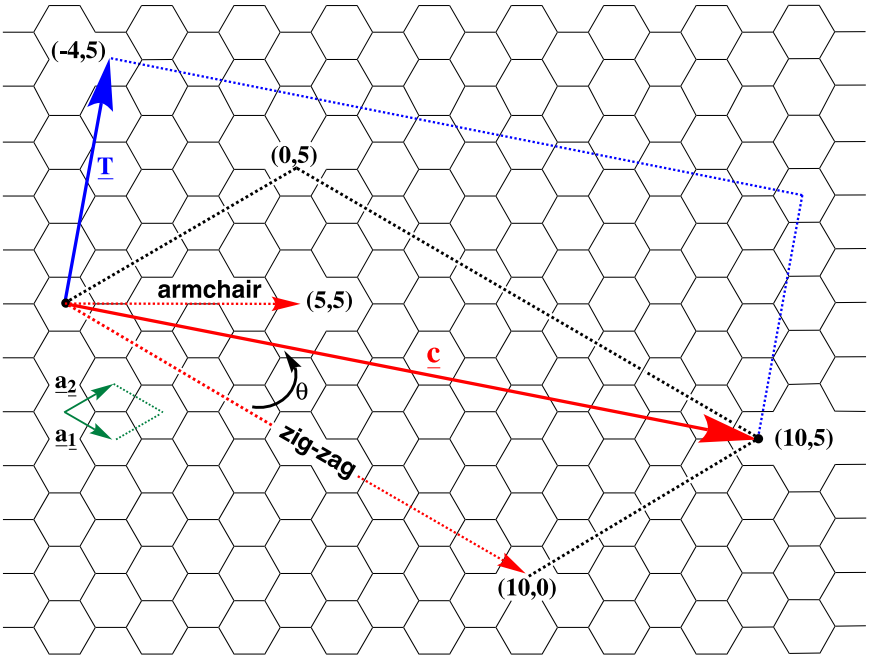

Figure 2.1: The notation used to characterise carbon nanotubes. The vectors $\mathbf{a_1}$ and $\mathbf{a_2}$ are basis vectors and span the space defined by the plane of the hexagonal graphene lattice. The chiral vector $\mathbf{c} = 10\mathbf{a_1} + 5\mathbf{a_2}$ (red arrow) joins the two points indicated and forms the circumference of a (10,5) nanotube. The translational vector $\mathbf{T}$ is orthogonal to $\mathbf{c}$. The chiral angle θ is also defined, and the chiral vectors of the special cases of zig-zag (10,0) and armchair (5,5) nanotubes are shown (red dotted arrows).

an equivalent one is found for $\theta \leq 60°$. Furthermore, for every $\theta \leq 30°$ the equivalent vector between 30° and 60° is found but of opposite handedness[1]. This means that the chiral angle can be restricted to $0° \leq \theta \leq 30°$. The special cases of $(n, 0)$ ($\theta = 0°$) and (n, n) ($\theta = 30°$) are referred to as zig-zag and armchair nanotubes, respectively, and classed as achiral nanotubes, whereas all other nanotubes are chiral nanotubes. Examples of such vectors are also shown in Fig. 2.1 and the resulting nanotubes are shown in Fig. 2.2.

The diameter d of the nanotube is determined by the chiral vector as:

$$d = \frac{|\mathbf{c}|}{\pi} = \frac{a_0}{\pi}\sqrt{n^2 + nm + m^2}. \tag{2.2}$$

[1]A chiral molecule is typically defined as one that has a non-superimposable mirror image giving rise to left- and right-handed enantiomers. In the case of the notation of nanotubes, the handedness is unimportant and the term chirality is used to refer to different (n, m) species.

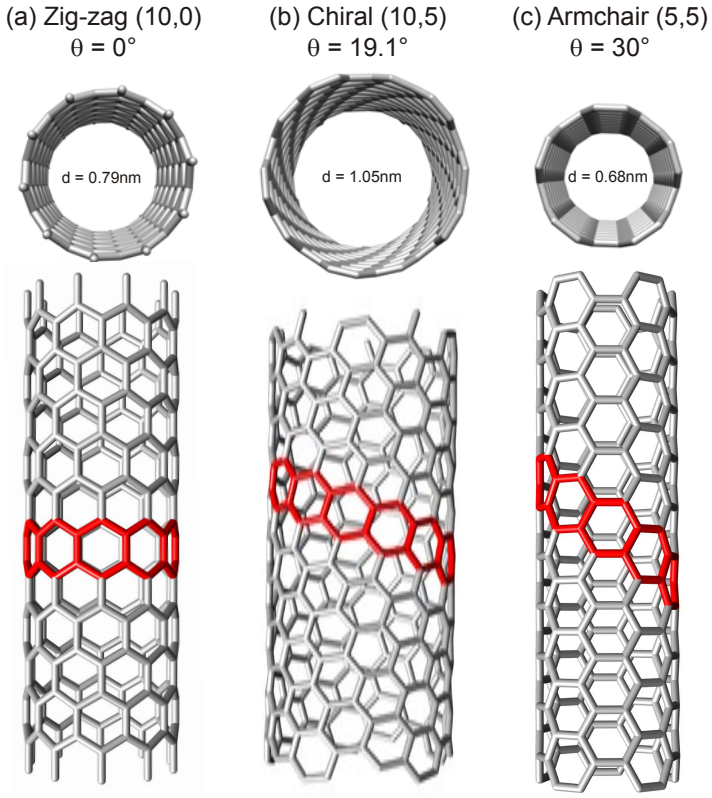

Figure 2.2: Figure showing the nanotubes constructed from the graphene sheet in Fig. 2.1 when viewed end-on (top) and side-on (bottom). The same segment of the graphene sheet is shown in red to emphasise the change in chiral angle as the tubes progress from (a) (10,0) zig-zag to (b) (10,5) chiral to (c) (5,5) armchair nanotubes.

The smallest graphene lattice vector $\mathbf{T}$ perpendicular to $\mathbf{c}$ gives the translational period $|\mathbf{T}| = a$ along the tube axis, given by:

$$\mathbf{T} = -\frac{n+2m}{jR}\mathbf{a_1} + \frac{2n+m}{jR}\mathbf{a_2}, \quad |\mathbf{T}| = a = \frac{\sqrt{3(n^2+nm+m^2)}}{jR}a_0 \tag{2.3}$$

where j is the greatest common divisor of both indices (n, m) and $R = 3$ if $(n - m)$ is a multiple of $3j$, otherwise $R = 1$. For the case of a (10,5) nanotube, $\mathbf{T} = -4\mathbf{a_1} + 5\mathbf{a_2}$, as shown in Fig. 2.1.

Finally, the nanotube unit cell is a cylinder of diameter d and height a which has an area defined by the parallelogram in Fig. 2.1 bound by the vectors $\mathbf{c}$ and $\mathbf{T}$ (*i.e.* $|\mathbf{c} \times \mathbf{T}|$).

The unit cell consists of a number Q of graphene hexagons given by the ratio of the area of the unit cell $S_{\text{unit cell}}$ to that of each hexagon S_{hex} such that:

$$Q = \frac{S_{\text{unit cell}}}{S_{\text{hex}}} = \frac{\frac{a_0^2\sqrt{3}(n^2+nm+m^2)}{jR}}{\frac{\sqrt{3}a_0^2}{2}} = \frac{2(n^2+nm+m^2)}{jR}. \tag{2.4}$$

2.1.3 Brillouin Zone

To derive the dispersion relation and other relevant quantities, we must work in reciprocal space and consider the Brillouin Zone of both graphene and carbon nanotubes. We first transform the lattice vectors $\mathbf{a_1}$ and $\mathbf{a_2}$, shown in Fig. 2.3 (a), to the corresponding reciprocal lattice vectors $\mathbf{k_1}$ and $\mathbf{k_2}$. The hexagonal Brillouin zone of graphene and high-symmetry points are shown in Fig. 2.3 (b), with the resulting vectors expressed in Cartesian coordinates [28].

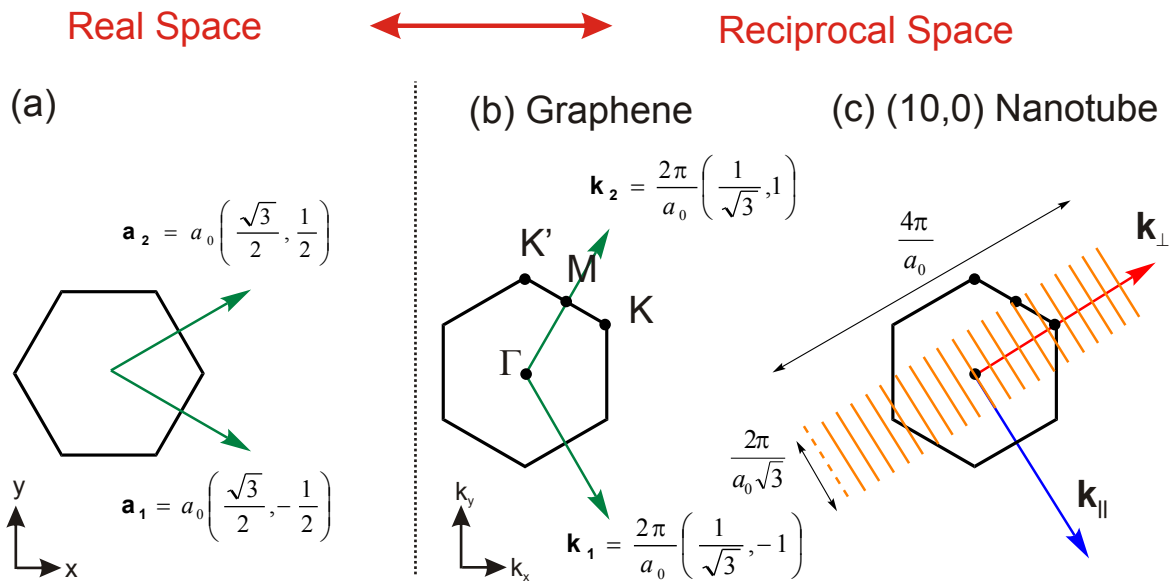

Figure 2.3: (a) A single graphene hexagon in real space with the lattice vectors $\mathbf{a_1}$ and $\mathbf{a_2}$ as defined in Fig. 2.1. (b) The hexagon in reciprocal space to show the graphene Brillouin zone, with the corresponding reciprocal lattice vectors $\mathbf{k_1}$ and $\mathbf{k_2}$ defined in Cartesian coordinates. The high-symmetry points Γ, M, K and K' are labelled, where the latter two are inequivalent points but degenerate under time-reversal [28]. (c) The Brillouin zone of a (10,0) nanotube showing the reciprocal vectors $\mathbf{k}_\parallel$ and $\mathbf{k}_\perp$ of the real-space vectors $\mathbf{T}$ and $\mathbf{c}$, respectively. Allowed wave vectors are shown in orange.

To obtain the nanotube Brillouin zone, we must transform the vectors $\mathbf{T}$ and $\mathbf{c}$ defining the unit cell of the nanotube to the reciprocal lattice vectors $\mathbf{k}_\parallel$ and $\mathbf{k}_\perp$, respectively, which can be expressed in terms of the reciprocal lattice vectors $\mathbf{k_1}$ and $\mathbf{k_2}$ as:

$$\mathbf{k}_\perp = \frac{2n+m}{QjR}\mathbf{k_1} + \frac{2m+n}{QjR}\mathbf{k_2}, \tag{2.5}$$

$$\mathbf{k}_\parallel = -\frac{m}{Q}\mathbf{k_1} + \frac{n}{Q}\mathbf{k_2}. \tag{2.6}$$

The length of the reciprocal translational vector is given by $\left|\mathbf{k}_\parallel\right| = k_\parallel = \frac{2\pi}{a}$ and the wave vector $\mathbf{k}_\parallel$ is continuous because the tube is regarded as infinitely long. Therefore, the first Brillouin zone along the tube length is in the interval $(-\pi/a, \pi/a]$ [12].

By contrast, the wave vector $\mathbf{k}_\perp$ corresponding to the circumference $\mathbf{c}$ of the nanotube must be quantised such that the wavefunctions of particles in nanotubes have phase shifts of integer multiples of 2π around the circumference and all other wavelengths vanish by interference [12]. That is,

$$|\mathbf{c}| = \pi \cdot d = i \cdot \lambda \quad \Longleftrightarrow \quad k_\perp = \frac{2\pi}{\lambda} = \frac{2\pi}{|\mathbf{c}|} \cdot i = \frac{2}{d} \cdot i, \tag{2.7}$$

where i takes integer values $\{-Q/2+1, \ldots, 0, 1, \ldots, Q/2\}$ (*i.e.* Q values). This means that the only allowed wave vectors in the $\mathbf{k}_\perp$ direction are discrete lines (continuous in the $\mathbf{k}_\parallel$ direction) spaced at a distance of $2/d$ apart. Therefore, the first Brillouin zone for nanotubes is given by Q lines of length $2\pi/a$ spaced at a distance of $2/d$ apart in the $\mathbf{k}_\perp$ direction, covering a total distance of $2Q/d$. This is illustrated for the (10,0) zig-zag nanotube in Fig. 2.3 (c).

2.1.4 Band Structure

The p_z-orbitals are perpendicular to the graphene plane and form the π-bonds, which can be represented by π (bonding) and π^* (antibonding) molecular orbitals. The p_z electrons can be treated independently of the other valence electrons and the electronic properties of graphene, and hence carbon nanotubes, can be derived by considering only these π-orbitals [12].

The band structure of graphene can be calculated using the tight-binding (TB) model first employed by Wallace in 1947 [29]. The solutions (eigenfunctions) of the Schrödinger equation are written as linear combinations of the Bloch functions which, in the TB approximation, are themselves written as linear combinations of the p_z-atomic wavefunctions (orbitals) [12]. The theory is further simplified by considering only the interactions between nearest neighbours (*i.e.* every atom interacts with itself and three other atoms only) and by treating the two carbon atoms in the graphene unit cell as identical. The eigenvalue solutions of the Schrödinger equation for the graphene system give the dispersion relation as[2]:

$$E_{2\mathrm{D}}^{\pm}(\mathbf{k}) = \frac{\epsilon_{2p} \pm \gamma_0 \sqrt{f(\mathbf{k})}}{1 \mp s_0 \sqrt{f(\mathbf{k})}}, \tag{2.8}$$

where E^+ and E^- are the conduction π^* and valence π energy bands, respectively, $\mathbf{k}$ is any wave vector, ϵ_{2p} is the site energy of the $2p_z$ atomic orbital, γ_0 is the carbon-carbon interaction energy (transfer integral) and s_0 is the overlap integral between a carbon atom and one of its neighbours [12, 28]. The function $f(\mathbf{k})$ is given by:

$$f(\mathbf{k}) = 3 + 2\cos(\mathbf{k}\cdot\mathbf{a_1}) + 2\cos(\mathbf{k}\cdot\mathbf{a_2}) + 2\cos(\mathbf{k}\cdot(\mathbf{a_2}-\mathbf{a_1})). \tag{2.9}$$

The values of γ_0 and s_0 are often used as fitting parameters or obtained from *ab initio* calculations. Near the K point, the function $f(\mathbf{k})$ vanishes and the valence and conduction bands are zero relative to the Fermi level and $\epsilon_{2p} = 0$. Often the wavefunction overlap

[2] A derivation is not provided here but the interested reader is directed to Ref. [12].

between the adjacent atoms and the site energy are both set to zero ($s_0 = 0$ and $\epsilon_{2p} = 0$), in which case Eq. 2.8 simplifies to the symmetric relation:

$$E_{2D}^{\pm}(k_x, k_y) = \pm\gamma_0\sqrt{1 + 4\cos\frac{\sqrt{3}k_x a_0}{2}\cos\frac{k_y a_0}{2} + 4\cos^2\frac{k_y a_0}{2}}, \tag{2.10}$$

where k_x and k_y are the Cartesian coordinates in reciprocal space. An energy contour plot of the conduction band energies of graphene is shown in Fig. 2.4 (a) using $\gamma_0 = 2.9\,\text{eV}$ [12].

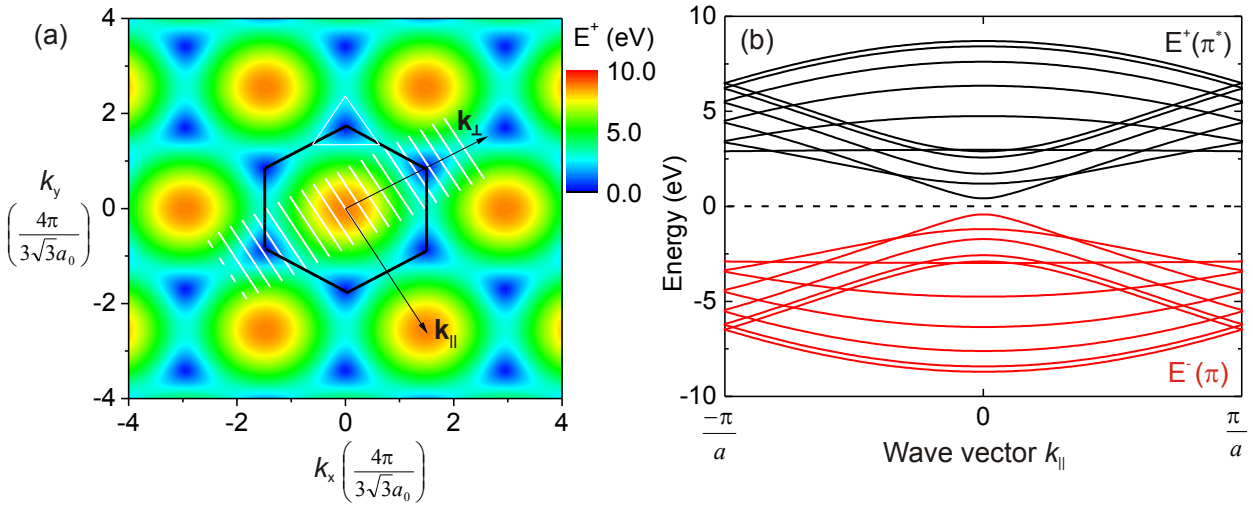

Figure 2.4: (a) Countour plot to show the E^+ values of graphene calculated from the tight-binding model (Eq. 2.10) using $\gamma_0 = 2.9\,\text{eV}$. The first Brillouin zone of graphene is denoted by the black hexagon and the first Brillouin zone of the (10,0) nanotube is shown by the white lines. The white triangle highlights the trigonal warping effect, as discussed in section 2.1.7. (b) The approximate (10,0) nanotube band structure given by the graphene electronic energies along the allowed k lines according to the zone-folding approximation. These are given by Eq. 2.11 and the different lines correspond to the range of values of i, where $\pm i$ values are degenerate.

We have seen that the nanotube circumferential wave vectors are quantised but those along the nanotube axis are continuous. The allowed wave vectors when overlaid onto the Brillouin zone of graphene are a series of parallel lines whose number, length and spacing depend on the nanotube's chiral indices (n, m). The ***zone-folding*** approximation takes the nanotube band structure as the graphene electronic levels along the allowed k lines [12] in the first Brillouin zone. That is, the nanotube energy dispersion relations are given by:

$$E^{\pm}_{\mathrm{SWNT}}(i, k_{\parallel}) = E^{\pm}_{\mathrm{2D}} \left(i\mathbf{k}_{\perp} + k_{\parallel} \frac{\mathbf{k}_{\parallel}}{|\mathbf{k}_{\parallel}|} \right), \tag{2.11}$$

where i again takes integer values $\{-Q/2+1, \ldots, 0, 1, \ldots, Q/2\}$ and $-\frac{\pi}{a} < k_{\parallel} < \frac{\pi}{a}$. The allowed wave vectors for the (10,0) nanotube are superimposed on the graphene Brillouin zone in Fig. 2.4 (a) and the corresponding slices of the graphene band structure at the allowed wave vectors (*i.e.* the carbon nanotube band structure) are shown in Fig. 2.4 (b).

2.1.5 Semiconducting and Metallic Nanotubes

The band structure shown in Fig. 2.4 (b) shows that a bandgap exists between the valence and conduction bands; a (10,0) nanotube is regarded as a semiconducting tube. However, the bands cross the Fermi level at the K points in the graphene band structure shown in Fig. 2.4 (a). Therefore, if one of the allowed wave vectors passes through the K point, the nanotube is metallic (*i.e.* has no bandgap). This situation is illustrated in Fig. 2.5 for (6,3) metallic and (6,5) semiconducting nanotubes.

The K point is given by $\mathbf{K} = \frac{1}{3}(\mathbf{k_1} - \mathbf{k_2})$ and a nanotube is metallic if:

$$\mathbf{K} \cdot \mathbf{c} = 2\pi p = 2\pi \cdot \frac{1}{3}(n-m) \Rightarrow (n-m) = 3p, \tag{2.12}$$

where p is an integer. This result was first shown by Hamada *et al.* [30] and Saito *et al.* [31] and states that a nanotube is metallic if $(n-m)$ is a multiple of 3. The condition can be generalised to give:

$$(n-m) = 3p + q, \quad q = \begin{cases} 0 & \text{metallic tubes} \\ \pm 1 & \text{semiconducting tubes} \end{cases} \tag{2.13}$$

Therefore, one third of all nanotubes are metallic while the remaining $q = \pm 1$ represent the two families of semiconducting tubes. All armchair nanotubes are metallic but zig-zag and

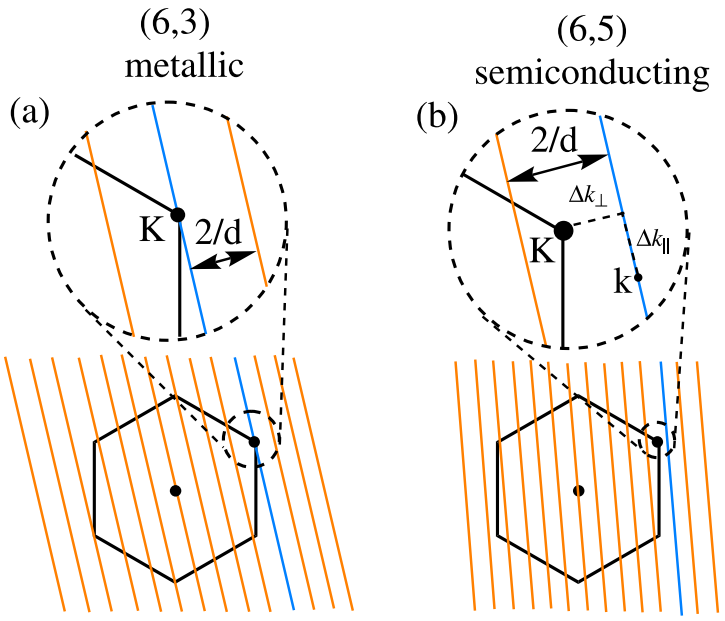

Figure 2.5: (a) Allowed k lines for a (6,3) nanotube. The dashed lines show the section zoomed in on the K point, where an allowed wave vector passes directly through the K point, making it a metallic tube. (b) Allowed wave vectors for a (6,5) semiconducting nanotube. The distances $\Delta k_{\|}$ and $\Delta k_{\perp}$ are defined about the K point, where the latter quantity is equal to $4/3d$ (*i.e.* the K point lies two-thirds of the distance $2/d$ between the allowed k lines).

general chiral tubes are only metallic if they satisfy Eq. 2.12. It follows that the K point lies at two-thirds of the distance $\frac{2}{d}$ between the allowed wave vectors for semiconducting tubes.

2.1.6 Density of States

The density of electronic states (DOS) gives the number of available sites for electrons to occupy in a given energy interval and its form depends strongly on the dimension of the system. The universal density of states for carbon nanotubes (one-dimensional systems) was derived by Mintmire and White [32] and is given by:

$$n(E) = \frac{2}{Q\left|\mathbf{k}_{\|}\right|} \sum_{\ell} \int dk_{\|} \delta(k_{\|} - k_{\ell}) \left| \frac{\partial E^{\pm}(k_{\perp}, k_{\|})}{\partial k_{\|}} \right|^{-1}, \tag{2.14}$$

where k_{ℓ} are the roots of $E - E(k_{\ell}) = 0$ and $Q\left|\mathbf{k}_{\|}\right| = 4\pi^2 d/\sqrt{3}a_0^2$. To calculate $n(E)$ at a vector $\mathbf{k}$ near the Fermi level and hence near the K point $\mathbf{K}$, it is useful to expand the

graphene energy bands in Eq. 2.10 to first order, to give the linear dispersion relation:

$$E^{\pm}(\mathbf{k}) \approx \pm\frac{\sqrt{3}}{2}a_0\gamma_0\left|\mathbf{k}-\mathbf{K}\right|. \tag{2.15}$$

The geometry of the problem is illustrated in Fig. 2.5 (b), where the distance to the point $\mathbf{k}$ is given by $|\mathbf{k}-\mathbf{K}| = \sqrt{\Delta k_{\parallel}^2 + \Delta k_{\perp}^2}$. The quantity $\Delta k_{\parallel}$ is the component parallel to $\mathbf{k}_{\parallel}$ and takes continuous values. By contrast, the quantity $\Delta k_{\perp}$ takes quantised values along the $\mathbf{k}_{\perp}$ direction given by the projection of $(\mathbf{k}-\mathbf{K})$ onto $\mathbf{k}_{\perp}$:

$$\Delta k_{\perp} = \left|(\mathbf{k}-\mathbf{K})\cdot\frac{\mathbf{k}_{\perp}}{|k_{\perp}|}\right| = \frac{2}{3d}\left|3i-q\right|, \tag{2.16}$$

where q is defined in Eq. 2.13 and i takes integer values. The derivative term is given by:

$$\left|\frac{\partial E^{\pm}(k_{\perp},k_{\parallel})}{\partial k_{\parallel}}\right|^{-1} = \left|\frac{\sqrt{3}}{2}a_0\gamma_0\frac{\partial\sqrt{\Delta k_{\parallel}^2+\Delta k_{\perp}^2}}{\partial k_{\parallel}}\right|^{-1} = \left(\frac{2}{\sqrt{3}a_0\gamma_0}\right)\frac{|E^{\pm}|}{\sqrt{(E^{\pm})^2-E_i^2}}, \tag{2.17}$$

with

$$E_i = \frac{\sqrt{3}}{2}a_0\gamma_0\Delta k_{\perp} = |3i-q|\,\frac{a_0\gamma_0}{\sqrt{3}d}. \tag{2.18}$$

Finally, inserting these expressions into Eq. 2.14 and integrating gives the density of states as:

$$n(E) = \frac{4a_0}{\pi^2 d\gamma_0}\sum_{i=-\infty}^{\infty} g(E,E_i), \quad g(E,E_i) = \begin{cases} \frac{|E|}{\sqrt{E^2-E_i^2}} & |E| > |E_i| \\ 0 & |E| < |E_i| \end{cases} \tag{2.19}$$

The singularities in the DOS at energies E_i are called the ***van Hove singularities*** [12]. These values are given by $E_i = ia_0\gamma_0/\sqrt{3}d$ where $i = 0, 3, 6, \ldots$ for metallic tubes and

$i = 1, 2, 4, 5, 7, \ldots$ for semiconducting tubes and, in this Mintmire and White approximation [32], depend only on the tube diameter d. Metallic nanotubes therefore have no bandgap but semiconducting tubes have a finite bandgap equal to:

$$E_{11}^{\mathrm{S}} = 2E_{i=1} = 2a_0\gamma_0/\sqrt{3}d. \tag{2.20}$$

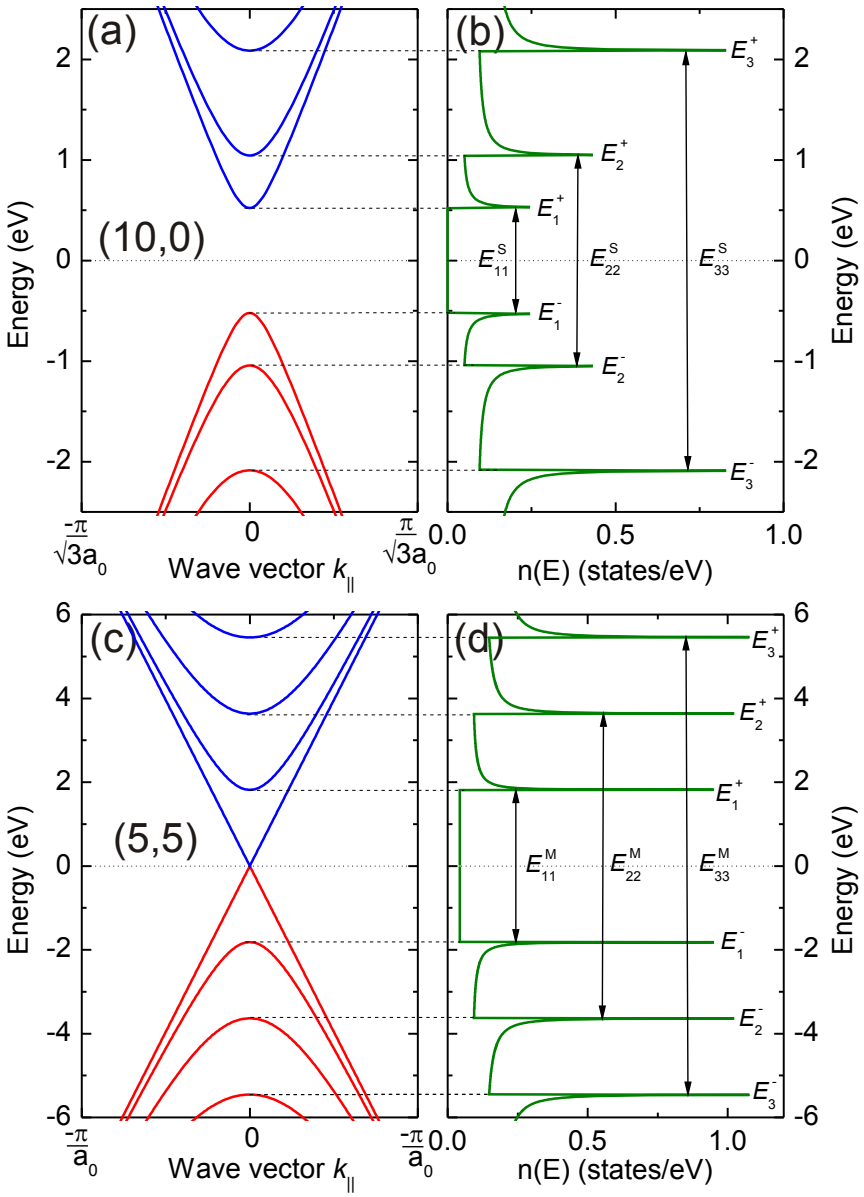

Figure 2.6: (a) and (c) Band structures near the K point under the linearised approximation given by Eq. 2.15 for the semiconducting (10,0) and metallic (5,5) tubes, respectively. The corresponding DOS governed by Eq. 2.19 are shown in (b) and (d), respectively. The relevant energy levels and gaps described in the text are labelled.

The band structure near the K point using the approximation in Eq. 2.15 is shown in Fig. 2.6 (a) for a (10,0) semiconducting nanotube and in Fig. 2.6 (c) for a (5,5) metallic nanotube. The corresponding DOS from Eq. 2.19 are shown in Fig. 2.6 (b) and (d), respectively, and the energy gaps between the i-th energy levels are also labelled for both metallic (E_{ii}^{M}) and semiconducting (E_{ii}^{S}) tubes.

2.1.7 Corrections to the Band Structure

Many simplifying approximations were made to derive the band structure and DOS expressions presented here. The energy bands were calculated using the nearest-neighbour TB approximation and an overlap parameter $s_0 = 0$ and were further approximated by considering a linear dispersion about the K point. The derived band structure requires several corrections to better approximate the entire band structure.

Near the K , K' and Γ points, the constant energy surfaces of the dispersion relation of graphene are circles and the approximations used earlier are valid. However, for intermediate wave vectors about the K and K' points, the equi-energy contours resemble triangles joining the nearest M points, as shown in Fig. 2.4 (a) [28]. Under the zone-folding approximation, the slices of the graphene dispersion relation corresponding to allowed wave vectors for nanotubes give the band structure, which are symmetrical for small wave vectors about the K and K' points. The triangular energy contours at larger wave vectors lead to asymmetries in the energy bands because the energy minima (energy at the point of vanishing slope) for each band are different either side of the K point. This distortion of energy contours away from circular in species with a three-fold symmetry axis is called the ***trigonal warping effect***. It leads to deviations in the bandgaps derived earlier [28, 33], where bandgap shifts are observed for semiconducting tubes and the DOS becomes split for non-armchair metallic nanotubes [33]. Since the chiral angle gives the angle of the allowed wave vector relative to the triangular equi-energy countours, the deviations are largest for smaller chiral angle tubes.

The earlier derivations would be equally valid for a long, narrow strip of graphene because

curvature of the nanotube walls was not taken into account. When rolled into a cylinder, the carbon-carbon bonds along and perpendicular to the tube axis deviate slightly and this results in different lengths of the basis vectors $\mathbf{a_1}$ and $\mathbf{a_2}$ [12]. The equivalence of neighbours used in the TB model is no longer valid. Furthermore, the p_z-orbitals are no longer parallel, giving different transfer integral values γ_0 between each carbon atom and its neighbours [34]. For an armchair tube, these effects shift the Fermi wave vector along an allowed wave vector and the tube remains truly metallic. By contrast, for non-armchair metallic tubes, the shift is not parallel to the allowed k lines and a small, finite secondary bandgap opens up ($\sim$10 meV) given by:

$$E'_{\text{gap}} = \frac{\gamma_0 a_0^2}{4d^2} \cos 3\theta. \tag{2.21}$$

Finally, on the curved nanotube wall, the π-orbitals can mix with the σ-orbitals to form new hybridised orbitals that are partly of sp^2 and partly of sp^3 character [35]. The mixing effect is more apparent for smaller diameter nanotubes and causes the σ^*- and π^*-bands to repel each other, effectively changing the energy and character of the lowest lying conduction band states.

2.1.8 Effects of Mechanical Strain

We now extend the theory to investigate the band structure changes following perturbations to the nanotube's structure (*e.g.* mechanical strain by radial compression or stretching along the tube axis). Strain deforms the hexagonal lattices, and the real space vectors in the undeformed lattice $\mathbf{r}$ transform to the deformed lattice vectors $\mathbf{r'} = (\mathbf{I} + \epsilon)\mathbf{r}$ under the action of a uniform 2D strain tensor ϵ (2x2 matrix). The Brillouin zone and allowed k lines are invariant and only the changes in the Fermi point $\mathbf{k_F}$ relative to the invariant k lines need to be considered [36].

We can describe a small shift $\Delta\mathbf{k_F}$ of the Fermi point $\mathbf{k_F}$ away from the K point $\mathbf{K}$ by $\mathbf{k'_F} = \mathbf{K} + \Delta\mathbf{k_F}$. The geometry of the situation is shown in Fig. 2.7 (a) and (b) for $q = \pm 1$

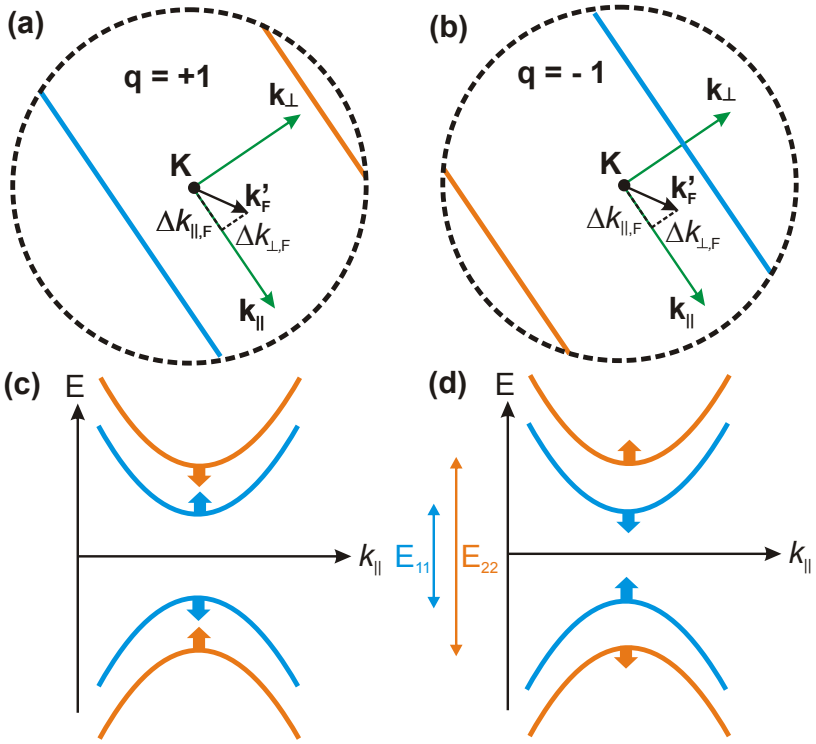

Figure 2.7: Brillouin zone about the K point $\mathbf{K}$ showing the shift in the Fermi point to $\mathbf{k'_F}$ due to strain applied to the nanotube for (a) $q = +1$ and (b) $q = -1$ semiconducting tubes. $\Delta\mathbf{k_F}$ is made up of magnitudes $\Delta k_{\parallel,\mathrm{F}}$ along $\mathbf{k}_\parallel$ and $\Delta k'_{\perp,\mathrm{F}}$ along $\mathbf{k}_\perp$. The corresponding changes to the E_{ii} bandgaps are shown in (c) and (d), respectively.

semiconducting tubes, respectively. We again expand the graphene dispersion relation to first order about the shifted Fermi point $\mathbf{k'_F}$ to obtain the same approximation as Eq. 2.15 ($\mathbf{K} \rightarrow \mathbf{k'_F}$). It follows that the DOS is again given by Eq. 2.19 except that the van Hove energies in Eq. 2.18 are altered to:

$$E_i = \frac{\sqrt{3}}{2} a_0 \gamma_0 \Delta k'_\perp, \quad \Delta k'_\perp = \left| \frac{2}{3d}(3i - q) - \Delta k_{\perp,\mathrm{F}} \right|, \tag{2.22}$$

where the quantised component along the circumference is:

$$\Delta k_{\perp,\mathrm{F}} = \frac{\sqrt{3}}{a_0} \left[(1+\nu)\epsilon_\parallel \cos 3\theta + \epsilon_\perp \sin 3\theta \right]. \tag{2.23}$$

Eq. 2.23 arises by solving the Schrödinger Equation at $\mathbf{k'_F}$ to first order in ϵ and $\Delta\mathbf{k_F}$.

$\epsilon_{\parallel}$ and $\epsilon_{\perp}$ are the strain components along the tube axis (uniaxial) and circumference (torsional), respectively, and ν is Poisson's ratio [36]. By combining this theory developed by Yang and Han [36] with the theory developed by others [37, 38], the overall change to the energy gap ΔE_{ii} under small strains is:

$$\Delta E_{ii} = -\frac{4\gamma_0 a_0 i}{\sqrt{3}d}(\epsilon_{\perp} - \nu\epsilon_{\parallel}) + 3(-1)^{q+1}(-1)^{i+1}\gamma_0[(1+\nu)\epsilon_{\parallel}\cos 3\theta + \epsilon_{\perp}\sin 3\theta]. \qquad (2.24)$$

The first term is related to the change in C-C bond lengths upon application of strain and the sign is independent of the transition level i [39]. The second term is dominant and comes directly from Eq. 2.23. It shows that the two families of semiconducting nanotubes ($q = \pm 1$) exhibit opposite behaviour under mechanical strain, with an increase in the E_{11} transition energy (bandgap) for $q = +1$ and a decrease in E_{11} for $q = -1$ tubes, with this behaviour reversed for E_{22} transitions [36, 40]. For $q = +1$ tubes, the Fermi point essentially moves further away from the allowed wave vector corresponding to the E_{11} transition (*i.e.* an energy increase) and closer to the wave vector corresponding to the E_{22} transitions (*i.e.* an energy decrease), with the opposite behaviour for $q = -1$. These changes are illustrated in Fig. 2.7 (c) and (d) for $q = \pm 1$ semiconducting tubes, respectively.

2.1.9 Optical Transitions

Now that the nanotube band structure has been described, the selection rules for optical transitions between the van Hove singularities can be considered. Any transition must obey conservation of energy and momentum. Conservation of linear momentum ($\Delta\mathbf{k} = \mathbf{0}$) means that only vertical transitions are allowed on plots such as Fig. 2.8 (a) [41]. The selection rules for conservation of angular momentum depend on the orientation of the electric field $\mathbf{E}$ of the light. When a nanotube aligned along $\mathbf{T}$ absorbs or emits a photon with angular momentum of ± 1, the selection rules are:

$$\Delta i = 0 \quad \text{for} \quad \mathbf{E} \parallel \mathbf{T}, \tag{2.25}$$

$$\Delta i = \pm 1 \quad \text{for} \quad \mathbf{E} \perp \mathbf{T}, \tag{2.26}$$

where i is the same integer quantum number used in Eq. 2.18 [41]. Therefore, the transitions E_{11}, E_{22}, E_{33} and higher orders are allowed for light polarised along the nanotube axis and transitions such as E_{21} are allowed for light polarised perpendicular to the tube axis; a selection of these transitions are shown in Fig. 2.8 (a). The perpendicular transitions are on average 5 times weaker than those corresponding to parallel excitations due to screening induced by the depolarisation (antenna) effect [12, 42].

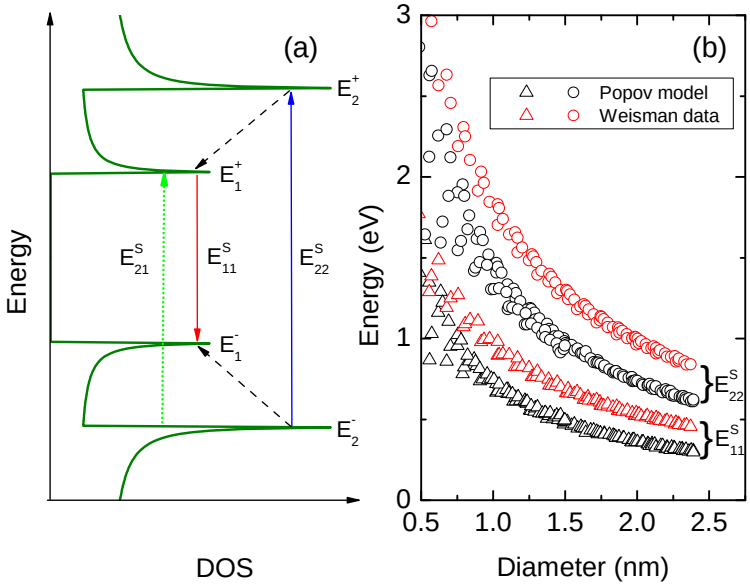

Figure 2.8: (a) DOS for a semiconducting nanotube showing some of the optical transitions. Absorption of light corresponding to E_{22} (blue solid line) promotes an electron from the valence E_2^- band to the conduction E_2^+ band and leaves a hole in E_2^-. Rapid relaxation of the electron and hole occurs to the E_1^+ and E_1^- bands, respectively, (dashed black lines) and the electron subsequently recombines with the hole, emitting a photon of energy E_{11} (solid red line). The perpendicular absorption transition E_{21} is also shown (dotted green line). (b) Kataura plot using the extended TB model developed by Popov *et al.* [43] (black symbols), along with the empirical data obtained by Weisman and Bachilo [44] (red symbols).

By Fermi's Golden Rule, the intensities of the absorption transitions E_{ij} depend on the matrix element given by the overlap between the wavefunctions of the initial valence band

state (at energy E_i^-) and the final conduction band state (at energy E_j^+) under the action of a perturbed Hamiltonian [45]. In an E_{ij} absorption transition, an electron is promoted from the valence band E_i^- to the conduction band E_j^+, leaving a hole in the E_i^- band.

If the excitation involves states higher than $E_1^\pm$, rapid relaxation (<100 fs) of the electron and hole occurs by phonon emission to the E_1^+ and E_1^- levels, respectively [46, 47]. The electron and hole subsequently recombine and a photon of energy E_{11} is emitted, *i.e.* photoluminescence. This chain of processes is often exploited experimentally to excite the nanotube E_{22} transitions and monitor the E_{11} emission using a technique called ***photoluminescence excitation (PLE) spectroscopy***, which was utilised in this thesis. Due to the large DOS at the van Hove singularities, carbon nanotubes have strong, narrow absorption and photoluminescence features. Recent experimental work has shown that the absorption cross-section of the E_{11} transition is $\sim 1.7\times10^{-17}\,\mathrm{cm}^2$ per carbon atom for (6,5) nanotubes [48]. The sets of transitions (E_{11},E_{22}) provide a unique fingerprint of each (n, m) nanotube and PLE spectroscopy provides a powerful optical characterisation tool.

2.1.10 Kataura Plot

The simple TB theory predicts that the nanotube transitions E_{ii} are inversely proportional to the tube diameter d (Eq. 2.20) and a plot of the two quantities was first presented by Kataura *et al.* in 1999 [49]. However, the differences between these values and the experimentally derived values are large, particularly for small chiral angles. To improve the approximation, an extended TB model was developed by Popov *et al.* [43], which included the effects of trigonal warping and rehybridisation arising from curvature. A 'Kataura plot' using the values from Popov *et al.* is shown in Fig. 2.8 (b) and it provides a very good model for the unperturbed band edge states.

An empirical model was proposed by Bachilo *et al.* [50] in 2002 from photoluminescence data and was subsequently refined by Weisman and Bachilo in 2003 [44]. The results are also presented in Fig. 2.8 (b) and these data allow easy identification of nanotubes in a distribution using optical experiments. The plot shows clear discrepancies between the Popov

model and the empirical values. The latter values are systematically blue-shifted with respect to the former and this deviation is known as the 'blue-shift problem'. Furthermore, both the simple (Eq. 2.18) and the Popov extended TB models predict the energy ratio $E_{22}/E_{11} = 2$ in the large-diameter limit in which trigonal warping and curvature effects are negligible. However, the ratio of the empirical Weisman values converge to $E_{22}/E_{11} \sim 1.75$ for large diameters; this discrepancy is called the 'ratio problem' [50]. These anomalies were able to be reconciled by including the effects of excitons and many-body interactions in nanotubes.

2.1.11 Excitons and Many-Body Effects

Excitons are quasi-particles comprised of electron-hole pairs that are Coulombically bound. Wannier-Mott excitons are often referred to as free excitons because they are delocalised over several unit cells and have low exciton binding energies ($\sim$0.01 eV) [51]. They are present in high dielectric materials where the screening of the Coulomb interactions is large, for example in traditional semiconductors such as GaAs (exciton binding energy $\sim$3 meV [10]). By contrast, Frenkel excitons are tightly bound and have radii comparable to the size of the unit cell. Their binding energies are much larger ($\sim$0.1-1 eV) and they are found in materials with poor dielectric screening such as organic semiconductors.

The importance of excitons in carbon nanotubes was first predicted by Ando in 1997 [52]. In 2004, *ab initio* studies including the effect of excitons were carried out and excellent fits to the Weisman and Bachilo experimental data were found, with large exciton binding energies for semiconducting tubes and the existence of bound excitons in metallic SWNTs predicted [53, 54, 55]. Conclusive experimental proof of nanotube excitons was provided in 2005 from two-photon absorption experiments [56, 57]. In this thesis, the unperturbed nanotube energy levels were therefore determined using the Popov model but the nanotube optical transitions and energy levels of photoexcited tubes were found using the Weisman and Bachilo empirical model.

Nanotube excitons are considered to have both Frenkel and Wannier-Mott character. They are delocalised over several unit cells along the tube length with exciton sizes

$\sim$1–3 nm [48, 58, 59, 60]. However, the binding energies, which were found to scale inversely with diameter, are large, with values typically $\sim$400 meV [56] but can be as large as 1 eV [59]. This is because of the reduced dimensionality and poor screening of an exciton in a tube in which the field lines lie mainly outside of the tube. Nanotube excitons were previously elusive because, in such 1-dimensional systems, nearly all of the oscillator strength is transferred to the exciton from the van Hove singularities, making it very difficult to assign without an accurate knowledge of the van Hove positions [52].

The presence of excitons and many-body effects leads to two counteracting corrections to the band gap values obtained in the extended TB approximations, E_{ii}^{TB}. The repulsive forces acting on the excited electron from the surrounding electrons will contribute to an increase in the gap value by an amount $E_{\mathrm{e-e}}$ (*i.e.* self-energy effects). However, the attractive Coulomb binding energy between the excited electron and remaining hole will contribute to a decrease in the gap value by the equivalent of the exciton binding energy, $E_{\mathrm{e-h}}$. Therefore, the experimentally measured optical transition is predicted to be:

$$E_{ii}^{\mathrm{exp}} = E_{ii}^{\mathrm{TB}} + E_{\mathrm{e-e}} - E_{\mathrm{e-h}}. \tag{2.27}$$

The net effect is a relatively small blue-shift [53, 61, 62], resolving the blue-shift problem. Furthermore, the correction is proportionately larger for E_{11} than for E_{22}, providing an explanation for the ratio problem [53, 61, 63].

The electron-electron $E_{\mathrm{e-e}}$ and electron-hole $E_{\mathrm{e-h}}$ Coulombic contributions are screened in the presence of dielectric material (dielectric constant ϵ_{r}) around the nanotube [64, 65] such as a solvent [66] or a dispersing surfactant [67]. It was found experimentally that the latter exciton binding energy component scales as $\epsilon^{-1.4}$ [58] and it has been argued that the electron-electron term scales as ϵ^{-1}, as predicted by classical theory [68, 69]. The net effect is a decrease (red-shift) in the optical transition energies E_{ii}^{exp} with increasing surrounding dielectric material because the relative magnitude of the blue-shifting $E_{\mathrm{e-e}}$ component is larger than the red-shifting $E_{\mathrm{e-h}}$ component [66].

In low density excitation processes, nanotube excitons were found to have lifetimes of the order of ∼10–100 ps [70, 71, 72] and corresponding diffusion lengths ranging from ∼10–100 nm for surfactant-wrapped tubes [60, 73, 74], up to ∼200–600 nm for air-suspended tubes [75, 76]. At higher excitation densities, where significant numbers of excitons are found on each nanotube, the exciton decay dynamics are dominated by exciton-exciton annihilation processes (Auger recombination), occurring on a 1–5 ps timescale [71, 72, 77, 78], in which one exciton rapidly relaxes by releasing its energy to a second exciton and promoting it to a higher-energy excited state [19].

2.1.12 Photoluminescence Quantum Efficiency

The excitonic states appear analogously to the Rydberg hydrogen series below the single-particle van Hove singularity continuum [56]. Within each Rydberg state, the energy levels are further split into a single 'bright' (optically active) and three 'dark' (optically inactive) states according to the excitonic selection rules [79]. By analogy to the processes represented in Fig. 2.6 (a), absorption to higher E_{ii} states in the excitonic model leads to rapid phonon-assisted cooling [46, 47] to the lowest E_{11} Rydberg state (1s), recombination of the exciton from the lowest optically bright state, and subsequent emission of a photon (*i.e.* photoluminescence). The intrinsic radiative lifetime for recombination is ∼10 ps but the effective radiative lifetime is ∼10 ns [80] because of momentum arguments and the presence of dark states. In particular, the absolute lowest energy state is actually dark [80] and lies ∼2–6 meV below the lowest bright state [81]. The bright state must be thermally populated to allow recombination [80], contributing in part to the low observed photoluminescence quantum efficiency values (0.1–0.01 % [82, 83, 84] with other reports showing higher values of 7 % [85]).

The intrinsic PL quantum efficiency of a nanotube depends on the (n, m) indices through the E_{22} absorption rate, the E_{11} emission rate and the relaxation processes between the two states [86]. Recent studies have shown that the $q = -1$ and larger chiral angle tubes have a greater PL quantum efficiency than those of the $q = +1$ family and near-zig-zag

configurations because of competing exciton-exciton resonances in the latter [86, 87].

2.1.13 Raman Features

Raman scattering is an inelastic photon scattering process involving the absorption or emission of phonons [12]. In a non-resonant scattering process, the incident photon excites an electron from the valence band to a virtual state close to a real state in the conduction band. In an elastic Rayleigh scattering process, the electron decays to the ground state with emission of a photon at the incident photon energy. A Raman scattering process is inelastic and the final and initial states differ, with an accompanying absorption (anti-Stokes scattering) or emission (Stokes scattering) of one or more phonons. The process requires conservation of energy and momentum and the resulting scattered photon will have a higher or lower energy relative to the incident photon (*i.e.* a Raman shift). Therefore, the scattering spectrum will consist of peaks spaced at multiples of $\pm\hbar\omega$ about the excitation peak, where ω is the angular frequency of the emitted or absorbed phonon. The transition intensities are significantly enhanced if the scattered or incident photons match an allowed optical transition and this is referred to as a resonant Raman process. In conjunction with absorption and photoluminescence features, the resulting Raman features allow nanotube optical spectra to be fully characterised and related to tube structure.

The radial breathing mode (RBM) is unique to carbon nanotubes and involves all carbon atoms moving in phase in the radial direction, creating a breathing-like vibration of the entire tube. It has the property that the RBM mode frequency is inversely proportional to the tube diameter [12] and is found at small Raman shifts (100–500 cm^{-1}). The G-Band in SWNTs is composed of two strong peaks (G^+ and G^-) at $\sim$1600 cm^{-1} related to the circumferential (TO) and axial (LO) atomic vibrations and the splitting of the two peaks depends on the tube-wall curvature and hence tube diameter. The D-Band ($\sim$1350 cm^{-1}) arises from a second-order process related either to the presence of defects in the tube walls or to amorphous-carbon material in the sample. It originates from symmetry breaking on the hexagonal sp^2-bonding lattices for graphite and nanotubes. Finally, the G' Band is at a

frequency of twice the D-Band and arises from a two-phonon process [19].

2.1.14 Other Properties

The electronic transport properties of nanotubes are intimately related to the electronic band structure. Conductance is a measure of the transmission of electrons through the entire device used to take the measurement (tube plus contacts) at the Fermi energy [19]. Truly metallic armchair SWNTs of 0.1–1μm in length have been shown to be ballistic conductors at room temperature, experimentally exhibiting the theoretically expected limit of two units of quantum conductance $2G_0 = 150\ \mu$S [12, 88]. Quasi-ballistic transport has been reported in semiconducting tubes, with a mean free path for elastic scattering of around 100 nm. This is because the conducting electrons come from degenerate states and therefore have the same symmetry such that, in contrast to metallic tubes, backscattering is consequently allowed [12, 89]. Nevertheless, the conductance approaches near ballistic transport at low temperatures [88].

The upper limit of the current that a metallic or semiconducting nanotube can carry is set by electron-phonon coupling because accelerating electrons to a high energy causes efficient relaxation by emission of optical or zone-boundary phonons [19, 90]. The maximum conductance grows with the diameter of the tube and the mobilities with the square of the diameter due to a decrease of both the effective mass and scattering rate with diameter [90]. Individual semiconducting nanotubes reach peak room temperature mobilities of $\sim$20,000 $\mathrm{cm^2V^{-1}s^{-1}}$ [90] but inefficient tube-to-tube transfer drops the value dramatically to $\sim$1000 $\mathrm{cm^2V^{-1}s^{-1}}$ for an aligned array of tubes [91] and $\sim$100 $\mathrm{cm^2V^{-1}s^{-1}}$ for a random array [92].

Individual carbon nanotubes exhibit large thermal conductivities of $\sim$3500 $\mathrm{Wm^{-1}K^{-1}}$ [22] that exceed those of diamond ($\sim$2500 $\mathrm{Wm^{-1}K^{-1}}$ [11]) and silver (430 $\mathrm{Wm^{-1}K^{-1}}$ [93]). They also have very good thermal stabilities, high tensile strengths of $\sim$30 GPa [94] and large stiffnesses, characterised by a Young's modulus of $\sim$1 TPa for isolated SWNTs and $\sim$0.5 TPa for bundles [95, 96]. These values exceed the corresponding values for steel, which exhibits

a tensile strength of 0.5 GPa and Young's modulus of 0.2 TPa [93]. The collection of these properties makes nanotubes highly suitable for implementation into optoelectronic devices.

2.2 Semiconducting Polymers

2.2.1 Polymer Classifications

Alan Heeger, Alan MacDiarmid and Hideki Shirakawa were awarded the 2000 Nobel Prize in Chemistry for "the discovery and development of conductive polymers". Conducting 'organic' polymers are made up of linked carbon-based repeating units forming long, linear chains. The carbon atoms comprising the backbone can be in an sp^3-hybridised form, termed saturated polymers, in which the four valence electrons are confined to be stationary in σ-bonds and no interesting electronic or optical properties arise [10]. Alternatively, the carbon atoms can be in an sp^2- (or sp-) hybridisation form in which one electron (π-electron) resides in a p_z-orbital which can be considered decoupled from the backbone σ-orbitals. These π-electrons can be delocalised along the chain and the resulting polymers are referred to as π-conjugated polymers. Conjugated polymers can be further classified into metallic or semiconducting depending on the respective absence or presence of a bandgap.

2.2.2 Electronic Band Structure

The electronic band structure of semiconducting polymers will be discussed using *trans*-polyacetylene as an example, whose structure is shown in Fig. 2.9 (a). Since each π-bond can accommodate up to two electrons, the π-band is half-filled around the Fermi level and *trans*-polyacetylene would naively be considered a metal (*i.e.* the dispersion relation follows that of a 1-dimensional free-electron gas model) with a unit cell length of $a = 0.12$ nm. However, 'real' polyacetylene has alternating single and double bonds with respectively longer and shorter lengths than equilibrium C-C bond lengths due to electron-phonon coupling [10]. The unit cell length is doubled due to the two degenerate configurations arising from swapping

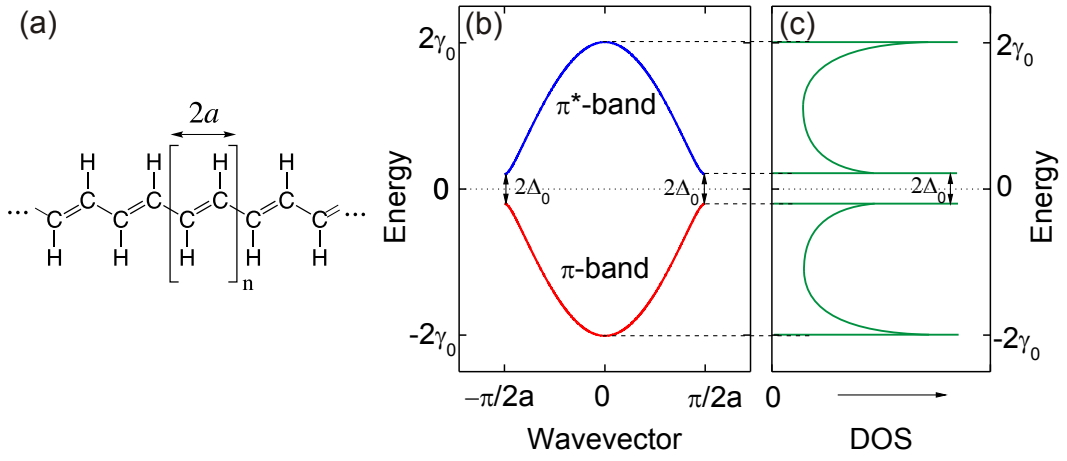

Figure 2.9: (a) Chemical structure of *trans*-polyacetylene, with the dimerised unit cell indicated. (b) The band structure of *trans*-polyacetylene in the first Brillouin zone given by Eq. 2.28, where the bandgap is given by $E_g = 2\Delta_0$. (c) The *trans*-polyacetylene DOS arising from the band structure.

the double and single bonds: this is called the dimerised form. This perturbation can be considered to be a Peierls instability of a 1-dimensional metal and the two degenerate states at the Fermi level split into one above and one below, effectively opening up a bandgap (Peierls gap) given by $E_g = 2\Delta_0$ [10].

The form of the π-electron dispersion relation can be derived using a TB model in an analagous way to that of graphene and carbon nanotubes (section 2.1.4). Again, the wavefunctions are assumed to be linear combinations of p_z-orbitals, contributions from other atomic orbitals are neglected and the transfer integral term, γ_0, is used to describe how an electron is transferred to its nearest neighbours. A detailed derivation of the dispersion relation is not provided here but the interested reader is directed to Ref. [10]. The Schrödinger Equation is solved using the Su-Schrieffer-Heeger (SSH) Hamiltonian in the dimerised form [97], which gives the dispersion relation in terms of the wavenumber k as:

$$E(k) = \pm\sqrt{\epsilon(k)^2 + \Delta_0^2}, \quad \epsilon(k) = 2t_0 \cos ka \tag{2.28}$$

The dispersion relation in the first Brillouin zone is plotted in Fig. 2.9 (b) and the corresponding DOS in Fig. 2.9 (c). The degenerate states split into the lower energy valence (π)

and higher energy conduction (π^*) bands, separated by $E_g = 2\Delta_0$. All states in the π-band are filled but all states in the π^*-band are empty.

The band structure has been presented here for the simplest π-conjugated polymer *trans*-polyacetylene, which contains 2 carbon atoms in the repeating unit (unit cell) and subsequently 2 π-bands. However, the theory can be extended to other conjugated polymers with larger and more complex repeating units, such as the polymers used in this thesis and introduced in Chapter 4. In general, a conjugated polymer with n atoms in the main chain of the repeating unit will have n π-bands further split into $n/2$ π-subbands and $n/2$ π^*-subbands [10]. The highest energy π-subband that is occupied is referred to as the HOMO (Highest Occupied Molecular Orbital) and the lowest energy π^*-band that is empty is referred to as the LUMO (Lowest Unoccupied Molecular Orbital) [51].

2.2.3 Optical Properties

When a polymer absorbs a photon, an electron is promoted from the valence π-band to the conduction π^*-band, leaving a hole behind. Conjugated polymers, like nanotubes, are 1-dimensional systems in which charges are confined in two dimensions and Coulomb effects are poorly screened by the low dielectric materials (typically $\epsilon_r \sim$2–4 [93]). This results in Frenkel-type excitons with binding energies ranging from <100 meV for the polyvinylenes and polythiophenes to ∼400 meV for the polyfluorenes and even larger values for other conjugated polymer systems [10]. However, the excitons show some Wannier-type character because the wavefunctions can also be delocalised over several repeating units and even onto neighbouring chains. Due to disorder in most prepared polymer samples, excitons are generally confined to single chains with a diffusion length of <10 nm [10].

Optical transitions must obey momentum and spin selection rules. The lowest energy optical transition is the HOMO-LUMO (π-π^*) transition and corresponds to a singlet S_0 to singlet S_1 electronic transition in which the electron spins remain antiparallel. Conjugated polymers exhibit strong electron-lattice coupling and each electronic S_i energy level is further split into vibrational energy levels approximated by the energy levels of the harmonic oscil-

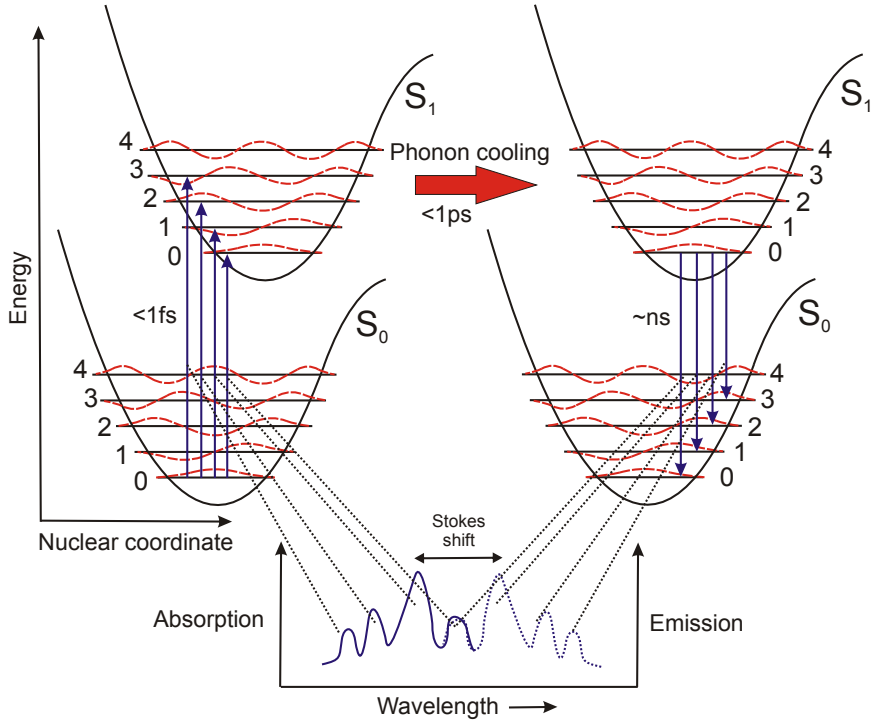

Figure 2.10: Schematic diagram to illustrate the Franck-Condon Principle and the Stokes shift between absorption and emission progressions.

lator. These levels are illustrated schematically in Fig. 2.10 under the Born-Oppenheimer approximation, which states that the electronic transitions and nuclear motions (*e.g.* vibrations) are independent. The Franck-Condon Principle follows directly from this; the lighter electrons are excited on a much faster time scale (sub-fs) than the motion of the heavier nuclei (∼100 fs) and hence electronic transitions in Fig. 2.10 are represented by vertical lines. When an electron is promoted from the S_0 to S_1 state it will generally be in a higher vibronic state. Rapid relaxation (sub-ps) occurs to the lowest S_1 vibrational state by phonon cooling and a transition occurs back to the S_0 state (∼ns), again to an excited vibrational state, with emission of a photon (fluorescence) [51]. Further vibrational relaxation returns the electron to the ground state. The intensities of the transitions are given by the overlap of the wavefunctions of the initial and final states in this Franck-Condon approximation [51].

Fig. 2.10 shows the chain of processes and reveals that the emission spectra are mirror images of the absorption spectra but with a red-shift. The difference between the 0-phonon absorption band edge and 0-phonon emission line is called the Stokes shift [10]. Stokes shift

values are ∼50 meV for semiconducting polymers [10, 98] but are negligible for the more rigid and ordered carbon nanotubes, in which excitons couple more weakly to nuclear motions [99].

In practice, absorption and emission spectra of π-conjugated polymers are significantly broadened [10] due to inhomogeneities in exciton energies arising from distributions in polymer conjugation length, effects caused by the chemical state of the polymer, torsional vibration leading to closely spaced replica, and lifetime-limiting effects, such as collisions in solution.

2.2.4 Polymer Aggregation and Chain Coupling

The simple Franck-Condon progression described previously holds for free and isolated polymer chains, such as when the polymer is dissolved in a 'good' solvent where the chains repel each other, resulting in well separated, stretched configurations. However, in 'poor' solvents or upon film formation, conjugated polymer chains tend to aggregate, forming ordered structures because of strong van der Waals interactions (π-π stacking) between chains that aren't overcome by stabilising solvent effects. In general, formation of aggregates increases the effective conjugation length of the system and leads to optical red-shifts because the chains extend and planarise and also leads to significant reductions in PL quantum efficiencies [100].

According to Kasha's exciton model, excitons on polymer chains can be considered as point dipoles [101]. The interaction between these dipoles is crucial in aggregated systems and determines the oscillator strengths for transitions. Fig. 2.11 (a) shows a transition between the energy levels for an isolated polymer chain corresponding to a 0-0 transition. The excitations are intra-chain only and the regular Franck-Condon progression is observed. However, parallel chains form H-aggregates [102] and the corresponding dipoles can couple in such a high symmetry ensemble state, effectively delocalising the excitation partly onto another chain. Parallel dipoles reinforce but antiparallel dipoles cancel, leading to a splitting of the energy levels into lower and higher energy components, respectively [101]. The transition dipole depends on the sum of the dipole vectors and hence the lowest energy transition,

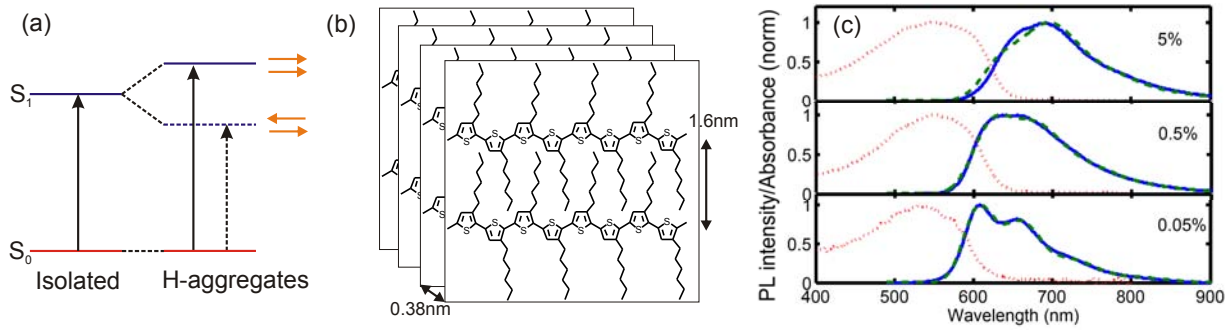

Figure 2.11: (a) Schematic energy diagram to show the splitting of the excitonic levels corresponding to the 0-0 transition due to chain-chain coupling, leading to a forbidden transition (dashed line). (b) Schematic diagram of P3HT lamellar aggregates showing the dimensions of interchain distances within and between π-stacks [105]. (c) Adapted from Ref [106]. PL (solid blue; green dashed shows fit using model proposed in Ref. [104]) and absorption spectra (red dotted) for samples progressing from isolated (0.05wt%) to aggregated (5wt%) P3HT suspended in an inert polyethylene matrix.

corresponding to the 0-0 transition, is forbidden[3]. By contrast, this symmetry is broken in higher vibronic states and the usual Franck-Condon progression is observed [103]. The net effect with increasing aggregation is an overall red-shift of all transitions, a reduction in PL intensities and a suppression of the 0-0 peak relative to the higher vibronic transitions [104].

A particularly important polymer system that demonstrates this behaviour is regioregular poly(3-hexylthiophene) (P3HT). The regioregular alternating alkyl side-chain geometry leads to the polymer chains forming 2-dimensional, highly ordered lamellar structures, as shown in Fig. 2.11 (b). The lamellae form by π-stacking of the conjugated backbones and the alkyl chains interdigitate within sheets. The dominant interactions are between the π-stacks due to the shorter stacking distance, and the aggregates can be considered as H-type [103].

Fig. 2.11 (c) compares the absorption and emission spectra obtained by Parkinson *et al.* from P3HT suspended in a matrix of inert polyethylene at low and high concentrations (*i.e.* isolated and aggregated chains, respectively) [106]. The PL shows that the 0-0 peak is suppressed in the aggregated samples and the higher vibronic peaks follow the usual Franck-Condon progression, with an overall underlying red-shift. These spectral changes provide an important probe to assess the morphology in P3HT samples and were utilised in this thesis.

[3]H-aggregates are so called because the coupling described here leads to a forbidden lower energy transition, giving an effective *hypsochromic* (*i.e.* blue) shift in their electronic transitions.

2.2.5 Polarons and Electrical Transport

A free charged particle (electron or hole) moving on a conducting polymer will deform the lattice structure [10]. The charge plus its associated polarisation field can be considered as a quasi-particle called a polaron. In a conjugated molecule such as polyacetylene or P3HT, the dimerisation of the two configurations of alternating double and single bonds is perturbed at the point of the polaron [107]. The relaxation of the bond dimerisation and lattice structure leads to two localised states in the HOMO-LUMO gap, resulting in two optical polaronic transitions. This is shown in Fig. 2.12 (a) for a hole confined to a 1D polymer chain, called a localised polaron P^+.

In a 2D polymer stucture, such as the lamellar networks formed by P3HT, the neighbouring chains are coupled and this causes a reduction of the HOMO-LUMO gap by an amount 2Δ, due to increased conjugation, and a splitting of each of the polaronic levels by the same amount [108]. The polaron can be considered as delocalised across several chains and is referred to as a delocalised polaron, shown in Fig. 2.12 (b) for the case of a hole (DP^+). These optical transitions provide a powerful tool to probe the presence and dynamics of free charges on conjugated polymers and were exploited in this thesis.

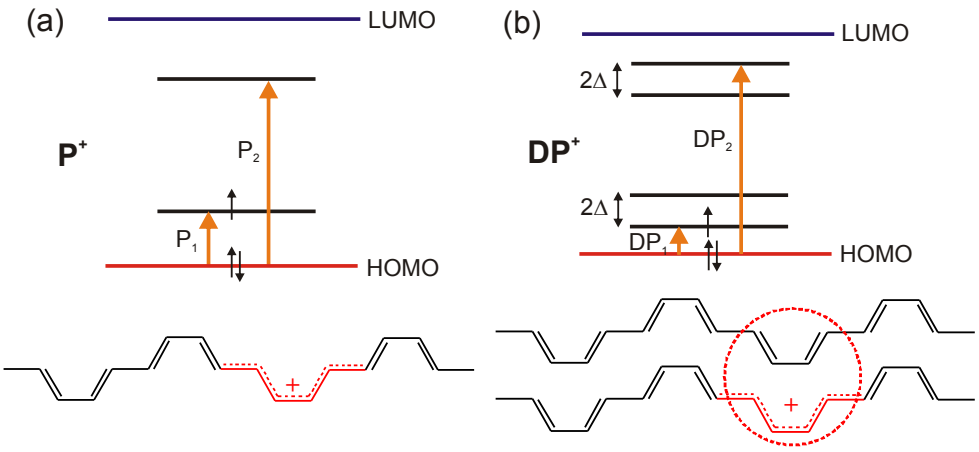

Figure 2.12: (a) A free hole on a 1D conjugated polymer chain backbone is a localised polaron P^+ and leads to two mid-gap states. (b) Coupling between adjacent chains in a 2D lamellar structure allows the hole to be delocalised across several chains, corresponding to a delocalised polaron DP^+ in which the polaronic states are themselves split. After Ref. [108].

Organic semiconductors such as π-conjugated polymers have electron and hole mobilities as low as $\sim 10^{-5}\,\mathrm{cm^2V^{-1}s^{-1}}$ [109], much lower than those of traditional inorganic semiconductors such as silicon ($\sim 1000\,\mathrm{cm^2V^{-1}s^{-1}}$ [110]) and other low-dimensional systems such as carbon nanotubes ($\sim 20{,}000\,\mathrm{cm^2V^{-1}s^{-1}}$ [90]). The discrepancy stems from the large disorder in organic polymer systems leading to transport barriers between chains [111], and increased scattering caused by strong electron-phonon lattice coupling [10]. Nevertheless, mobility values as high as $0.1\,\mathrm{cm^2V^{-1}s^{-1}}$ can be achieved in highly ordered networks of polymer such as in the lamellar structures formed by P3HT [112].

2.3 Organic Photovoltaics (OPVs)

2.3.1 Energy Transfer Processes

A composite material consisting of suitable donor and acceptor materials will form an electronic heterojunction at their interface. A type-I heterojunction, shown in Fig. 2.13 (a), forms when the HOMO-LUMO gap of the acceptor lies between the gap of the donor. In a donor-acceptor blend exhibiting a type-I alignment or, more generally, if the bandgap of the donor exceeds that of the acceptor, the photoexcited exciton on the donor can transfer non-radiatively to the acceptor in a process called ***energy transfer***. The exciton on the acceptor can then recombine radiatively (or non-radiatively), meaning that photoexciting the donor and monitoring emission from the acceptor provides a tool to probe energy transfer processes.

In the Förster Resonance Energy Transfer (FRET) mechanism, the transfer involves the coupling of electric dipoles on the donor and acceptor [113]. The transfer rate k_{FRET} can be derived from Fermi's Golden rule and is given by:

$$k_{\mathrm{FRET}} = \frac{1}{\tau_{\mathrm{D}}} \left(\frac{R_0}{R} \right)^6, \tag{2.29}$$

where τ_D is the donor radiative decay time constant and R is the distance between the donor and acceptor. R_0 is the Förster radius, representing the distance at which the efficiency of energy transfer is 50%, and is given by:

$$R_0^6 = \frac{9\kappa^2\phi_D}{128\pi^6 n^4} J, \quad J = \int \frac{f_D(\nu)\sigma_A(\nu)}{\nu^4} d\nu. \tag{2.30}$$

Here n is the refractive index of the medium between the donor and acceptor, κ is the orientation factor between donor and acceptor, ϕ_D is the PL quantum efficiency of the donor, and the integral term J represents the spectral overlap between the donor emission f_D and the acceptor absorption (cross-section) σ_A weighted with a factor involving the wavenumber of light ν [113, 114]. Typical Förster radii are 1–10 nm and the transfer rate drops significantly at larger distances because of the R^{-6} dependence in Eq. 2.29 [113].

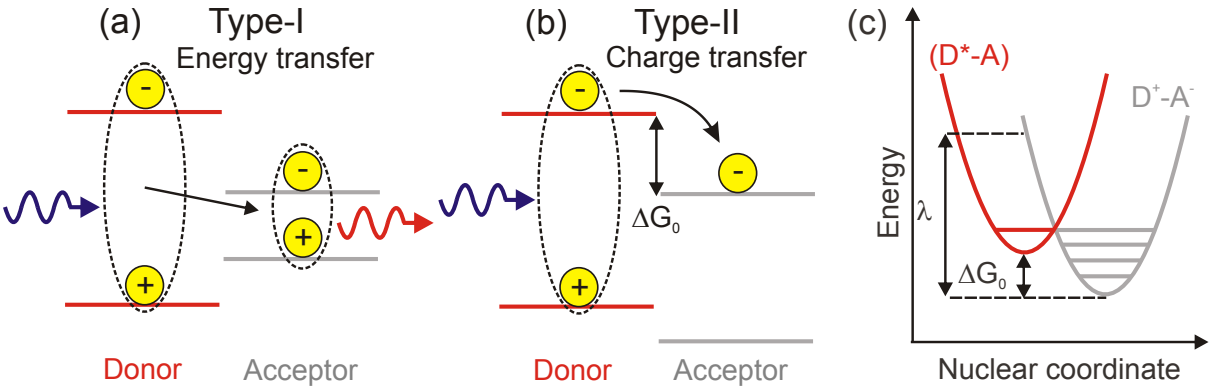

Figure 2.13: A donor-acceptor blend forming a type-I (a) and type-II (b) heterojunction interface at which energy and charge transfer occur, respectively. (c) Charge transfer between a photoexcited donor D^* and acceptor A is governed by semi-classical Marcus theory. The rate is determined by the overlap of the vibrational wavefunctions of the acceptor with those of the ground vibrational state of the donor and the reduction in free energy ΔG_0 relative to the total reorganisation energy λ.

However, the point-dipole approximation breaks down in certain situations [115], particularly at very short distances ($R < 1$ nm) when there is considerable overlap of the donor and acceptor exciton wavefunctions. Dexter extended the Förster theory to include higher order multipoles and wavefunction overlap [116]. This leads to an electron exchange mechanism (Dexter exchange) whereby energy transfer occurs by simultaneous transfer of an electron

from the donor to the acceptor LUMO and another from the acceptor to the donor HOMO. The rate of Dexter transfer k_{Dexter} is given by:

$$k_{\text{Dexter}} \propto J' e^{-2R/L}, \tag{2.31}$$

where J' is the same spectral overlap integral as in Eq. 2.30 except without the ν^4 weighting, L is an effective average Bohr radius for the excited and unexcited states of the donor and acceptor and the exponential term arises from the wavefunction overlap. The exchange mechanism can only occur over a very short distance, typically an order of magnitude less than a Förster mechanism [116].

2.3.2 Charge Transfer and Charge Separation Processes

A type-II heterojunction forms between a donor and acceptor exhibiting a staggered alignment of energy levels, as shown in Fig. 2.13 (b). Photoinduced charge transfer can occur across the materials provided there is a significant driving force that can overcome the binding energy of the exciton on the donor [10]. The driving force is given by the difference between the LUMOs of the donor and acceptor ΔG_0, as labelled on Fig. 2.13 (b). The hole remains on the donor because the staggered alignment leads to an energetic barrier for hole transfer. Nevertheless, if the bandgap of the donor exceeds that of the acceptor, energy (exciton) transfer will also be a competing process. Charge and energy transfer processes compete with direct recombination of the excitons and thus the excitation transfer pathways quench the donor's photoluminescence.

The charge transfer process can be described by considering the overlap between the lowest vibrational state in the donor's excited state with an acceptor vibrational state of similar energy, as shown in Fig. 2.13 (c). Although there is a reduction in free energy driven by the energy difference ΔG_0 (driving force), there is a barrier to transfer in the form of a reorganisation energy λ, which incorporates components from the change in molecular shape (λ_0) and the reorientation of dipoles due to the placement of the transferred charge [117].

The rate of charge transfer between conjugated systems satisfying the Franck-Condon principle is given by the semi-classical Marcus theory [117, 118, 119, 120] as:

$$k_{\mathrm{CT}} = \frac{2\pi}{\hbar} H^2 \left(\frac{1}{4\pi\lambda_0 kT} \right)^2 (FC), \quad \text{where} \tag{2.32}$$

$$(FC) = \sum_{n=0}^{\infty} \exp(-S) \frac{S^n}{n!} \exp\left(\frac{-(\lambda_0 + n\hbar\omega + \Delta G_0)^2}{4\lambda_0 kT} \right). \tag{2.33}$$

Here, the first factor (H^2) is the coupling matrix element between the donor and acceptor electronic states and the second factor arises from the classical density of states. The Franck-Condon (FC) factor is a sum over all possible vibrational overlap integrals between the initial 0-th vibrational donor level and the n-th vibrational level of the acceptor, where the exponential factor $\exp(-S)$ accounts for the effective electron-phonon coupling S and $S^n/n!$ describes the population probability of the acceptor's vibrational states with harmonic oscillator vibration frequency ω. The final exponential factor is a Boltzmann term describing the probability of the transfer, showing that the rate is maximised if there is a close match between the energy released ΔG_0 and the sum of the acceptor vibrational energy and reorganisation energy λ_0 [117].

The charge transfer process at the donor-acceptor interface leads to a Coulombically bound electron-hole pair (*i.e.* exciton) across the interface. An ***exciplex*** can be considered as a hybrid state with part charge-transfer character and part local excitation on one or across both moieties of the donor-acceptor system [119]. Exciplexes have binding energies as large as 100–300 meV for polymer–polymer interfaces [121, 122]. In the extreme exciplex case, where the electron-hole are Coulombically bound but exist on two different molecules, the charge-transfer species is referred to as a ***polaron pair***.

The excited 'hot' charge-transfer species may relax to an equilibrium level and recombine geminately[4] either non-radiatively by phonon emission or radiatively. Radiative exciplex recombination in polymer–polymer blends leads to long-lived (∼100 ns), red-shifted spectral

[4]Geminately because the constituents originate from the same donor excitation [119].

signatures [123]. A competing process to recombination is dissociation of polaron-pairs into free charges (polarons), leading to ***charge separation***. The sequence of events from photoexcitation to charge separation is summarised in Fig. 2.14. The free polarons that are produced may also recombine non-geminately at donor-acceptor interfaces to reform charge-transfer states [119].

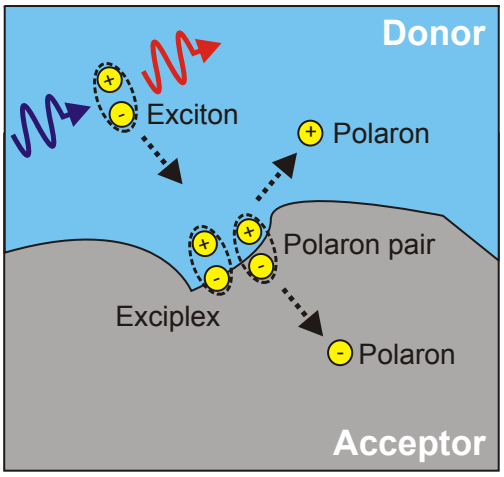

Figure 2.14: Schematic diagram to describe the various intermediate states leading to charge separation across a type-II interface in a photo-excited donor-acceptor blend. The exciton formed by photoexcitation may either recombine radiatively or migrate to an interface with the acceptor. At the interface, charge transfer occurs and the electron can be delocalised partly (exciplex) or completely (polaron pair) onto the acceptor but Coulombically bound to the hole. Dissociation leads to free polaron formation.

There is currently debate over the mechanism for dissociation of the polaron pairs and two limiting cases are usually considered [124]. The first is the Onsager-Braun theory of separation of ions [125] whereby the 'hot' charge-transfer state first thermalises quickly to an equilibrated polaron pair. Recombination of this pair then competes with dissociation into free polarons by hopping and the dissociation rate is given by:

$$k_{\text{diss}} = k_R \frac{3}{4\pi a^3} e^{-E_B/kT} \left[1 + b + \frac{b^2}{3} + \frac{b^3}{18} + \ldots\right], \quad b = e^3 E / 8\pi\epsilon_0\epsilon_r k^2 T^2, \tag{2.34}$$

where k_R is the recombination rate of the dissociated charges, a is the separation of the charges, E_B is the polaron-pair binding energy, T is the temperature and E is an external

or built-in electric field across the blend.

More recently, a model involving an ultrafast charge separation of the hot charge-transfer state directly into free polarons was proposed [124]. The excess energy of the hot charge-transfer state is transferred to kinetic energy of the polarons and helps to overcome the binding energy. While the matter is yet to be resolved, it is likely that both processes may compete in this final step to charge separation. In any case, the overall charge separation yield has been shown to be strongly correlated with the driving force ΔG_0 in many donor-acceptor systems [126, 127].

2.3.3 OPV Device Structure and Terminology

A photovoltaic cell converts light energy into electrical current by photogenerating electrons and holes and collecting them at opposite electrodes where the power can be delivered to an external load [10]. Traditional solar cells utilise materials such as crystalline silicon where exciton binding energies are low and free electrons and holes are readily generated at built-in p-n junctions. However, organic materials have large exciton binding energies and require a second acceptor material, which forms a type-II heterojunction with the donor, to dissociate excitons and generate separated charges [10, 128].

Fig. 2.15 (a) shows a typical OPV device architecture and (b) shows the electronic processes occurring. Three key steps can be identified:

(1) Photoexcitation of the donor species in the active layer, producing excitons which migrate to an interface with an acceptor.

(2) Charge transfer at the interface leading to charge-transfer states (exciplexes or polaron pairs) which can dissociate to give free polarons (*i.e.* charge separation).

(3) Charge transport and collection of electrons and holes at electrodes

Photoexcitation typically occurs through a bottom transparent electrode such as indium tin oxide (ITO). Electrons are transported through the hole and exciton blocking layer

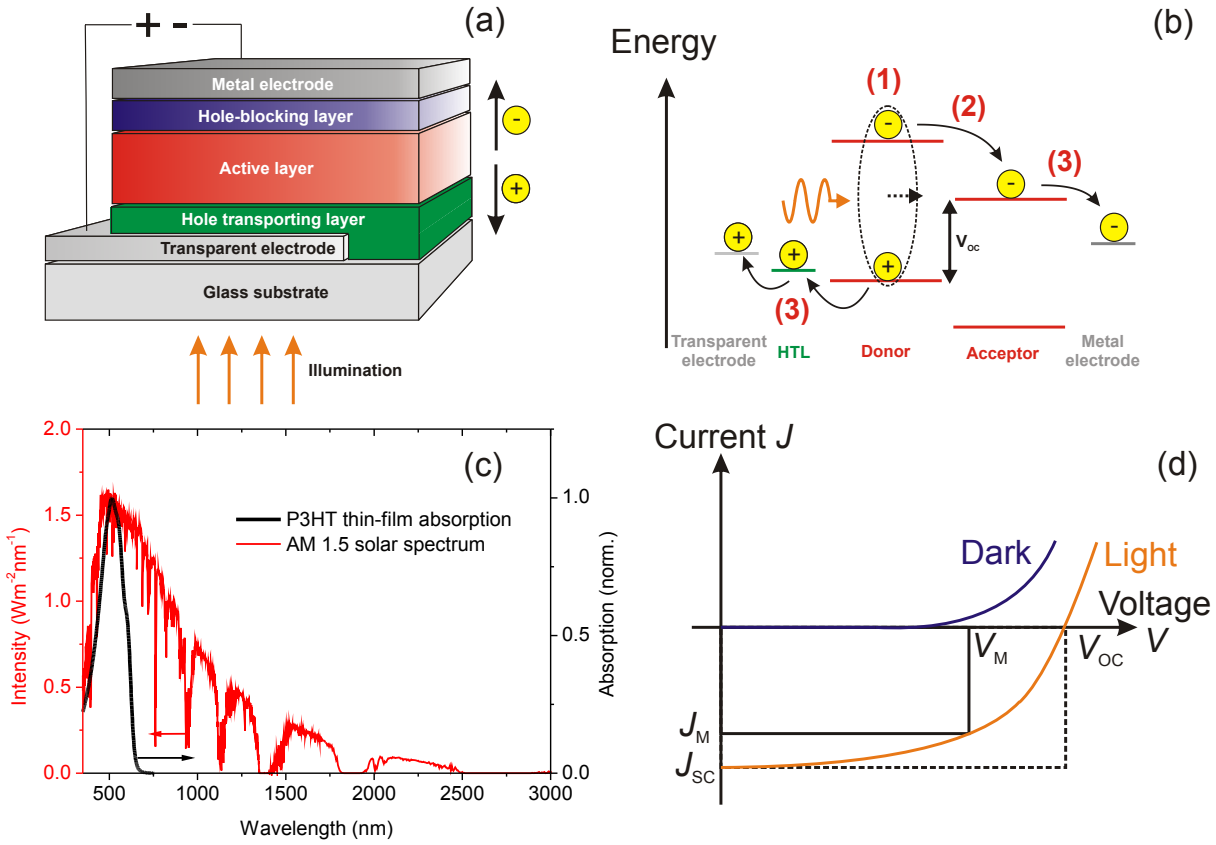

Figure 2.15: (a) Schematic diagram of a typical OPV device layered architecture. (b) Schematic energy level diagram showing the key processes occurring in an operating OPV device, as described in the text. (c) The normalised AM 1.5 solar spectrum incident on a surface tilted at 37° obtained from the model in Ref. [129]. The absorption spectrum of a thin film of the light-harvesting semiconducting polymer P3HT is also overlaid. (d) Typical *J*-*V* light and dark curves for an OPV device, with some of the key parameters labelled.

(*e.g.* bathocuproine BCP) to the metal electrode (typically aluminium), while holes are transported through the hole transporting layer (typically a PEDOT:PSS polymer blend) to the transparent electrode. The directional transport is due to the internal electric field created both by the work function difference of the electrodes and by the heterojunctions in the active layer, generating a photocurrent through the circuit. A photovoltage is also established across the terminals due to the charge imbalance, driving electrons through a load in the external circuit to do electrical work.

OPV devices are tested under simulated sunlight, which is standardised to be the intensity ($\sim$100 mW/cm^2) of the solar spectrum (air mass 1.5; AM 1.5) representing the average of the 48 contiguous states of the US [129]. A normalised AM 1.5 solar spectrum is shown in

Fig. 2.15 (c) with the absorption spectrum of a thin film of P3HT overlaid. The overlap shows that P3HT is a good choice for a solar light-harvester but the absorption would ideally be extended to cover a wider range of the spectrum by using multiple harvesters with different bandgaps (*e.g.* by clever device design such as tandem cells) while also ensuring that a type-II heterojunction exists between the harvesting donors and the acceptors.

Measurements are taken by applying an opposing external voltage across the device and reading the current with and without illumination to yield light and dark current-voltage ($J-V$) curves, respectively. A typical $J-V$ curve is shown in Fig. 2.15 (d) and allows the key parameters to be defined. The ***short-circuit current*** J_{SC} is the current flowing when there is no external field applied. It is determined by the charge separation efficiency, electrical transport through the materials and rate of carrier recombination during transport [10]. The ***open-circuit voltage*** V_{OC} is the external voltage when no net current flows in the device. It represents the maximum voltage that can be generated in the device and is a property of the donor-acceptor blend – the V_{OC} is given approximately by the energy difference between the donor HOMO level and acceptor LUMO level [130], as shown in Fig. 2.15 (b). The ***fill factor*** FF is the ratio of the maximum obtainable power $V_{\mathrm{M}}J_{\mathrm{M}}$ to the theoretical power at both V_{OC} and J_{SC} together and can be interpreted as the ratio of the areas of the rectangles shown in Fig. 2.15 (d). The FF gives a measure of the quality of the solar cell and decreases in the presence of a large series resistance, corresponding to high internal losses. These parameters can be combined to give the overall power conversion efficiency η by:

$$\eta = \frac{P_{\mathrm{out}}}{P_{\mathrm{in}}} = \frac{V_{\mathrm{OC}}J_{\mathrm{SC}}FF}{P_{\mathrm{in}}}, \quad FF = \frac{V_{\mathrm{M}}J_{\mathrm{M}}}{V_{\mathrm{OC}}J_{\mathrm{SC}}}, \tag{2.35}$$

where P_{in} is the incident light power and P_{out} is the electrical power output of the device.

2.3.4 Bulk Heterojunction Solar Cells

Bilayer devices, in which the donor-acceptor photoactive materials are in separate layers, exhibit selective transport of electrons or holes to electrodes but have only a planar interface

for exciton dissociation. Exciton diffusion lengths in semiconducting polymer donors are typically <10 nm, limiting the layers to low thicknesses with optical densities that are far too low to absorb sufficient incident photons [10]. By contrast, bulk heterojunctions have a nanostructured phase-separated morphology in which each of the two components self-assembles to form continuous interpenetrating networks. The nanoscale network ensures that nearly all the absorbed photons are converted into separated charges and then transported to the electrodes through continuous pathways [10, 131].

Polymer–polymer blends have been proposed as photoactive layers in bulk heterojunction OPV devices [132]. However, problems with morphology [133, 134, 135] and the large binding energies of polaron pairs [121, 122] have significantly hindered charge separation efficiencies, leading to efficiencies typically below ∼2 % [132].

The current benchmark organic solar cells utilise polymers as donors blended with substituted fullerenes as electron acceptors [136]. By using recently synthesised low bandgap polymers as donors, efficiencies have reached 5-8 %, with internal quantum efficiencies approaching unity (*i.e.* nearly all absorbed photons are converted into free polarons that are collected at the electrodes) [137, 138, 139], and a commercial market has recently emerged [136]. The most heavily investigated system consists of regioregular P3HT blended with phenyl-C_{61}-butyric acid methyl ester (PCBM), a fullerene with a solubilising side group. The success of this blend can be attributed to two key factors. First, the P3HT and PCBM components segregate into crystalline phases upon thermal annealing, providing separate and continuous networks to transport the electrons and holes to respective electrodes [136]. Second, PCBM has a very deep LUMO level (*i.e.* high electron affinity), leading to a very large driving force (ΔG_0 ∼1 eV) for charge transfer from P3HT. The relatively large polaron pair binding energies are thought to be overcome by the excess energy from the charge transfer process (hot polaron pairs) [126], the large local mobilities in the crystalline regions [140] or, perhaps most significantly, the delocalisation of charge carriers within conjugated segments of the polymer chain [141].

Group	Year	Photoactive Layer Composition	η (%)
Nanotubes as hole acceptors			
Chaudhary *et al.* [142]	2007	SWNT-P3HT-PCBM	3.7
Bindl *et al.* [143]	2011	SWNT-PFO-PCBM	0.6
Kymakis *et al.* [144]	2012	SWNT-P3HT-PCBM	3
Nanotubes as electron acceptors			
Kymakis *et al.* [3]	2003	P3OT-SWNT	0.06
Kazaoui *et al.* [145]	2005	P3OT-SWNT	0.1
		MEHPPV-SWNT	0.001
Kymakis *et al.* [146]	2006	P3OT-SWNT	0.2
Ham *et al.* [147]	2010	P3HT-SWNT	3[1]
Ren *et al.* [148]	2012	P3HT-SWNT	0.7

[1] Efficiency per nanotube

Table 2.1: Summary of progress in the field of OPV devices utilising carbon nanotube–polymer blends. The list is not exhaustive but shows the key progressions over time. All tabulated results were recorded under simulated solar light (100 mW/cm^2, AM 1.5).

2.3.5 Literature Review: Carbon Nanotube–Polymer Blends as the Photoactive Layer

Although P3HT-PCBM devices have shown very good perfomance, the relatively low electron and hole mobilities of the two organic phases may limit the efficiency of the devices. Replacement of either of the components with carbon nanotubes, which have much higher charge mobilities and aspect ratios, has been proposed. To this end, SWNTs have been used in the OPV photoactive layers with three possible roles: as electron or hole acceptors or as the light-harvesting donor material. Table 2.1 summarises the progress in this emerging field, restricted to systems utilising single-walled nanotubes which have not been chemically modified (*e.g.* by covalent functionalisation), such that they preserve their intrinsic properties. While efficiencies may appear low, it should be noted that all cells showed significant increases in photocurrents when compared to analogous devices without nanotubes.

Nanotubes have been incorporated into OPV devices as hole acceptors either by tuning the nanotube Fermi level [149] or by blending SWNTs with fullerenes, which have a larger electron affinity. These devices demonstrated increased efficiencies compared to those without nanotubes, which were attributed to increased hole mobilities and enhanced exciton

dissociation [142, 144]. A particularly interesting OPV device attempt utilised SWNTs as the light-harvesting material, with exciton dissociation and electron transfer to a PCBM acceptor [143, 150]. While efficiencies of 0.6 % were obtained, the quantum efficiencies were only significant at the sharp van Hove singularities and hence it was not possible to harvest much of the solar spectrum.

The majority of work has been focused on the use of SWNTs as the electron acceptor material by directly replacing PCBM in polymer devices. Most studies reported on devices made of mixtures of large-diameter semiconducting and metallic arc-discharge SWNTs blended with polythiophene polymers similar to P3HT, namely poly(3-octylthiophene) (P3OT), where the hexyl side chains are replaced with octyl chains. Performances were low (η <0.1 %) but peculiarly high V_{OC} values of 0.7–1 V were observed [3, 5, 151, 152]. These values were far higher than the predicted values from the energy level differences shown schematically in Fig. 2.15 (b), suggesting that a different model may be required to describe the OPV blends which incorporate SWNTs. Similarly poor device efficiencies were obtained using blends with larger bandgap polymers such as poly(2-methoxy-5-(2-ethylhexyloxy)-1,4-phenylenevinylene) (MEHPPV) [145]. Improved efficiencies (η =0.22 %) were obtained by use of annealing treatments, which lead to more crystalline polythiophene phases [146, 153]. Furthermore, a concentration dependence found that the optimum nanotube weight percentage in the P3OT polymer matrix was just ∼1 % [154], due to better polymer carrier transport and more effective charge separation. Finally, it is also noted that efficiencies of ∼3 % per nanotube were obtained from P3HT-based planar devices in which very long nanotubes were grown to directly connect to the metal electrode [147]. Care must be taken to compare this result to values from other devices because a measurement per nanotube artificially scales up the current densities.

The low observed efficiencies in nanotube-polymer blends can be explained by recent theoretical [155] and experimental work [156] showing that the required type-II heterojunction only forms between P3HT and *small-diameter, semiconducting* nanotubes (discussed in detail in Chapters 4 and 5). In these cases, the driving forces for charge transfer (ΔG_0 ∼1.2 eV)

even exceed that for PCBM as the acceptor material (∼0.9 eV) [127]. Metallic nanotubes were also shown to be detrimental to device performance by acting as efficient recombination centres, quenching both excitons and free charges [157, 158]. All previous work has utilised large-diameter nanotubes with mixtures of both metallic and semiconducting species, which only form type-I heterojunction alignments, and unwanted energy transfer is the dominant process over exciton dissociation. Moreover, the polymer-nanotube blend structures were not well characterised, leading to less than optimal interfaces and morphologies.

The literature taken as a whole suggests that efficient devices utilising nanotubes as the electron acceptors will require the use of well optimised nanotube-polymer structures, where the nanotube components are only present in small percentages and purely as small-diameter, semiconducting tubes. The aim of this thesis was to implement these criteria into OPV material design by focusing on photoexcitation and charge separation (bullet points (1) and (2) on page 44). Ren *et al.* recently validated and used the results presented here to incorporate nanofilaments comprised of small-diameter, semiconducting nanotubes coated with P3HT polymer into OPV devices, observing a record efficiency of 0.73 % with a nanotube weight percentage of 3 % [148].

2.4 Summary

- Single-Walled Carbon Nanotubes (SWNTs)
  - SWNTs can be classified as chiral (n, m) or as the special cases of zig-zag $(n, 0)$ or armchair (n, n) tubes, where the chiral indices (n, m) dictate the tube's chiral angle θ and diameter d. Nanotubes are metallic if $(n - m)$ is a multiple of 3; otherwise they are semiconducting with bandgaps.
  - The band structures of nanotubes are given by slices through the graphene band structure at allowed wave vectors (zone-folding approximation). The density of states exhibits van Hove singularities between which optical transitions occur.

  - The Popov tight-binding model [43] can accurately describe single-particle nanotube energy levels but excitonic and many-body effects are required to reproduce optical transition data. Chirality (n, m) assignments can be made from optical spectra using the empirical model of Weisman and Bachilo [44].
  - Nanotubes have many other properties that make them ideal for OPVs, including large aspect ratios, very high mobilities and large Young's moduli.

- Semiconducting Polymers
  - Conjugated polymers are 1-dimensional systems with bandgaps from Peierls instabilities. The lowest optical transition corresponds to the HOMO-LUMO gap.
  - Absorption and emission spectra show Franck-Condon progressions with a Stokes shift. Aggregated samples exhibit altered progressions due to chain coupling.
  - Free charges on conjugated polymers distort the lattice and are quasi-particles called polarons.

- Organic Photovoltaics (OPVs)
  - An OPV device requires a type-II heterojunction between a donor and acceptor blend to dissociate donor excitons and transfer electrons to the acceptor. The electron and hole remain bound as a charge-transfer state but can further dissociate to produce free polarons, resulting in charge separation. The charges are transported and collected at respective electrodes.
  - The benchmark OPV devices currently use P3HT-PCBM blends. Efficiencies could be improved by replacing the electron acceptor component (PCBM) with SWNTs, which exhibit higher charge mobilities and aspect ratios. However, purely polymer–nanotube blend OPV devices have to date shown poor performance ($\eta < 0.2\,\%$). The literature suggests that polymer–nanotube OPV devices need to utilise materials containing small proportions of well optimised nanostructures comprised of polymers blended with small diameter, semiconducting nanotubes only.

Chapter 3

Experimental Methods

3.1 Steady-State Optical Techniques

Steady-state techniques provide a wealth of spectroscopic information about organic semiconductor samples. These techniques probe systems in which excited states are continually created and eliminated, resulting in a constant concentration of excited states in dynamic equilibrium. Here, the techniques and principles utilised to obtain absorption and near-infrared (NIR) photoluminescence measurements are introduced. The visible–NIR steady-state photoluminescence setup is discussed at the end of Section 3.2.2 in conjunction with the time-resolved techniques where the same detector setup was used.

3.1.1 Absorption Spectroscopy

Absorption spectroscopy is a powerful tool to probe and characterise both polymer and nanotube species simultaneously in a dilute solution or thin film. The measurement exploits the Beer-Lambert Law, which states that a logarithmic relationship exists between the transmission of light through the sample and the product of the absorption coefficient of the substance α and the path length ℓ through which the light travels [51]. The absorption coefficient can also be expressed as the product of an absorption cross section σ and the number density of

absorbers N. However, the absorption coefficient is most often expressed in terms of a molar extinction coefficient ϵ and molar concentration c of the absorbing species in the sample. These parameters can be mathematically related in terms of an optical density (O.D.) or *absorbance* A as:

$$A = -\log_{10}\left(\frac{I}{I_0}\right) = \frac{\alpha\ell}{\ln 10} = \frac{\sigma N\ell}{\ln 10} = \epsilon\ell c, \tag{3.1}$$

where I and I_0 are the transmitted and incident light intensities, respectively [51]. The absorption of light by species in the sample is highly wavelength dependent and absorbance values obtained across a wavelength range yield information about their electronic transitions. The situation and parameters are illustrated in Fig. 3.1.

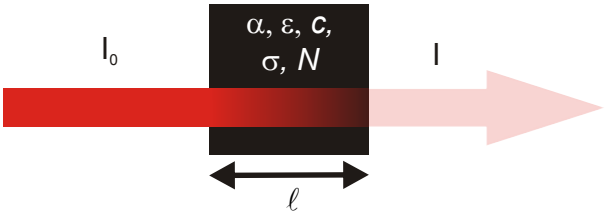

Figure 3.1: Diagram to illustrate the parameters involved in the definition of the Beer-Lambert Law, where light is absorbed as it passes through a sample.

Absorption measurements were carried out on a Perkin-Elmer Lambda 9 UV-Vis-NIR Spectrophotometer, with a dual beam setup, sensitive enough to detect optical densities of up to 6. Measurements were taken on either thin films or dilute solutions over the spectral region 300–1700 nm to cover the key polymer and nanotube (E_{11} and E_{22}) transitions. Small apertures were used for thin film measurements to prevent artifacts arising from spatial 'wander' of the beam.

3.1.2 Photoluminescence Excitation (PLE) Spectroscopy

The most powerful tool for characterising nanotube dispersions is photoluminescence excitation (PLE) spectroscopy. The technique involves photoexciting the nanotube E_{22} transitions (visible region), leading to rapid relaxation to the bandgap edge, then monitoring the

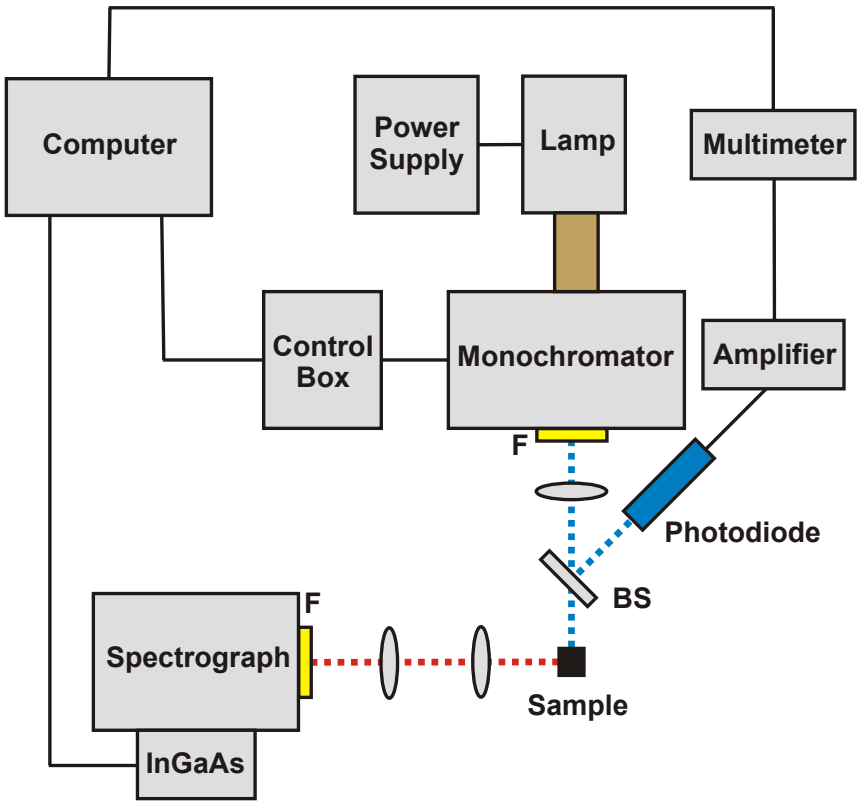

Figure 3.2: Schematic diagram showing the custom built experimental setup used for PLE measurements in this work. Components and beam paths are detailed in the text.

subsequent E_{11} emission (NIR). The PLE measurements in this work were conducted using a custom built setup as first described in Ref. [159] and shown in Fig. 3.2. A 75 W Xenon lamp (Photon Technology International, Inc.) was used as a white light source and the beam passes through a 30 cm monochromator with slits optimised to give excitation FWHM below 5 nm. Unwanted higher order wavelengths emerging from the monochromator were removed by using appropriate filters (F). Typically, a water filter was used to eliminate longer wavelengths and a long-pass filter was used to remove second order UV radiation. The monochromatic light was focused onto the sample which was either a solution cuvette or a thin film on a quartz substrate and the sample position was adjusted using an xy-stage.

An automated Labview program was used to increment the excitation wavelengths over the range 300–1000 nm in 5 nm steps by means of a spectrometer control box. In order to correct for the Xenon lamp's spectral output and monochromator's spectral response over this range, a quartz beam splitter (BS) was used to divert a fraction of the beam onto a silicon

photodiode and the photovoltage values were read using an amplifier and multimeter to directly normalise and correct the collected photoluminescence data. The spectral response of the photodiode was corrected for using the manufacturer supplied response curve.

The photoluminescence emitted from the photoexcited sample was collected along a path at 90° to the excitation focal point and was itself focused into a 30 cm spectrograph. Only dilute solutions were used to minimise reabsorption affects and ensure a constant photon flux at the spectrograph focal point. Thin film measurements were taken with the film oriented away from 45° to minimise directly reflected excitation light reaching the detector. Appropriate long-pass filters (F) were used to minimise scatter from the excitation source reaching the detector. The PL intensities in the range 900–1600 nm were recorded with appropriate acquisition times using a liquid nitrogen cooled InGaAs 512 pixel photodiode array (OMA V, Princeton Instruments). The spectrograph and detector were calibrated using a Neon lamp and instrumental response corrected for using a tungsten filament lamp of known emissivity. PL spectra were acquired at each excitation wavelength and therefore 2-D contour PLE 'maps' were created to present the data, with excitation and emission wavelengths on the x- and y-axes, respectively, and a colour scale to represent the (normalised) PL intensities.

3.2 Time-Resolved Techniques

Time-resolved spectroscopy covers any measurements taken over time after a system has been perturbed from its equilibrium state, such as by an optical pulse. Generally, detection utilises high speed electronics, which are easy to implement. However, the temporal resolution in such *electronically*-gated techniques is limited by the speed of the electronics comprising the detector system. This is typically tens of nanoseconds [160], with high-speed transistors achieving switching times of a few hundreds of picoseconds [161]. In order to resolve the dynamic processes occurring in organic semiconductors (time scales of femtoseconds to tens of picoseconds), *optically*-gated techniques are required [162]. In this section, the physics of non-linear optics are first introduced to allow an explanation of the optically-gated photolu-

minescence up-conversion (PLUC) technique. This is contrasted to the electronically-gated time-correlated single photon counting (TCSPC) technique. Finally, the optically-gated transient absorption technique is briefly discussed.

3.2.1 Non-Linear Optics

In most instances, it is assumed that optical properties of materials, such as refractive indices and absorption coefficients, are independent of the optical power. However, in the case of laser systems where high powers are achieved, the assumption becomes invalid and the formulation must be generalised to include *non-linear* optics [51]. This regime gives rise to important effects such as frequency-mixing, exploited in the experimental techniques described later.

The various optical properties of materials are derived from the electric susceptibility, χ. In linear optics, it is assumed that the polarisation $\mathbf{P}$ of the medium has a linear relationship with the electric field $\mathbf{E}$ of the light, such that:

$$\mathbf{P} = \epsilon_0 \chi \mathbf{E}, \tag{3.2}$$

where ϵ_0 is the vacuum permittivity. However, in the non-linear optics regime the expression in Eqn. 3.2 must be generalised. This is done by first considering a non-linear medium in which the polarisation is parallel to the electric field and the polarisation P and electric field E can be treated as scalar quantities. The generalised non-linear polarisation is then written as the sum of components of increasing order, that is:

$$\mathrm{P}_{\mathrm{non-linear}} = \mathrm{P}_1 + \mathrm{P}_2 + \mathrm{P}_3 + \ldots = \epsilon_0(\chi_1 \mathrm{E} + \chi_2 \mathrm{E}^2 + \chi_3 \mathrm{E}^3 + \ldots), \tag{3.3}$$

where E is the magnitude of the electric field, and P_n and χ_n are the n-th order non-linear polarisations and susceptibilities, respectively, and χ_1 is the normal linear susceptibility. In general, each susceptibility order component will be a tensor quantity because the non-linear

response of the medium will depend on the directions of the applied fields and they will not necessarily be parallel.

Non-Linear Frequency Mixing

The majority of phenomena of interest are attributed to either the second- or third-order terms, χ_2 or χ_3, but the discussion here will be limited to second-order effects. If two incident sinusoidal waves with frequency ω_i of the form $\mathrm{E}_i(t) = \mathrm{E}_i \cos \omega_i t$ are considered and, again, χ_2 is considered as a scalar component, the second-order non-linear polarisation will take the form:

$$\begin{aligned} \mathrm{P}_2(t) &= \epsilon_0 \chi_2 (\mathrm{E}_1(t) \times \mathrm{E}_2(t)) && (3.4) \\ &= \epsilon_0 \chi_2 \mathrm{E}_1 \mathrm{E}_2 \frac{1}{2} \left[\cos(\omega_1 + \omega_2)t + \cos(\omega_1 - \omega_2)t\right]. && (3.5) \end{aligned}$$

The non-linear response at second-order generates polarisation waves at both the sum $\omega_1 + \omega_2$ and difference $\omega_1 - \omega_2$ frequencies of the incident light and this effect is called *non-linear frequency mixing*.

To ensure a high conversion efficiency from these weak processes, the phases of the non-linear waves generated throughout the medium need to add together coherently. This is called *phase matching* and is achieved by applying conservation of momentum, $\mathbf{k} = \mathbf{k_1} + \mathbf{k_2}$, where the wavevector $\mathbf{k}$ is generated by mixing two photons with wave vectors $\mathbf{k_1}$ and $\mathbf{k_2}$. This phase-matching condition becomes a constraint on the refractive indices n_{ω_i} of the material for each frequency and polarisation and is often satisfied by exploiting the birefringent properties of the non-linear crystal medium. In practice, the condition can only be achieved if the crystal is oriented in a very precise direction.

Applications

A common application of non-linear frequency mixing is *frequency-doubling*, where the incident directions of propagation are co-linear in a non-linear crystal and $\omega_1 = \omega_2$ such that the emitted light has a frequency of 2ω. This is particularly useful for generating the frequencies required to excite organic semiconductors from a Ti:Sapphire laser system and will be utilised in the techniques described later. To satisfy the phase matching condition, the fundamental wave is polarised perpendicular to the crystal optical axis in order to propagate with constant refractive index n_o. The frequency-doubled waves have components both parallel and perpendicular to the optical axis with a refractive index depending on the angle between the propagation direction and optical axis. A crystal angle can therefore be found to satisfy the phase matching condition, namely $n_\omega = n_{2\omega} = n_o$ [51].

Another application is found in the *photoluminescence up-conversion* (PLUC) process and this is demonstrated in Fig. 3.3. Here, the photoluminescence photons from a sample $\omega_1 = \omega_{\mathrm{PL}}$ are added to those from a suitably delayed gate laser pulse $\omega_2 = \omega_{\mathrm{gate}}$ to produce 'up-converted' photons of frequency $\omega_{\mathrm{PL}} + \omega_{\mathrm{gate}}$. The sum-frequency signal is generated only during the gating laser pulse and this provides an all-optical method of temporally resolving the photoluminescence [163]. Moreover, inspection of Eq. 3.5 shows that the up-converted signal intensity is proportional to the photoluminescence as a function of time after the initial sample excitation $\mathrm{E}_1(t)$ because the gating laser E_2 is fixed [162]. The crystal angle to satisfy the phase matching condition will be specific for the PL photons under investigation and thus only these photons will be detected.

In order to observe second-order non-linear processes, a non-centrosymmetric crystal must be used because otherwise $\chi_2 = 0$ [51]. In addition, it is desirable that the crystal has a high χ_2 value and low absorption in the incident and generated photon range to ensure an adequate generation efficiency [162]. In the experimental setups presented here, the non-linear processes described above were achieved using beta barium borate (β-$\mathrm{BaB_2O_2}$; BBO) crystals because of the high value of χ_2 =1.78 $\mathrm{pmV^{-1}}$ and low absorption above 200 nm [164].

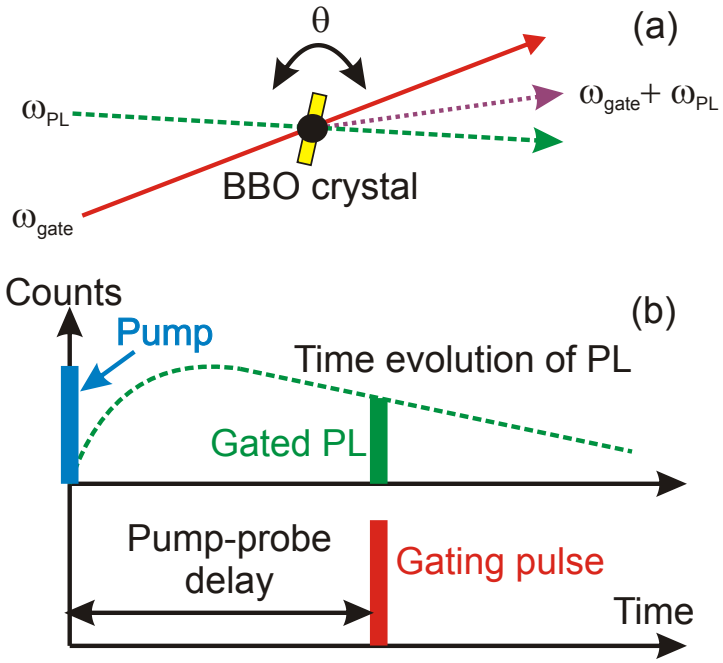

Figure 3.3: Schematic diagram to represent the processes involved in the PLUC technique. After photoexcitation of the sample, PL photons of frequency ω_{PL} are made to overlap spatially and temporally with gate photons of frequency ω_{gate} in a non-linear crystal, producing up-converted photons of frequency $\omega_{\mathrm{PL}} + \omega_{\mathrm{gate}}$. The lower plots illustrate how sum frequency generation acts as a gate, where the up-converted photons used to detect the PL are only produced during the gating laser pulse [163].

3.2.2 Photoluminescence Up-Conversion (PLUC) Spectroscopy

As described above, PLUC is an optically-gated technique to measure the time-resolved photoluminescence of a sample by utilising a non-linear crystal. The technique has low sensitivity due to the weak second-order nature of the process. However, a very high time resolution of 220 fs could be achieved in the setup described here.

The PLUC measurements were carried out in conjunction with Dr Patrick Parkinson and Chaw Keong Yong (Physics Department, University of Oxford) and the setup, shown in Fig. 3.4, will only be schematically described here; further details can be found in Ref. [162]. The output from the pumped Ti:Sapphire laser consists of laser pulses of 100 fs duration, a repetition rate of 80 MHz, tuneable centre wavelength between ∼750–900 nm and typical pulse energies of 11 nJ. For all experiments in this thesis, the centre wavelength was 800 nm.

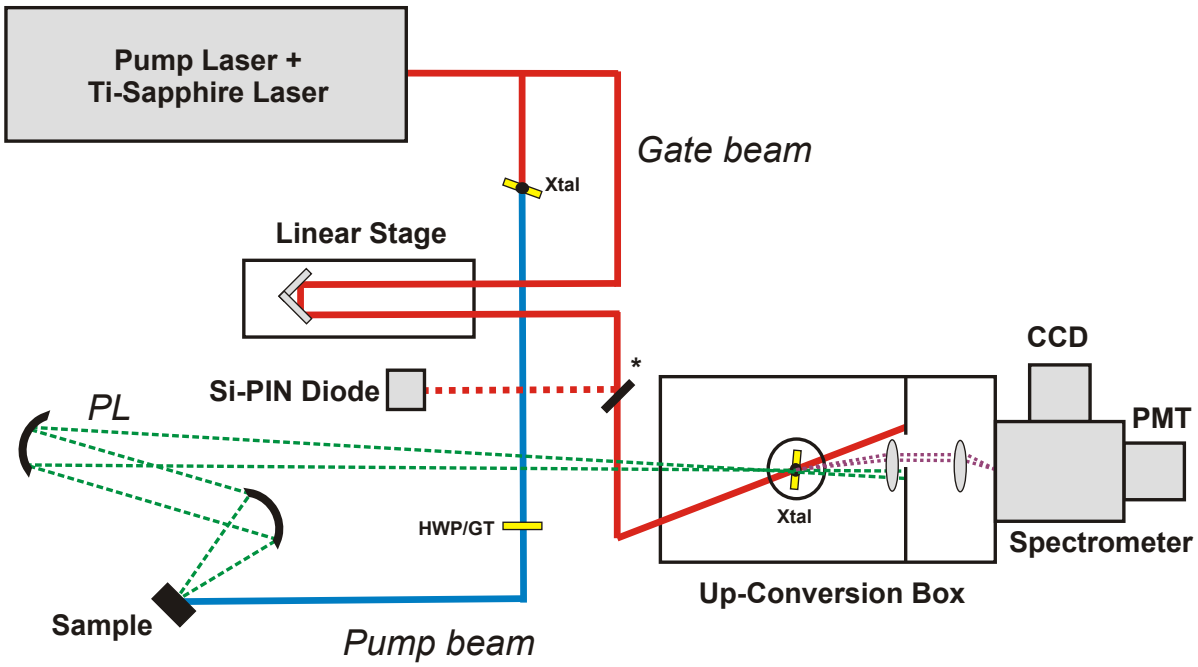

Figure 3.4: Schematic diagram of the experimental setup used for PLUC and TCSPC measurements in this work. The general beam paths and key components are described in the text. The starred mirror is only present in the TCSPC setup.

The output was split into two beams, namely the *gate* beam and the *pump* beam. The gate beam was directed onto a linear delay stage and then into the up-conversion box. Meanwhile, the pump beam was frequency-doubled to 400 nm using second-harmonic generation in a BBO crystal (Xtal) and the power and polarisation adjusted using the combination of a half-wave plate (HWP) and Glan Thompson (GT) polarising prism. A fluence of 0.15 μJ/cm^2 was used for all PLUC measurements in this work. The beam was then focused onto a thin film sample, which was held in a purpose-built sample holder under vacuum ($< 10^{-5}$ mbar). Its photoluminescence was collected and collimated into the up-conversion box.

In the up-conversion box, the photoluminescence and gate beam were incident on another BBO crystal (Xtal). To enable the phase-matching conditions to be satisfied for the given wavelength, the crystal was mounted in a rotation stage and a careful calibration of optimal crystal angle for each wavelength allowed the correct crystal angle to be set. The up-converted photons were then detected using a liquid nitrogen cooled silicon CCD array and the instrumental response of the detector corrected using a tungsten filament lamp of

known emissivity. Appropriate filters were used to remove any unwanted gate, pump or photoluminescence beam scatter. Up-conversion decay curves were obtained using automated software to vary the delay stage across the desired pump-probe delay range, with integration times between 1 and 30 seconds for each delay. The power dependence was tested for all of the samples under analysis (data not shown) and a linear response was observed, indicating that this fluence was suitable to use.

The same setup was also used to measure the steady-state visible-NIR PL of the sample except with the up-conversion crystal removed, the gate beam blocked and the excitation fluence lowered to $9\,\mathrm{nJ/cm^2}$.

3.2.3 Time-Correlated Single Photon Counting (TCSPC)

While PLUC is an optical-gated technique, TCSPC utilises electronic gating and therefore gives a lower temporal resolution ($\sim$120 ps on the system described here). However, it offers high sensitivity and can achieve a dynamic range of up to five decades [165].

The principles of the technique are illustrated in Fig. 3.5. A pump pulse photoexcites the sample synchronously with a trigger pulse on a Si-PIN Diode, defining the start of a measurement period. The sample photoluminesces and either the detection of a PL photon or the next laser pulse ($\sim$12 ns later) defines the end of the measurement period. After many signal periods, a histogram of photon arrival times is built up and a PL decay curve is obtained. For low level, high repetition rate signals, the light intensity is low enough that the probability of detecting a photon during one signal period is much less than one [165].

The setup for TCSPC used the same overall schematic layout as for the PLUC shown in Fig. 3.4, except for a few key differences. First, the starred mirror in the figure was inserted and directed the gate beam onto a Si-PIN Diode. This provided the trigger pulse for a signal period for the measurements. Meanwhile, the up-conversion crystal (Xtal) was removed and the PL was directed into the spectrometer and onto a photomultiplier tube (PMT) with use of appropriate filters. The pump fluence was also lowered to $9\,\mathrm{nJ/cm^2}$.

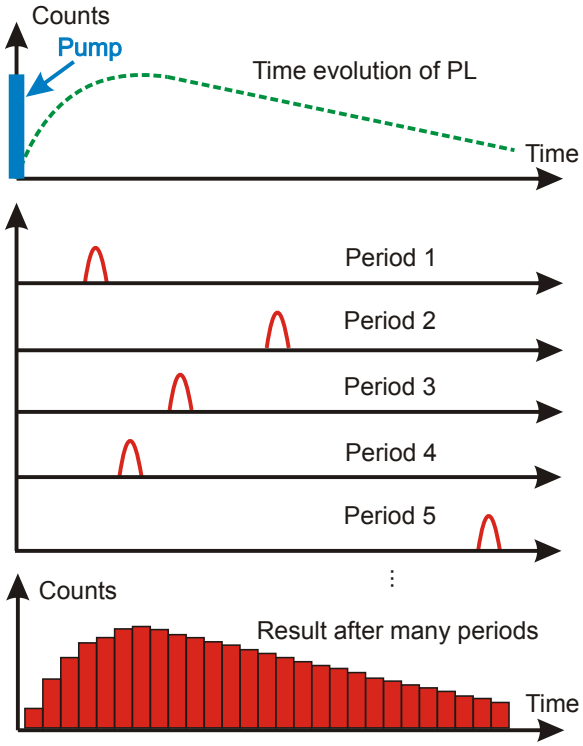

Figure 3.5: Schematic diagram to illustrate the principles of the TCSPC technique. During each signal period, at most one photon is detected. After many signal periods, a histogram of arrival times is acquired and traces the actual PL profile shown in the top curve.

3.2.4 Transient Absorption (TA) Spectroscopy

Transient absorption (TA) is a pump-probe technique where the absorbance of a sample is measured as a function of time after photoexcitation. In particular, the data are presented to describe the changes in absorption, relative to the steady-state absorption spectrum, as a function of pump-probe delay. The technique allows particular species to be selectively monitored, such as free polarons in polymers. The TA experiments in this work, presented at the end of Chapter 5, were undertaken by Christian Weisspfennig (Physics Department, University of Oxford) and only the basic details of the setup will be described here.

A schematic of the TA experimental technique is shown in Fig. 3.6. The output of a Ti:Sapphire regenerative laser amplifier system with a pulse duration of 50 fs was split into two beams, namely the pump and probe beams. The pump beam was frequency-doubled to a wavelength of 400 nm and focused onto the thin-film sample under vacuum with a pump

fluence of 50 μJ/cm^2 for all experiments. The probe beam was variably delayed using a linear delay stage and was focused onto a sapphire window to generate a white light continuum, part of which passed through the photoexcited sample and part of which acted as a reference beam. The desired wavelength (730 nm) was selected using an interference-pass filter (F) and the beam detected using photodiodes coupled to an integrator and a lock-in amplifier. The change in transmission was then determined by chopping the pump beam at half of the regenerative amplifier frequency (at 550 Hz), creating a 'pump on' and 'pump off' signal, and measuring the difference between the two signals. A temporal resolution of 75 fs was achieved.

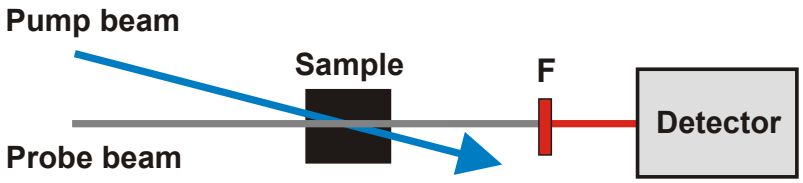

Figure 3.6: Schematic diagram of the experimental technique used for Transient Absorption measurements in this work. Beam paths are described in the text.

3.3 Microscopy

To resolve structures with dimensions on the order of the wavelength of visible light (nano to micrometers), optical microscopy is insufficient. Instead, techniques such as scanning probe and electron microscopy need to be utilised and these images can yield rich information about nanostructures.

3.3.1 Atomic Force Microscopy (AFM)

Scanning probe microscopy is an imaging tool spanning the regimes of both optical and electron microscopes. It can profile samples with high 3-D resolution and is now used in a variety of disciplines to image objects ranging from silicon atoms to surface protrusions in biological cells [166].

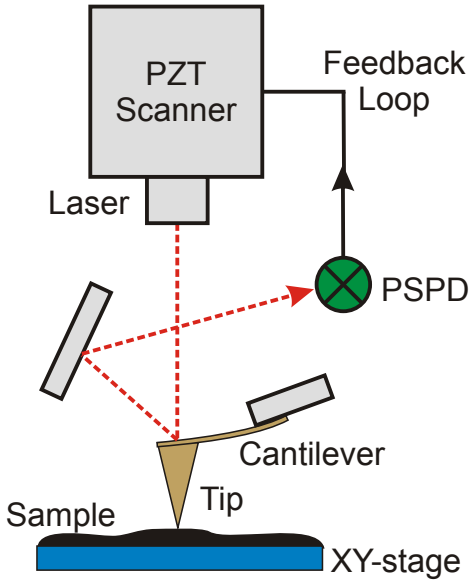

Figure 3.7: Schematic diagram of the detection system used in atomic force microscopy [167].

Atomic force microscopy (AFM) is a scanning probe microscopic technique that can be used to image nanostructures to a vertical resolution of ∼1 Å. A schematic diagram of the detection setup is shown in Fig. 3.7. The surface of a sample is probed with a sharp tip of a few microns length and less than 100 Å diameter, located at the free end of a cantilever of a few hundred microns length [166]. In non-contact mode, the cantilever is made to oscillate at a certain frequency above the sample. A laser diode illuminates the tip of the cantilever and the reflection is detected by a position-sensitive photodetector (PSPD) consisting of four photodiodes. This setup allows detection of any deflection of the laser beam arising from movement of the cantilever. When the probe is brought close to the sample surface, forces are exerted on the oscillating tip from interaction with the atoms in the sample. The forces most commonly arising from organic materials at distances of 1-10 nm are van der Waals forces, as discussed in Chapter 4. These forces alter the oscillation amplitude of the tip and the changes can be detected by the laser probe system. By means of a feedback system that moves the PZT piezoelectric scanner up and down, the system maintains a constant oscillating frequency. The tip is scanned across the sample using an xy-stage and the changes in van der Waals interactions are detected and used to generate a map of surface topography. The lateral resolution when sweeping across the sample (∼10 nm) is limited by the geometry

of the tip and is two orders of magnitude lower than the vertical resolution (sub-nm) [167].

The AFM images presented in this work were obtained in conjunction with Jack Alexander-Webber (Physics Department, University of Oxford) using a ThermoMicroscope AutoProbe M5 instrument housed in an acoustic isolation enclosure in non-contact mode. Aluminium coated tips (Veeco) were used, with typical tip radii of 10 nm, resonant frequencies in the range 73-109 kHz, and stiffness of 3 N/m. The cantilevers were made of phosphorus doped silicon with reflective aluminium coatings on the back to maximise the laser signal. The images in Chapters 5-7 were obtained by either spin-coating (1000–4000 rpm) or drop-casting dilute solutions onto flat silicon wafers or quartz substrates and specific conditions will be detailed in the relevant chapters.

3.3.2 High-Res. Transmission Electron Microscopy (HRTEM)

Transmission electron microscopy (TEM) is a technique to obtain images from transmitted electron beams that have interacted with a sample. High-resolution TEM (HRTEM) is an imaging mode of TEM that allows the crystallographic structure of a sample to be imaged on an atomic scale [168]. The images are formed by phase contrast, where the phases of electron waves differ after interaction within the sample. The HRTEM images presented in Chapter 8 were obtained by Dr Jamie Warner (Materials Department, University of Oxford) from solutions deposited onto lacey carbon grids.

3.4 Summary

The experimental techniques used in this thesis are summarised below:

- Absorption spectroscopy uses the Beer-Lambert Law to monitor absorption of light passing through a sample and is a useful tool to simultaneously characterise both polymer and nanotube transitions in a sample.

- Photoluminescence Excitation (PLE) Spectroscopy is a technique where the photoluminescence from a sample is collected as the excitation is incremented through a range of wavelengths. This is the most powerful way to characterise nanotubes in a distribution, where emission in the NIR (E_{11} transitions) is detected after excitation in the visible (E_{22} transitions).

- Photoluminescence Up-Conversion (PLUC) Spectroscopy is a pump-probe technique using frequency-mixing to optically gate the PL from a photoexcited sample. A high resolution ($\sim$220 fs here) is achieved, allowing resolution of ultrafast processes.

- Time-Correlated Single Photon Counting (TCSPC) is another technique to detect time-resolved PL from a photoexcited sample. A histogram of arrival times of photons is built up and an electronic gate is used in the detection system. As such, TCSPC is a lower resolution technique ($\sim$120 ps here) but has a greater sensitivity than PLUC and allows the long time behaviour to be examined.

- Transient Absorption (TA) is a pump-probe technique where the absorption of a sample is monitored over time following photoexcitation. A resolution of 75 fs was achieved here. Particular species can be selectively monitored, such as the presence of free charges on polymers.

- Atomic Force Microscopy (AFM) and High-Resolution Transmission Electron Microscopy (HRTEM) are complementary imaging techniques to characterise nanostructures with resolutions on the atomic scale.

Chapter 4

Synthesis of Nanotube–Polymer Nanohybrids

4.1 Introduction and Background

Fundamental studies and applications of carbon nanotubes have been hindered by their lack of solubility in common organic solvents [169]. Nanotubes tend to bundle together due to significant van der Waals interactions (π-π stacking) between the sidewalls of tubes. SWNT solubilities in commonly used organic solvents are shown in Table 4.1. The highest nanotube solubility (dichlorobenzene) is only 95 mg/L and it is likely that many of these tubes still

Solvent	SWNT Solubility (mg/L) [169]	Density (g/cm^3) at 20 °C [93, 170]	Dielectric constant ϵ_r [93, 170]
1,2-dichlorobenzene	95	1.305	9.93 (25 °C)
Chlorobenzene	∼60[1]	1.106	5.62 (25 °C)
Chloroform	31	1.483	4.81 (20 °C)
Tetrahydrofuran	4.9	0.889	7.52 (20 °C)
o-xylene	4.7	0.880	2.57 (20 °C)
Toluene	<1	0.869	2.38 (25 °C)

[1] SWNTs exhibit solubilities in chlorobenzene which are intermediate between those in dichlorobenzene and chloroform.

Table 4.1: Physical properties of organic solvents used in this work and SWNT solubilities in each.

exist in small invisible bundles [169].

The PL efficiency is significantly reduced in bundled nanotube samples because rapid energy transfer occurs from semiconducting to metallic nanotubes on which excitons recombine non-radiatively [12]. A breakthrough came in 2002 when O'Connell *et al.* were able to use ultrasonication to break up nanotube bundles and disperse the individual tubes using an aqueous surfactant, sodium dodecyl sulfate (SDS) [83]. The favourable interactions between the hydrophobic nanotube surfaces and hydrophobic component of the surfactants led to micelle formation. The micelles prevented the nanotubes from rebundling and ultracentrifugation allowed removal of the higher density micelles containing bundles ($1.2\,\mathrm{g/cm^3}$) from the lower density micelles containing individual tubes ($1.0\,\mathrm{g/cm^3}$). Thus, PL from individual nanotubes was observed for the first time [83].

Another obstacle to nanotube applications is polydispersity – each distribution contains many different chiralities of both semiconducting and metallic tubes. Selective synthesis has not yet been achieved and, consequently, a lot of research attention has been given to post-synthesis tube sorting. In 2006, Arnold *et al.* developed a technique called density-gradient ultracentrifugation (DGU) in which individual nanotubes were centrifugally sorted to a high purity (>97 %) from subtle differences in their densities when dispersed by a range of surfactants [171]. More recently, a scalable and efficient gel chromatography process was developed to separate individual chirality species [172]. However, such techniques are often complex or require specialised equipment.

In contrast to surfactants which disperse all of the material in a distribution, Zheng *et al.* showed that DNA segments can selectively disperse only nanotubes. The binding is due to π-π stacking interactions which lead to a helical wrapping [173]. It was later shown that specific DNA sequences could selectively bind to certain nanotube structures, providing a tunable but somewhat tedious method to sort nanotubes [174].

O'Connell *et al.* demonstrated that conjugated polymers can also bind to nanotubes via strong π-π interactions and efficiently disperse tubes [175]. In 2007, Nish *et al.* showed that polyfluorene polymers preferentially bind to certain semiconducting nanotube species [176].

This allowed exclusion of other species such as metallic nanotubes using simple solution processing techniques. Moreover, the method required one and two orders of magnitude lower centrifugation speeds and times, respectively, compared to the surfactant dispersions. The tube-selectivity was found to depend on the solvent and polymer side-chains, which was maximised for the polymer poly(9,9-dioctylfluorenyl-2,7-diyl) (PFO; structure shown in Fig. 4.3 (a)), high chiral angle nanotubes and the poor nanotube and polymer solvents toluene and *o*-xylene [176, 177, 178].

Many other dispersing semiconducting polymers and surfactants have been used over the years [179]. In this chapter, the methods to produce the surfactant- and polymer-dispersed samples used in Chapters 5–8 are described and the nanostructures characterised.

4.1.1 Van Der Waals Interactions

Conjugated polymers and carbon nanotubes are non-polar molecules and the dominant interactions are induced-dipole van der Waals forces [180]. These interactions can be demonstrated by considering two non-polar molecules separated by a distance r. The electron clouds are fluctuating, resulting in instantaneous dipoles which vary in direction and magnitude. If an instantaneous dipole forms in one molecule it will polarise the other molecule and induce in it a corresponding instantaneous dipole. The two dipoles bind together providing an attractive force. As the first dipole changes direction, the second will follow it and thus the attractive effect does not average to zero. For the case of conjugated polymers and nanotubes, the many π-electrons lead to strong induced-dipole forces between the π-electron clouds and the π-planes stack on top of each other (π-π stacking).

Although these forces are weakly attractive at large distances, the nuclear and electronic repulsions begin to dominate at short distances. The overall behaviour can be approximated using the Lennard-Jones potential:

$$V(r) = 4\epsilon \left[(\sigma/r)^{12} - (\sigma/r)^{6} \right], \tag{4.1}$$

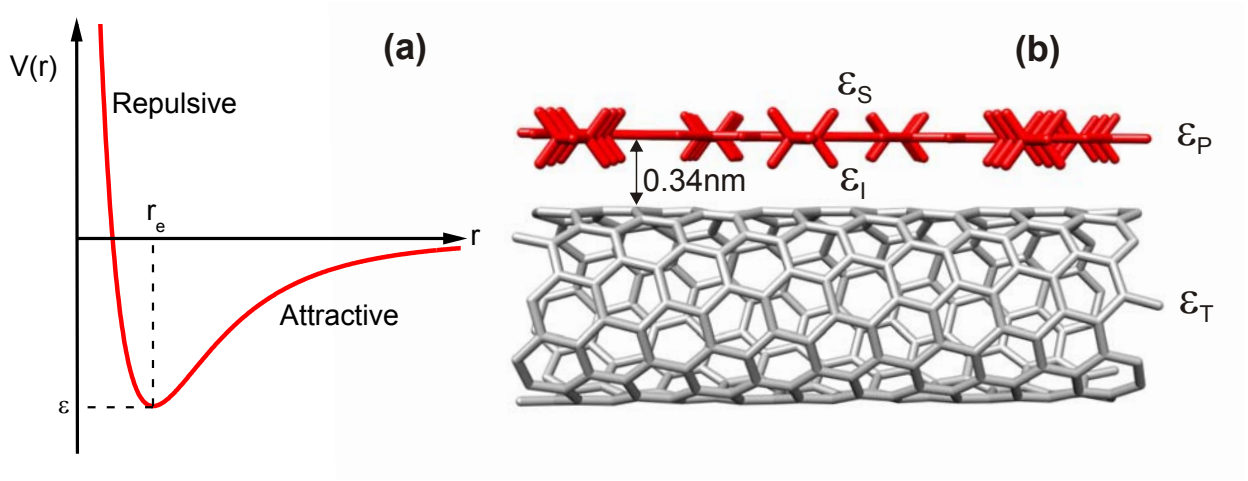

Figure 4.1: (a) The Lennard-Jones potential to approximate the potential between two molecules. (b) Schematic diagram of a nanotube with a polymer chain bound to the surface with a separation of 0.34 nm. The relevant dielectric constants for the system are also labelled, namely those of the tube ϵ_{T}, the interface layer between the materials ϵ_{I}, the polymer ϵ_{P} and the surrounding solvent ϵ_{S}.

and the function form is shown in Fig. 4.1 (a) [180]. The parameter ϵ is the depth of the potential well and is located at the equilibrium separation distance $r_e = 2^{1/6}\sigma$.

The Lennard-Jones potential and others of similar form are used to model inter-molecular interactions in molecular dynamics and Monte Carlo simulations [181, 182]. A nanotube-polymer system is shown schematically in Fig. 4.1 (b) for a short polymer chain segment. The effective potential felt by a polymer 'particle' i at a distance r_i from the surface of the tube can be obtained from the spatial integration of a continuous Lennard-Jones potential field due to a cylindrical shell [182]. The total potential energy of the system will be given by the sum of these interactions as well as the sum of standard Lennard-Jones interactions between particles in different polymer chains and a harmonic bending potential contribution to account for polymer chain stiffness [182]. Simulations and experiments have shown that a helical binding is the most favourable configuration for the majority of polymer-nanotube systems [173, 182, 183, 184, 185, 186]. Furthermore, the nanotube-polymer π-π stacking distance is twice the van der Waals radius of carbon (0.34 nm) [187], as observed for the stacking distance in graphite [11].

4.1.2 Environmental Dielectric Screening Effects

The screening of the Coulomb interactions in nanotubes due to a dielectric environment was introduced in Chapter 2. The effect leads to a larger relative reduction of the electron-electron than the electron-hole interactions, resulting in an overall red-shift of nanotube transitions compared to a bare nanotube in vacuum. Ohno *et al.* immersed individual tubes bridging trenches in solvents with a range of dielectric constants. They showed that the E_{11} and E_{22} transition energies red-shift by ∼30–50 meV due to the screening effect, but the effect saturates at a solvent dielectric constant of $\epsilon_S \sim 5$ [66].

Fig. 4.1 (b) shows the interfaces formed within a nanotube-polymer system in a solvent, where the dielectric constants are given for the nanotube ϵ_T, the interface layer between the materials ϵ_I, the polymer/surfactant ϵ_P and the surrounding solvent ϵ_S. These surrounding dielectric materials influence the nanotube transition energies. Ohno *et al.* showed that the nanotube transition energies in the presence of an aqueous SDS surfactant were red-shifted by ∼10–20 meV compared to bare nanotubes [188]. In the presence of wrapping conjugated polymers, the red-shifts due to the dielectric polymer were calculated to be greater again, ∼20-30 meV red-shifted relative to the SDS-nanotube system [156, 176]. These effects have been found to be independent of the solvent ϵ_S, implying that the interface gap is a vacuum (*i.e.* $\epsilon_I = 1$) which excludes all solvent [156] and the presence of the surrounding solvent does not contribute to the dielectric effects. Finally, Chuang *et al.* empirically determined the relationship between the nanotube diameter d and the observed red-shift ΔE arising from Coulomb corrections in the presence of a range of conjugated polymers to be $\Delta E \propto d^{-0.55}$ [189]. Thus, nanotubes coated in conjugated polymers show weakly diameter-dependent red-shifts of the E_{11} and E_{22} transition energies by ∼20-30 meV relative to the Weisman and Bachilo SDS-dispersed values.

4.2 Starting Nanotube Materials

The SWNT starting material used in the majority of this thesis was purchased from South-West NanoTechnologies (SWeNT) in powder form and used without further purification. The tubes were synthesised by the manufacturers using the CoMoCAT process and the resulting 'SG65' distribution contained 90 % carbon material by weight, and the remainder consisted of impurities such as metal catalysts. The tubes were specified to be >90 % semiconducting of which >50 % were of the (6,5) chirality. The distribution contained tubes of typical length >1μm and of average diameter 0.7–0.9 nm, providing some of the smallest diameter tubes commercially available.

Powdered SWNTs produced by the HiPCO process were purchased from Carbon Nanotechnologies Incorporated (CNI; now Unidym) with lengths 100–1000 nm and an intermediate diameter distribution of 0.8–1.2 nm. The samples used in this thesis were purchased as 'purified' tubes (<15 wt % iron catalyst impurities). However, it has recently been shown that the manufacturer's acid purification process protonates tubes and significantly reduces PL and dispersing efficiencies [190]. Future work should utilise the more pristine 'raw' HiPCO tubes and any additional iron catalysts (<35 wt %) are simply removed in the sample preparation routines described in this chapter.

4.3 [SDBS-NT] Aqueous Dispersions

The surfactant sodium dodecyl benzene sulfonate (SDBS), the structure of which is shown in Fig. 4.2 (d), was used instead of SDS because it has been found to be a superior nanotube dispersant [191]. SDBS was purchased from Sigma-Aldrich, added to deuterated water (D_2O[1]) to reach a concentration of 10 mg/mL (350 mg in 35 mL) and dissolved using gentle warming in a sonic bath. Nanotubes (either CoMoCAT or HiPCO) were added to achieve a concentration of 0.4 mg/mL (15 mg) and the mixture treated in a high power ultrasonic disintegrator

[1]Deuterated water was used instead of H_2O to ensure the water absorption peaks were sufficiently red-shifted out of the PLE spectral range under investigation.

at a frequency of 23 kHz (10 μm amplitude) for 30 minutes. This breaks up the nanotube bundles and allows the dispersant to coat the tube surfaces and prevent rebundling. The remaining bundle micelles were removed by ultracentrifugation at 100,000 $\times$g for 4 hours at room temperature. The upper 85 % of the supernatant, containing the individually dispersed SWNTs, was retained and the dispersion referred to as [SDBS-NT].

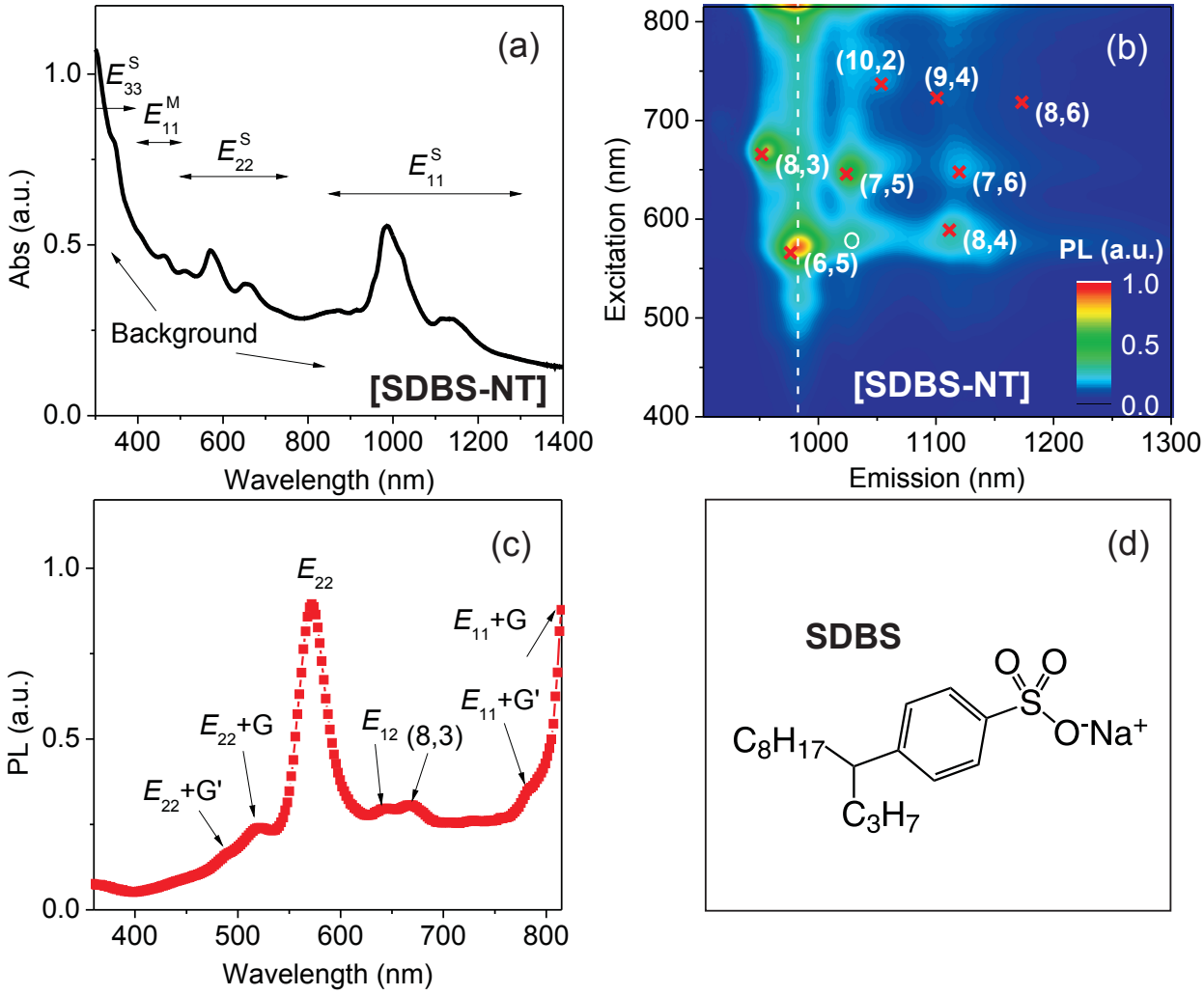

Figure 4.2: (a) An absorption spectrum of the [SDBS-NT] sample in D_2O highlighting the nanotube E_{ii} transitions. (b) PLE map of the [SDBS-NT] sample in D_2O. Nanotube species were assigned using the Weisman and Bachilo empirical model [44]. A tube-tube energy transfer process is highlighted with a circle. (c) An excitation spectrum representing emission from the (6,5) species, corresponding to the vertical dashed line in (b). The relevant resonant and satellite peaks were assigned to various processes, as discussed in the text. (d) Chemical structure of the SDBS surfactant.

Since the surfactant dispersing procedure is not tube-selective, the SDBS dispersions provide ideal controls of the starting nanotube chirality distributions. Fig. 4.2 (a) shows an

absorption spectrum of the [SDBS-NT] distribution using CoMoCAT nanotubes. The semiconducting E_{11}^S transitions are seen in the NIR range and the semiconducting E_{22}^S transitions in the visible region. The other metallic and higher order transitions are noted here but this work was focused on the lower semiconducting transitions, which will be referred to as E_{11} and E_{22} from herein. A broad underlying, featureless background is also present and its origin is still debated in the nanotube community. A recent study [192] showed that there are several contributions to the background, including light scattering effects, carbon impurities contributing to a broad π-π plasmon, nanotube defects, metallic nanotubes and spectral congestion. Crucially, spectra of purified metallic nanotubes showed broad backgrounds which were absent in pure semiconducting SWNT samples, indicating a strong metallic tube contribution.

Due to spectral congestion, it is difficult to unambiguously assign each peak in absorption spectra, especially when a large number of nanotube species are present. By contrast, PLE maps provide a powerful tool to identify semiconducting nanotube species using their unique (E_{11},E_{22}) fingerprints. Fig. 4.2 (b) shows the PLE map of the aqueous [SDBS-NT] solution. The resonant nanotube peaks were assigned using the Weisman and Bachilo empirical model [44] and the small deviations (<10 meV) are due to the slightly different screening effect of the SDBS surfactant compared to SDS. It is clear that the dominant species is the (6,5) chirality, with decreasing amounts of (8,3), (7,5), (8,4) and (7,6) tubes and traces of (10,2), (9,4) and (8,6) species. In addition, some intertube FRET energy transfer cross-peaks are seen, such as the one highlighted with a circle, where energy transfer occurs from the photoexcited (6,5) tubes to the smaller bandgap (7,5) tubes which photoluminesce. These transfer processes occur between rebundled but isolated SWNTs [193].

Fig. 4.2 (c) shows the excitation slice corresponding to emission from the (6,5) tube at 980 nm, as indicated by the vertical dashed line in Fig. 4.2 (b). In addition to the E_{22} resonance, several satellite peaks are observed which arise from absorption by phonon-assisted transitions followed by E_{11} emission of the (6,5) tube. The creation of a G-band phonon with electronic excitation leads to satellite peaks at $E_{11} + 200\,\text{meV} \approx 840\,\text{nm}$ and

$E_{22} + 200\,\text{meV} \approx 520\,\text{nm}$ [194, 195]. The satellite peaks corresponding to the weaker two-photon G' process are also observed at $E_{11} + 350\,\text{meV} \approx 780\,\text{nm}$ and $E_{22} + 350\,\text{meV} \approx 490\,\text{nm}$. In general, the non-resonant Raman features also appear as diagonal lines on PLE maps at energies ∼200 meV and ∼350 meV below the excitation wavelength, corresponding to the G and G' bands, respectively [196]. Finally, the E_{21} transition is observed but is weak due to the depolarisation effect [189].

4.4 [PFO-NT] Nanohybrids

4.4.1 Synthesis

The PFO-nanotube dispersing method was based on the toluene dispersion procedure developed by Nish *et al.* [176, 177] but the technique was optimised here with *o*-xylene to give a greater nanohybrid yield and to remove the excess polymer. PFO was purchased from American Dye Source (MW 36,000 gmol^{-1}) and its structure is shown in Fig. 4.3 (a). CoMoCAT material (5 mg) was mixed with a 0.6 mg/mL *o*-xylene solution of PFO (6 mg in 10 mL) to give a tube concentration of 0.5 mg/mL and the mixture was treated in an ultrasonic disintegrator for 15 minutes to break up bundles and allow the polymer chains to interact with the tube surfaces. This was followed by ultracentrifugation for 8 minutes at 10,000 ×g and retainment of the upper 85% of supernatant, which contained the dispersed tubes. The entire procedure was repeated 5 times to increase the total volume of nanohybrid solution to ∼35 mL.

In order to remove the excess polymer and purify the nanohybrid samples, a purification procedure was used whereby aggregation of the nanohybrid species was induced to allow extraction of these species while the unbound polymer remained in solution [187]. However, the dispersion process resulted in low yields and the nanohybrids were present in the PFO-*o*-xylene solution at a concentration too low to easily induce aggregation[2]. Therefore, the

[2]If the solutions were left for a sufficient time (∼3 days), aggregation occurred and no rotary evaporation step was required.

total volume of nanohybrids was reduced to about $1/5^{\text{th}}$ of the original volume using a rotary evaporator at 70 °C to controllably remove the solvent. The nanohybrids aggregated spontaneously at increased concentration and were precipitated by centrifugation for 4 minutes at 16,000 $\times g$. The supernatant containing the unbound PFO was discarded and the residue, containing the nanostructures, was redissolved in a small volume of fresh *o*-xylene ($\sim$2 mL). The sample was briefly tip-sonicated (10 seconds) to break up any pure PFO aggregates and nanohybrid aggregation was again induced by gently warming in a sonic bath ($\sim$15 minutes), followed by another centrifugation step. The process was repeated a total of 3 times to ensure adequate polymer removal. The resulting [PFO-NT] sample was redissolved in minimal *o*-xylene solution (typical final PFO concentrations of $\sim$0.1 mg/mL) and diluted further for solution measurements. It is noted that this is the first time that simple processing techniques have been used to remove the excess polymer from [PFO-NT] nanohybrids and concentrate the structures.

4.4.2 Characterisation

The purified [PFO-NT] absorption spectrum is shown in Fig. 4.3 (a) (black line) and is strikingly different to the [SDBS-NT] spectrum (dashed black line). First, the featureless background is absent due to the removal of metallic nanotubes and other carbonaceous impurities. Second, the dominant species is the (7,5) tube with E_{11} and E_{22} resonances at 1045 nm and 652 nm, respectively. Small fractions of (6,5), (7,6) and (8,6) tubes are present from their respective E_{11} peaks at 992 nm, 1135 nm and 1194 nm, but these species comprise less than 30 % of the total. Thus, the PFO dispersion process shows strong selectivity for semiconducting nanotubes, particularly (7,5) species. The nanotube peaks are red-shifted relative to the [SDBS-NT] distribution because of the dielectric screening of the Coulomb interactions in the nanotubes by the wrapping PFO [176].

The PFO absorption is seen in the region 320–500 nm and shows peaks at $\sim$375–395 nm and 437 nm, attributed to the relatively disordered α- and aggregated β-phases of the polymer, respectively [198]. The aggregated β-phase is also seen in a free PFO sample (red

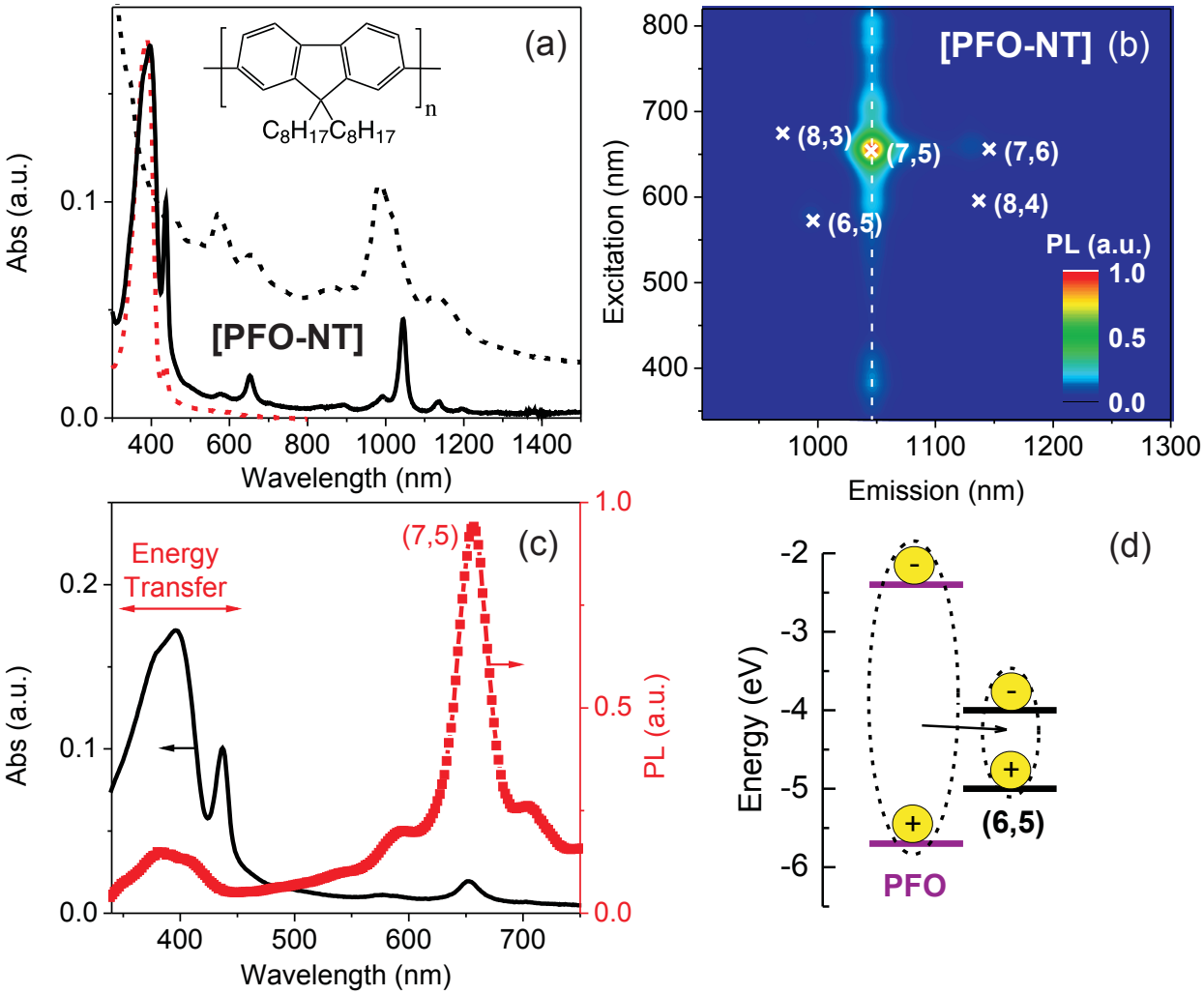

Figure 4.3: (a) Absorption spectra of the [PFO-NT] nanohybrids (black line) diluted 1/20 and pure PFO (red dashed line, 5×10^{-3} mg/mL) in *o*-xylene solution, and [SDBS-NT] in D_2O (black dashed line). The inset shows the chemical structure of PFO. (b) PLE map of the [PFO-NT] nanohybrids in *o*-xylene. Species were labelled using the Weisman and Bachilo empirical model [44] with a global red-shift of 25 meV. (c) Excitation spectrum corresponding to (7,5) emission (red squares), as extracted from the dotted white line in (b), along with the absorption spectrum of [PFO-NT] nanohybrids (black line). (d) Schematic energy level diagram showing the type-I heterojunction between PFO and (6,5) nanotubes leading to energy (exciton) transfer being the dominant transfer process. Energy levels (with respect to vacuum) were taken from Refs [156] and [197] and discussed in the text.

dashed line) because of the the poor solubility of PFO in solvents such as xylenes [199, 200]. However, the [PFO-NT] sample has a larger β-phase component because the nanotubes act as templates for aggregation of PFO [186].

Fig. 4.3 (b) shows the PLE map of the [PFO-NT] nanohybrids in *o*-xylene. The species were assigned using the Weisman and Bachilo empirical model [44] with a global red-shift of 25 meV to account for the environmental screening effects. The dominant species is clearly the (7,5) semiconducting tube with only traces of the other semiconducting tubes. The vertical excitation slice corresponding to the emission from the (7,5) tube is shown in Fig. 4.3 (c), showing the dominant resonant E_{22} absorption. In addition, a 320–500 nm band, corresponding to PFO absorption, also gives rise to emission from the nanotubes. This is the signature of an energy transfer process, where excitons on the PFO are non-radiatively transferred to the nanotube on which they subsequently recombine. This energy transfer band is tunable with an increasing excess of PFO because of the formation of more extended polymer aggregates on the tube surface [201].

The electronic energy level alignment of the PFO and nanotubes is shown in Fig. 4.3 (d). The nanotube valence (VB) and conduction bands (CB) were estimated using the method of Schuettfort *et al.* [156]. That is, the energies from the single-particle tight-binding model of Popov *et al.* [43] were split equally about the constant work function of -4.5 eV, since tubes with diameters >0.7 nm have been found to have work functions within 100 meV of this value [202]. The HOMO and LUMO levels of the polymer PFO were taken from Ref. [197]. The heterojunction is clearly of type-I character and thus energy transfer would be dominant over charge transfer. A FRET energy transfer mechanism has been proposed for these systems [187] but the unique coaxial geometry and short-distance ($\sim$0.3 nm) suggests that a Dexter electron exchange mechanism may be more appropriate [203, 204].

4.4.3 Selectivity Mechanism

The selectivity mechanism has not yet been fully elucidated but it is likely to be related to the structural properties of the PFO-*o*-xylene (or toluene) solvent system, because car-

rying out the same preparation route with good nanotube and polymer solvents such as chlorobenzene does not produce the strong semiconducting selectivity. Polyfluorenes readily form stabilised β-aggregates by interlocking lateral side-chains (*i.e.* 'zipping'). These interactions are optimised for octyl chains (PFO) and readily form in poor solvents such as toluene and *o*-xylene [198, 199, 200]. It has been suggested that the selectivity arises from a similar mechanism – the alkyl chains of neighbouring PFO polymer chains zip and align on similar zig-zag motifs on the tube walls. An optimal coverage is obtained when the zipped polymer chains adopt a helical conformation, consistent with experiment, which maximises both the π-π interactions between the tube walls and fluorene units and the network of octyl-octyl tails and the zig-zag structure on the tube walls [186]. Simulations showed that such interactions are optimised for certain diameters and chiral angles of tubes, reproducing the widely experimentally observed trend of decreasing selectivity: (8,6)>(9,7)>(8,7)>(7,5)>(7,6) [186]. Centrifugation removes the tubes that are not well bound by PFO, leaving the 'selected' tubes dispersed in solution.

4.5 [P3HT-NT] Nanohybrids

4.5.1 Synthesis

The polythiophene-SWNT dispersing procedure was based on that developed by Schuettfort *et al.* [187] but with the proportions and scale optimised to ensure a maximum (6,5) nanotube enrichment. Regioregular poly(3-hexylthiophene-2,5-diyl) (P3HT), with molecular weight 25,000–35,000 gmol^{-1} and structure shown in Fig. 4.5 (a), was manufactured by Plextronics, Inc. and purchased from Sigma-Aldrich. Chlorobenzene was used as a solvent because it was found that negligible yields were obtained using the poor nanotube solvents toluene, THF and *o*-xylene [187].

The P3HT was dissolved in chlorobenzene solution to a 0.6 mg/mL concentration (17 mg in 30 mL) by gentle warming in a sonic bath and CoMoCAT material was added to achieve

a tube concentration of 0.3 mg/mL (9 mg). The resulting dispersion was treated in an ultrasonic disintegrator for 15 minutes, followed by centrifugation for 8 minutes at 10,000 $\times g$. The upper 85 % of the supernatant, which contained high concentrations of the individually dispersed [P3HT-NT] structures, was retained.

To remove excess polymer, spontaneous aggregation was induced by adding toluene to the nanohybrid solutions in a volume to match that of the chlorobenzene [187]. Toluene acts as an orthogonal solvent, keeping the P3HT polymer suspended but causing aggregation of the nanostructures. The process was aided by warming in a sonic bath for 15 minutes and the aggregates were precipitated by centrifugation (4 minutes at 16,000 $\times g$). The supernatant containing unbound P3HT was discarded and the residue, containing the nanostructures, was redissolved in fresh toluene ($\sim$10 mL) and aggregation again induced using a sonic bath. The procedure was repeated a total of three times to ensure all unbound polymer was removed. The final residue was dried, weighed and redissolved in minimal chloroform solution to produce concentrated and highly purified [P3HT-NT] nanohybrid solutions that could be cast into films or diluted further for solution measurements.

4.5.2 Characterisation

In these purified nanohybrids, the P3HT organises into a sheath-like morphology on the tubes, aligned at an approximate angle of 48° with respect to the SWNT axis [205]. This is shown in the schematic model in Fig. 4.4 (a), which was constructed by Torben Schüttfort (Physics Department, University of Oxford). An AFM image of the nanohybrids taken by an MPhys Student, Hannah Swain, is shown in Fig. 4.4 (b). The image was obtained in non-contact mode after drop casting a diluted [P3HT-NT] solution on a flat silicon wafer. The height analysis is consistent with the diameter of a CoMoCAT nanotube ($\sim$0.7–0.9 nm) with a monolayer coating of polymer at a distance of twice the van der Waals radius (0.34 nm) from the tube [187]. In addition, a small number of isolated P3HT nanocrystals (typical dimensions of $\sim$3–5 nm) are observed attached to the P3HT sheath enveloping the tubes, as seen elsewhere [153, 187].

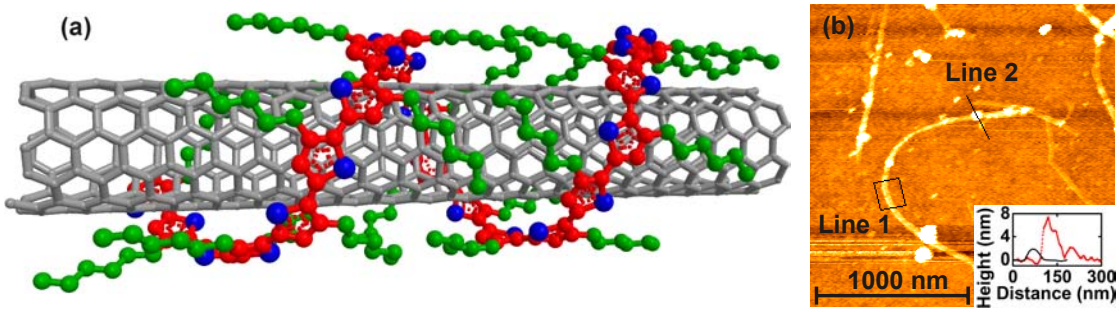

Figure 4.4: (a) Schematic diagram of a (6,5) SWNT coated with a monolayer of sheath P3HT. Sulfur atoms are coloured blue, the carbon backbone is red and the side-chains are green. (b) AFM image showing the isolated nanotubes coated with P3HT sheath and the scattered P3HT nanocrystals. *Inset*: Heights of AFM slices marked on image, where Line 1 is the black solid line and Line 2 is the broken red line. Reproduced in part with permission from Ref. [206]. Copyright 2011 American Chemical Society.

Fig. 4.5 (a) shows an absorption spectrum of the [P3HT-NT] nanohybrids diluted in chloroform solution, with the E_{11} transitions seen in the region 900–1300 nm. The P3HT absorption is seen in the range 400–700 nm and can be compared to P3HT in solution and as a spun-cast film[3]. The film spectrum is significantly red-shifted relative to the solution spectrum because of the increased conjugation and planarisation of chains in the highly ordered lamellar structures [100]. The spectral shape of the P3HT in the [P3HT-NT] sample resembles the film with a small contribution from solution P3HT due to trace amounts of remaining unbound polymer. This shows that the P3HT chains are highly planarised and extended on the nanotubes, as has been reported elsewhere [185, 187]. Furthermore, the relatively strong contribution of the lowest energy 0-0 peak relative to 0-1 shows that the P3HT chains are not strongly coupled to other chains [104]. This is because the π-π interactions of the chains in a monolayer coating are predominantly with the tube surfaces on which they are bound. The spectroscopy is discussed further in Chapter 5.

The P3HT concentration was determined by comparing the absorption spectrum of [P3HT-NT] with that of a known solution of P3HT, as shown in Fig. 4.5 (a), yielding typical P3HT concentrations of 0.6 mg/mL. By weighing the product, the total mass of material was determined. The mass was used to calculate the nanotube component to also be 0.6 mg/mL,

[3]Unless otherwise specified, polymer films were spun-cast on quartz substrates from a solution of polymer in chloroform (10 mg/mL) at 1000 rpm, followed by an annealing treatment at 120°C for 30 minutes.

such that each nanohybrid contains equal mass of nanotube and polymer.

The absorption spectra of the [P3HT-NT] and [SDBS-NT] samples are also compared in Fig. 4.5 (a). The comparison shows that the P3HT dispersing process is not tube-selective and the overall spectral shapes appear similar, including the presence of the broad background. However, recent work showed that polythiophenes with longer side-chains can preferentially disperse semiconducting tubes over metallic species at higher temperatures [207]. The selectivity was also attributed to the formation of polymer shells of interdigitating polymer side-chains, matching the diameters of the selected SWNTs. Unlike PFO, the selectivity for particular semiconducting species was only marginal.

The absorption spectra also show that the nanotube transitions are significantly red-shifted in the [P3HT-NT] sample relative to the [SDBS-NT] sample. This is also seen in the PLE map of the [P3HT-NT] nanohybrids, which is shown in Fig. 4.5 (b). The tube species were assigned using the Weisman and Bachilo empirical model for SDS-dispersed tubes but with a global red-shift of 45 meV for the E_{11} and E_{22} transitions. The large red-shift is partly attributed to an environmental component, owing to the dielectric shielding effect from the polymer (∼20–30 meV). The additional red-shift was found to result from the type-II electronic alignment of the polymer and nanotubes, as shown in Fig. 4.5 (d) and discussed in section 4.5.3 below.

The PLE map also shows enhanced emission from all tubes following excitation in the region 450–700 nm, which corresponds to absorption by the P3HT component. A vertical excitation slice corresponding to emission from the (7,5) tube species is shown in Fig. 4.5 (c) and compared to the sample absorption spectrum. The emission arises partly from direct absorption in the (7,5) E_{22} transition (∼660 nm) but also from the region corresponding to the P3HT transitions (450–700 nm). This energy transfer process competes with charge transfer, which will be discussed in Chapter 5. The absolute PL intensities from P3HT-dispersed tubes were always considerably weaker than from tubes at the same concentration but dispersed with other polymers, suggesting that the non-radiative charge transfer pathway in [P3HT-NT] complexes is significant.

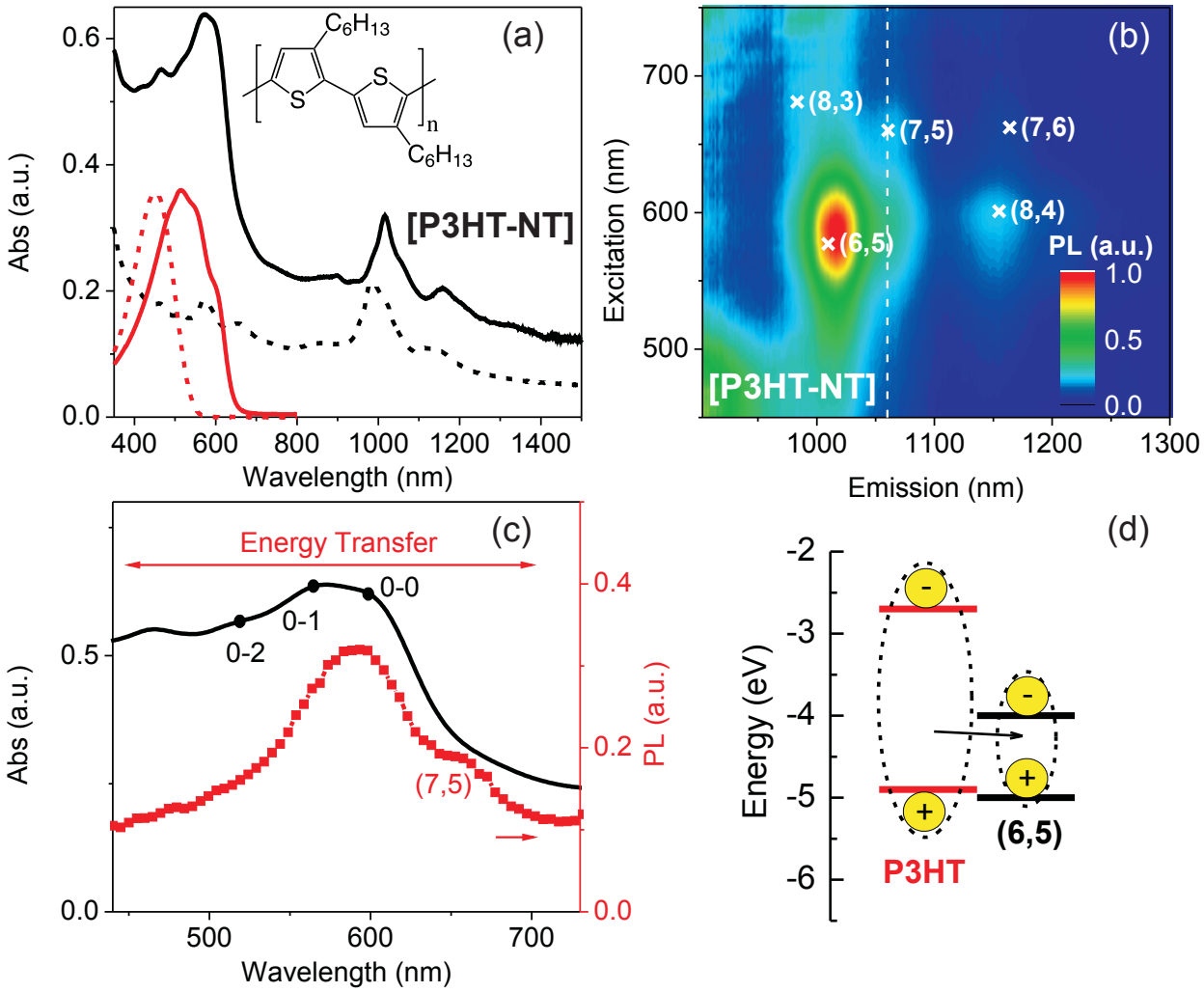

Figure 4.5: (a) Absorption spectra of purified [P3HT-NT] nanohybrids diluted 1/50 (black solid line) and pure P3HT (red dashed line, 7×10^{-3} mg/mL) in chloroform solution. An [SDBS-NT] dispersion in D_2O (black dashed line) and a P3HT thin film (red solid line), scaled to match the P3HT solution, are shown for comparison. The inset shows the chemical structure of regioregular P3HT. (b) PLE map of the purified [P3HT-NT] nanohybrids diluted in chloroform solution. Species were labelled using the Weisman and Bachilo empirical model [44], with a global red-shift of 45 meV. (c) An excitation spectrum representing emission from the (7,5) species (red squares), corresponding to the vertical dashed line in (b), along with the absorption spectrum of the [P3HT-NT] solution (black line). The polymer transitions [187] and the direct E_{22} resonance are also labelled. (d) The type-II heterojunction between P3HT and a (6,5) nanotube. The energy transfer process is shown here but competes with charge transfer (Chapter 5). Energy levels were taken from Ref. [156].

4.5.3 Type-II Heterojunction Effects

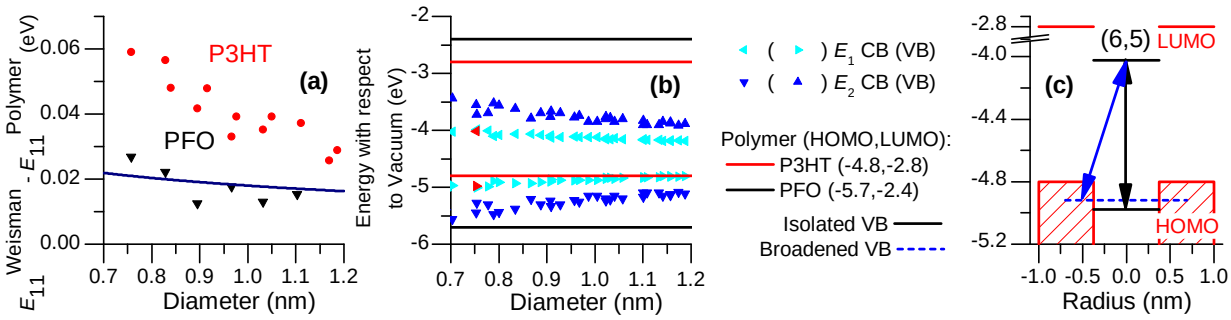

Figure 4.6: (a) E_{11} red-shifts obtained from PLE maps of P3HT- and PFO-wrapped nanotubes plotted as a function of nanotube diameter. The blue solid line shows the Coulomb screening $\Delta E \propto d^{-0.55}$ found empirically [189]. (b) HOMO and LUMO energy levels of the polymers and VB and CB of the nanotubes. Nanotube levels were calculated using the method described at the end of section 4.4.2. The (6,5) tube levels are highlighted in red. (c) Energy levels of an isolated (6,5) nanotube compared to a (6,5) tube coated in a monolayer of P3HT where the hole is delocalised onto the polymer. Figures adapted from Ref. [156].

The large nanotube E_{11} and E_{22} PLE red-shifts were first reported and discussed by Schuettfort *et al.* [156]. The E_{11} red-shifts found in that work are plotted in Fig. 4.6 (a) for tubes of various diameters coated in P3HT and PFO polymers, where the shifts are given relative to values obtained by Weisman and Bachilo for SDS-dispersed tubes [44]. The PFO-wrapped tubes show only a weak diameter dependence that follows the trend observed for Coulomb interactions ($\Delta E \propto d^{-0.55}$), consistent with the dielectric screening imparted on the tubes by the polymer [189]. By contrast, the tubes dispersed with P3HT show red-shifts of much larger magnitude, with a strong diameter dependence. This is explained by considering the energy alignment of the polymers with the nanotubes, which are shown in Fig. 4.6 (b). A type-I heterojunction forms between PFO and all nanotubes, and the only effect on the tube transitions is from the screening of Coulomb interactions by the wrapping polymer. However, a type-II heterojunction forms between P3HT and small-diameter nanotubes, such as (6,5) tubes. Due to the type-II alignment, the wavefunction of the hole in a nanotube exciton may be extended onto the P3HT polymer leading to a reduction of the Coulomb interactions, particularly the dominant electron-electron interactions, and hence giving a red-shift in the optical transitions. This is illustrated in Fig. 4.6 (c) and the

wavefunction extension effect is enhanced for smaller-diameter tubes where the type-II interface is more pronounced. Therefore, the large red-shifts with strong diameter dependence provide direct evidence for a type-II heterojunction between small-diameter semiconducting SWNTs and P3HT. This is in agreement with recent theoretical work, which predicts these type-II alignments [155].

4.6 [F8BT-NT] Nanohybrids

4.6.1 Synthesis

The same nanotube dispersing procedure as described in section 4.5.1 was carried out using a co-polymer containing one PFO (F8) and one benzothiadiazole (BT) unit called poly(9,9'-dioctylfluorene-*co*-benzothiadiazole) (F8BT). The chemical structure of F8BT is shown in Fig. 4.7 (a) and the polymer was purchased from American Dye Source (ADS; MW 96,000 $\mathrm{g\,mol^{-1}}$). The procedure and polymer removal process were identical to that for P3HT but using starting CoMoCAT and F8BT concentrations of 0.5 mg/mL (5 mg of each in 10 mL chlorobenzene). Again, negligible yields were obtained using toluene, THF or *o*-xylene as the starting solvent. Typical final solutions of the [F8BT-NT] nanohybrids contained 0.4 mg/mL of F8BT polymer and AFM images showed similar monolayer coatings (data not shown).

4.6.2 Characterisation

The absorption spectrum of the [F8BT-NT] nanohybrid sample in chloroform solution is shown in Fig. 4.7 (a). The bound F8BT polymer is seen in the region 350–520 nm by comparison with the pure F8BT solution and film spectra. As previously, the bound F8BT polymer spectrum resembles the pure polymer film spectrum more closely than the pure solution spectrum because the bound chains are planarised on the nanotubes, leading to a longer effective conjugation length (red-shift) [208]. It is noted that the F8BT red-shift

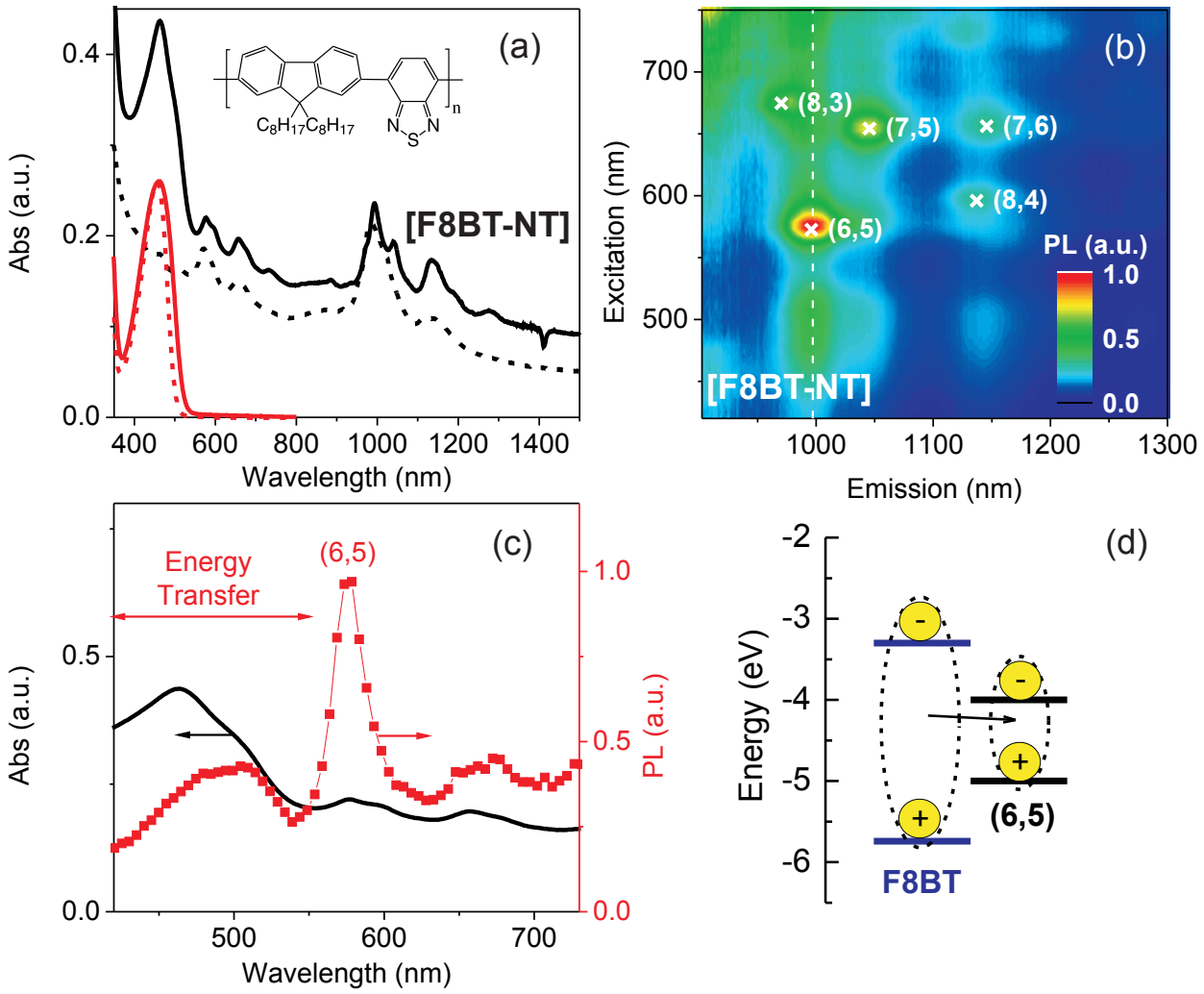

Figure 4.7: (a) Absorption spectra of the [F8BT-NT] nanohybrids (black line) diluted 1/20 and pure F8BT (red dashed line, 5.5×10^{-3} mg/mL) in chloroform solution, along with an F8BT film sample (red solid line), scaled to match the solution spectrum, and [SDBS-NT] in D_2O (black dashed line). The inset shows the chemical structure of F8BT. (b) PLE map of the [F8BT-NT] nanohybrids diluted in chloroform. Species were labelled using the Weisman and Bachilo empirical model [44] with a global red-shift of 25 meV. (c) Excitation spectrum corresponding to (6,5) emission (red squares), as extracted from the dotted white line in (b), along with the absorption spectrum of the [F8BT-NT] nanohybrids (black line). (d) The type-I heterojunction alignment between F8BT and (6,5) nanotubes leads to energy transfer being the dominant transfer process. Energy levels were taken from Refs [156] and [133].

from solution to either film formation or chains bound on nanotubes is very small (∼5 meV). This is because the spectral changes in F8BT are primarily due to intra-chain effects and depend on the torsion angles between the F8 and BT units, reaching a maximum red-shift of ∼300 meV, for complete flattening of the chain, relative to torsionally-free configurations [209]. Therefore, the planarisation of the F8 and BT units is not complete after film formation and, hence, nor is it upon binding to nanotubes.

The nanotube E_{22} and E_{11} transitions are seen in the regions 520–800 nm and 900–1300 nm, respectively. A comparison with the [SDBS-NT] sample shows that the F8BT sample exhibits a small degree of selectivity against the (6,5) tube relative to the other species. F8BT has also demonstrated strong selectivity in solvents such as toluene [176], particularly for large-diameter tubes [210].

As with other nanotube–polymer blends, red-shifted nanotube transitions are seen in both the absorption spectrum and PLE map, which is shown in Fig. 4.7 (b). The tubes were labelled using the Weisman and Bachilo empirical model [44] with a global red-shift of 25 meV, attributed solely to the environmental screening effect of the polymer because only a type-I heterojunction forms between F8BT and the tubes (Fig. 4.7 (d)). The PLE map also shows strong emission from the nanotubes when the samples were photoexcited in the region 420–550 nm. A vertical excitation slice corresponding to emission from the (6,5) tubes (∼997 nm) is shown in Fig. 4.7 (c) and compared to the sample absorption spectrum. Emission is seen corresponding to direct excitation in the E_{22} transition (∼580 nm). However, emission is also observed corresponding to absorption by the F8BT component (<550 nm). This again corresponds to a polymer to nanotube energy transfer process and has been reported elsewhere [177]. The type-I heterojunction suggests that energy transfer dominates over charge transfer processes.

4.7 Summary

Fundamental carbon nanotube studies and applications require well dispersed, individual tubes. Aqueous surfactants such as SDBS disperse all nanotube species and provide good controls to determine chirality distributions in a given sample using spectroscopic techniques. Conjugated polymers disperse nanotubes and can helically 'wrap' around tubes due to strong π-π interactions, forming a monolayer polymer coating.

In this chapter, the methods to disperse individual nanotubes using simple solution processing techniques, namely sonication and centrifugation, were described. Nanohybrids containing SWNTs dispersed by SDBS and the polymers PFO, P3HT and F8BT were synthesised and the excess, unbound polymer removed. This is the first time the polymer removal has been achieved for [PFO-NT] nanohybrids using simple solution processing. Spectroscopic measurements showed red-shifts ($\sim$20-30 meV) in the nanotube transitions due to the dielectric screening of the Coulomb interactions by the surrounding polymers. The red-shifts in small-diameter P3HT-coated tubes ($\sim$40–60 meV) were even larger again than with the other polymers, with the additional shifts attributed to the type-II heterojunction between the materials. PFO showed strong selectivity for semiconducting (7,5) nanotubes, with removal of all metallic nanotubes. All polymers showed signatures of polymer to tube energy transfer processes. The samples [SDBS-NT], [PFO-NT], [P3HT-NT] and [F8BT-NT] were used as starting materials for the experiments presented in Chapters 5–8.

Chapter 5

Ultrafast Charge Separation at a Polymer–Single-Walled Carbon Nanotube Molecular Junction

The work in this chapter has been reproduced in part with permission from:
S. D. Stranks, C. Weisspfennig, P. Parkinson, M. B. Johnston, L. M. Herz and R. J. Nicholas. Ultrafast charge separation at a polymer–single-walled carbon nanotube molecular junction. *Nano Letters*, **11**:66–72, 2011. [206] Copyright 2011 American Chemical Society.

5.1 Introduction and Background

As explained in Chapter 2, the majority of OPV devices utilise exciton dissociation at the interface between two materials which exhibit a type-II heterojunction alignment [128], resulting in interfacial charge separation and free polarons in the materials. However, it has been shown that for many OPV materials, such as polymer-polymer blends, exciton dissociation leads to the formation of an interfacial bound charge-transfer complex, termed an exciplex [121, 126, 211, 212, 213]. This species can be strongly bound and long-lived, significantly lowering charge separation efficiencies.

SWNTs are promising candidates for use in OPV devices because of their large aspect ratios, high carrier mobilities and their controllable solubilisation in polymer solution [12, 176, 177]. Despite these favourable properties, devices based on SWNT blends with conjugated polymers have shown poor performance to date [5, 148, 153, 154], as highlighted in Chapter 2.

In order to understand the poor device performance for P3HT-SWNT blends, Kanai and Grossman [155] carried out theoretical density functional theory (DFT) calculations on interfaces formed between P3HT and small-diameter metallic and semiconducting SWNTs. For the case of metallic tubes, they showed that significant charge transfer from P3HT to the tubes occurs in the ground state. This renders photoexcited electron transfer to the tubes unfavourable because the P3HT becomes attractive for the negative charges at the interface. Furthermore, no type-II heterojunction was observed such that the alignment would not lead to interfacial charge separation. By contrast, their results showed that a clear type-II interaction is formed between P3HT and small-diameter semiconducting tubes. The interaction in the ground state was found to be minor and the resulting heterojunction is as would be predicted from the individual non-interacting properties of the two materials. This theoretical work was experimentally verified by Schuettfort *et al.* [156] using the PLE red-shifts discussed in Chapter 4. Therefore, the poor device results may be explained by these theoretical and experimental studies demonstrating that a type-II heterojunction only exists for certain interfaces, such as between small-diameter semiconducting SWNTs and regioregular P3HT. Even for such blends, energy transfer from the polymer to the SWNTs may compete effectively against charge transfer.

In the work presented in this chapter, the ability for charge transfer and subsequent charge separation to occur within these materials was directly investigated. The results showed that charge transfer across the interface between individually dispersed SWNTs wrapped in a monolayer sheath of P3HT occurs on an ultrafast (430 fs) time scale. Generated charge pairs relax into a bound interfacial charge-transfer state or via non-radiative recombination of excitons within the nanotubes and no long-lived free polarons are observed. However, in

the presence of an excess P3HT network, charge separation at room temperature is long-lived and comparable to that in a conventional P3HT-fullerene blend. This is the first time such blends have been studied using femtosecond time resolution, and the observed charge transfer time is three orders of magnitude faster than reported previously [201, 214]. In addition, significant long-term charge separation was observed for the first time in SWNT-polymer blends. The results lead to the conclusion that charge separation is only possible if small-diameter semiconducting tubes are individually embedded in an excess P3HT matrix. The findings explain the poor polymer-SWNT device behaviour to date and provide a promising route to incorporation of SWNT-polymer blends into OPV devices.

5.2 Sample Preparation

The highly purified [P3HT-NT] nanohybrid solutions described in Chapter 4 were used in this work. The nanohybrids consisted of SWNTs coated with monolayer coatings of P3HT and a small number of isolated P3HT nanocrystals of typical dimensions of 3–5 nm were also observed attached to the P3HT sheath enveloping the tubes. These morphologies will be referred to as *P3HT sheath* and *P3HT nanocrystals*, respectively.

Five thin-film samples were prepared and studied: (1) a bulk P3HT control, (2) [P3HT-NT] nanohybrids, and (3) [P3HT-NT](1%) consisting of an overall concentration of 1% SWNTs wrapped in a P3HT sheath surrounded by excess P3HT, or *network P3HT*. Finally, sample (4), a conventional 60:40 blend of P3HT:PCBM, and sample (5), a film of SWNTs embedded in an inert gelatin matrix, were prepared to allow comparative studies.

Thin, uniform films were prepared by spin-coating concentrated chloroform solutions of the [P3HT-NT] composite onto plasma-etched quartz substrates with a spin speed of 100 rpm for 120 seconds. [P3HT-NT] composite solutions containing 15 mg/mL excess P3HT ([P3HT-NT](1%)) as well as P3HT-only solutions (15 mg/mL) were prepared and treated in the ultrasonic disintegrator for 15 mins and then used to spin-coat onto plasma-etched quartz substrates (1000 rpm, 60 seconds). A PCBM (American Dye Source)-P3HT com-

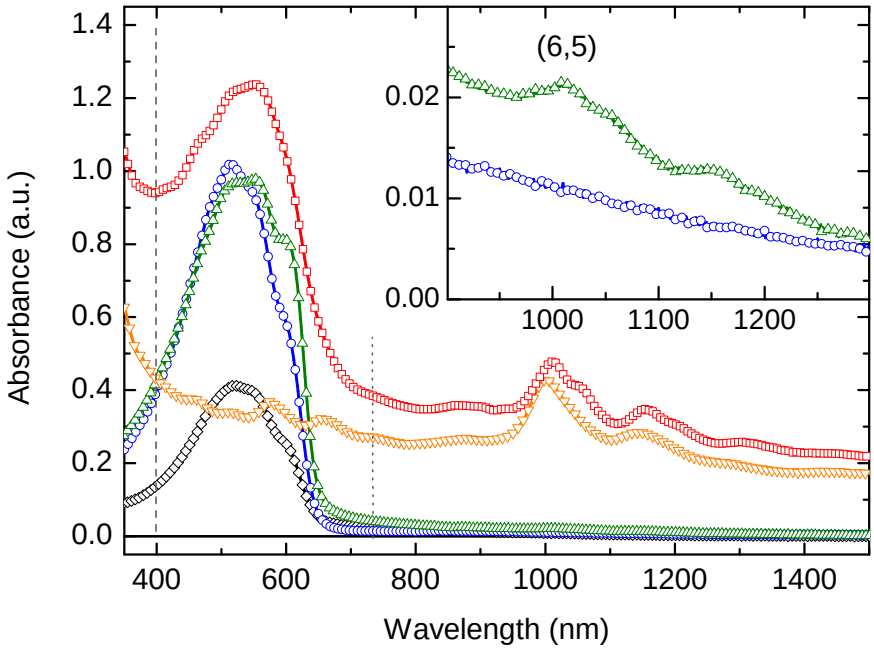

Figure 5.1: Absorption spectra for P3HT (blue circles), [P3HT-NT] (red squares), [P3HT-NT](1%) (green triangles) and P3HT:PCBM (black diamonds) samples as spun-cast on quartz, along with that for the gelatin-NT sample (orange inverted triangles). The grey dashed vertical line shows the excitation wavelength used for time-resolved measurements (400 nm), while the grey dotted vertical line shows the probe wavelength for transient absorption measurements (730 nm). *Inset:* Region clearly showing the E_{11} nanotube peaks in the [P3HT-NT](1%) sample, with the (6,5) species labelled.

posite was also prepared by spin coating at 1000 rpm a 1:0.7 P3HT-PCBM solution with a P3HT concentration of 10 mg/mL. Films were annealed at 120°C for 15 minutes. To prevent degradation, all film preparation and storage was conducted in a nitrogen glovebox with an oxygen concentration of <1.5 ppm.

Finally, [SDBS-NT] nanohybrids in D_2O solutions were prepared as detailed in Chapter 4. Films were made using gelatin as a matrix by dissolving 0.06 g of gelatin per millilitre of [SDBS-NT] in D_2O solution. The mixture was deposited on a substrate, desiccated in air and then lifted off to provide free-standing NT-gelatin films.

5.3 Nanotube Characterisation

Absorption measurements of the films are presented in Fig. 5.1. For the P3HT-containing samples the spectral region between 350–650 nm is dominated by P3HT absorption. As expected, the nanotube E_{11} transitions in the region 950–1350 nm do not appear in the bulk P3HT control and the nanotube E_{22} transitions are clearly seen in the NT-gelatin control (400–800 nm). A PLE map for the [P3HT-NT] film sample is also presented in Fig. 5.2. The P3HT film absorption spectrum is overlaid to emphasise that the results are consistent with those obtained previously in solution [187]; namely, the emission from the nanotubes correlates strongly with absorption in the polymer. Together, these measurements demonstrate that (6,5) semiconducting nanotubes are the dominant species in the films. In addition, the manufacturers (SWeNT) specify that less than 10% of the nanotubes are metallic.

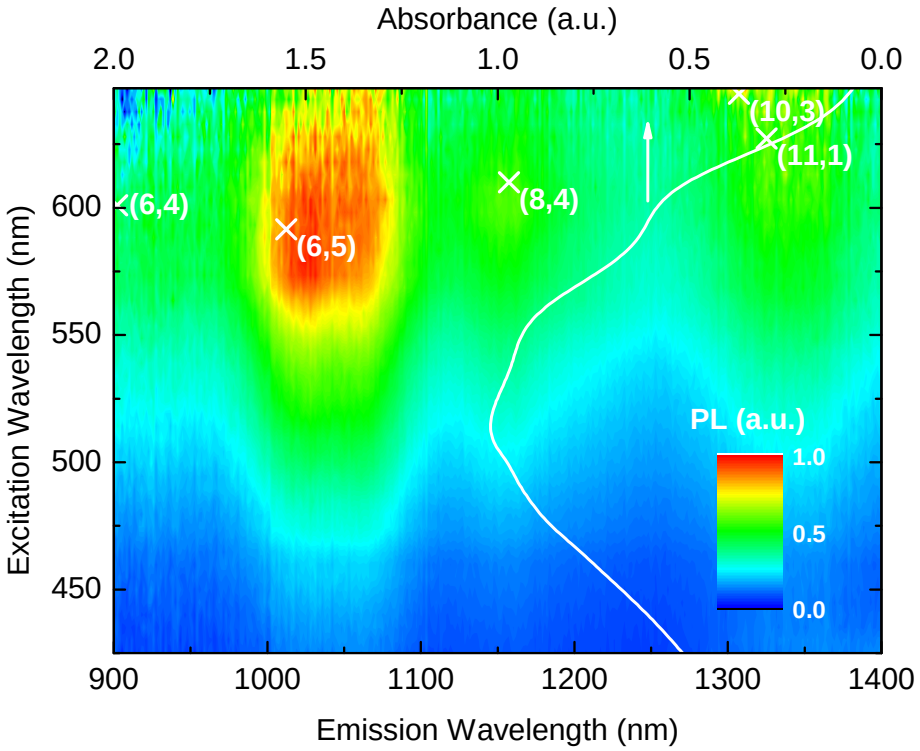

Figure 5.2: PLE map for the [P3HT-NT] sample film on a quartz substrate. The resonant nanotube transition values were estimated by red-shifting the Weisman and Bachilo [44] empirical values by 50 meV. The white solid line shows the P3HT film absorption spectrum.

5.4 Steady-State Polymer Emission

Fig. 5.3 shows the steady-state photoluminescence (PL) spectra for the P3HT-containing samples. The infrared regions of the spectra were recorded using an InGaAs photodiode array detector with an appropriate grating to allow maximum overlap of the P3HT (visible) and nanotube (IR) emissions. The excitation source was a 10-mW laser diode with peak wavelength at 405 nm. The visible regions were acquired using a Si CCD detector with excitation from the output of a pumped Ti:Sapphire laser consisting of 100 fs laser pulses at a repetition rate of 80 MHz and frequency-doubled to 400 nm. The spectra measured using the Si CCD and InGaAs detectors were scaled linearly to overlap over a 30-nm region and displayed using the InGaAs data above 745 nm wavelength and the CCD data below this cutoff.

Significant NT emission (950–1100 nm) was only observed from the [P3HT-NT] sample and exhibits a large red-shift relative to the empirical values deduced by Weisman and Bachilo [44], as is also seen in the PLE map. This red-shift is a direct result of the surrounding dielectric material and the type-II heterojunction alignment of the materials, as described in Chapter 4 [155, 156]. The observed NT emission results from the transfer of excitations from P3HT to the NTs, as 400-nm photons are predominantly absorbed by the P3HT and none of the van Hove singularities of the nanotubes present fall into this region.

All three P3HT-containing samples show emission associated with P3HT (Fig. 5.3, 600–900 nm), but with very different intensities and spectral shapes. The pure P3HT control sample shows a PL spectrum typical for aggregated P3HT, whose lamellar structure permits efficient electronic coupling between parallel chains leading to a red-shift in the emission and the suppression of the lowest (0-0) peak in the Franck-Condon series associated with the C-C stretch vibration [104, 106, 215, 216, 217, 218], as described in Chapter 2. By contrast, the P3HT emission from the [P3HT-NT] sample shows a clear 0-0 emission peak and a blue shift with respect to the bulk P3HT emission. This suggests that for the [P3HT-NT] sample, emission originates from the P3HT sheath, which comprises a polymer monolayer whose π-π interactions are with the NT only, and therefore is not subject to emission quenching arising

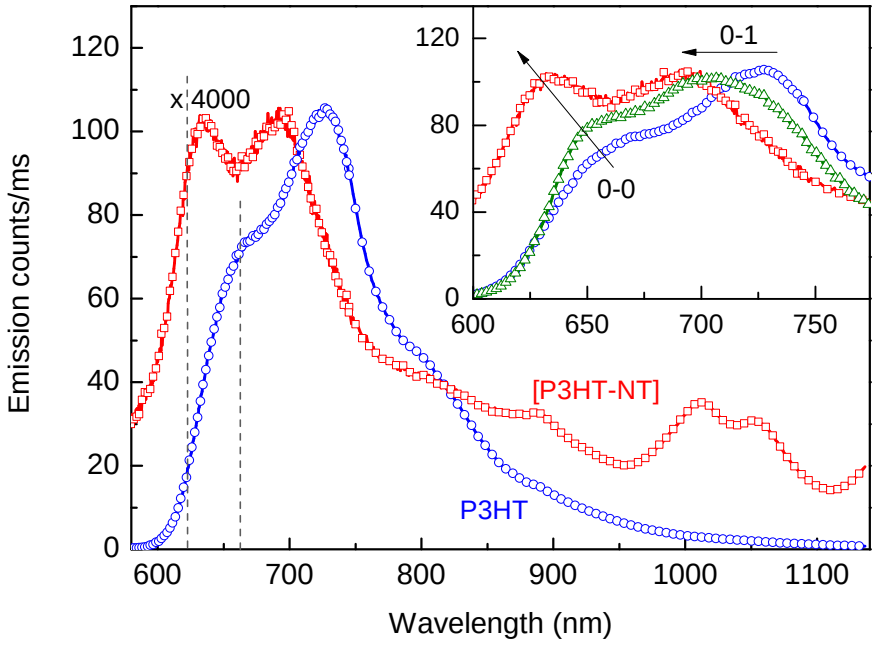

Figure 5.3: Steady-state PL spectra for P3HT (blue circles) and [P3HT-NT] (red squares, × 4000) samples. Data were taken with an InGaAs detector above 745 nm and a Si CCD below, and scaled to match and allow comparison. The grey dashed lines indicate the detection wavelength used for the TCSPC and up-conversion measurements for each sample, namely the 0-0 P3HT transition wavelength in the bulk P3HT (660 nm) and [P3HT-NT] (620 nm) samples. *Inset*: Magnified view of the P3HT emission from the samples, including that from the [P3HT-NT](1%) sample (green triangles, ×40).

from such symmetry constraints. Additional P3HT nanocrystalline aggregates present in the [P3HT-NT] samples do not appear to contribute to the emission, probably because the PL quantum efficiency for the chain-like P3HT sheath is 10% as opposed to <1% for aggregates [219, 220, 221] and their small size and proximity to the NT will also cause some PL quenching. For the [P3HT-NT](1%) sample the P3HT emission has a shape between that of the [P3HT-NT] and the bulk P3HT samples, but resembling more closely the latter, suggesting a dominant contribution from aggregated network P3HT.

Fig. 5.3 also shows that, in the presence of nanotubes, significant quenching of the sheath P3HT emission is observed. The intensity differences of the emission are striking – the spectrum from bulk P3HT is of the order of 4000 times more intense than from [P3HT-NT] and 40 times more intense than for the [P3HT-NT](1%). These observations suggest that the intimate contact between sheath P3HT and the nanotubes leads to highly efficient quenching of the excitations placed on the P3HT.

5.5 Time-Resolved Polymer Emission

In order to determine the speed and mechanism for the quenching of photoexcitations on the P3HT, both time-resolved PL and transient absorption (TA) measurements were conducted with sub-picosecond time resolution. As detailed below, the PL measurements allowed determination of the dynamics of photoexcitation quenching on P3HT while TA experiments (section 5.6) yielded information about the time-scales and extent of the free charge generation.

Time-resolved photoluminescence of the P3HT component in the samples was measured using the two techniques described in Chapter 3: TCSPC with time resolution of ∼120 ps and PLUC with resolution of 220 fs. Measurements were taken at the peaks corresponding to the steady-state P3HT 0-0 transition in each sample, *i.e.* 620 nm for the [P3HT-NT] sample and 660 nm for the pure P3HT and [P3HT-NT](1%) samples.

Fig. 5.4 shows the time-resolved PL decay measured for bulk P3HT and [P3HT-NT] samples using the high-resolution PLUC technique[1]. Low-resolution TCSPC data (inset) for the bulk P3HT and [P3HT-NT](1%) samples display a faster PL decay for the latter, with mono-exponential fits yielding lifetimes of 689 ps and 508 ps, respectively. However, the TCSPC technique was unable to time-resolve the PL from the [P3HT-NT] sample sufficiently since the measured decay (τ ∼117 ps) is identical to the instrument response. The PLUC data, on the other hand, reveal ultrafast PL decay components for the three samples. In order to extract time constants for these ultrafast components, the PL decay for the [P3HT-NT] sample was fitted with a single exponential, and that for the P3HT sample with the sum of two exponentials, with one of the two time-constants set to that of the observed long-term decay (689 ps). These functions were convoluted with a Gaussian system response function of width 220 fs, with best fits obtained shown in Fig. 5.4 as solid lines.

For bulk P3HT a fast initial component with time constant of 1.7 ps was extracted, which is likely to be caused by initial excitation relaxation processes mediated *e.g.* by vibrational

[1]The [P3HT-NT](1%) PLUC data exhibit a very similar behaviour to the bulk P3HT sample over the displayed time window and hence are not shown.

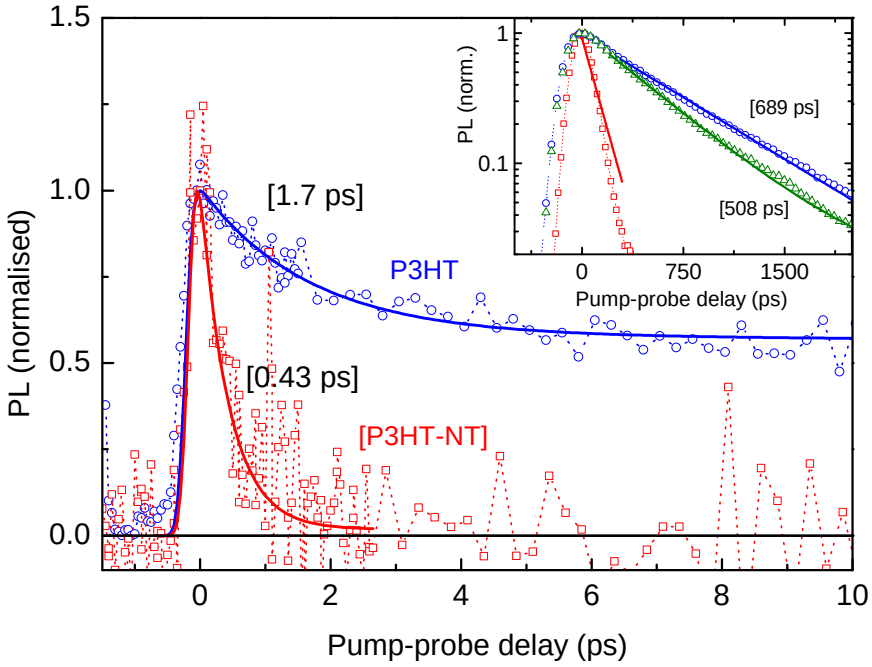

Figure 5.4: Normalised PLUC results for the samples following 400-nm sample excitation. The emission from the P3HT sample (blue circles) was detected at 660 nm and that for the [P3HT-NT] (red squares) was detected at 620 nm, where detection wavelengths correspond to the P3HT 0-0 transition in each sample. Similar dynamics were also observed for the bulk sample when excited at 620 nm. Appropriate fits gave fast time constants of 0.43 and 1.7 ps for [P3HT-NT] and P3HT samples, respectively, including a slow component for the P3HT sample only. *Inset:* TCSPC decay curves at the same probe wavelengths used for PLUC following excitation at 400 nm. The [P3HT-NT](1%) (green triangles) sample was also detected at 660 nm.

or torsional cooling and migration through a density of states associated with energetic disorder [106, 222, 223, 224]. Following such relaxation, the emission from bulk P3HT is generally long-lived, as would be expected. By contrast, the sheath emission in the [P3HT-NT] sample decays almost completely to zero with an ultrafast time constant of 0.43 ps. This extremely rapid decay of the P3HT emission from [P3HT-NT] films is consistent with the factor 4000 quenching of its time-integrated emission relative to that of the bulk P3HT (Fig. 5.3), as discussed previously.

These observations can be compared with previous results by Geng *et al.* [214] and Chen *et al.* [201] who studied P3HT and PFO wrapped SWNTs, respectively, using TCSPC to conclude that energy transfer occurs on a timescale of order 400–500 ps. However, these studies were based on films that had a large amount of excess free polymer dominating the

emission. The TCSPC data for the film containing excess P3HT, [P3HT-NT](1%), shows a decay of the residual P3HT emission of 508 ps that is only slightly faster than the bulk P3HT (689 ps), probably due to regions of excess polymer far from an interface with a NT, in agreement with these previous studies. However, as demonstrated here, the low resolution of TCSPC masks the fast exciton quenching processes occurring directly at the polymer-NT heterointerface. Therefore, only the use of the PLUC technique has allowed the observation of the true polymer exciton quenching in the presence of NTs, which is three orders of magnitude faster than suggested by previous studies.

5.6 Transient Absorption Studies

In order to determine whether the P3HT emission quenching in the blend samples is caused by charge separation at the interface, ultrafast transient absorption measurements were conducted by Christian Weisspfennig (Physics Department, University of Oxford). The presence of free charges was monitored as a function of time after excitation by measuring the pump-induced changes in transmission of a probe at a wavelength of 730 nm, the peak of the absorption for the P3HT delocalised polaron [108]. The exciting pump pulse was at a photon wavelength of 400 nm and had a fluence of 50 μJ/cm^2 at the focus.

Fig. 5.5 displays the transient absorption ($-\Delta$T/T) data obtained for the four P3HT-containing samples. P3HT:PCBM blends are known for their significant photon-to-charge conversion ratios [225] and the expected well known trend for the P3HT:PCBM (60:40) control sample is observed, with a long-lived absorption arising from charge separated polaron pairs [226, 227]. The transient response from the P3HT bulk sample is also consistent with previously reported observations showing an initial decreased absorption that has been attributed to stimulated emission from excitons originating from some regions of regiorandom P3HT [219, 226, 227]. Exciton-exciton annihilation processes, which are significant with the fluences used here [228], cause a fast decay of the absorption signal, which may also contain a very small transient component arising from charge absorption originating from internal

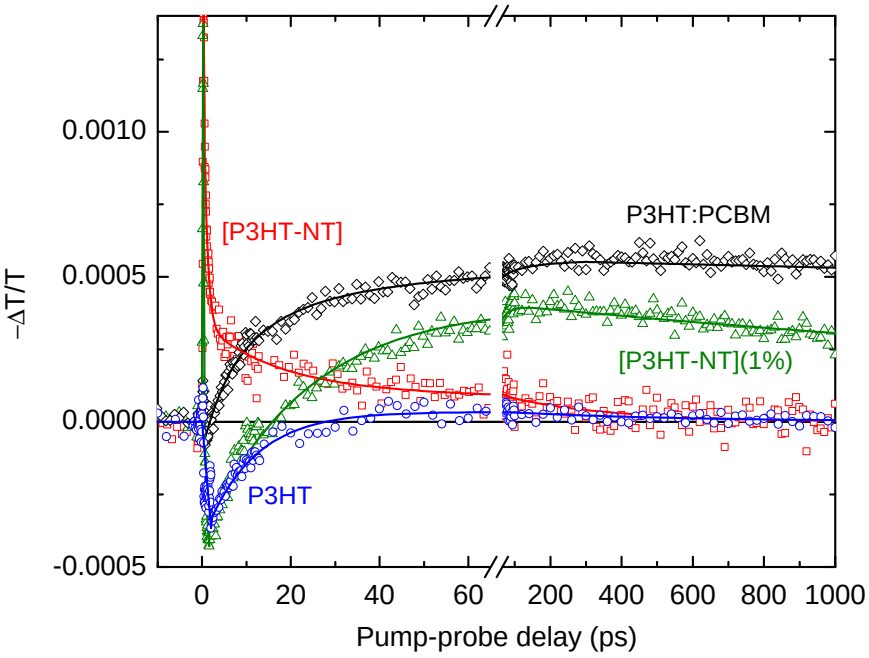

Figure 5.5: Relative transmission changes for varying pump-probe delays for the P3HT:PCBM (black diamonds), P3HT (blue circles), [P3HT-NT] (red squares) and [P3HT-NT](1%) (green triangles) samples when excited at 400 nm and probed at 730 nm. Solid lines are a guide to the eye.

hot exciton dissociation intrinsic to the polymer [229, 230, 231]. As expected, no long-term charge-separated state exists for the bulk P3HT sample.

The [P3HT-NT] signal shows no negative stimulated emission signal but rather an increased absorption which, in contrast to P3HT:PCBM, decays relatively quickly to zero. The absence of the stimulated emission signal is expected given that PLUC data show the quenching of sheath P3HT excitons on an ultrafast time scale of 400 fs. In addition, the P3HT nanocrystals attached to some of the NTs are highly regioregular with no regiorandom domains, and thus very low stimulated emission rates should be expected [219, 226, 227]. The strong absorption signal has an ultrafast (∼350 fs) rise and a decay that occurs on several time scales. These data suggest that fast quenching of the P3HT emission in [P3HT-NT] films is accompanied by a rise in the presence of free charges on the P3HT. However, these free charges are clearly not long-lived, with the majority of the charge absorption disappearing within 10 ps after excitation and most of the rest decaying within another ∼100 ps. The free holes must therefore be rapidly transferred to states with low quantum efficiency, to

account for the strong (4000×) PL quenching. These could either be the nanotube excitons, which are known to have strong Auger recombination at high excitation intensities occurring on a timescale of 1-5 ps [71, 72, 77, 78], or bound charge-transfer complexes formed across the interface, similar to exciplexes, which are known to have low radiative efficiencies [121, 211, 213]. Fig. 5.3 shows that, although weak in absolute terms, the nanotube PL becomes relatively more significant due to its shorter exciton lifetimes (∼100 ps [70, 71, 72]) whereas no exciplex emission, which should occur in a similar wavelength region, is obviously visible. The NT emission is expected to dominate since exciplex lifetimes are known to be of order nanoseconds and above [121, 211, 213]. Nevertheless, such exciplex-like states have been shown to play a significant role in a variety of polymer-containing blends with type-II heterointerfaces [121, 126, 211, 212, 213] and are thus likely to be also of importance here.

However, the [P3HT-NT](1%) sample containing excess P3HT shows significantly different behaviour. During the first 10 ps the data reveal enhanced transmission arising from stimulated emission, caused by the majority of carriers which are excited in the network P3HT (including some regiorandom) regions. The subsequent dynamics are similar to those for the P3HT:PCBM sample: a rapid growth in the free polaron absorption indicates an effective charge separation process with a rise time of 20–30 ps reflecting the migration time of excitons to the heterointerface. The peak value of the charge absorption signal is also similar to that observed for the P3HT:PCBM sample. Accounting for differences in sample absorption at the excitation wavelength, the peak charge generation efficiency in the [P3HT-NT](1%) sample was estimated to be 40% of that found for the standard P3HT:PCBM blend with an optimised mass ratio [226]. The fact that the quenched PL data show a dominant contribution from aggregated network P3HT indicates that there are occasional large regions of purely bulk P3HT in the [P3HT-NT](1%) sample. The small fraction of P3HT excitons formed in these domains are unable to reach a P3HT:NT interface before recombining and hence do not contribute to free charge generation. Therefore, further optimisation of both the film morphology and the P3HT:NT blend ratio may result in an even higher charge-generation being obtained. Removal of any remaining metallic nanotubes (<10 %), which are liable to lead to energy transfer, would also improve the charge generation. The

free-charge absorption for the [P3HT-NT](1%) sample also shows a slight decline over the time window (1 ns) investigated. However, an accurate determination of the charge lifetime in these systems will require measurements over μ-second timescales, *e.g.* as those described in Ref. [126]. In recent preliminary work, the time window was extended to 2 ns and the absorption peak reached a plateau, suggesting long-lived charges (data not shown).

5.7 Interpretation

In order to understand the dynamic processes occurring at the polymer:NT heterointerface, the schematic shown in Fig. 5.6 is considered. For an exciton excited within the polymer, charge transfer at an interface will result in the electron being clearly confined to the nanotube. The energy offset controlling the hole behaviour is, however, marginal. As a result, although the hole is most likely to reside on the polymer side of the interface, it probably also has a significant probability for activated transfer to the NT. For the sheath morphology, the hole located on the polymer is geometrically constrained to be in close proximity to the nanotube and the formation of a bound state charge-transfer complex (or 'exciplex') is therefore a likely scenario. However, such a charge-transfer state at the interface will differ from those typically observed for polymer-polymer heterojunctions, where it exists across two strands with similar dimensions in which fairly localised particles have similar effective masses. For the NT:polymer interface, by contrast, the electron on the nanotube is delocalised around the tube and has a mass for motion along the tube of only one-tenth of the free electron mass [232]. There is therefore a large mismatch in both wavefunction spread and particle masses for an exciplex composed of a charge pair across a nanotube-polymer interface. Using a conservative estimate, this will reduce the binding energy of any exciplex by a factor of order 4 [58] compared to polymer-polymer heterojunction analogues [121] where binding energies are typically 100-200 meV. In summary, examination of the band structures leads to the conclusion that at the NT:polymer interface, the generated charge pairs will experience weak Coulomb interactions and comprise an electron wavefunction that is delocalised along the NT and a hole wavefunction that is mainly located on the

polymer but may cross over into the NT. The charge pairs may therefore decay either through recombination of the charges across the interface, or while they are both located on the NT.

The addition of network polymer, as in the [P3HT-NT](1%) sample, will significantly alter this picture by allowing the hole to migrate away from the interface thus eluding such recombination processes. In addition, the expanded dielectric environment of the complex may subtly alter the energetic level alignment at the interface making stable charge separation more favourable and further decreasing the exciplex binding energy. As a result, efficient long-lived charge separation is expected once additional P3HT is added to the individually polymer-wrapped nanotubes.

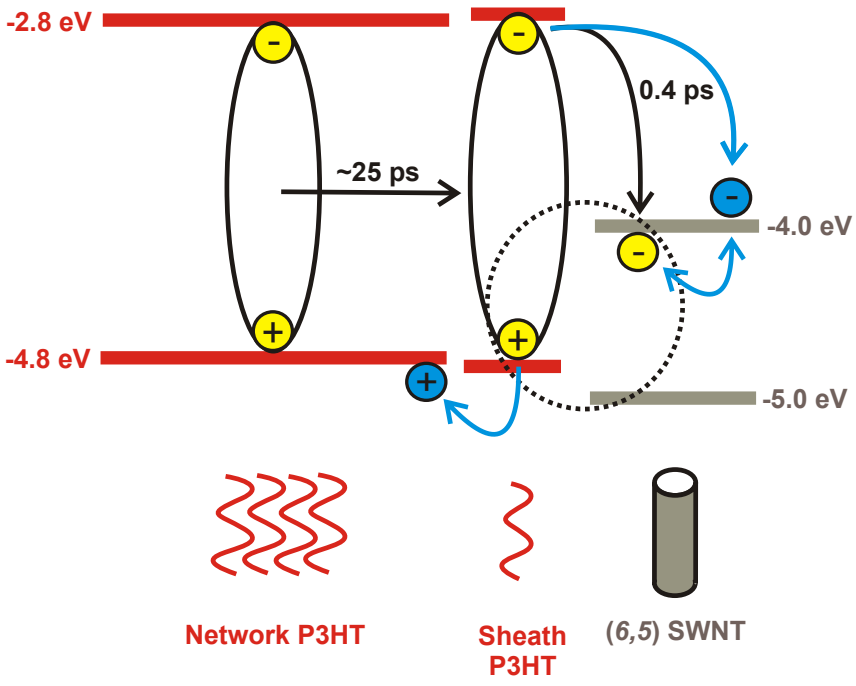

Figure 5.6: Scheme to illustrate the observed charge generation dynamics for a P3HT sheath monolayer around a (6,5) SWNT with an excess of P3HT acting as a surrounding network. A bound exciton is created on the network P3HT and migrates to a sheath-P3HT:NT interface within ∼25 ps. At the interface the exciton dissociates and an electron is transferred to the nanotube while the hole remains on the P3HT. This produces free polarons (blue). In the presence of the network P3HT, the hole can migrate away from the interface (blue) and immediate charge separation is achieved. In the absence of network P3HT, the free polarons form a weakly bound exciplex or recombine non-radiatively as excitons within the nanotubes (both processes represented by dotted line). Vacuum energy level values were taken from Ref. [156] and described in Chapter 4, with a slightly larger bandgap for sheath P3HT than network P3HT in line with observed absorption (Fig. 5.1) and PL (Fig. 5.3) data.

In the [P3HT-NT] sample, the PLUC data show that the exciton, which is created on the sheath P3HT, is quenched on a timescale of 0.4 ps. Transient absorption traces indicate that free polarons are produced within this time and then decay away on a time scale of order 10-100 ps. These observations are attributed to the ultrafast charge dissociation of P3HT excitons at the heterointerface. However, because the nanotubes are wrapped by individual P3HT chains, the positive charge on the P3HT cannot move away from the interface and the generated charge pair will decay through recombination of the charges either across the interface, or while they are both located on the NT.

When the network P3HT is added, the majority of excitons are generated initially in the network P3HT. Transient absorption data show that free charges form in P3HT on a time scale of 20–30 ps (signal rise time), as the excitons move to an interface between a sheath-P3HT layer and a NT. This value is consistent with the quenching of the time-integrated polymer PL intensity by a factor of 40 relative to the bulk P3HT sample. At the interface, rapid dissociation of the exciton into free polarons again occurs but the majority of free holes generated are now long-lived. This is consistent with the picture that holes on the P3HT are now able to migrate away from the P3HT:NT interface thereby eluding capture. Therefore, the excess P3HT network provides a medium allowing extraction of the free holes and effective charge separation, in accordance with the predictions by Schuettfort *et al.* [156] and Kanai and Grossman [155].

It is emphasised that the scheme presented in Fig. 5.6 is only valid for small-diameter nanotubes which establish a defined type-II alignment with P3HT and for the case of well-dispersed nanotubes. For larger diameter tubes, the alignment becomes type-I and, as observed experimentally [187], energy transfer becomes the dominant process. Lioudakis *et al.* [233] also conducted transient absorption studies on polymer-NT films, but examined larger diameter HiPCO nanotubes dispersed by P3HT. Consequently, their data do not show any evidence of charge separation even with the same polymer:SWNT ratio as that used in the work presented here. In other recent work, Ferguson *et al.* [234] used transient microwave conductivity measurements to show that long-lived charge separation is seen for

blends comprised of large-diameter tubes, prepared by laser vaporisation, in a matrix of P3HT. However, the nature of the photoexcited species is not clear and it is not evident that the charge generation yield is comparable to a P3HT:PCBM blend. The study presented in this chapter has shown, therefore, that significantly improved photovoltaic devices need to utilise suspensions of these purified, small-diameter nanohybrids incorporated at small volume fractions in a polymer matrix. Devices to date have yet to satisfy both conditions since all have so far incorporated larger diameter HiPCO, arc-discharge or chemical vapour deposition tubes [5, 153, 154].

Many of the results reported in this work were recently verified by Ren *et al.* [148]. Devices were fabricated using purchased purified semiconducting SWNTs (98% semiconducting purity) with diameters in the range 1.2–1.7 nm and various proportions of excess P3HT. They achieved a maximum device efficiency of 0.72%, the highest conversion efficiency in these blends to date, using a nanotube loading of 3%. They argue that the optimum diameter range is 1.3-1.5 nm because of a compromise between smaller diameter tubes (greater charge generation) and larger diameter tubes which have larger carrier mobilities in the diffusive regime (scale as d^2 [235]) and lower exciton binding energies (scale as $1/d$ [59]). Nevertheless, the charge generation yield is likely to be most crucial in producing efficient SWNT-polymer OPV devices. The use of purely semiconducting small-diameter tubes, produced using the technique described in Chapter 7, will be the subject of immediate future device work.

5.8 Conclusion

In conclusion, the charge photogeneration dynamics at the interface formed between small-diameter semiconducting SWNTs and a monolayer coating of P3HT have been investigated. Despite the poor performance shown by devices to date, such blend materials are promising candidates for use in OPV devices owing to their type-II heterojunction alignment [155, 156], high mobilities and large aspect ratios [12, 112]. This work has demonstrated that photoexcitation of the sheath P3HT leads to an ultrafast electron transfer to the nanotube on a time

scale of 400 fs. This is the first time such blends have been studied using femtosecond time resolution, and the observed charge transfer time is three orders of magnitudes faster than reported previously [201, 214]. Since the remaining hole on the P3HT is confined to this single molecular layer, either a bound charge-transfer complex forms across the interface or non-radiative recombination occurs on the nanotube and no generation of free charge occurs. However, the introduction of an excess of P3HT surrounding the molecular complexes allows transport of the hole away from the interface, leading to long-term charge separation. These results suggest that small-diameter SWNT-P3HT nanohybrids act as efficient charge generation interfaces for use in photovoltaic devices, provided that they are embedded in a matrix with a sufficient excess of P3HT. The nanotube-polymer interfaces can provide comparable or better dissociation interfaces than all-polymer junctions. In addition, nanotubes offer greater electron mobility and longer percolation paths than conjugated polymers, suggesting that polymer-nanotube composites may be more effective active media in OPV devices than polymer-polymer or polymer-fullerene blends. Significantly, this work has demonstrated that the presence of only 1% nanotubes is able to produce a similar efficiency of charge separation to that observed in an optimised 60:40 blend of P3HT:fullerene, in which the fullerene electron acceptor does not contribute to light absorption. These findings thus establish a promising route for developing efficient OPV devices utilising polymer-SWNT blends.

Chapter 6

Nano-Engineering Coaxial Carbon Nanotube–Dual Polymer Heterostructures

The work in this chapter has been reproduced in part with permission from ACS Nano, submitted for publication.

S. D. Stranks, C. Yong, J. A. Alexander-Webber, C. Weisspfennig, M. B. Johnston, L. M. Herz and R. J. Nicholas. Nano-engineering coaxial carbon nanotube–dual polymer heterostructures. Unpublished work copyright 2012 American Chemical Society.

6.1 Introduction and Background

As shown in Chapters 4 and 5, combining nanotubes with semiconducting polymers allows the creation of new nanohybrid structures where a layer of polymer is strongly bound to the nanotubes through π–π interactions. The polymer layer both prevents nanotube bundling and significantly modifies the electronic and mechanical properties of the nanohybrid structures. An extensive range of polymers have been utilised to date, with the polymers chosen to give enhanced diameter selectivity [176, 236], improved mechanical properties for the blend [237, 238] or controlled electronic modifications. A particularly important

example is the formation of a type-II heterojunction energy level alignment between small-diameter SWNTs and P3HT (Chapter 4) [155, 156] or porphyrin oligomers (Chapter 8) [239]. In Chapter 5 it was shown that long-lived charge separation can be achieved when the [P3HT-NT] nanohybrids are embedded in an excess matrix of P3HT [206], demonstrating the potential of this system for improving OPV device performance [148]. In the work described in this chapter, it is shown that the introduction of a second polymer layer allows further control of the electronic properties by molecular engineering the structures to give specific attributes, such as stabilised charge separation. This was done using simple solution processing methods and by making use of competitive binding properties between the polymers and nanotubes.

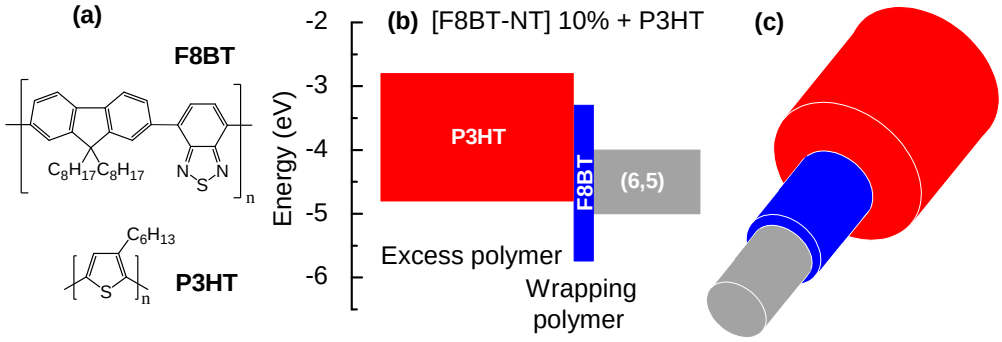

Figure 6.1: (a) Chemical structures of F8BT (upper) and P3HT (lower). (b) Schematic energy level diagram of nanohybrids consisting of nanotubes wrapped in F8BT polymer and embedded in an excess P3HT matrix, such that the F8BT constitutes 10% of the total polymer mass. Energies are given with respect to vacuum and were taken from Refs [156] and [133]. (c) Schematic cartoon to depict the structure described in (b).

Competitive binding processes are ubiquitous in biological systems. For example many drugs act as enzyme inhibitors by dominating a competitive binding process at the active site for the enzyme [240, 241]. Reports of the competitive binding of different species to a nanotube are just beginning to appear. Ju *et al.* have exploited the ready displacement of chirality-selective flavin mononucleotides by a surfactant to give significant nanotube chirality enrichment [242], while Chen *et al.* have observed large differences in the degree of binding of fluorene-based polymers from the same family [201]. Finally, it is shown in Chapter 8 that there is a large oligomer length dependence of the binding of porphyrin oligomers to nanotubes, with binding constants differing by orders of magnitude [243]. However, none

of these studies have yet shown any degree of tunability of the displacement or binding of each species.

Here, it is shown that competitive binding processes can be controlled to nano-engineer dual polymer–SWNT structures consisting of nanohybrids of SWNTs coated first with either P3HT or F8BT and a second coating of the other polymer, as shown schematically in Figure 6.1 (c). Spectroscopic and molecular dynamics studies were used to investigate the binding competition between the two polymers in solution. It is shown that, despite the intrinsically stronger binding of P3HT to nanotubes compared to F8BT, the order of the wrapping can still be selectively manipulated to produce a range of different self-assembled structures in the solid-state. Finally, ultrafast photoluminescence spectroscopy was used to investigate the dynamics of the optical and electronic processes occurring in the nanostructures and to infer information about their compositions.

The ability to design and construct such nanostructures using simple solution processing techniques opens up an entirely new set of potential applications. For instance, a structure with a monolayer of F8BT coating a SWNT embedded in an excess matrix of P3HT (Fig. 6.1 (b) and (c)) could further improve P3HT-SWNT charge separation by cascading electrons onto the nanotube while using the F8BT to block recombination of P3HT holes with nanotube electrons. Alternatively, reversing the polymer ordering could allow the nanotubes to act as hole collectors as well as to control the polymer morphology, a crucial step to improve polymer–polymer blends for OPV devices [132, 134, 135, 244].

6.2 Solution Binding Competition

The binding competition between polymers was investigated by studying the optical properties of nanohybrids prepared first with one polymer and then with the addition of an excess of the second polymer to the solution. The nanohybrids consisting of CoMoCAT SWNTs coated with P3HT[1] or F8BT polymers were synthesised as described in Chapter 4 and de-

[1]For the experiments in this chapter, regioregular P3HT was purchased from Rieke Metals, Inc., with average molecular weight 50,000 $gmol^{-1}$.

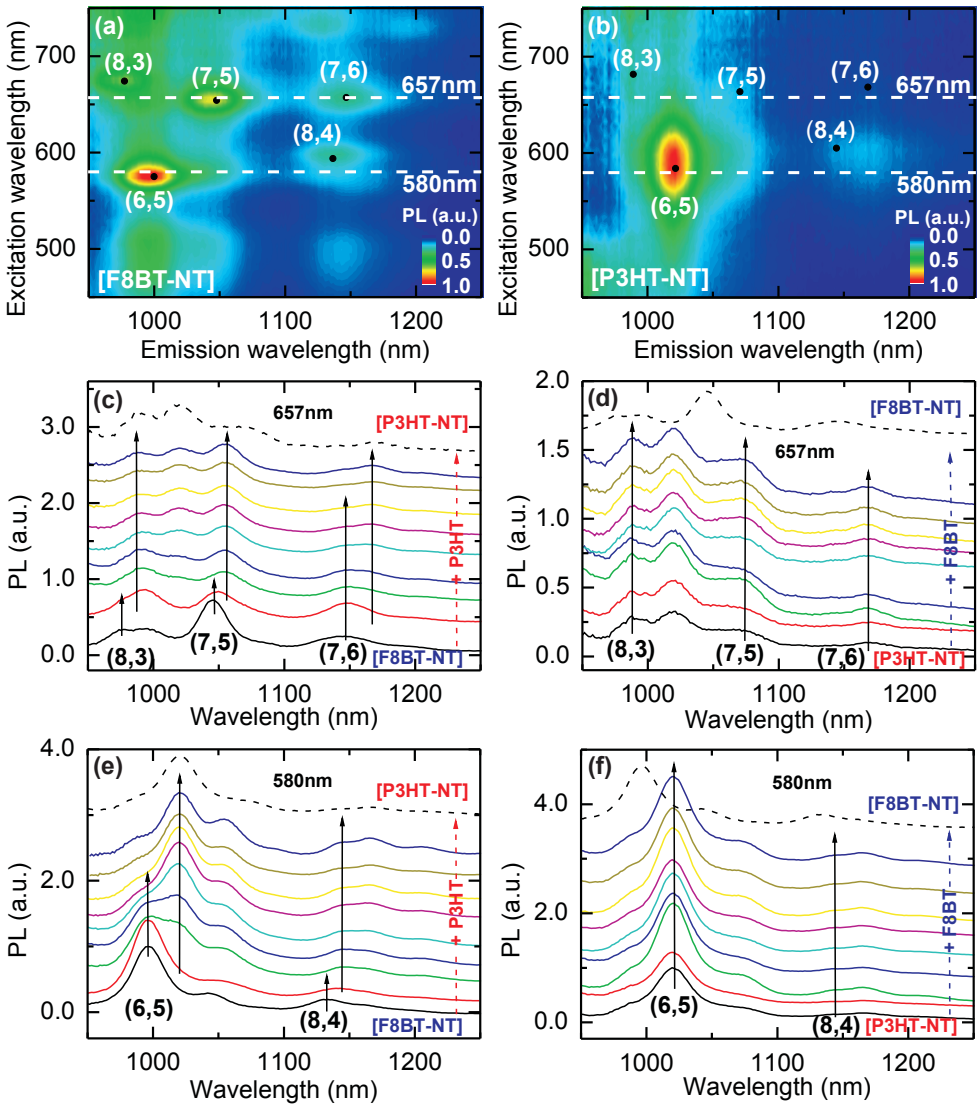

Figure 6.2: PLE maps of (a) [F8BT-NT] and (b) [P3HT-NT] nanohybrids in chloroform solution with resonant nanotube peaks labelled. The concentration of the wrapping polymer in solution was fixed to an absolute value of 0.006 mg/ml. The other spectra in (c) and (e) correspond to the [F8BT-NT] solutions in (a) excited at 657 and 580 nm, respectively, with an increasing amount of excess P3HT. The same spectra are shown in (d) and (f) but for the [P3HT-NT] solutions in (b) with an increasing amount of excess F8BT. Measurements were taken 10 days after addition of excess polymer. The nanohybrid proportions progress through 100, 50, 20, 15, 10, 5, 2, 1 and 0.5% from bottom to top of each and spectra are offset for clarity with any excess polymer emission tail subtracted. For reference, the dotted line spectra in (c),(e) and (d),(f) are the emission from the [P3HT-NT] and [F8BT-NT] nanohybrids, respectively.

noted [P3HT-NT] and [F8BT-NT], respectively. A series of these nanohybrids in chloroform were diluted (1/100) and briefly tip sonicated (30 seconds) to prevent aggregation. In these pure ("100%") nanohybrids, the only polymer present is attached to the tubes. Increasing amounts of excess polymers were added to the solutions to give a range of concentrations denoted, for example, as [F8BT-NT] X % + P3HT, where X is the mass percentage of the initial wrapping polymer (F8BT) in the excess polymer (P3HT), as labelled in Fig. 6.1 (b).

A semiconducting polymer bound to a nanotube screens the electron–electron interactions within the tube, thus reducing the Coulomb interaction energy and giving red-shifts of the optical transition energies relative to a bare nanotube [156]. When the energy levels in the polymer form a type-II heterojunction, as occurs for P3HT with small-diameter nanotubes, the wavefunction of the hole on the nanotube is also extended onto the polymer. This leads to a further red-shift of the transition energies compared to other polymers (such as F8BT) that only establish a type-I heterojunction with the nanotubes. Therefore, the enhanced red-shifts of the E_{11} or E_{22} transitions are used to probe the immediate environment of the nanotubes and determine which polymer is bound.

PLE maps of the [F8BT-NT] and [P3HT-NT] nanohybrid samples taken in chloroform solution are presented in Fig. 6.2 (a) and (b), respectively. The individual nanotube emission resonances of the distribution are observed, along with emission resulting from energy transfer to the nanotube following absorption in either F8BT [177] (450–550 nm) or P3HT [187] (450–650 nm), as discussed in Chapter 4.

PL emission spectra were also taken at excitation wavelengths of 580 nm and 657 nm with multiple accummulations, narrow slit widths and a larger excitation power than the maps to resolve the different nanotube peaks. An emission spectrum for the 100% [F8BT-NT] solution is shown at the bottom of Fig. 6.2 (e) for selective excitation at the E_{22} transitions of the (6,5) and (8,4) tubes at 580 nm, and for 100% [P3HT-NT] in Fig. 6.2 (f). The E_{11} transitions for [F8BT-NT] are at 998 nm and 1133 nm, respectively, and for [P3HT-NT] the additional red-shift moves them to 1021 nm and 1141 nm. When an increasing proportion of P3HT is added to the [F8BT-NT] solution (Fig. 6.2 (e)) the spectra show a progressive exchange

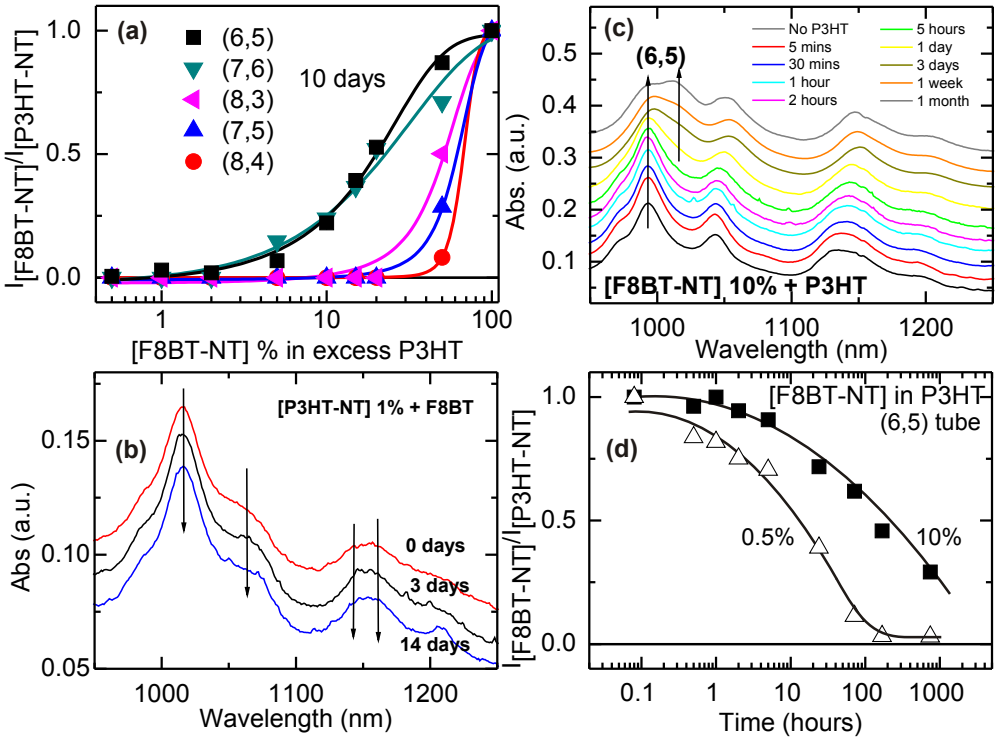

Figure 6.3: (a) Relative proportion of F8BT-nanotube peaks to P3HT-nanotube peaks with increasing excess P3HT added to [F8BT-NT] from right to left, as fitted from spectra in Fig. 6.2 (c) and (e). Solid lines are guides to the eye. (b) Absorption spectra of the [P3HT-NT] 1% + F8BT nanohybrids taken 0, 3 and 14 days after polymer addition, showing that no change is observed over time. All spectra are offset for clarity. (c) [F8BT-NT] 10% + P3HT nanohybrid absorption spectra taken over a 1 month period to demonstrate the dynamic substitution process, with the F8BT on the (6,5) nanotube becoming increasingly substituted by the excess P3HT. (d) The same ratio as in (a) but following the time evolution of the (6,5) tubes over a period of 1 month for 10 % and 0.5 % [F8BT-NT] proportions in excess P3HT. To obtain these data, fits were carried out on absorption spectra in (c) (0.5 % spectra not shown). Solid lines are guides to the eye.

of intensity from the original peak to one which corresponds to tubes coated with P3HT. Similar behaviour is also observed for (7,5) and (7,6) tubes with excitation at 657 nm, as seen in Fig. 6.2 (c), and from absorption spectra. These observations provide direct evidence for a substitution process, where the F8BT chains on the nanotubes are being substituted by the excess P3HT chains.

The proportions of each nanotube environment (F8BT or P3HT) were deduced using multi-peak fits to the intensities of each peak in the spectra in Fig. 6.2 (c) and (e). The peaks were fixed at positions corresponding to the [F8BT-NT] and [P3HT-NT] environments for each nanotube species as ascertained from pure [F8BT-NT] and [P3HT-NT] 100% solutions.

The proportions are plotted in Fig. 6.3 (a) for four nanotube chiralities. The substitution process appears to depend on the type of tube, with a larger excess of P3HT required to displace F8BT from (6,5) and (7,6) tubes than from the other tube species.

The process also has a considerable time dependence, as shown by the absorption spectra taken over a 1 month period in Fig. 6.3 (c) for an [F8BT-NT] 10 % + P3HT sample. To quantify this, the proportions of each nanotube environment were fitted for the (6,5) tubes. The underlying (8,3) and (7,3) peaks were estimated using fits to the spectrum of the [F8BT-NT] 100% sample (containing no P3HT). These peaks were subtracted from the subsequent time-dependent spectra to approximately isolate the (6,5) peaks. The (6,5) peak proportions are plotted in Fig. 6.3 (d) for [F8BT-NT] 10 % and 0.5 % in excess P3HT. The substitution exhibits a fast component occurring within minutes to hours and a slow component ocurring over many days and weeks. The process is faster when the proportion of excess polymer is higher and faster substitution is also expected for larger absolute concentrations, as in the solutions used to cast thin films. By contrast, no substitution is observed for the addition of F8BT to [P3HT-NT] (Fig. 6.2 (d) and (f)) on any timescale (Fig. 6.3 (b)). This indicates that the binding to nanotubes by P3HT is much stronger than by F8BT.

6.3 Isolating Substituted Nanohybrids

The final equilibrium state of the dual polymer structures was studied by isolating the substituted polymer-wrapped nanotubes following immersion in a large excess of the second polymer. Diluted (1/100) chloroform solutions containing [P3HT-NT] and [F8BT-NT] nanohybrids were briefly tip sonicated (30 seconds) and each combination of excess polymer was added to achieve nanohybrid concentrations of 1%. The solutions were left for 3 days after polymer addition and, after this time, the [F8BT-NT] 1% + P3HT sample was observed to be completely substituted using absorption and PL spectra. The purification process described in Chapter 4 was again used to remove excess polymer. Briefly, toluene was added to the solutions (twice the original volume) to induce aggregation and the solutions were

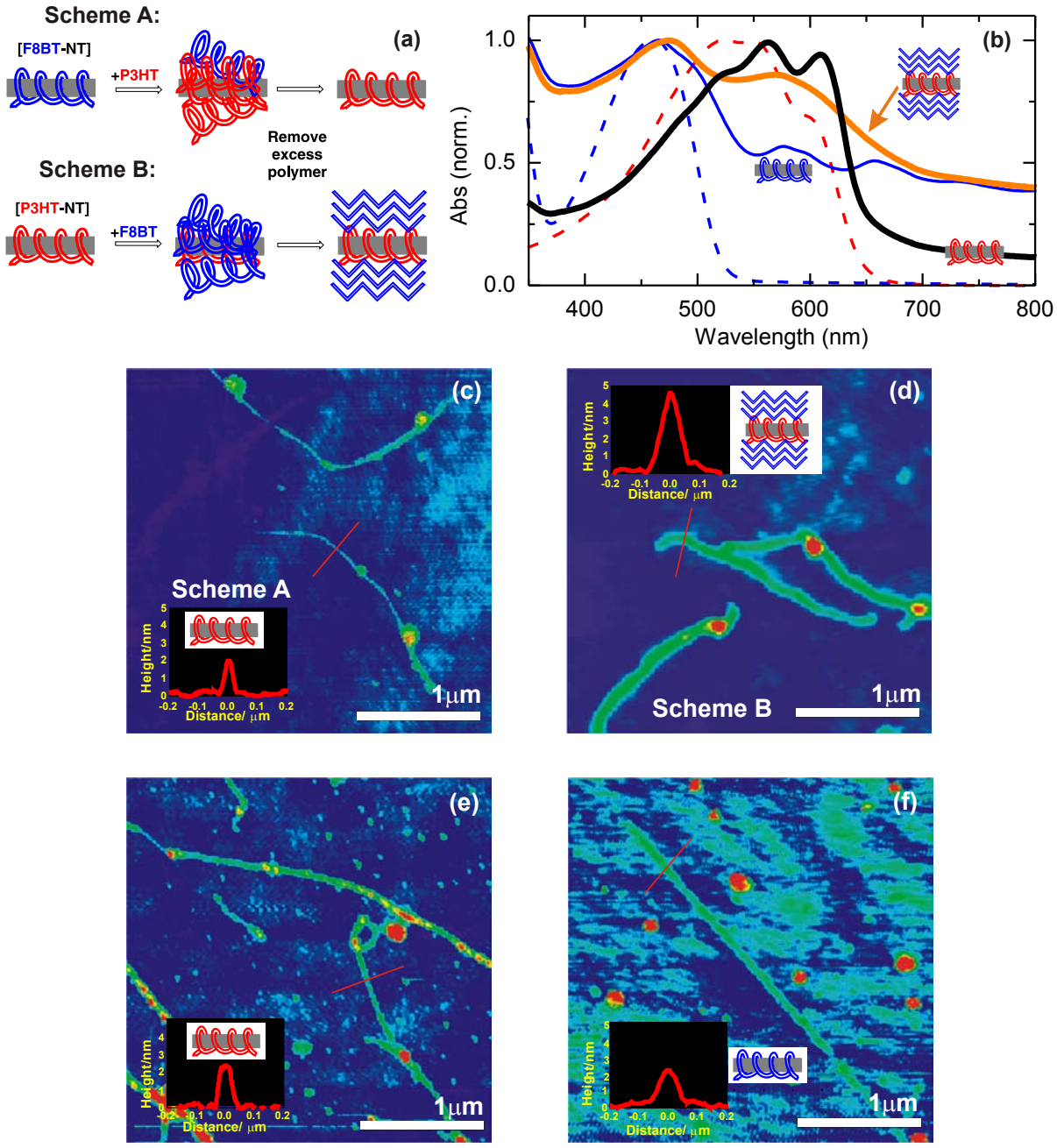

Figure 6.4: The isolation of nanohybrid species following substitution. (a) Scheme A shows excess P3HT being added to [F8BT-NT] nanohybrids, such that there is a 1% concentration of wrapped polymer out of total polymer. 3 days after the addition of excess polymer, any unbound polymer is removed (polymers inverted in Scheme B). The products are discussed in the text. (b) The absorption spectra of the final products taken from spin-coated films are shown in the black line (Scheme A) and orange line (Scheme B). [F8BT-NT] nanohybrid (blue line), F8BT (dashed blue line) and P3HT (dashed red line) spectra are presented for reference and all spectra are normalised at the polymer peaks. (c) and (d) False-colour AFM images of the products from Scheme A and Scheme B, respectively. The analagous control processes, where P3HT was added to [P3HT-NT] and F8BT to [F8BT-NT], are shown in (e) and (f), respectively. The insets show the height analyses across the sections indicated.

centrifuged for 4 minutes at 16,000 $\times g$. The supernatant containing the unbound excess polymer was discarded and the pellet residue redissolved in fresh toluene and the process repeated at least five times. The final residue was redissolved in a concentrated chloroform solution and a portion used to spin-coat a film on plasma-etched quartz substrates (120 seconds, 200 rpm), followed by an annealing treatment at 120°C for 30 minutes.

The processes are shown schematically as schemes A and B in Fig. 6.4 (a) and absorption spectra for the films are shown in Fig. 6.4 (b). The product of Scheme A, for which excess P3HT was added to [F8BT-NT] nanohybrids, shows no evidence of the F8BT absorption at 450 nm and therefore only contains P3HT and nanotubes. The P3HT entirely displaces the bound F8BT, which is then removed in the purification process. Conversely, the product of Scheme B, where excess F8BT was added to [P3HT-NT] nanohybrids, contains both F8BT and P3HT in an approximately 1:1 ratio. While F8BT does not induce displacement of P3HT from the nanotubes, F8BT binds to the [P3HT-NT] system and is not removed even under the vigorous solvent extraction process.

AFM images were obtained using a ThermoMicroscope M5 in non-contact mode by Jack Alexander-Webber (Physics Department, University of Oxford). Samples were prepared by spin-coating a diluted (1/100) solution at 2000 rpm on a flat quartz substrate, followed by annealing at 180°C for 15 minutes. An AFM image of the product of Scheme A, where only P3HT remains, is shown in Fig. 6.4 (c) and reveals typical heights of ∼2 nm. This is consistent with the binding of only 1–2 layers of polymer to a typical nanotube (height 0.7–0.9 nm for CoMoCAT tubes) separated by twice the van der Waals radius of carbon (0.34 nm) [187]. In addition, some large, isolated P3HT nanocrystals are also observed [187]. Very similar images and height analyses are found when an analogous process of adding excess P3HT to [P3HT-NT] nanohybrids and removing any excess polymer is performed (Fig. 6.4 (e)). This suggests that the nanohybrids only bind a single P3HT layer and that any further binding is inhibited by the structure which is formed.

By contrast, the image of the product of Scheme B in Fig. 6.4 (d) shows much thicker uniform polymer coatings ∼5 nm in height. The absorption measurements indicate that

the two polymers are present in a 1:1 ratio but that some polymer is contained in isolated nanocrystals, probably formed from P3HT [187]. The absorption and emission spectroscopy show that the tubes are still coated entirely by a first layer of P3HT. This leads to the conclusion that there is a very strong binding between the excess F8BT and the initial P3HT wrapping layer. Once F8BT is bound to the structure this continues to seed further deposition of F8BT chains resulting in the formation of thick outer layers of F8BT. By contrast, if the same process is performed with F8BT as the initial coating, only 1-2 excess F8BT polymer layers bind to the tube (Fig. 6.4 (f)).

6.4 Thin Film Substitution Studies

The solution studies have shown that excess P3HT added to [F8BT-NT] nanohybrids will eventually displace the F8BT from the tube surface. However, a significant amount of the displacement occurs over a period of several hours, meaning that it is possible to retain the F8BT inner layer and create a nanohybrid heterostructure provided that the [F8BT-NT] + P3HT films are prepared quickly in order to 'fix' the desired polymer configurations. Conversely, [P3HT-NT] + F8BT nanohybrids can be created without any time constraint because the excess F8BT does not displace the bound P3HT, even after several months.

To investigate the formation of 'fixed' nanohybrids in the solid state, thin uniform films were prepared by spin-coating [P3HT-NT] and [F8BT-NT] nanohybrid solutions with a range of concentrations of either excess F8BT or P3HT as described below. All films were cast by spin-coating the solutions onto plasma-etched quartz substrates within 2 hours of adding excess polymer. Polymer controls containing no nanotubes were also spin-coated (1000 rpm, 60 seconds) from solutions with a total polymer concentration fixed at 10 mg/mL. All films were annealed at 120°C for 30 minutes and all preparation and storage was conducted in a nitrogen glovebox.

The 100 % films were prepared by spin-coating the concentrated chloroform solutions of [P3HT-NT] and [F8BT-NT] nanohybrids at 200 rpm for 120 seconds. In order to make

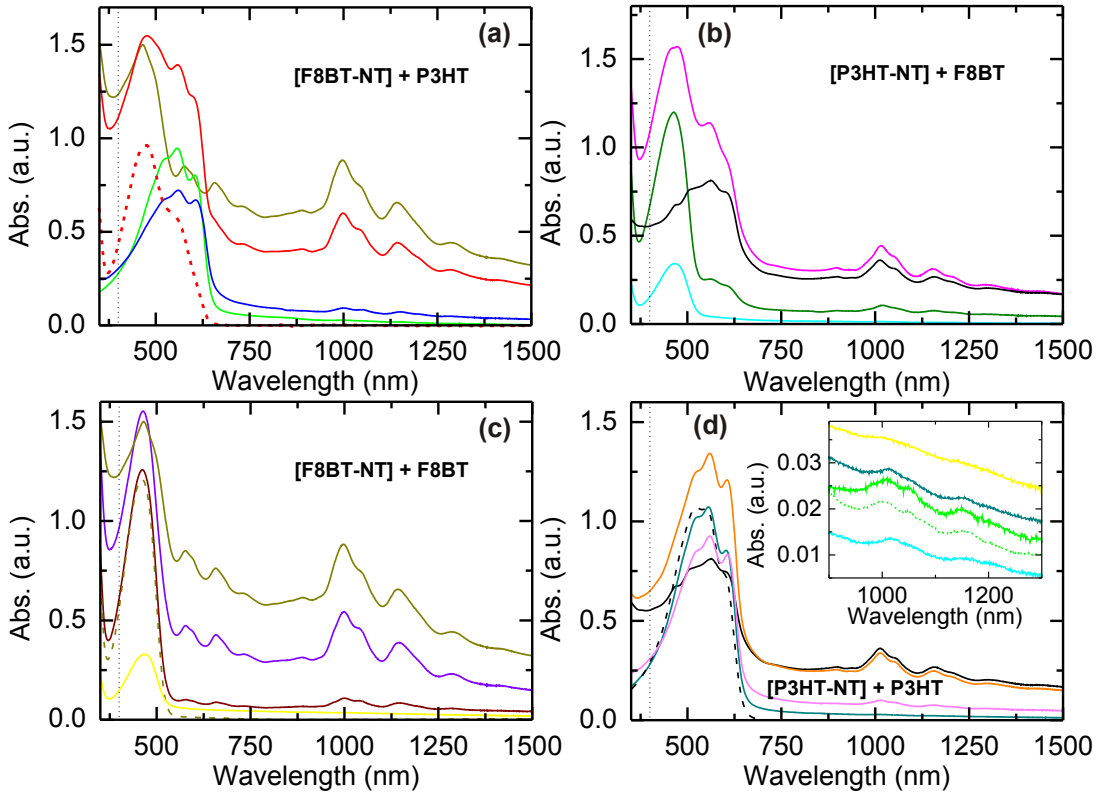

Figure 6.5: Absorption spectra of films spun-cast within 2 hours of adding various excess polymer to nanohybrid solutions. No scaling or background subtractions were applied. The vertical dotted lines show the excitation wavelength (400 nm) for the steady state and time-resolved polymer PL measurements. (a) [F8BT-NT] X% + P3HT films with X = 100 (dark yellow), 50 (red), 10 (blue) and 1 (green), along with an all-polymer 50:50 F8BT:P3HT blend. (b) [P3HT-NT] X% + F8BT films with X = 100 (black), 50 (magenta), 10 (dark green) and 1 (cyan). (c) F8BT (dark yellow dashed) and [F8BT-NT] X% + F8BT films with X = 100 (dark yellow), 50 (violet), 10 (dark red) and 1 (yellow). (d) P3HT (black dashed) and [P3HT-NT] X% + P3HT films with X = 100 (black), 50 (orange), 10 (pink) and 1 (dark cyan). *Inset*: Enlarged view of the nanotube E_{11} region of the 1% samples in (a)–(d), along with a [F8BT-NT] 1% + P3HT sample cast within ten minutes (dotted green).

50 % blends, an equal mass concentration of the desired excess polymer was added from a concentrated stock solution and films spun in a similar manner. Since the polymers aggregate significantly when spun-cast slowly at high concentrations, higher spin speeds (1000 rpm, 60 seconds) were required to achieve uniform films for the nanohybrid concentrations of 20% and below. In addition, the differing densities and solubilities of the polymer and nanohybrid species meant that the final ratios did not scale linearly with starting concentration. As such, the total mass concentration was varied between 5–10 mg/mL and the films were checked to have the correct ratios using absorption spectroscopy (Fig. 6.5). The ratio of

the polymer to E_{11} (6,5) nanotube peaks in the absorption spectra of the [F8BT-NT] and [P3HT-NT] films were used to define 100% of each nanohybrid, where it is understood all of the polymer present was wrapped on the tubes. Using this ratio, the absorption magnitude of wrapping polymer in any given sample could be calculated directly from the E_{11} (6,5) nanotube peak. The excess polymer component was calculated by subtracting the scaled polymer absorption spectrum of the appropriate wrapped 100% nanohybrid film from the spectrum of the sample under investigation. Finally, for those samples containing both polymers, the relative absorption magnitudes were scaled with the appropriate absorption coefficients at the peak ($\sim 1.1 \times 10^{-5}\,\mathrm{cm}^{-1}$ for F8BT, $\sim 1.3 \times 10^{-5}\,\mathrm{cm}^{-1}$ for P3HT [244]). Therefore, the ratio of the wrapping to excess polymer could be calculated and used to define the percentage of nanohybrids in each excess polymer matrix.

The nanotube environments were probed by extracting the position of the (6,5) E_{11} absorption peaks from fits to the spectra in Fig. 6.5 and the positions are plotted in Fig. 6.6. For both [F8BT-NT] and [P3HT-NT] nanohybrids, a small red-shift is observed as an increasing excess of the same polymer is added. This shift is attributed to an increased thickness of dielectric material around the tubes, further decreasing the Coulomb interactions and red-shifting the transitions [156]. This effect is particularly large when F8BT is added to the [P3HT-NT] nanohybrids, supporting the conclusions of the previous section that thick layers of F8BT bind strongly to the [P3HT-NT] nanohybrids and provide additional dielectric screening.

When P3HT is added to [F8BT-NT] nanohybrids, the same effect is seen until the nanohybrid concentration falls below ∼10%, at which point the transitions begin to red-shift rapidly and approach the P3HT-like (6,5) values. This confirms the conclusions from the solution studies of a substitution process, where the bound F8BT is displaced by P3HT when in a large excess. The film properties are stable and this shows that the preparation time window of 2 hours is sufficient to 'fix' the structure and prevent the displacement processes for samples with a nanohybrid concentration of greater than ∼10%. The substitution can be prevented for films with a larger excess of polymer by casting films on an even faster time

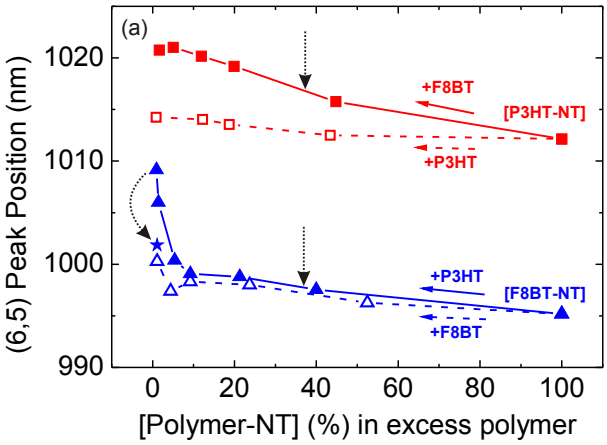

Figure 6.6: Position of the (6,5) nanotube peak as fitted from absorption spectra of these films (Fig. 6.5) spun-cast within 2 hours of adding various excess polymer to [P3HT-NT] or [F8BT-NT] solutions. The blue triangle series shows [F8BT-NT] nanohybrids with increasing F8BT (open symbols) and P3HT (closed symbols) from right to left, while the red square series shows [P3HT-NT] nanohybrids with increasing P3HT (open symbols) and F8BT (closed symbols). The blue starred symbol represents a [F8BT-NT] 1% + P3HT sample prepared quickly (∼10 minutes). The vertical arrows indicate the nanohybrid proportions corresponding to the structures from molecular dynamics simulations (Fig. 6.9 (d) and (h)).

scale, as can be seen by the peak position of a [F8BT-NT] 1% + P3HT sample prepared in ∼10 minutes (starred symbol), which shows significantly less red-shift. To ensure that the desired polymer configurations were maintained in the following studies, the low nanohybrid concentration films were all prepared with casting times <10 minutes.

Further evidence for the structure of the nanohybrids comes from studying the photoluminescence (PL) from the polymers excited at 400 nm, as shown in Fig. 6.7 (a) for the [F8BT-NT] + P3HT series. As the proportion of [F8BT-NT] nanohybrids in the excess P3HT matrix increases from 1 % to 50 %, the P3HT component (600–850 nm) blue-shifts with a corresponding increase in the highest energy (0-0) peak relative to the lower energy peaks. This is attributed to a disruption of the P3HT aggregation [104] by the addition of nanohybrids, as discussed in Chapter 5 [206].

Fig. 6.7 (c) shows the spectra for the [P3HT-NT] + excess F8BT series of structures. As increasing amounts of F8BT are added to the [P3HT-NT] nanohybrids, the P3HT emission shows a significantly larger blue-shift with an even greater increase in the 0-0 peak. This

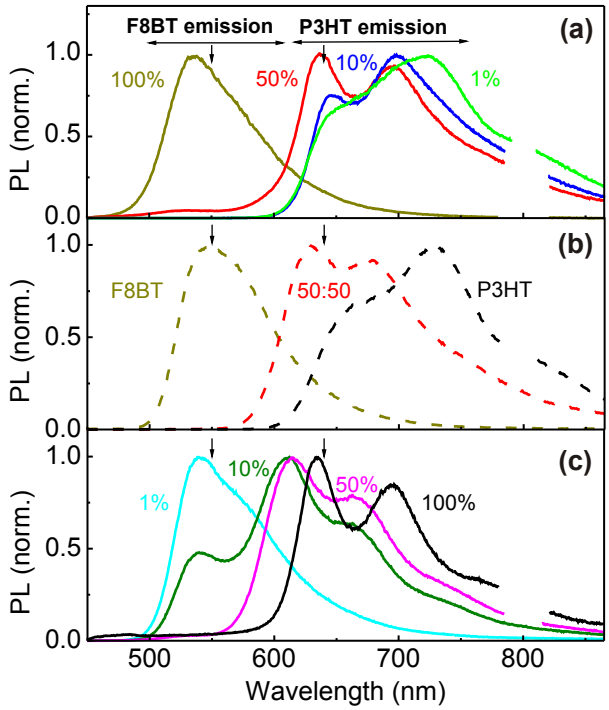

Figure 6.7: Steady-state PL polymer spectra from film samples of (a) [F8BT-NT] 1% (green), 10% (blue) and 50% (red) in excess P3HT, and [F8BT-NT] 100% (dark yellow), (b) P3HT (black dashed), F8BT (dark yellow dashed) and 50:50 F8BT:P3HT (red dashed) and (c) [P3HT-NT] 1% (cyan), 10% (dark green) and 50% (magenta) in excess F8BT, and [P3HT-NT] 100% (black). Samples were excited at 400 nm and spectra are normalised to the peak emission. The arrows indicate probe wavelengths for time-resolved measurements and the laser fundamental peaks at 800 nm have been removed.

can be attributed to a phase separation on a single chain level. The blue shift is enhanced because the P3HT chains have been further isolated by the thick F8BT coatings as observed in AFM images (Fig. 6.4 (d)). In all cases, significant F8BT emission is only observed when there is very little or no P3HT present.

6.5 Molecular Dynamics Simulations

In order to understand the observed differences in substitution dynamics for the nanostructures and visualise the final structures, molecular dynamics simulations were carried out. Molecular structures were constructed using HyperChem (Hypercube Inc.) software with the (6,5) carbon nanotube coordinates (length 30 nm) generated using Nanotube Mod-

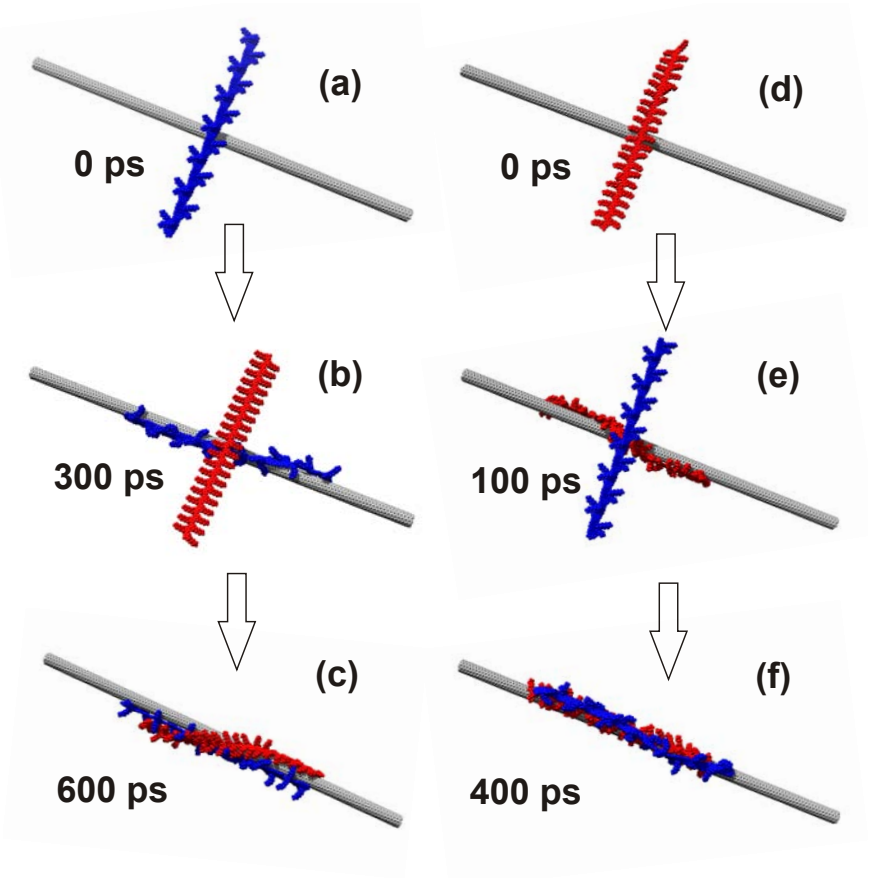

Figure 6.8: Single chain molecular dynamics results, with P3HT chains in red, F8BT chains in blue and (6,5) nanotubes in grey. (a) An F8BT chain was first simulated binding to a (6,5) nanotube. After 300 ps, a P3HT chain was added (b) and the result after a further 300 ps of simulation is shown in (c). The same results with the chains reversed are shown in (d)–(f), except the F8BT chain was added after only 100 ps because the [P3HT-NT] system reached equilibrium more quickly than [F8BT-NT].

eler. F8BT chains consisting of 13 repeat units (∼1/3 of the length of actual F8BT chains) matched in length to P3HT chains (40 thiophene repeating units; ∼1/7 of the length of actual P3HT chains) were built and relaxed with the conjugate gradient method. Simulations were carried out using the Tinker package [245] with the MM3 force field [181], which describes the van der Waals interactions using a potential similar to the Lennard-Jones potential (Chapter 4) but with an exponential function for the repulsive component. Molecular dynamics time steps of 1.0 fs were taken by means of a Modified Beeman Algorithm [246], a Bussi-Parrinello thermostat [247] was used for temperature control (298 K) and a vacuum simulation box of size 2000 × 2000 × 2000 $Å^3$ was used. Carbon nanotube atoms were fixed to reduce computation time, as has been implemented elsewhere [185, 248], and this was not

seen to affect the adsorption dynamics or energies. The starting positions and orientations of the polymers did not significantly affect the final results. Ray-traced images of the results were created using POV-Ray in the UCSF Chimera package [249].

Fig. 6.8 (a)–(c) shows the series in which the binding of a single F8BT chain was first simulated and then a P3HT chain was added after 300 ps. After another 300 ps of simulation, equilibrium was again reached and it was apparent that the added P3HT chain bound predominantly to the nanotube and still attempted to 'wrap' the tube regardless of the presence of the F8BT.

The series for multiple P3HT chains binding to [F8BT-NT] structures, which themselves contain multiple F8BT chains, is shown in Fig. 6.9 (a)–(d). Three F8BT chains binding to a (6,5) nanotube were first simulated. After 300 ps, equilibrium was reached and two more chains were added to the system and, after another 150 ps, a sixth chain was added[2] and run for another 200 ps. Six chains of P3HT aligned along the tube axis were then added to the system (Fig. 6.9 (b)) and equilibrium reached after 150 ps (Fig. 6.9 (c)). Two more P3HT chains were added and a final two added after another 100 ps, with equilibrium again reached after a further 200 ps. The final structure (Fig. 6.9 (d)) is comprised of 10 P3HT chains and 6 F8BT chains and corresponds to one of the proportions highlighted in Fig. 6.6. The single and multiple chain simulations show that P3HT does not favourably bind to F8BT but rather preferentially binds to any exposed areas of nanotubes. The P3HT monomers are less rigid than those of F8BT, imparting a greater flexibility on the polymer to explore any exposed nanotube surfaces. This could explain the observed substitution process, whereby the P3HT chains bind more strongly to the nanotubes than they do to the already bound F8BT chains.

The inverse polymer situation, where the binding of F8BT to [P3HT-NT] nanohybrids was simulated, is shown in Fig. 6.8 (d)–(f) for single-chain simulations. The P3HT chain bound to the tube and reached equilibrium in 100 ps as seen elsewhere [185], more quickly

[2]It is noted that simulations where all six initial chains were added simultaneously led to polymer 'knots' forming, similar to those observed when using a much longer length of polymer both here (data not shown) and elsewhere [185].

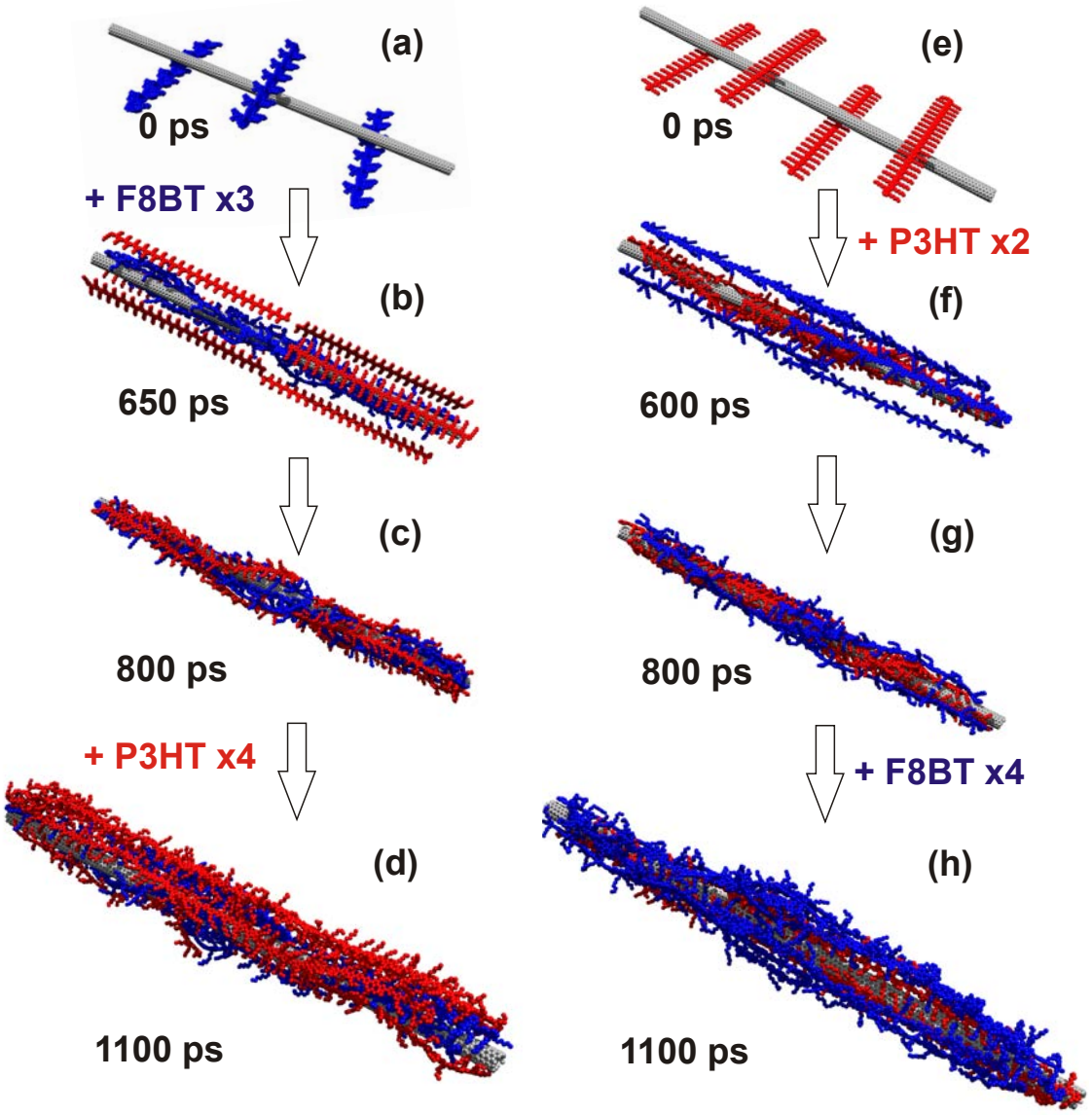

Figure 6.9: Multiple chain molecular dynamics results to visualise the (a)–(d) [F8BT-NT] + P3HT and (e)–(h) [P3HT-NT] + F8BT structures, with P3HT chains in red, F8BT chains in blue and (6,5) nanotubes in grey. (a) The binding of three F8BT chains to a (6,5) nanotube was first simulated. Another two F8BT chains were added after 300 ps and a sixth chain was added after another 150 ps, reaching equilibrium after another 200 ps. (b)–(d) P3HT chains were sequentially added to the system as described in the text. The final [F8BT-NT] + P3HT structure in (d) is comprised of 10 P3HT chains and 6 F8BT chains. (e) Four P3HT chains binding to a (6,5) nanotube were simulated. After 200 ps, two more chains were added to the system and equilibrium reached after another 400 ps. (f)–(h) F8BT chains were sequentially added to the system and the final [P3HT-NT] + F8BT structure in (h) is comprised of 10 F8BT chains and 6 P3HT chains.

than for F8BT. The added F8BT chain bound directly to the P3HT chain only and remained attached. The corresponding multiple chain simulations are shown in Fig. 6.9 (e)–(h). The binding of four P3HT chains to a (6,5) nanotube was first simulated and equilibrium reached after 200 ps. Two more P3HT chains were added to the system and equilibrium again reached after 400 ps. Six F8BT chains aligned along the tube axis were added (Fig. 6.9 (f)) and the system simulated until equilibrium (200 ps; Fig. 6.9 (g)). To create the structure in Fig. 6.9 (h), which is comprised of 10 F8BT chains and 6 P3HT chains and corresponds to one of the proportions highlighted in Fig. 6.6, two more F8BT chains were added and a final two added after another 100 ps, with equilibrium again reached after a final 200 ps. These single and multiple chain simulations show that the F8BT chains favourably adsorb to the already bound P3HT chains. This results in a uniform outside coating of relatively flat F8BT chains onto which additional F8BT chains can bind, explaining the ability to form thick F8BT layers on these structures.

6.6 Time-Resolved Spectroscopy

To investigate the electronic dynamics in the nanohybrid structures formed, the time-dependent photoluminescence of the wrapping and excess polymers in the prepared films was studied using TCSPC and PL up-conversion with time resolutions of 120 ps and 220 fs, respectively. All measurements were taken with an excitation wavelength of 400 nm and detection wavelengths of 640 nm and 550 nm corresponding to P3HT and F8BT emission, respectively.

Fig. 6.10 (a) and (b) show the TCSPC results for F8BT emission (550 nm) from the samples. The [F8BT-NT] + P3HT samples in (a) show a response on the order of the system resolution (∼120 ps) because the emission from wrapped F8BT is significantly quenched by the tubes and/or P3HT. The decay curves for the [P3HT-NT] + F8BT samples in (b) become increasingly faster as the [P3HT-NT] nanohybrid proportions and hence density of quenching centres increase, reaching the instrument resolution for the 50 % samples.

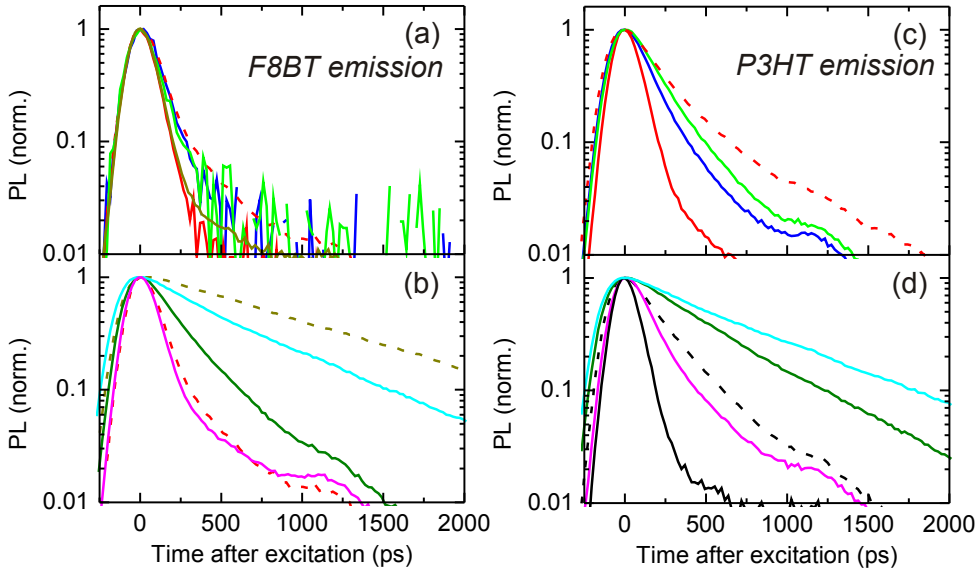

Figure 6.10: TCSPC measurements following photoexcitation at 400 nm to time-resolve the (a) and (b) F8BT emission at 550 nm and (c) and (d) P3HT emission at 640 nm from film samples. Results for the [F8BT-NT] + P3HT series, namely 50:50 F8BT:P3HT (red dashed), [F8BT-NT] 1% (green), 10% (blue) and 50% (red) in excess P3HT and [F8BT-NT] 100% (dark yellow), are shown in (a) and (c). (b) and (d) show the same results but taken from the [P3HT-NT] + F8BT series, namely F8BT (dark yellow dashed), 50:50 F8BT:P3HT (red dashed), [P3HT-NT] 1% (cyan), [P3HT-NT] 10% (dark green) and 50% (magenta) in excess F8BT, along with [P3HT-NT] 100% (black) and P3HT (black dashed).

The TCSPC results for P3HT emission (640 nm) from the samples are shown in Fig. 6.10 (c) and (d). As the [F8BT-NT] proportion increases in (c), the P3HT emission shows an increasingly faster decay that cannot be resolved for the [F8BT-NT] 50% + P3HT sample. For the [P3HT-NT] + F8BT samples, shown in (d), the [P3HT-NT] 10% and 1% in excess F8BT samples show long-lived decays that are attributed to probing the tail of the dominant long-lived F8BT emission. The emission from the pure [P3HT-NT] nanohybrids shows a system-limited response, as seen in Chapter 5.

To fully describe the dynamics of these systems and resolve the faster dynamic processes, the higher resolution PLUC technique was used. PLUC measurements presented here were taken by Chaw Keong Yong (Physics Department, University of Oxford). The discussion concentrates on the 50 % blend samples, for which excitons are created in the F8BT and P3HT components in a ratio of ∼2:1 according to absorption spectra. PLUC data were fitted using mono- or bi-exponential functions convoluted with the Gaussian system response function

(220 fs). For bi-exponential fits, the time constants corresponding to the slow components were fixed to the values obtained from mono-exponential fits to the TCSPC data.

Fig. 6.11 (a) and (b) show that the emission from F8BT (550 nm) is quenched remarkably quickly in the presence of either nanotubes or P3HT. Films of F8BT alone have a relatively long emission lifetime of over 1000 ps while all blends investigated show rapid quenching with lifetimes below 0.8 ps and close to the time-resolution limit of the system (220 fs). The reasons for these fast dynamics lie both in the electronic structure and morphology of these nanoscale interfaces. Energy level schematics shown in Fig. 6.11 (e) and (f) illustrate that F8BT excitons may be quenched through both energy and charge transfer at interfaces with either P3HT or (6,5) nanotubes, thus opening a multitude of decay pathways. The favourable binding of F8BT to P3HT, as illustrated by the molecular modelling simulations in section 6.5, also aids the overall fast excitation transfer into P3HT. The short F8BT emission lifetime of 0.42 ps measured for all-polymer 50:50 P3HT:F8BT blend films (Fig. 6.11 (a)) suggests that intimate mixing of these two polymers alone is sufficient to induce rapid exciton quenching in the F8BT phase. In addition, the order of arrangement in the coaxial nanotube polymer structures clearly influences the excitation transfer dynamics. For dual-polymer wrapped nanotubes containing F8BT on the outside ([P3HT-NT] 50% + F8BT – Fig. 6.11 (b)) the quenching of F8BT emission is slower (0.77 ps lifetime) than for the case for which F8BT is sandwiched between P3HT and the nanotubes ([F8BT-NT] 50% + P3HT – Fig. 6.11 (a) – 0.29 ps lifetime).

Fig. 6.11 (c) shows that the time dependence of P3HT emission at 640nm is appreciably slower than the dynamics observed for F8BT emission for all samples investigated. The reasons for such slowed dynamics can be mostly attributed to the absence of efficient excitation transfer from P3HT to F8BT. The P3HT emission from the F8BT:P3HT 50:50 blend is dominated by a long-lived 220 ps component also observed in the TCSPC results (Fig. 6.10 (c)). By contrast, the presence of carbon nanotubes, around which both P3HT and F8BT wrap, introduces rapid decay mechanisms for P3HT excitations. Fig. 6.11 (c) shows that the P3HT emission for the [F8BT-NT] 50% + P3HT sample has an initial decay time constant

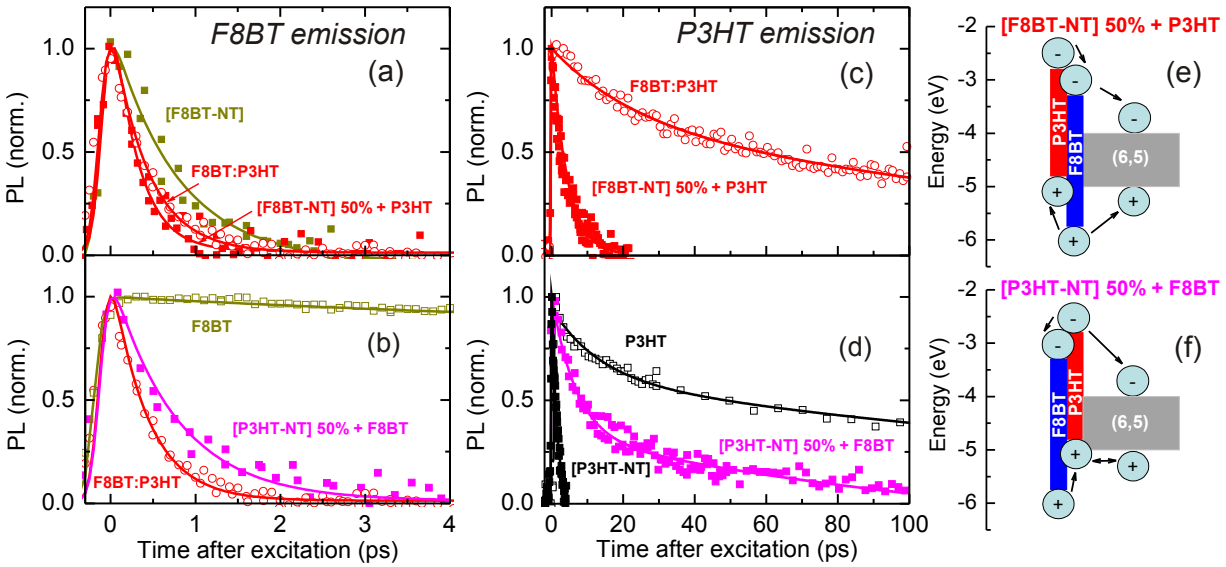

Figure 6.11: PLUC measurements following photoexcitation at 400 nm to time-resolve the (a) and (b) F8BT emission at 550 nm and (c) and (d) P3HT emission at 640 nm from film samples of [F8BT-NT] 50% + P3HT (red closed squares), 50:50 F8BT:P3HT (red open circles), [F8BT-NT] (dark yellow closed squares), F8BT (dark yellow open squares), [P3HT-NT] 50% + F8BT (magenta closed squares), [P3HT-NT] 100% (black closed squares) and P3HT (black open squares). Solid lines represent mono- and multi-exponential fits to the data, convoluted with the Gaussian system response function (220 fs). (e) and (f) Schematics to show the energy level alignments of the species in the [F8BT-NT] 50% + P3HT and [P3HT-NT] 50% + F8BT nanohybrids, respectively, and the electronic processes occurring between the materials.

of 4.4 ps and is quenched almost completely to zero within 20 ps after excitation. These decay dynamics are slower than those observed for pure [P3HT-NT] nanohybrids (Fig. 6.11 (d)) for which a picosecond P3HT emission decay is observed. The introduction of an F8BT layer between P3HT and the nanotubes thus leads to a measurable inhibition of excitation transfer between the two and, in the reverse process, will block recombination once charge separation has been established. Fig. 6.11 (e) illustrates these processes: excitons created on the P3HT can be dissociated at the interface with F8BT, with electrons cascading to the F8BT and then to the nanotube, while holes may remain within the P3HT.

By contrast, reversing the ordering of the wrapping, *i.e.* [P3HT-NT] 50% + F8BT, leads to a two-component longer lived decay of the P3HT emission (Fig. 6.11 (d)). The initial fast component decays with a time constant of 6.8 ps, followed by a slower component with time constant of ∼150 ps. The appearance of a much longer lived component demonstrates the

influence of the very different electronic structure for the [P3HT-NT] + F8BT nanohybrids, as illustrated in Fig. 6.11 (f). The addition of F8BT to [P3HT-NT] provides an alternative pathway for excitons on P3HT chains to dissociate by transferring electrons into the F8BT cladding layer. A significant number of the electrons that are transferred to the F8BT are likely to eventually tunnel back into the P3HT in the varied energy landscape that will be created by the polymer wrapping process (Fig. 6.9 (h)), thus enabling them to recombine with the longer lived excess holes in the [P3HT-NT] and giving rise to the longer lived component of the P3HT emission.

6.7 Applications

The energy levels shown in Fig. 6.11 (e) and (f) suggest that both [F8BT-NT] + P3HT and [P3HT-NT] + F8BT structures can offer important advantages for nanotechnology applications. When the inital layer is F8BT it acts as a blocking layer preventing holes on the secondary layer of P3HT from recombining with electrons on the nanotubes. Therefore, the structure provides a means to physically separate electrons and holes onto different materials separated by an energetic barrier, through bottom-up self-assembly. By incorporating an excess of P3HT to allow the hole to move away from the interface (Chapter 5) [206], these structures may be successfully integrated into OPVs using the nanotubes as electron transporters [148]. When P3HT is the initial wrapper, the [P3HT-NT] nanohybrids act as a template to bind thick layers of F8BT polymer. Such preferential binding effects may prove useful in providing nanotube-seeded blend morphologies optimised for OPV that are difficult to achieve in polymer–polymer blends [132, 134, 244]. The electronic arrangement may even allow these structures to act as hole collectors.

6.8 Conclusion

This work has reported the nano-engineering of a new form of nanostructure consisting of single-walled carbon nanotubes coated with sequential layers of the semiconducting polymers P3HT and F8BT. Absorption and photoluminescence spectroscopy revealed a competition between the two polymers for binding to the nanotubes in solution. P3HT has a much stronger binding affinity to the nanotubes and, in the presence of a large excess, slowly displaces F8BT from the tube surface. However, despite the intrinsic differences in binding strength, it was shown that a wide range of final structures with different ordering and proportions of the wrapping polymers can be achieved in the solid-state for both cases provided the films are prepared quickly. These final structures were visualised using molecular dynamics simulations.

Nanotubes coated in F8BT and surrounded by P3HT can establish an electron cascade to the nanotube, with the F8BT layer able to act as a blocking layer to prevent holes on the P3HT from recombining with electrons on the nanotubes. Reversing the order of the polymers blocks the electron flow creating a hole collection into the nanotubes. In addition, nanohybrids consisting of nanotubes wrapped in P3HT can act as seeds to bind F8BT polymer chains, thus achieving ordered P3HT:F8BT polymer–polymer blends. By exploiting the binding abilities of both polymers, the favourable energy alignments and the high mobilities of the nanotubes, these novel nanostructures will be useful for a variety of devices such as organic photovoltaics.

Chapter 7

Dispersing a Single Chirality of Semiconducting Carbon Nanotubes with Desired Conjugated Polymers

The work in this chapter has been reproduced in part with permission from the Journal of the American Chemical Society, submitted for publication.
S. D. Stranks, A. M. R. Baker, J. A. Alexander-Webber and R. J. Nicholas. Production of high purity single chirality carbon nanotube hybrids by selective polymer exchange. Unpublished work copyright 2012 American Chemical Society.

7.1 Introduction and Background

The synthesis of SWNTs produces bundles consisting of a mixture of different chiralities of both semiconducting and metallic nanotubes. The ensemble of different tubes makes characterisation and repeatable device preparation difficult. Furthermore, metallic nanotubes can be detrimental to optoelectronic device performance because their lack of bandgap can lead to quenching of excitons and charges in OPV devices, for example [158]. The synthesis of a single chirality of semiconducting nanotubes still remains an elusive goal.

As presented in Chapters 4–6, bundling of individual SWNTs can be prevented by dispersing nanotubes with surfactants such as SDBS or with semiconducting conjugated polymers. The non-covalent nature of the polymer binding means that the intrinsic properties of the tubes can be preserved while utilising the favourable properties of the polymer. There is a wide range of polymer families available to wrap the tubes [179] and the polymers can be chosen either for their favourable optical, electrical and mechanical properties or for the strong binding selectivity they have for certain tubes in the distribution.

In Chapter 4 it was shown that the semiconducting polymer PFO can selectively disperse a narrow chirality distribution of semiconducting tubes and exclude all metallic tubes [176]. While the removal of metallics has allowed promising OPV devices to be constructed using the blend [143], the large bandgap and low mobility of PFO renders it of limited use in OPV devices. By contrast, the smaller bandgap polymer P3HT exhibits high carrier mobilities [112] and forms a favourable type-II heterojunction electronic alignment with small-diameter nanotubes [156]. The results in Chapter 5 showed that significantly long-lived free charges can be generated in these [P3HT-NT] blends [206, 234], demonstrating promise for OPV applications. Furthermore, it was shown in Chapter 6 that a coating of F8BT on SWNTs can act as a hole blocking layer when surrounded by a thick coating of P3HT, also rendering these coaxial nanohybrids promising for use in OPV devices. Despite some larger diameter tube selectivity by F8BT [210], neither polymer is able to sufficiently select only specific SWNT species. For nanotube–polymer blends to find ultimate optoelectronic application, the polymer with desired mechanical and electrical properties must coat only a single species of semiconducting nanotube.

In this work, the PFO-dispersing process was first utilised to select predominantly (7,5) semiconducting SWNTs from a distribution. The PFO wrapping polymer was then entirely substituted by a preferable polymer in solution. As first examples, this was demonstrated for P3HT and F8BT polymers but the method could equally be applied using other desired polymers. Absorption and photoluminesence spectroscopy as well as AFM images show that the nanohybrids consisting of almost solely (7,5) semiconducting tubes coated in the

desired polymer can be isolated with all excess polymer and metallic nanotubes removed. This simple and scalable processing technique allows these purified polymer-coated (7,5) nanohybrids to be synthesised in any desired solvent and concentration, making them suitable for optoelectronic applications. For instance, since (7,5) tubes form the required type-II heterojunction with P3HT, these nanohybrids will be suitable for implementation into OPV devices.

7.2 Sample Preparation

CoMoCAT SWNTs were directly dispersed with SDBS in D_2O using the procedure described in Chapter 4, producing [SDBS-NT] distributions. SWNTs were also directly dispersed with the semiconducting polymers PFO, F8BT and P3HT in *o*-xylene using the method outlined in Chapter 4 to disperse tubes with PFO. Briefly, CoMoCAT material was mixed with a 0.6 mg/mL *o*-xylene solution of polymer to a tube concentration of 0.5 mg/mL and the mixture treated in an ultrasonic disintegrator for 15 minutes. This was followed by centrifugation for 8 minutes at 10,000 ×g and retainment of the upper 85% of supernatant containing the dispersed tubes. The F8BT and P3HT dispersions were named [F8BT-NT] and [P3HT-NT], respectively, but that with PFO was termed [PFO-(7,5)] due to its enhanced selectivity for (7,5) tubes.

Using a sonic bath, F8BT and P3HT were then dissolved in separate [PFO-(7,5)] solutions to a concentration to match the excess PFO (0.6 mg/mL). The mixtures were treated in an ultrasonic disintegrator for a further 15 minutes to ensure complete displacement of the PFO by the added polymer, giving solutions named [F8BT-(7,5)] and [P3HT-(7,5)]. The processing routes for the samples presented in this chapter are summarised in the scheme in Fig. 7.1, using P3HT as an example.

To remove the excess and/or displaced polymer from each solution, the purification method introduced in Chapter 4 was used. The purification first involved inducing aggregation of the nanohybrids, which was achieved using a rotary evaporation step for the

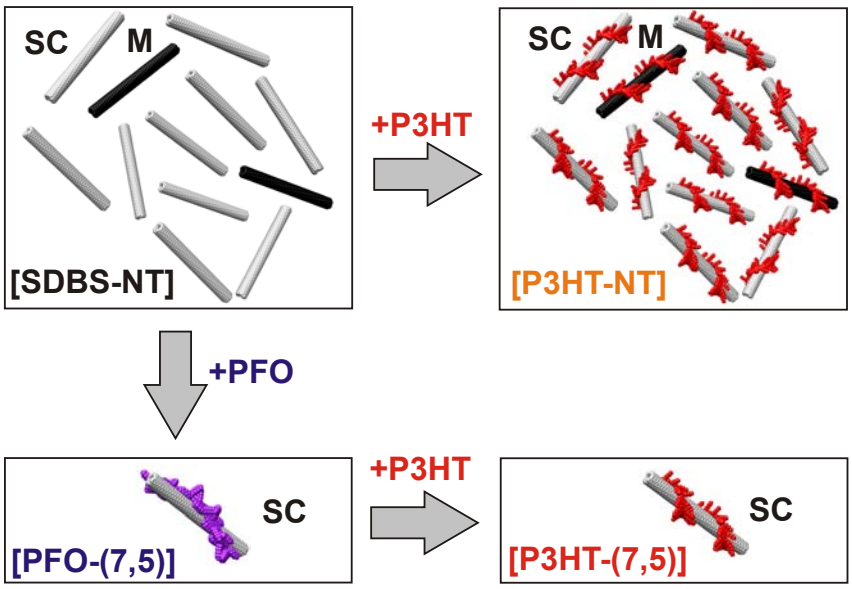

Figure 7.1: Scheme to illustrate the different sample preparation routes used in this work, using P3HT samples as an example. The starting material, containing both metallic (M) and semiconducting (SC) tubes, can be dispersed in SDBS to give [SDBS-NT] nanohybrids. The tubes can also be directly dispersed with P3HT, termed [P3HT-NT], retaining all of the original species. Alternatively, the (7,5) SC tubes can be selectively wrapped by dispersion in PFO, [PFO-(7,5)]. The PFO can then be displaced by P3HT, giving [P3HT-(7,5)] nanohybrids.

[PFO-(7,5)] nanohybrids with excess PFO, but simply by gentle warming in a sonic bath for 1 hour for all other solutions because they contained either larger amounts of excess material and/or the nanostructures were less stable in *o*-xylene solution. The mixtures were then centrifuged for 4 minutes at 16,000 ×g and the supernatants containing excess polymer discarded and the residues redissolved in fresh *o*-xylene to less than half of the original volumes. The solutions were briefly subjected to tip sonication (10 seconds) followed by 15 minutes in a sonic bath to induce re-aggregation. The mixtures were centrifuged again and the process repeated a total of three to four times to ensure removal of as much excess polymer as possible. The final residues were redissolved in *o*-xylene to ensure the same solvent was used for optical measurements, but it is noted that any desired solvent can be used.

7.3 Absorption Spectroscopy

The absorption spectra of the directly dispersed samples are presented in Fig. 7.2 (a). The [SDBS-NT] sample shows the entire distribution of tubes and the E_{11} and E_{22} semiconducting nanotube transitions are clearly seen in the regions 900–1300 nm and 500–800 nm, respectively. Some metallic E_{11} transitions are seen below 500 nm and the broad background is also primarily attributed to metallic species [192].

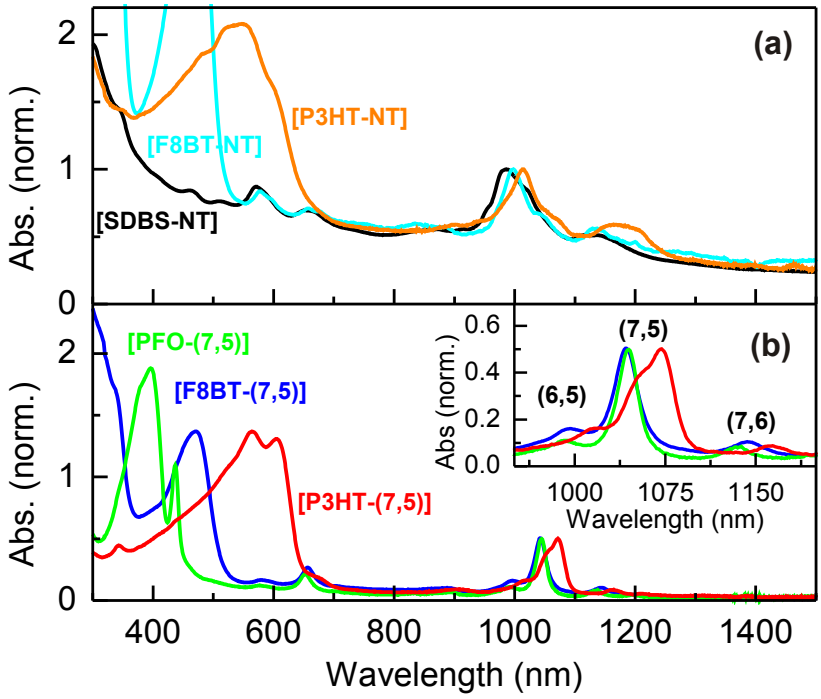

Figure 7.2: Absorption spectra of the samples under investigation with excess polymer removed. (a) [SDBS-NT] in D_2O, and [F8BT-NT] and [P3HT-NT] in *o*-xylene, where the tube E_{11} peaks are normalised to 1. (b) [PFO-(7,5)], [F8BT-(7,5)] and [P3HT-(7,5)] in *o*-xylene, with the E_{11} absolute peak heights scaled to match those in (a). *Inset*: Expanded view of the E_{11} transitions with tube species labelled.

The spectra of the tubes directly dispersed with F8BT and P3HT, namely the [F8BT-NT] and [P3HT-NT] samples, are also shown in Fig. 7.2 (a). The F8BT and P3HT polymer absorptions are observed in the region below 500 nm and 400–700 nm, respectively. It is noted that this includes some free polymer that could not be effectively removed, even after 4–5 purification steps. The P3HT 0-0 transition is strongly suppressed because of strong inter-chain coupling [104]. This suggests that a significant amount of the P3HT is in aggre-

gates, likely due to the poor solubility of P3HT in *o*-xylene. In both samples, the nanotube transitions are red-shifted relative to the [SDBS-NT] dispersion and, as discussed in Chapter 4, are attributed to the dielectric material (polymer) surrounding the nanotubes acting to reduce the Coulomb energies in the tubes [66]. The P3HT-coated nanotube transitions are red-shifted even further due to the delocalisation of the hole of the exciton onto the polymer owing to the type-II heterojunction between P3HT and the tubes, an effect which is enhanced for the smaller diameter tubes. In summary, neither polymer shows particular tube selectivity and the metallic background remains.

The absorption spectrum of the [PFO-(7,5)] sample is shown in Fig. 7.2 (b) and the dominant species is clearly the (7,5) tube with E_{11} and E_{22} resonances at 1045 nm and 652 nm, respectively. Small fractions of (6,5), (7,6) and (8,6) tubes are present from their respective E_{11} peaks at 992 nm, 1135 nm and 1194 nm, but these species comprise less than 30 % of the total. Again, the nanotube peaks are red-shifted relative to the [SDBS-NT] distribution because of the dielectric screening of the Coulomb interactions in the nanotubes by the wrapping PFO [176]. Most importantly, the metallic background is completely removed when compared to the spectra in Fig. 7.2 (a). The PFO absorption is seen in the region 320–500 nm and the polymer is in a highly aggregated state, as discussed in Chapter 4.

The absorption spectra of the [F8BT-(7,5)] and [P3HT-(7,5)] samples are also shown in Fig. 7.2 (b). The [F8BT-(7,5)] nanotube transitions show only small shifts relative to the [PFO-(7,5)] sample. Nevertheless, it is concluded that the PFO was entirely displaced by F8BT because no PFO polymer absorption (350-500 nm) remains and from the PLE results which will be discussed in section 7.4. The [P3HT-(7,5)] spectrum shows a very similar spectral shape in the nanotube E_{11} regions but red-shifted further to peaks that correspond to P3HT-wrapped tubes, matching the positions of the relevant peaks in the [P3HT-NT] sample. The remaining P3HT exhibits strong 0-0 transitions, suggesting that the chains appear in monolayer coatings having π-π interactions with the tubes only and are not subject to coupling with adjacent chains. Moreover, no evidence of PFO absorption remains. These observations provide direct evidence that the P3HT has displaced the PFO

on the nanotubes. The removal of the absorption background and dramatic enrichment of the (7,5) species, when compared to the corresponding nanohybrids prepared by direct dispersion (Fig. 7.2 (a)), shows that this synthesis route has yielded purely semiconducting nanotubes coated with the desired F8BT or P3HT polymers.

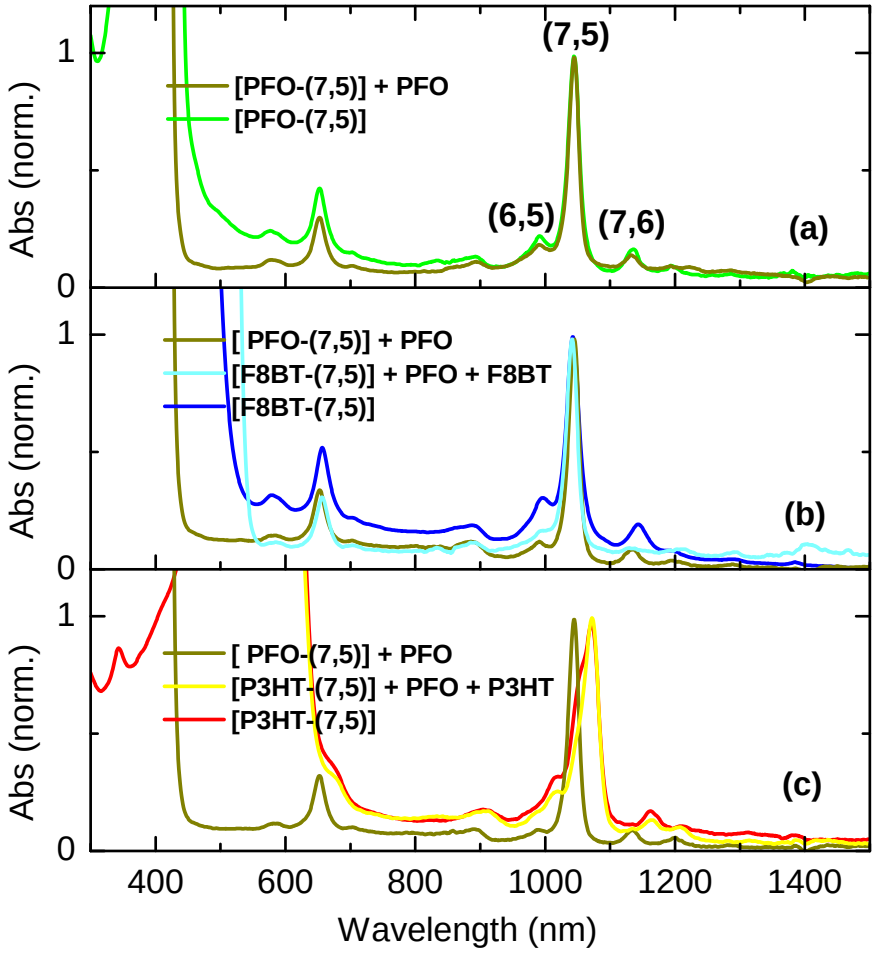

Figure 7.3: Absorption spectra of samples before and after substitution and following excess polymer removal, with the (7,5) E_{11} transition peaks normalised to 1. (a) The initial [PFO-(7,5)] sample before and after the excess polymer was removed. (b) F8BT was added to the [PFO-(7,5)] sample to a concentration to match the excess PFO and the sample tip sonicated for 15 minutes to give a sample containing [F8BT-(7,5)] along with excess PFO and F8BT. Finally, the remaining polymer was removed to give the purified [F8BT-(7,5)] sample. (c) As for (b) but using P3HT instead of F8BT.

To investigate the relative proportions of the various nanotube species before and after the substitution processes and following excess polymer removal, the absorption spectra of the [PFO-(7,5)], [F8BT-(7,5)] and [P3HT-(7,5)] samples at various stages are shown in Fig. 7.3 (a), (b) and (c), respectively. In all three series, the proportion of (7,5) tubes, relative

to the other semiconducting tubes such as (6,5) and (7,6), decreases after the removal of free polymer. This is because the polymer removal process involves inducing the aggregation and precipitation from solution of the desired tubes. However, the most soluble and well dispersed tubes are the (7,5) tubes, removing a proportion of these tubes with the discarded supernatant in each step. The effect is most evident for the P3HT and F8BT samples where more purification steps were undertaken to ensure complete removal of the two excess polymers in these solutions. Since the PFO polymer was seen to be almost entirely removed in the first two purification routines (data not shown), a greater proportion of (7,5) tubes could be obtained if only two purification steps are undertaken. This leaves a sample suitable for most applications, such as the samples described in Chapters 5 and 6 where excess polymer is desired.

In both Fig. 7.2 (b) and Fig. 7.3 (c), the (7,5) E_{11} transitions in the P3HT-wrapped nanotubes samples are split into a peak red-shifted to 1057 nm and one red-shifted further to 1072 nm. Both peaks are red-shifted with respect to the PFO-dispersed (7,5) peak (1045 nm) and both are seen in the [P3HT-NT] distribution (Fig. 7.2 (a)) and in other reports [187] but are not observed for other tubes. These peaks are attributed to P3HT-dispersed (7,5) tubes but with varying effectiveness of P3HT wrapping, where the 1072 nm peak corresponds to a more complete P3HT coating. Fig. 7.3 (c) shows that after polymer substitution the peak at 1072 nm dominates with only a small 1057 nm component. However, following the polymer removal, the peak at 1057 nm increases significantly relative to the 1072 nm peak. Although this change of relative intensity also occurred with much longer sonication times (data not shown), the polymer removal process involved only very brief sonication and this would not be the likely cause. The reduction of the 1072 nm peak is attributed to the same mechanism as the previous paragraph, *i.e.* fractions of the more soluble and more completely coated (7,5) tubes, corresponding to the 1072 nm peak, remained in the discarded supernatant in each polymer removal step. Nevertheless, a more detailed study would be required to determine the exact environment of the (7,5) tubes in each case.

7.4 PLE Spectroscopy

In order to ascertain which nanotube species were present in the samples, PLE maps were taken. Fig. 7.4 (a) shows the PLE map of the [SDBS-NT] starting distribution in D_2O and the nanotube species were assigned using the empirical formulae for the E_{11} and E_{22} transitions from Weisman and Bachilo [44]. The weak E_{33} resonances are also seen in the region below 420 nm [250].

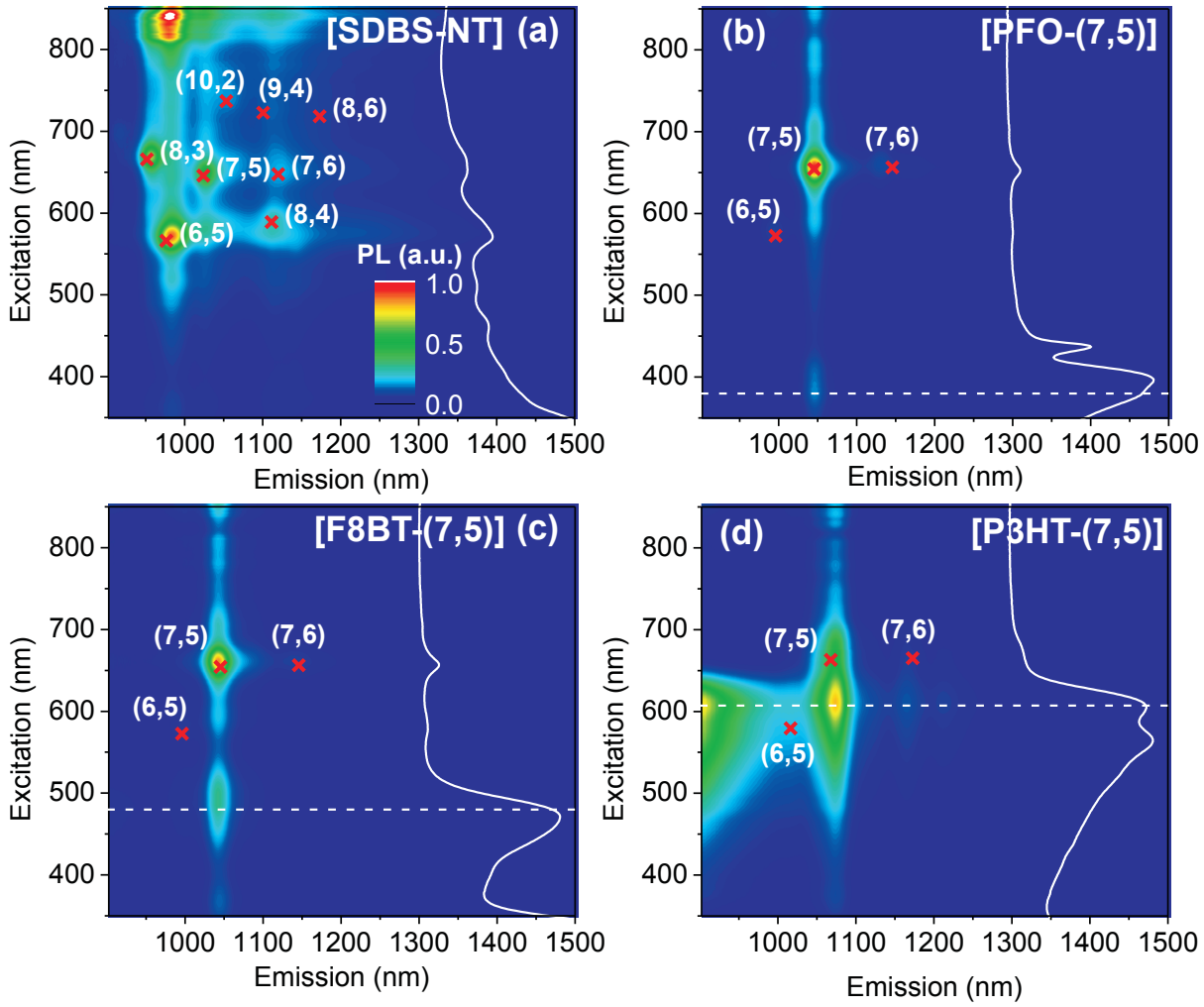

Figure 7.4: (a) PLE map of [SDBS-NT] in D_2O. PLE maps of the purified nanohybrids (b) [PFO-(7,5)], (c) [F8BT-(7,5)] and (d) [P3HT-(7,5)] in *o*-xylene with excess polymer removed. The absorption spectra of each sample are overlaid and the dashed lines highlight energy transfer bands following absorption in the corresponding polymer. Nanotube species were assigned using the values from Weisman and Bachilo [44], red-shifted by 25 meV for PFO and F8BT and 50 meV for P3HT.

Fig. 7.4 (b) shows the PLE map of the purified [PFO-(7,5)] sample with the absorption spectrum overlaid vertically. The sample contains mostly (7,5) tubes but traces of (7,6) and (6,5) tubes are present, as seen from the weak direct resonances at ∼658 nm and ∼580 nm, respectively. The tube emission peaks are again red-shifted relative to the SDBS sample, as observed from absorption measurements. The energy transfer band is denoted by the dashed line and corresponds to absorption by PFO at 350–440 nm and emission from the nanotube E_{11} transitions. This is distinguishable from the E_{33} direct absorption for the (7,5) tube (344 nm) but overlaps exactly with the (7,6) E_{33} (376 nm) transition [174, 250]. Nevertheless, it is unambiguously concluded that there is an energy transfer band because the peak is seen to be tunable to ∼440 nm in the presence of excess PFO polymer (data not shown), as reported elsewhere [201].

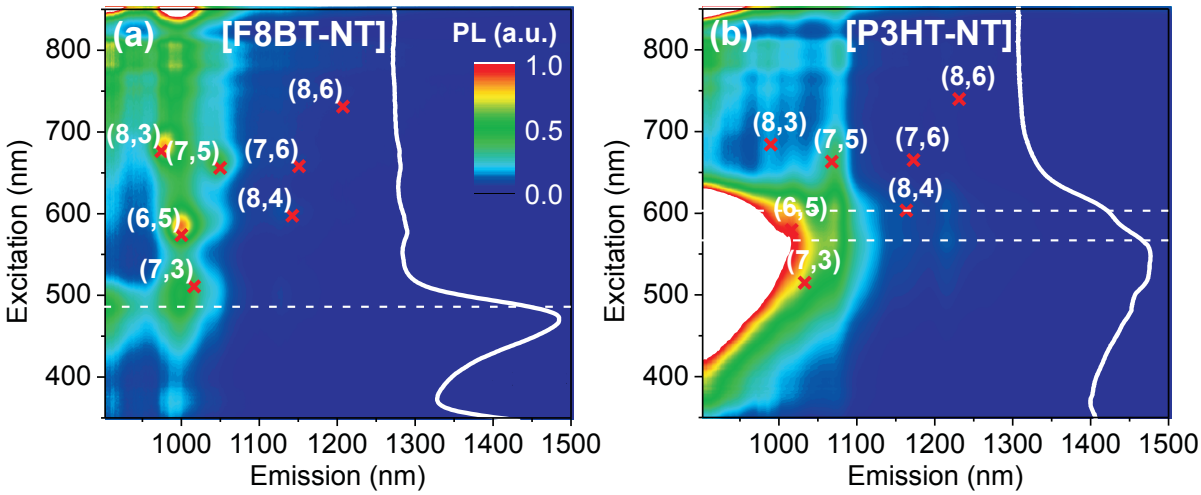

Figure 7.5: PLE maps of the purified nanohybrids (a) [F8BT-NT] and (b) [P3HT-NT] in *o*-xylene with most of the excess polymer removed. The absorption spectra of each sample are overlaid and the dashed lines highlight energy transfer following absorption in the corresponding polymer. Nanotube species were assigned using the values from Weisman and Bachilo [44], red-shifted by 25 meV for F8BT and 50 meV for P3HT [156].

Fig. 7.4 (c) and (d) show the PLE maps with absorption spectra (overlaid) of the [F8BT-(7,5)] and [P3HT-(7,5)] samples, respectively. Again, the dominant species are the (7,5) tubes and the emission peaks are red-shifted relative to the SDBS samples, with the largest shifts for the P3HT sample. Broad energy transfer bands are seen corresponding to absorption at 400–550 nm by bound F8BT [177, 251] in (c) and at 400–650 nm by bound P3HT [187] in

(d). The weak E_{33} transitions are also seen below 400 nm. Finally, in the [P3HT-(7,5)] map, emission from a small amount of unremoved excess P3HT is seen as a tail below 1000 nm. This is due to the low solubility of P3HT in *o*-xylene, meaning that some excess polymer remained in small aggregates that were difficult to entirely remove. Most importantly, no PFO energy transfer band is observed in either sample and it is concluded that PFO has been entirely displaced by the P3HT or F8BT polymers and subsequently removed during the purification processes.

By contrast, the PLE maps of the directly dispersed [F8BT-NT] and [P3HT-NT] samples are shown in Fig. 7.5 (a) and (b), respectively. In both maps, almost all of the original species from the CoMoCAT distribution remain dispersed. As observed in absorption spectra, even 4–5 polymer removal steps did not allow all of the excess polymer to be removed. In Fig. 7.5 (a), this is evident from an emission tail from unbound F8BT seen in the region 900–1000 nm, corresponding to absorption in F8BT at ∼470 nm. In Fig. 7.5 (b), a large P3HT emission tail dominates the spectrum in the region 900–1050 nm arising from absorption of P3HT at 450–600 nm. This corresponds to aggregated P3HT in *o*-xylene, as discussed in section 7.3. The excess polymer components are much more significant in these maps than in those from the samples prepared using the PFO step. It is concluded that the PFO synthesis route not only selects a narrow distribution of semiconducting tubes of the (7,5) chirality, but also yields more purified products than the direct dispersion pathways.

7.5 Atomic Force Microscopy Images

Fig. 7.6 (a) shows an AFM image of a purified [P3HT-(7,5)] nanohybrid acquired by Jack Alexander-Webber (Physics Department, University of Oxford). The sample was prepared on a quartz substrate by spin-coating at 1000 rpm from an *o*-xylene solution, which had been briefly tip sonicated to break up any nanotube bundles. The tubes are several microns long and thus the length had been preserved and not shortened by the sonication processes. The height analysis shows that the structures are ∼1.7 nm, consistent with the diameter of

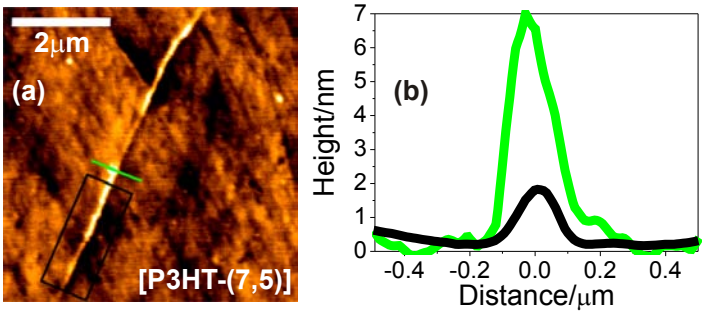

Figure 7.6: (a) AFM image of a [P3HT-(7,5)] nanohybrid. (b) Height analyses across a typical segment of the tube (black) and a nanocrystal (green).

a (7,5) nanotube (∼0.8 nm) and a monolayer polymer coating at a distance of twice the van der Waals radius of carbon (0.34 nm) from the tube. In addition, nanocrystals of P3HT of heights up to 10 nm are observed, which are likely to give rise to the trace polymer emission seen in PLE maps. These results are consistent with those reported previously for P3HT-coated tubes [187] (Chapters 5 and 6) and it is concluded that the tube dimensions had been preserved and a monolayer coating of P3HT achieved using this new processing technique to select predominantly (7,5) tubes.

7.6 Additional Remarks

In Chapter 6, it was shown that F8BT that is bound to nanotubes can be displaced by P3HT, but not vice versa. Here, it was shown that both polymers can readily displace PFO. The displacement of PFO has also been reported elsewhere for a polymer similar to F8BT, namely poly(9,9'-dioctylfluorene-*co*-bithiophene) (F8T2) [201]. Therefore, a heirarchy of binding ability emerges (PFO $<$ F8T2 $\sim$ F8BT $<$ P3HT), which appears to correlate inversely with tube selectivity. This is because the selectivity mechanism of PFO exploits the poor binding of the polymer to all tubes apart from a narrow distribution of species, such as (7,5), to which it binds marginally. By contrast, P3HT binds strongly and efficiently to all tubes and therefore shows little selectivity. The processing techniques described here are applicable to any polymer able to displace the highly selective but weakly binding PFO, suggesting that a large majority of π-conjugated polymers will be able to be used. Further study would be

required to quantify the binding constants and extend the series to more polymer structures.

P3HT forms a type-II heterojunction with small-diameter nanotubes such as the (7,5) species. PFO is able to selectively disperse (7,5) tubes but its large bandgap and resulting type-I heterojunction with nanotubes prohibit its effective use in OPV devices. This work has exploited these two important results to selectively make type-II heterojunctions using simple solution processing techniques, providing a significant advance towards the incorporation of nanotubes into optoelectronic applications.

7.7 Conclusion

This chapter reported on the synthesis of highly purified nanohybrids consisting entirely of semiconducting pristine nanotubes, predominantly of the (7,5) chirality, dispersed with either P3HT, F8BT or PFO polymer. The preparation route involved exploiting the high selectivity of PFO for semiconducting (7,5) nanotubes and then displacement of PFO with either P3HT or F8BT polymers. Absorption and photoluminescence spectroscopy were used to verify that the desired polymer coated the nanotubes and that the PFO could be entirely removed. Atomic force microscopy was also used to verify that the tubes were coated with just a monolayer of polymer and that the tubes retained their intrinsic dimensions. The method could be extended to other polymers, allowing dispersion of a narrow distribution of semiconducting nanotubes using desired polymers. The process is scalable and the products can be dissolved in any solvent to any desired concentration, making it particularly suitable for preparing the highly purified samples required for optoelectronic applications.

Chapter 8

Electronic and Mechanical Modification of Single-Walled Carbon Nanotubes by Binding to Porphyrin Oligomers

The work in this chapter has been reproduced in part with permission from:

S. D. Stranks, J. K. Sprafke, H. L. Anderson and R. J. Nicholas. Electronic and mechanical modification of single-walled carbon nanotubes by binding to porphyrin oligomers. *ACS Nano*, **5**:2307-2315, 2011. [239] Copyright 2011 American Chemical Society.

J. K. Sprafke, S. D. Stranks, J. H. Warner, R. J. Nicholas and H. L. Anderson. Noncovalent binding of carbon nanotubes by porphyrin oligomers. *Angewandte Chemie International Edition*, **50**:2313–2316, 2011. [243]

8.1 Introduction and Background

Porphyrins are a class of macrocyclic organic compound comprised of four interconnected pyrrole subunits often coordinating to a metal centre. They are found in many important biological systems such as the heme group, the pigment in red blood cells responsible for

transporting oxygen around the body. Porphyrins and porphyrinoids are also nature's light-harvesting system, and they are the primary chromophores in photosynthesis [252]. They have also been proposed as light-harvesting components in OPV devices.

While the individual porphyrin macrocycles are aromatic and hence highly conjugated structures, the conjugation length can be increased further by linking several monomer units together to form oligomers, such as those shown in Fig. 8.1. This leads to strong absorption bands in both the visible and near-infrared regions, making them particularly effective at capturing a broad range of the solar spectrum. Conjugated porphyrin oligomers also demonstrate high intra-chain hole mobilities of 0.1 $cm^2V^{-1}s^{-1}$ (measured at microwave frequencies) [253, 254], comparable to the highest mobility semiconducting polymers such as P3HT [112]. Furthermore, planarised porphyrin oligomers exhibit an order of magnitude increase in intra-chain mobility, reaching values of 1 $cm^2V^{-1}s^{-1}$.

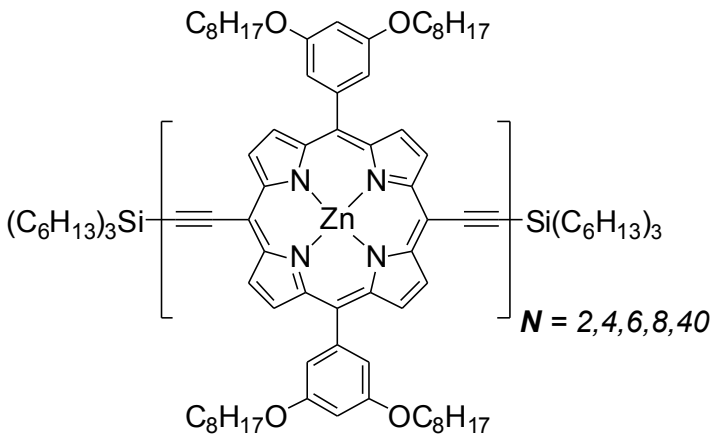

Figure 8.1: The chemical structure of the family of porphyrin oligomers **P*N*** used in this work.

Porphyrins bind strongly to SWNTs due to significant π-π-stacking between the aromatic, planar porphyrin groups and the π-conjugated nanotube surfaces [255]. To date, most work has concentrated on monomeric porphyrins binding to nanotubes. Casey *et al.* [256] observed a very efficient energy transfer process between a monomeric porphyrin unit and a SWNT to which it is bound and they proposed a Dexter transfer mechanism. Roquelet *et al.* developed a novel method to disperse these porphyrin-nanotube complexes in individual micelles [257] and also observed a very efficient energy transfer process [258] with transfer

quantum efficiencies approaching unity [259]. Recently, the same group investigated the dynamics of the interaction with a sub-picosecond time-resolution and observed energy transfer times on similar scales to those observed for charge transfer in the [P3HT-NT] complexes described in Chapter 5 [204]. They also proposed a Dexter energy transfer process in the porphyrin-SWNT system but highlighted the possibility of a shared mechanism with [P3HT-NT] complexes due to the similar dynamics. Long-lived charge separation has been reported in supramolecular SWNT complexes with porphyrin-like groups [260, 261, 262, 263] but the type-I heterojunction between these materials suggests significant energy transfer processes would still compete and perhaps dominate. Finally, Li *et al.* [264] synthesised a porphyrin monomer that could selectively bind to semiconducting SWNTs and exclude metallic tubes.

Monomeric porphyrins are less efficient at harvesting the solar spectrum and have less scope for charge transport than oligomeric porphyrins. Only a few studies have investigated the binding of oligomeric porphyrins to SWNTs [255, 265] partly due to the greater difficulty of oligomer synthesis. A planarisation of the oligomers on the SWNTs has been observed but no report has been given to excitation transfer between the species. Furthermore, there has been no thorough investigation of the electronic interaction with the carbon nanotubes nor of the energy level alignments.

The effects of mechanical strain on the band structure of carbon nanotubes were introduced in Chapter 2. To summarise, the two families of semiconducting nanotubes ($q = \pm 1$) exhibit opposite behaviour under mechanical strain, with an increase in the E_{11} transition energy (bandgap) for $q = +1$ and a decrease in E_{11} for $q = -1$ tubes, with this behaviour reversed for E_{22} transitions [36, 40]. The changes in the optical transitions with strain have been demonstrated experimentally for hydrostatic strain [39], uniaxial strain [266, 267, 268] and combinations of the two [269], and they provide a powerful optical tool for investigating the magnitudes of the strain components [36].

In this work, the binding of porphyrin oligomers of increasing length to SWNTs was investigated. As the porphyrin oligomers increase in length in the SWNT–porphyrin hybrids, there is an unusually strong red-shift of the porphyrin $\pi - \pi^*$ absorption bands, due to

planarisation. As a result there is a transition from a type-I to a type-II heterojunction which causes an increasing red-shift of the nanotube emission energies. These observations are consistent with the band levels calculated from theory and experiment and show that SWNT–porphyrin oligomer blends would be excellent candidates for use in OPV devices. The porphyrin-SWNT interaction is so strong that it induces mechanical strain in the nanotubes. This changes their bandgaps and can be fitted to experimental and theoretical strain models to give a direct measurement of the resulting strain energy. The significant interaction is consistent with the extremely high binding constants obtained from photoluminescence and absorption titrations.

8.2 Sample Preparation

The sample preparation was carried out by Johannes K Sprafke (Chemistry Department, University of Oxford). The porphyrin oligomers, namely the dimer **P2** [270], tetramer **P4** [270], hexamer **P6** [271], octamer **P8** [272] and polymer **P*N*** ($N \sim 40$) [253], were synthesised according to published procedures and their structures are shown in Fig. 8.1. The monomer **P1** does not solubilise SWNTs under these conditions and hence results are not shown for these complexes. Carbon nanotubes with either predominantly smaller diameter (SG65 CoMoCAT; SWeNT) or larger diameter (Purified HiPCO; CNI) nanotubes were purchased and both types were used without further treatment.

In a typical experiment, 2 mg of porphyrin and 1 mg of SWNT were sonicated for 1 hour in 4 mL of tetrahydrofuran (THF) using a Branson 1510E-MT sonicator bath (80 W, 40 kHz) cooled with ice. The resulting dark solution was centrifuged for 1.5 hours at 4800 rpm and passed over glass wool to remove insoluble carbonaceous residues. The porphyrin–nanotube complex was isolated using a microfilter (nylon, pore size 200 nm) and then washed with THF until the excess porphyrin was removed and the filtrate was colourless. To redisperse the nanotubes in solvent, the nylon membrane with the nanotube film was sonicated for a few seconds in 2 mL THF using an ultrasonic bath. Generally, HiPCO solutions were

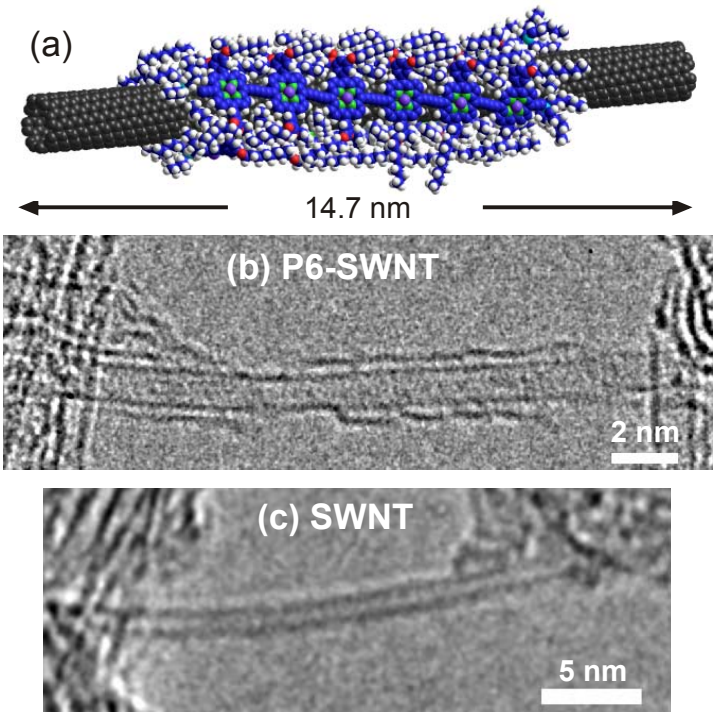

Figure 8.2: (a) Optimised molecular mechanics structure containing three **P6** units bound to a length of (8,6) SWNT based on the mass ratio calculated in Section 8.7. HRTEM images of a **P6**-SWNT complex (b) and a HiPCO SWNT sample containing no porphyrin (c). Figures adapted from Refs [243] and [273].

more stable than CoMoCAT solutions while **P*N***-CoMoCAT solutions and all **P2** solutions required a large excess of oligomer to prevent significant nanotube aggregation. SDBS-wrapped nanotubes in D_2O were also prepared, following the procedure in Chapter 4, to provide nanotube controls containing no porphyrin.

Fig. 8.2 (b) shows a HRTEM image of a **P6**-SWNT complex taken by Dr Jamie Warner (Materials Department, University of Oxford). The **P6** oligomer coating on the SWNT surface can be clearly identified and is notably absent in the image of a pure SWNT sample containing no porphyrin in Fig. 8.2 (c), providing direct evidence for the binding of hexameric oligomer to the SWNT walls. Time-series of images following electron beam radiation showed that the oligomers are mobile on the surface of the SWNTs (data not shown) [243].

8.3 Absorption Spectra

Fig. 8.3 (a) shows the absorption spectra of the family of oligomers **P2**–**P*N*** in THF. The two primary bands observed are the split Soret band (400–550 nm) and the Q-band (650–850 nm). With increasing oligomer length, the higher energy component of the Soret band remains unchanged while the lower energy component increases in intensity. However, no shift in either peak position is observed. The splitting and spectral shape of the Soret bands can be explained using the point-dipole exciton coupling Kasha model [274]. The x- and y-transition dipoles in each porphyrin monomer unit, where the x-direction denotes the long oligomer axis, are able to couple with those in adjacent porphyrin units in the same chain, splitting the excited state [275]. The porphyrin units can undergo torsion about the linking butadiyne groups. The lower energy component of the Soret band is due to a planarised configuration of units leading to an effective coupling of the y-components, which increases for longer oligomers. The higher energy component has contributions from both the twisted and planar forms [276] and little effect is seen with oligomer length.

The Q-band represents an averaged ensemble of the combinations of configurations of porphyrin units at various torsion angles [276]. The highest energy peaks of the Q-band correspond to orthogonal configurations with minimal coupling and hence remain unchanged with increasing oligomer length. The lowest energy Q-band contributions reflect the difference of the HOMO and LUMO levels (bandgap) and correspond to more planarised configurations. These peaks significantly red-shift with increasing oligomer length due to increasing conjugation (excitation delocalisation) along the polymer axis [275, 277].

The absorption spectra of the HiPCO–oligomer composites in the region of the bound porphyrin are shown in Fig. 8.3 (b). Some weak nanotube E_{22} peaks are also present, as can be seen from the [SDBS-NT] spectrum (dashed line). Fig. 8.3 (c) shows the lowest energy Q-band porphyrin peak positions found in (a) and (b). The free porphyrin shows the well-known red-shift of up to ∼140 meV with increasing length [224, 276]. For the NT-bound porphyrin the shifts are even larger, with a difference from free to bound polymer of up to ∼200 meV and a change with length of up to ∼300 meV from bound **P2** to the bound

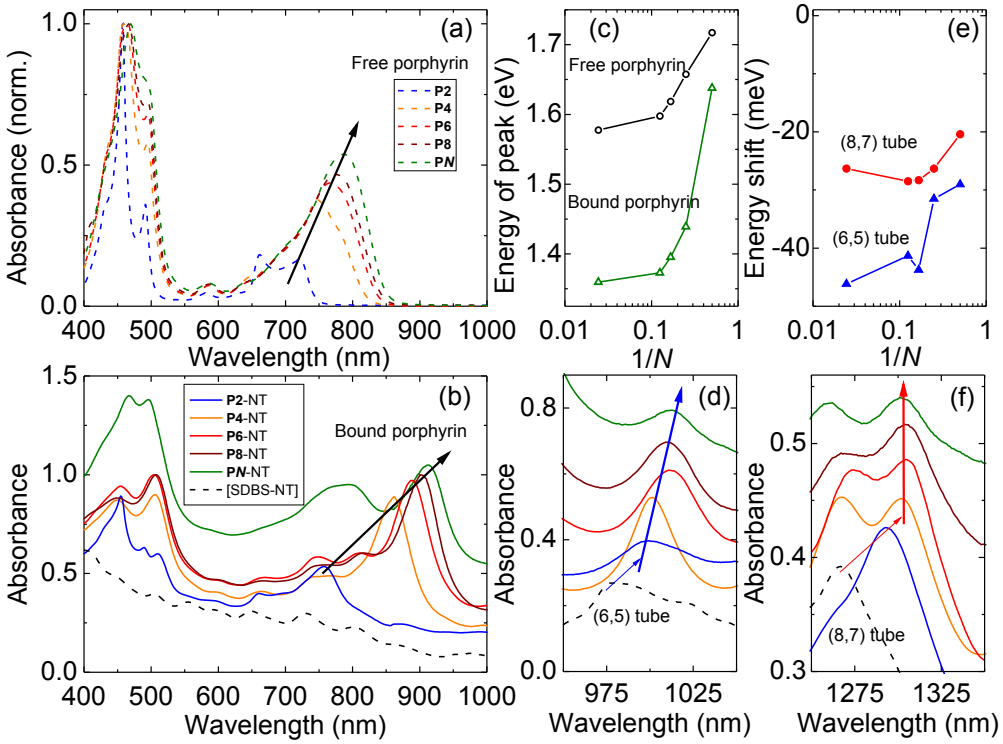

Figure 8.3: Absorption spectra of the samples under investigation, normalised and offset for clarity. (a) The family of porphyrin oligomers in THF solution. The red-shift of the Q-band with increasing oligomer length is labelled with the black arrow. (b) The porphyrin oligomers when bound to HiPCO nanotubes in THF. The black arrow again shows the red-shift of the Q-band with increasing oligomer length. The black dashed line is the SDBS–HiPCO in D_2O, clearly showing the SWNT E_{22} resonances. (c) Comparing the Q-band porphyrin peak position for the free and bound porphyrin (open circles and triangles, respectively). (d) and (f) The porphyrin–CoMoCAT and porphyrin–HiPCO composites showing the region of the (6,5) and (8,7) nanotube E_{11} transitions, respectively. The thin arrows highlight the red-shift from the relevant SDBS–SWNT peak (black dashed lines) and the bold arrows show the trend with increasing oligomer length. (e) Comparing the red-shifts for the (6,5) and (8,7) tubes relative to the SDBS samples.

polymer **P*N***. This is primarily attributed to increased conjugation along the length of the oligomer [278] owing to planarisation [255] of the porphyrin oligomers upon binding to the SWNTs. Any environmental contribution to this red-shift is estimated to be of order 20-30 meV, by comparison with the reduction in nanotube Coulomb energies [156]. A similar planarisation of monomer units was recently observed when P3HT polymers attached to nanotubes in [P3HT-NT] complexes and it has been proposed that such a planar configuration may improve charge transfer between the materials [185]. The absolute shifts are even larger than those observed in porphyrin oligomers in double-stranded ladder complexes, or

when bound to radial oligopyridine templates, where typical red-shifts relative to the free polymer are of order ∼80 meV [224, 276]. This suggests that the planarisation of porphyrins is significantly more effective when binding to nanotubes.

Fig. 8.3 (d) shows the absorption spectra of CoMoCAT–oligomer composites in the region of the small diameter (6,5) E_{11} transition. It is clear that there is a large red-shift of the (6,5) peak position relative to the SDBS–CoMoCAT sample. Importantly, the red-shift increases as the oligomer length progresses from **P2** to **P*N***. This strong oligomer length dependence is not, however, observed for larger diameter nanotubes such as (8,7), as shown in Fig. 8.3 (f) for the HiPCO–oligomer samples. The energy shifts are summarised in Fig. 8.3 (e), where the length dependence and larger red-shifts are clear for the smaller diameter (6,5) tubes.

8.4 Energy Levels

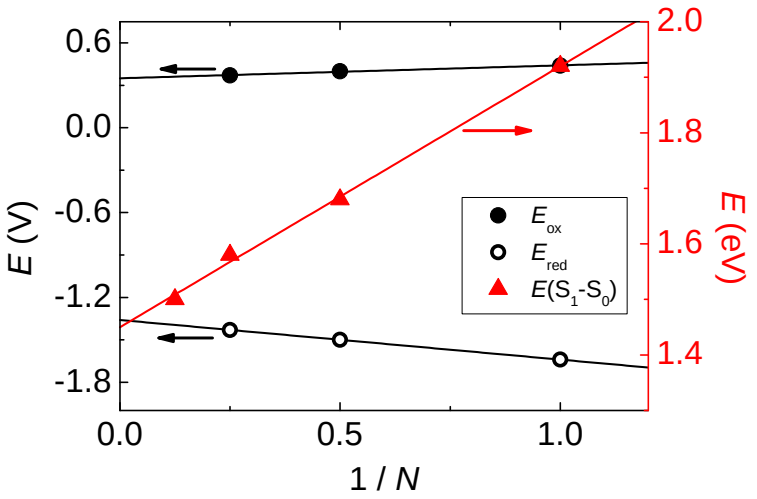

Figure 8.4: Plots of redox potentials obtained by Winters *et al.* [270], with linear fits to determine values for $N = 6$, 8 and ∞ by extrapolation. Singlet energies $E(S_1\text{-}S_0)$ were taken from Kuimova *et al.* [279] and linear fits were used to calculate values for $N = 6$ and $N = \infty$ by extrapolation and interpolation, respectively.

The results described above demonstrate a strong perturbation of both SWNT and porphyrin energy levels in the composites. The findings can be understood by comparing the HOMO and LUMO levels of each bound oligomer with the valence (VB) and conduction

bands (CB) of the nanotubes. Nanotube energy levels were obtained using the method described in Chapter 4 [156]. HOMO and LUMO levels of the free oligomers were calculated by Prof. Harry Anderson (Chemistry Department, University of Oxford) as follows. Oxidation E_{ox} and reduction E_{red} potential values were taken from cyclic voltammetry data measured by Winters *et al.* [270] for **P1**, **P2** and **P4** in THF containing 0.1 M tetrabutylammonium tetrafluoroborate. These values are plotted in Fig. 8.4 and values for **P6**, **P8** and $\mathbf{P}\boldsymbol{N}$ ($\boldsymbol{N} = \infty$) were determined by extrapolation. The HOMO and LUMO levels of the porphyrins, E_{HOMO} and E_{LUMO}, were calculated by using the following empirical equations from D'Andrade *et al.* [280]:

$$E_{\mathrm{HOMO}} = -1.4E_{\mathrm{ox}} - 4.6\,\mathrm{eV} \tag{8.1}$$

$$E_{\mathrm{LUMO}} = E_{\mathrm{HOMO}} + (E_{\mathrm{ox}} - E_{\mathrm{red}}). \tag{8.2}$$

Singlet transition values $E(\mathrm{S_1}\text{-}\mathrm{S_0})$ were measured by Kuimova *et al.* [279] in toluene containing 1 % pyridine. These values are also plotted in Fig. 8.4, allowing values for **P6** and $\mathbf{P}\boldsymbol{N}$ to be obtained by interpolation and extrapolation, respectively. The differences between the HOMO-LUMO gaps and these values were taken as the exciton binding energies (∼220–260 meV). The HOMO and LUMO levels were then adjusted evenly to subtract this binding energy and give an accurate approximation to the true free polymer energy levels. Finally, the red-shift observed upon binding to nanotubes (∼200 meV; ∼80 meV for **P2**) was accounted for by subtracting evenly from the HOMO and LUMO levels, giving a reasonable approximation to the bound porphyrin oligomer levels.

The bound oligomer HOMO and LUMO levels and nanotube VB and CB are shown in Fig. 8.5. It is clear that, for the smaller diameter tubes (<0.9 nm), a type-II heterojunction is expected to form between all porphyrin oligomers longer than **P2** and the SWNTs. The band overlap becomes larger for longer oligomers and it follows that effects resulting from this type-II interface will be most pronounced for the smallest tubes and the longest oligomers.

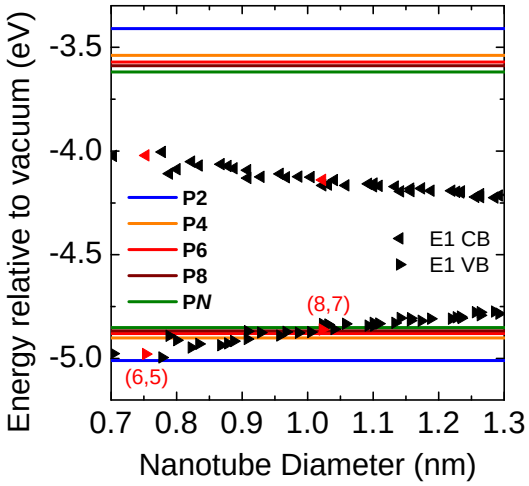

Figure 8.5: Horizontal lines represent HOMO and LUMO levels of the porphyrin oligomers, with values calculated as discussed in the text. The right and left triangles show the SWNT valence and conduction bands, respectively, plotted as a function of nanotube diameter. The (6,5) and (8,7) tubes are labelled in red for comparison.

This staggered alignment is similar to that at a P3HT–SWNT interface (Chapter 4) and, therefore, one would expect a similar diameter dependence of the SWNT red-shifts to those observed by Schuettfort *et al.* [156]. The NT red-shifts described in section 8.3 are attributed to a charge-transfer interaction where the wavefunction of a hole on the nanotube extends onto the porphyrin oligomer owing to their staggered band alignments, influencing the final exciton transition energy. This acts to raise the effective energy level of the hole and leads to a red-shift of the recombining nanotube exciton. This is only possible for a type-II heterojunction and the effect is more significant for larger bandgap (*i.e.* smaller diameter) tubes where the offset between the oligomer HOMO and SWNT VB is larger. A further consequence of this is that the charge transfer may also be contributing to the red-shift of the porphyrin oligomers, in which case this will primarily influence the HOMO level and lead to an even more pronounced type-II alignment.

8.5 PLE Measurements

In order to carry out a more quantitative analysis, PLE maps of the solutions were taken. Fig. 8.6 (a) and (c) show the SDBS–SWNT maps for the smaller diameter CoMoCAT and

larger diameter HiPCO materials, respectively, and the corresponding maps with the **P6** oligomer are shown in Fig. 8.6 (b) and (d), respectively. The peak positions were deduced from the maps by fitting with Lorentzian curves [156] and care was taken to account for any excess porphyrin emission tail, while the SDBS–SWNT peaks were labelled according to the values and assignments reported by Weisman and Bachilo [44]. The horizontal scales for the porphyrin maps are transposed by 50 nm to allow the family behaviour to be compared, as a result of the large red-shift of the nanotube transitions upon binding with the porphyrin.

In addition, non-selective nanotube emission is observed upon excitation of the porphyrin in either the Soret (∼500 nm) or Q-bands (∼850–900 nm, dashed white lines). This corresponds to energy transfer from the porphyrin to the nanotube and has been seen in other nanotube-porphyrin systems [256, 258, 259]. Using the CoMoCAT distribution, the energy transfer efficiency to the (6,5) tubes was estimated to be ∼30% by comparing the (6,5) tube emission intensity (at 1015 nm) from direct excitation in the E_{22} (588 nm) with that arising from excitation in the **P6** oligomer (890 nm), while also accounting for the absorption components of each [243]. Finally, the emission intensity of each tube, when weighted with tube absorption, is greater for the larger chiral angle tubes and the $q = -1$ family due to the dependence of PL quantum efficiencies on chirality and family [86, 87].

SWNT–porphyrin maps with **P2** and **P4** are presented in Fig. 8.7 and those with **P8** and **P*N*** are shown in Fig. 8.8 and similar phenomena to the **P6** maps are observed. The **P2**–CoMoCAT and both **P*N*** maps are dominated by emission from the excess porphyrin, which is required for stability, due to its higher quantum efficiency [271]. Nevertheless, significant energy transfer peaks are observed in the **P*N***–HiPCO map, indicating that all oligomers are able to disperse SWNTs. The energy transfer efficiencies from **P4** and **P8** to (6,5) tubes were also estimated to be in the range 20-30%, but there was too much spectral overlap to provide an estimate from **P2** and **P*N*** oligomers. **P4** and **P6**–SWNT maps show the most well-resolved peaks, indicating the most efficient dispersions.

The emission from porphyrin oligomers is also quenched when bound to SWNTs. The observed porphyrin emission in the PLE maps, as indicated by black arrows, arises only

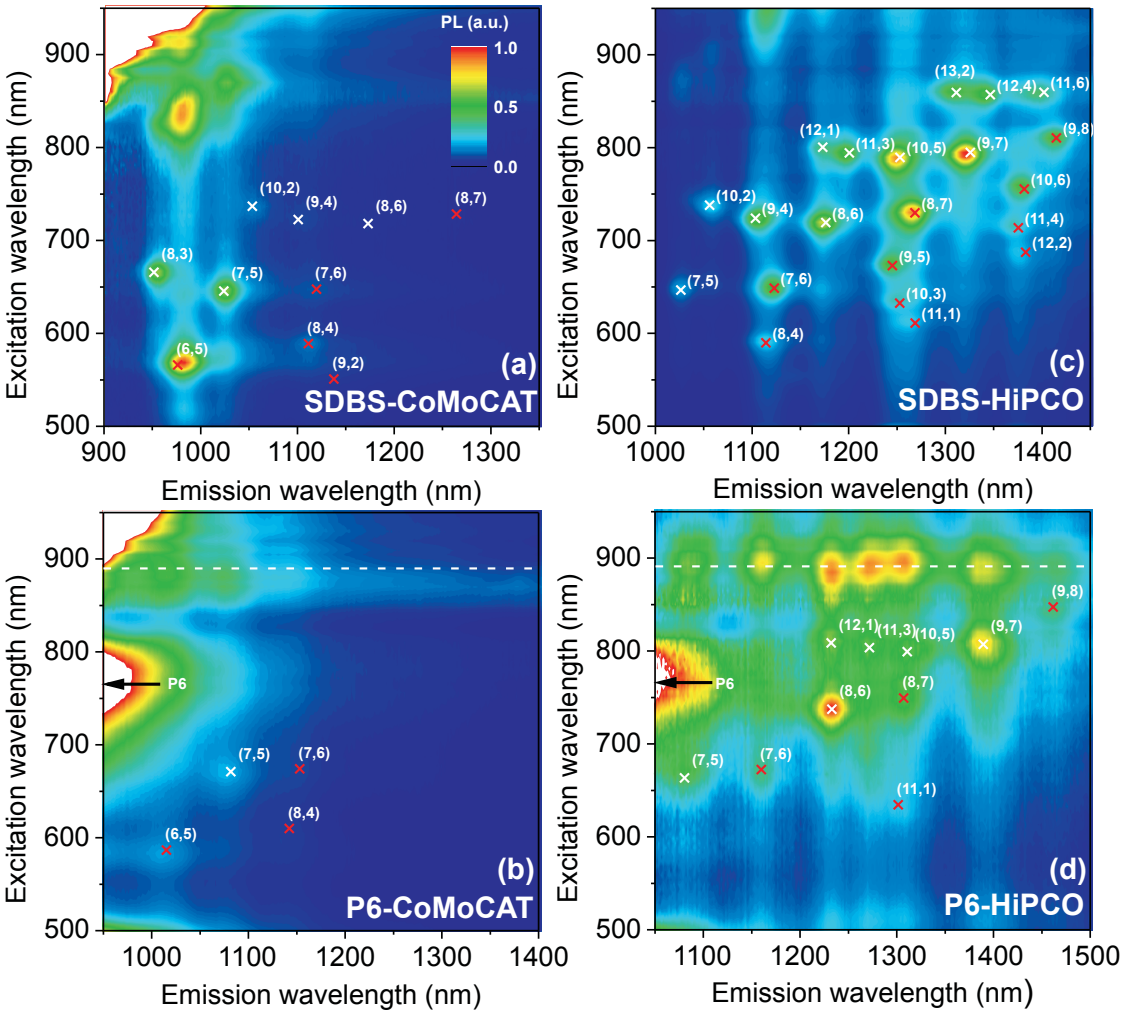

Figure 8.6: PLE maps of (a) SDBS–CoMoCAT in D_2O, (b) **P6**–CoMoCAT in THF, (c) SDBS–HiPCO in D_2O, and (d) **P6**–HiPCO in THF. Dashed white lines indicate energy transfer bands. To emphasise the red-shifts, THF solution abscissa in (b) and (d) are transposed by 50 nm and the emission tails corresponding to excess porphyrin in these maps are labelled with black arrows. Transition wavelengths for type +1 (−1) nanotubes are labelled with red (white) crosses. Cross-peaks appear in the corners of (a) and (d) from the excitation source.

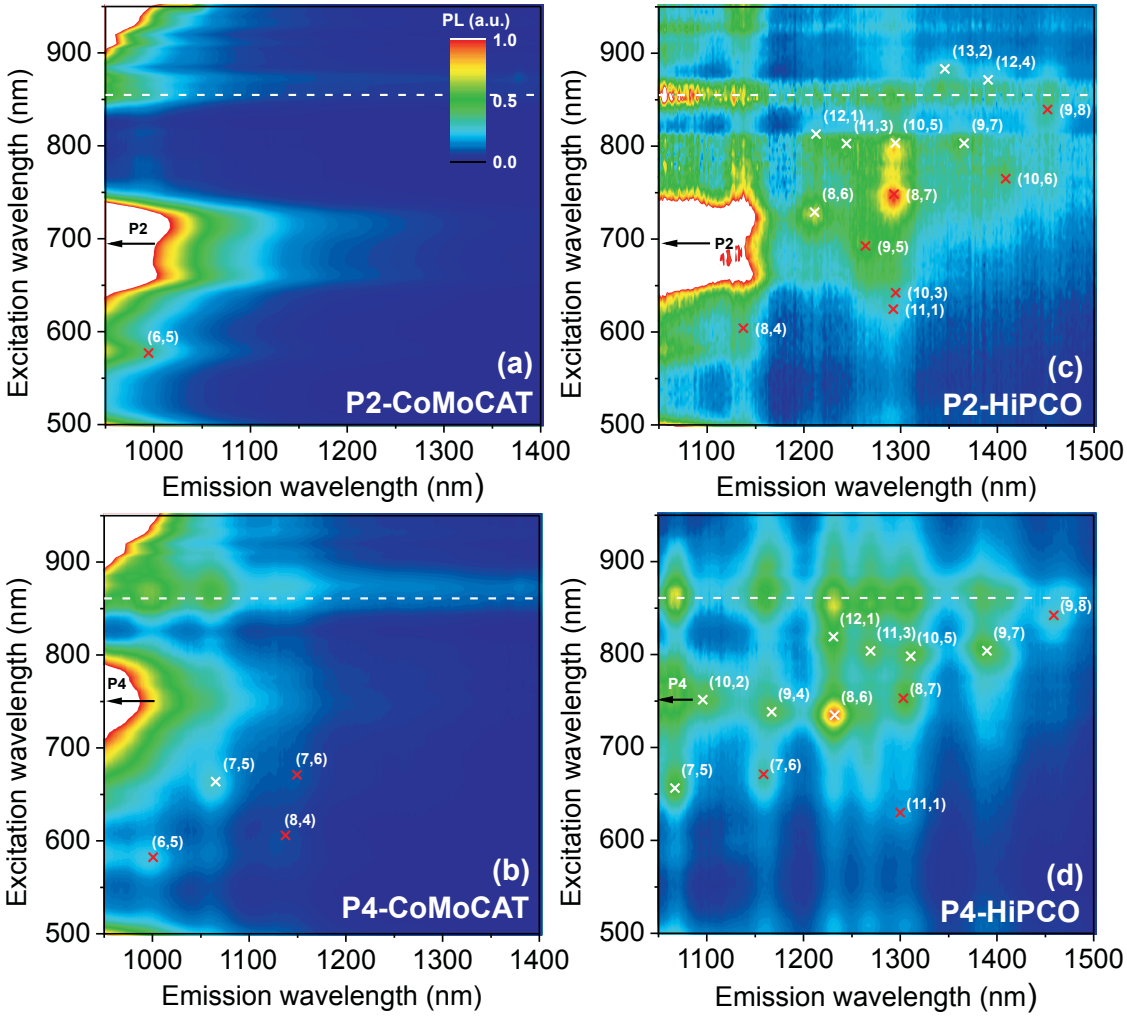

Figure 8.7: PLE maps of (a) **P2**–CoMoCAT, (b) **P4**–CoMoCAT, (c) **P2**–HiPCO, (d) **P4**–HiPCO in THF solution. White dashed lines indicate energy transfer bands. Emission tails corresponding to excess porphyrin are labelled with black arrows. Transition wavelengths for type +1 (−1) nanotubes are labelled with red (white) crosses. Cross-peaks appear in the corners of (a) and (b) from the excitation sources.

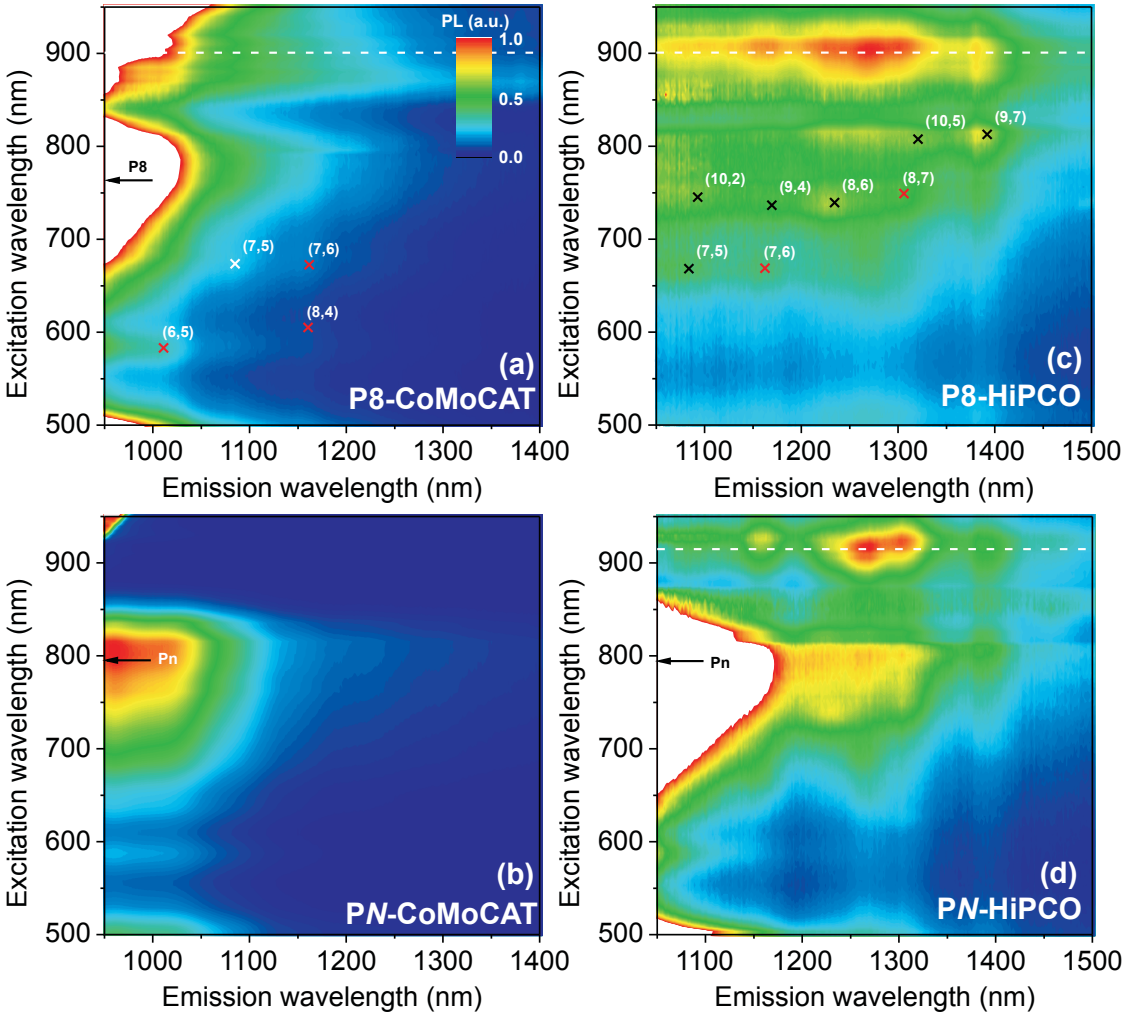

Figure 8.8: PLE maps of (a) **P8**–CoMoCAT, (b) **P*N***–CoMoCAT, (c) **P8**–HiPCO, (d) **P*N***–HiPCO in THF solution. White dashed lines indicate energy transfer bands. Emission tails corresponding to excess porphyrin are labelled with black arrows. Transition wavelengths for type +1 (−1) nanotubes are labelled with red (white) crosses. Cross-peaks appear in the corners of (a) and (b) from the excitation source. The **P*N*** maps are dominated by excess polymer emission and nanotube peaks cannot be extracted. However, the characteristic energy transfer bands appear at ∼915 nm and ∼500 nm, indicating an effective dispersion process.

from traces of unbound oligomers [243]. Despite the efficient quenching of the oligomer emission, the energy transfer efficiencies of 20-30% are significantly lower than the near unity transfer quantum efficiencies observed elsewhere for monomeric porphyrins [259]. The presence of a type-II heterojunction between the two materials, as described later in this chapter, shows that significant charge transfer between the materials may be a competing process to energy transfer. The yield of free charge generation is likely to be significantly higher than reported in other SWNT–porphyrin based supramolecular systems with type-I heterojunction interfaces [260, 261, 262, 263].

8.6 Quantifying Red-Shifts

In order to quantify the red-shifts from the PLE maps, a similar analysis to Schuettfort *et al.* [156] (described in Chapter 4) was carried out, where the red-shifts were given relative to the values fitted by Weisman and Bachilo [44] for SDS–SWNT species such that:

$$\Delta E_{ii} = E_{ii} - E_{ii}^{\text{Weisman}}. \tag{8.3}$$

Fig. 8.9 shows the SWNT red-shifts in both E_{11} and E_{22} for the porphyrin–SWNT composites. It is clear from these plots that there is an increasing mean red-shift as the oligomer is increased from **P2** to **P8** and the two semiconducting NT families ($q = \pm 1$) exhibit significantly different behaviour. For $q = +1$ tubes, the red-shifts in E_{22} exceed the shifts in E_{11}, but the opposite behaviour is observed for $q = -1$ tubes. In addition this difference becomes larger as the chiral angle becomes smaller ($n \gg m$). This behaviour is consistent with the presence of a large contribution from mechanical strain effects, as introduced in Chapter 2 and described below. The analysis could not be carried out for the polymer **P*N*** because the free polymer emission was red-shifted far enough to mask the nanotube E_{11} transitions in the PLE maps. It is also noted that the E_{11} emission energies agree well with the values observed for E_{11} in absorption, indicating that no significant Stokes shifts due to exciton localisation are present.

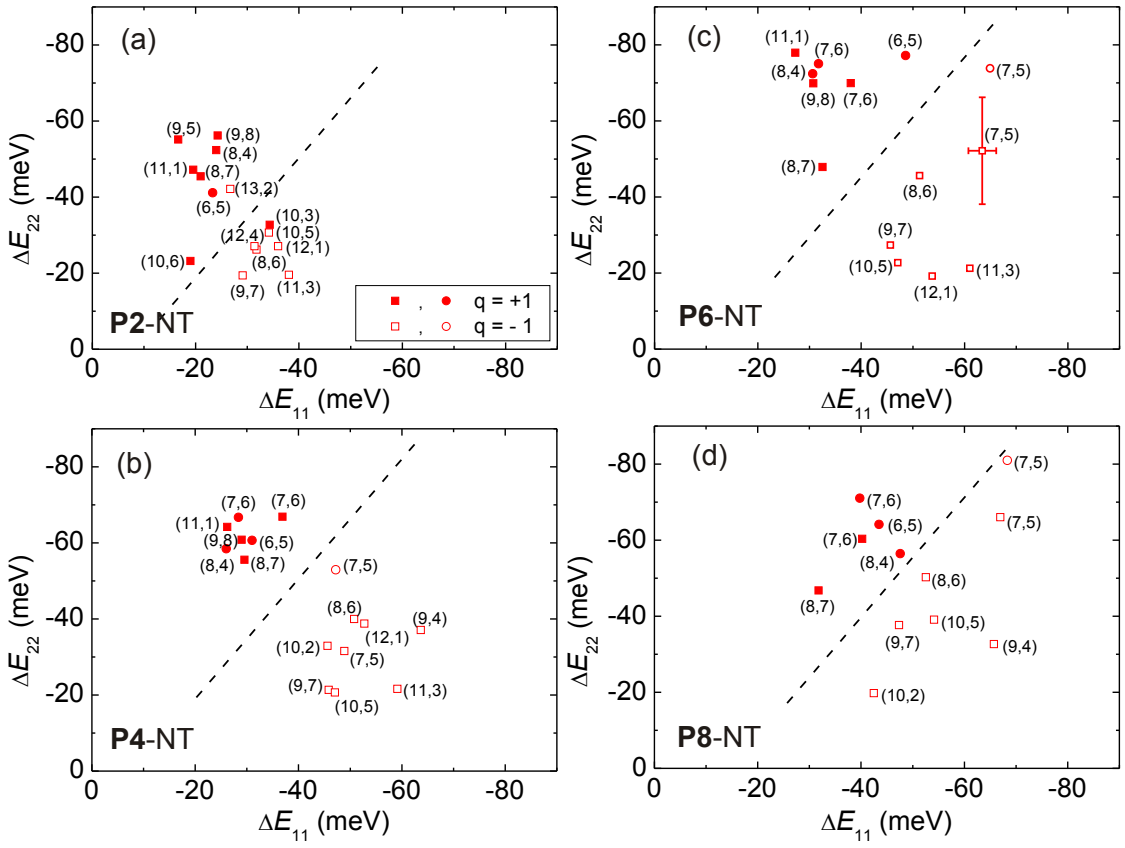

Figure 8.9: Red-shifts in E_{11} and E_{22} transitions, relative to the Weisman and Bachilo values [44], as determined from PLE maps of (a) **P2**–SWNT, (b) **P4**–SWNT, (c) **P6**–SWNT and (d) **P8**–SWNT composites. The dashed lines are guides to the eye to highlight the different behaviour of each family. Circular symbol points are obtained from the CoMoCAT maps, square symbols from the HiPCO maps. A representative error bar is shown in (c), estimated from the instrument resolution and errors in peak fitting.

The very close type-II alignment deduced from Fig. 8.5 resembles that observed by Schuettfort *et al.* for [P3HT-NT] composites [156]. As such, one should expect a similar diameter dependence of the red-shift. This was shown to be qualitatively true from absorption measurements (Fig. 8.3) but the red-shifts obtained from PLE maps (Figs 8.6–8.8) show that strain needs to be included in addition to any electronic effects from the type-II alignment and the environment. Therefore, the two contributions to the total red-shift on a given transition, ΔE_{ii}, are written as:

$$\Delta E_{ii} = \Delta E_{\text{electronic}} + \Delta E_{\text{strain}}, \tag{8.4}$$

where $\Delta E_{\text{electronic}}$ is the red-shift contribution from the polymer and environment which has previously been shown to be the same for E_{11} and E_{22} to within experimental error [156]. The environment component of $\Delta E_{\text{electronic}}$ (*e.g.* dielectric or solvent effects) is of order 20-30 meV and almost independent of oligomer length and nanotube diameter [156], as explained in Chapter 4. The contribution ΔE_{strain} is the red-shift induced by mechanical strain on the nanotubes (positive about $\Delta E_{\text{electronic}}$ for $q = +1, i = 1$ and $q = -1, i = 2$; negative for $q = -1, i = 1$ and $q = +1, i = 2$). Since the strain contributions to the E_{11} and E_{22} red-shifts are of opposite signs and are close to equal magnitude, the $\Delta E_{\text{electronic}}$ component was taken as $(\Delta E_{11} + \Delta E_{22})/2$ using the data shown in Fig. 8.9. The ΔE_{strain} component was then given by half of the difference of the E_{11} and E_{22} shifts.

8.6.1 Electronic Component of Red-Shifts

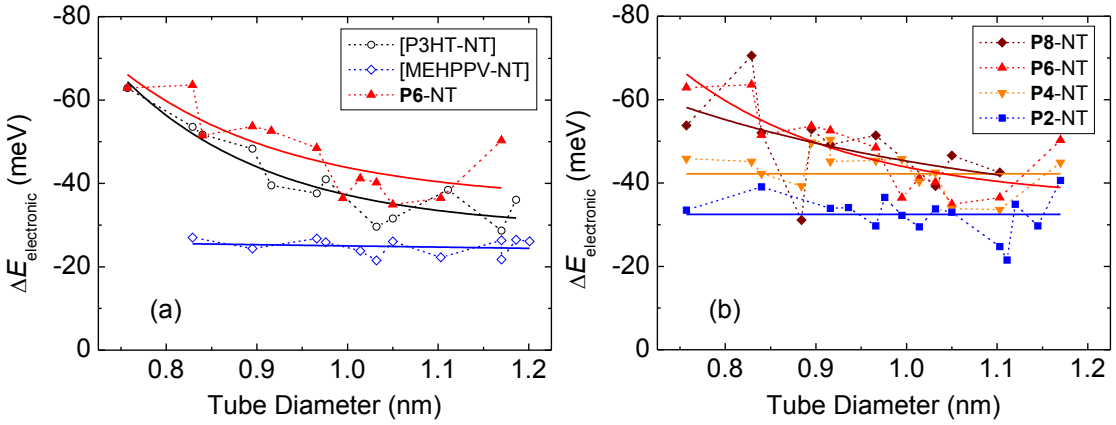

Figure 8.10: (a) $\Delta E_{\text{electronic}}$ components of SWNT red-shifts, when in composites with **P6**, P3HT and MEHPPV, as a function of nanotube diameter. P3HT and MEHPPV data were taken from Schuettfort *et al.* [156]. (b) Comparing $\Delta E_{\text{electronic}}$ components for the series of oligomers investigated in this study. In both (a) and (b), solid lines are fitted exponential decays to act as guides to the eye.

The $\Delta E_{\text{electronic}}$ components of the SWNT red-shifts are plotted as a function of diameter in Fig. 8.10 (a) for the **P6** oligomer. A clear diameter dependence is observed, with a monotonically increasing red-shift as the SWNT diameter is decreased. The trend of the red-shifts is similar to the data for P3HT–SWNT composites found by Schuettfort *et al.* [156], which are also plotted in Fig. 8.10 (a), and the magnitudes are slightly larger. For further

comparison, data taken using a polymer with a known type-I alignment with all SWNT species (MEHPPV) is also plotted and clearly exhibits much smaller shifts and no diameter dependence, as expected. Furthermore, no diameter dependence was observed for any other type-I polymers investigated, namely PFO (Chapter 4), poly(9,9'-dioctylfluorene-*co*-bis-*N,N'*-(4-butylphenyl)-bis-*N,N'*-phenyl-1,4-phenylenediamine) (PFB) and poly(indenofluorene) (PIF) [156] (data not shown), where all the red-shifts can be accounted for by simple dielectric effects in the polymer which reduce the magnitude of the Coulomb interactions [189]. Finally, no strain effects were observed for SWNT composites with any polymer investigated here, as discussed in section 8.6.2. As such, all red-shifts observed for these polymers are electronic effects alone, however data are plotted as $(\Delta E_{11} + \Delta E_{22})/2$ to allow direct comparison with the SWNT–porphyrin data.

Fig. 8.10 (b) shows the $\Delta E_{\text{electronic}}$ components as a function of SWNT diameter for the family of oligomers **P2**–**P8**. The shifts increase with oligomer length and develop a strong diameter dependence for **P6** and **P8**, perhaps an intermediate dependence for **P4** and a negligible dependence for **P2**. This is entirely consistent with the band alignments and interpretation presented in Fig. 8.5, where a clear type-II heterojunction is established only for the longest oligomers and smallest diameter SWNTs. For **P2**–SWNT composites the behaviour suggests a type-I interface occurs where the hole remains confined entirely within the nanotube and consequently the red-shifts are smaller and almost constant. This leads to the conclusion that a type-II heterojunction exists between the longer porphyrin oligomers and smaller diameter nanotubes and this combination provides promise for use in OPV devices.

8.6.2 Strain Component of Red-Shifts

The strain contribution to the red-shifts, ΔE_{strain}, deduced from Eq. 8.4, is now considered and the results are shown in Fig. 8.11. The theory introduced in Chapter 2 predicts the nanotube bandgap change under small strains to be:

$$\Delta E_{\text{strain}} = (\Delta E_{11} - \Delta E_{22})/2 = (\frac{2\gamma_0 a_{C-C}}{d})(\epsilon_\perp - \nu\epsilon_\parallel) + 3(-1)^{q+1}\gamma_0[(1+\nu)\epsilon_\parallel \cos 3\theta + \epsilon_\perp \sin 3\theta], \tag{8.5}$$

where γ_0 and a_{C-C} are the transfer integral and bond length, respectively, d is the nanotube diameter, ν is Poisson's ratio and θ is the chiral angle. $\epsilon_\parallel$ and $\epsilon_\perp$ are the strains along the tube axis (uniaxial) and circumference (torsional), respectively, and were used as fitting parameters. The fits used values of $\gamma_0 = 3.0\,\text{eV}$, $a_{C-C} = 1.432\,\text{Å}$, and $\nu = 0.20$, with d in the range 0.7–1.2 nm [269]. The solid lines in Fig. 8.11 (a)–(d) show fits to this equation for $q = \pm 1$ families with each oligomer, yielding values of $\epsilon_\parallel = 0.19 \pm 0.07\%$ and $\epsilon_\perp = 0.06 \pm 0.03\%$ with **P6**. Fig. 8.11 (e) shows the two components of SWNT strain obtained for each oligomer. The uniaxial component is proportionately larger for the **P6** and **P8** oligomers, perhaps consistent with the increasing oligomer length which binds along the same axis.

These values are comparable to those found in dried polymer-NT films made from either organic [281] or aqueous solutions [269] and due to differential contraction caused by temperature variation (cooling 260 K–80 K) [269]. However, no NT strain effects have been reported or observed from other semiconducting polymer solutions such as those investigated by Schuettfort *et al.* [156], namely P3HT, MEHPPV, PFO, PIF and PFB (data not shown), demonstrating the very strong binding of the porphyrin to the nanotubes. The most energetically favourable configuration for many composites involves the polymer wrapping in a helical manner around the SWNTs [183, 184, 185, 186]. The polymers used in these studies are much longer but have smaller repeating units when compared to the porphyrin oligomers. The more rigid and larger porphyrin units exceed the nanotube diameters presented here and will tend to lie flat on the nanotube surface as they have been observed to do on gold substrates [282]. Even despite similar planar configurations [185], the larger size of the porphyrin units compared to the repeating units of the previously studied conjugated polymers will result in a significantly increased surface area for π–π interactions. These large π-π forces will lead to the mechanical strain on the nanotubes, resulting in a predominantly axial deformation of the tube.

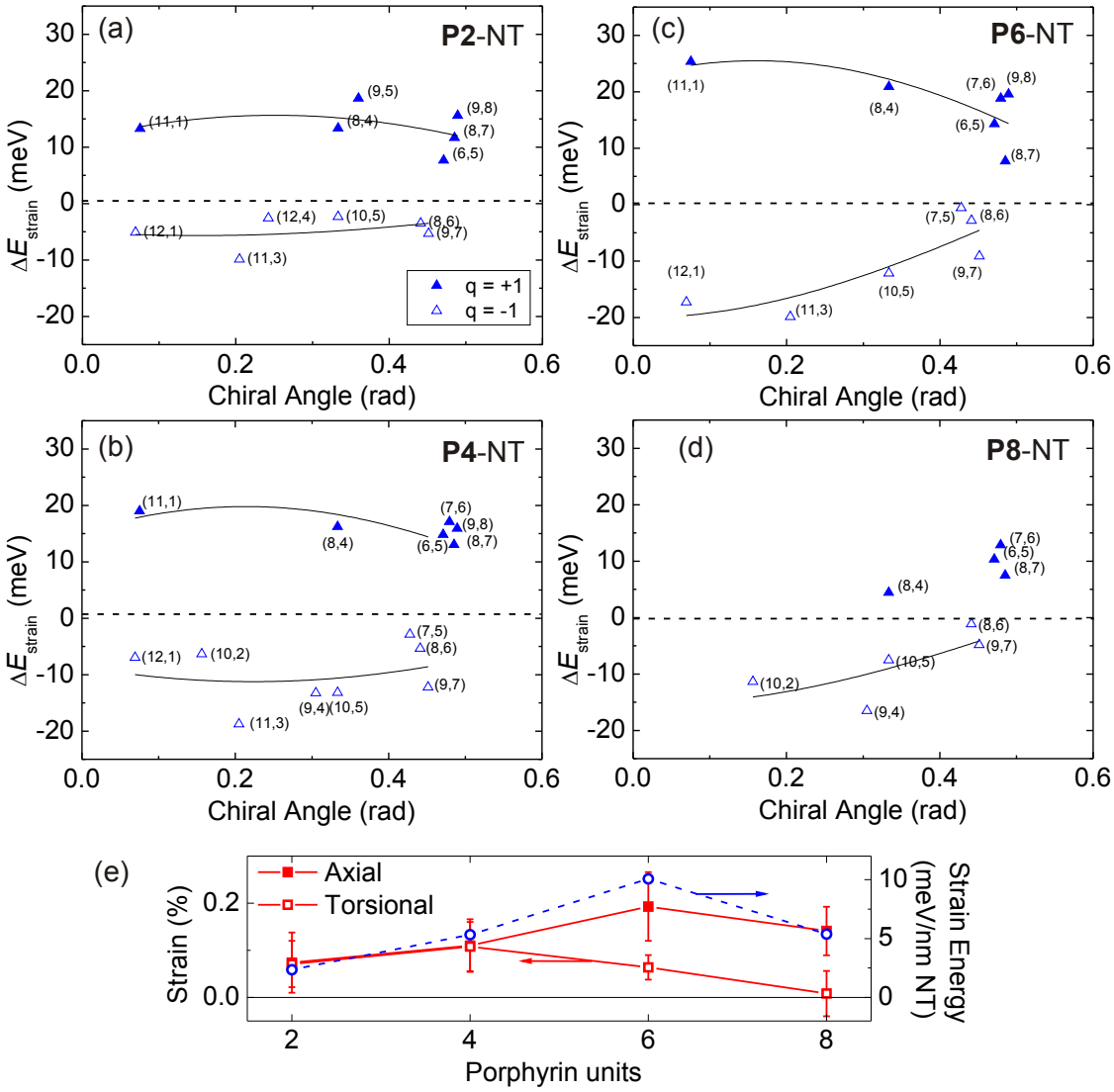

Figure 8.11: (a)-(d) Strain components of red-shifts for **P2**–SWNT, **P4**–SWNT, **P6**–SWNT and **P8**–SWNT composites, respectively. Curves show fits to the data using the Yang and Han model for small strain described in Chapter 2, with the constant term in Eq. 8.5 represented by the dashed lines. (e) Summary of the axial and torsional strain values obtained for the family of oligomers using the Yang and Han model. Points are mean values of those obtained for the $q = \pm 1$ family for each data set. The total strain energy per unit length of NT, calculated in section 8.6.3, is also displayed.

8.6.3 Calculating Strain Energy

The fits in Fig. 8.11 gave the contributions of uniaxial strain, $\epsilon_{\parallel}$, and torsional strain, $\epsilon_{\perp}$, to the strain induced on the length L of the tube, ϵ_z, and the radius R, ϵ_r. The former parameters from the Yang and Han theory [36, 40] can be related to the latter parameters in the Capaz *et al.* [38] formulation by:

$$\epsilon_z = \epsilon_{\parallel}, \quad \epsilon_r = \epsilon_{\perp}\beta - \nu\epsilon_{\parallel}, \tag{8.6}$$

where $\beta = r_{it}/r_{ic}$ is the ratio of the axial to the circumferential components of the unstrained carbon-carbon bond, which is close to unity for chiral nanotubes. These strains are related to an effective pressure, P (force per unit area), by radial and elastic constants defined as $C_r = P/\epsilon_r$ and $C_z = P/\epsilon_z$, respectively [38]. These constants are given by:

$$C_r = \frac{4YR\Delta R}{R_0(2R - \nu R_0)}, \quad C_z = \frac{4YR\Delta R}{R_0(R_0 - 2\nu R)}, \tag{8.7}$$

where $Y = 1010\,\text{GPa}$ is the Young's modulus of the nanotubes, $R_0 = R + \Delta R$ is the nanotube external radius and $\Delta R = 1.675\,\text{Å}$ is the van der Waal's "exclusion distance". With an average nanotube radius of 0.5 nm, the values $C_r = 585\,\text{GPa}$ and $C_z = 1080\,\text{GPa}$ were obtained.

The interaction energy involved in inducing the strains can be estimated by considering the work done by the porphyrin oligomers on the nanotubes. Fig. 8.12 (a) shows the cross-section of the nanotube with the porphyrin straining the tube radius R to increase by r, quantified by the radial strain $\epsilon_r = r/R$. The force involved in this interaction is given by $F = P \times \text{Area} = P \times 2\pi RL = 2\pi LC_r r$ and the work done per unit length is:

$$W/L = \int_0^r (F/L)\mathrm{d}r' = 2\pi C_r \int_0^r r'\mathrm{d}r' = \pi C_r R^2 \epsilon_r^2. \tag{8.8}$$

For **P6**–SWNT composites, the combined effect of the torsional ($\epsilon_{\perp} = 0.0006$) and axial

($\epsilon_{\|} = 0.002$) strains gives an effective *increase* in the nanotube radius given by a positive strain $\epsilon_r = 0.0002$, yielding a value of $W/L \approx 0.1$ meV per nm of nanotube. In Section 8.7, it is estimated that there is 4.9 nm of nanotube per **P6** molecule [243], giving a value of 0.05 kJ/mol of oligomer for the radial contribution.

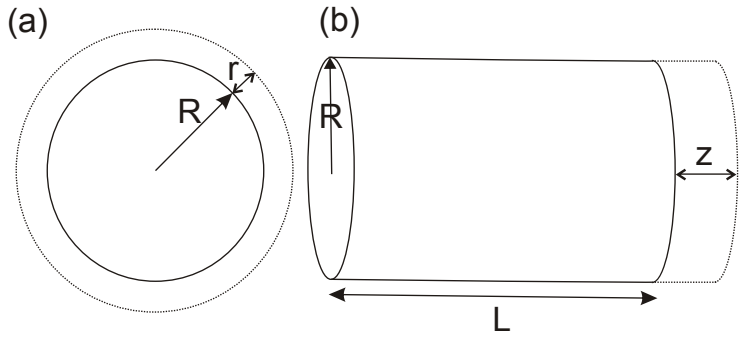

Figure 8.12: Schematic diagram showing the resulting strains induced on the nanotubes when viewed from (a) end-on (radial strain) and (b) side-on (axial strain). Parameters used in strain energy calculations are also defined.

Similarly, Fig. 8.12 (b) shows a side-on view of the tube with axial strains increasing the length L by z, quantified by the axial strain $\epsilon = z/L$. Again, the force involved is given by $F = P \times \text{Area} = P \times \pi R^2 = \pi R^2 C_z z/L$ and this is integrated to calculate the work per unit length to be:

$$W/L = \int_0^z (F/L)\mathrm{d}z' = \pi R^2 (C_z/L^2) \int_0^z z'\mathrm{d}z' = \frac{1}{2}\pi C_z R^2 \epsilon_z^2. \tag{8.9}$$

The axial calculations gave a value of ≈10 meV per nm of nanotube or 4 kJ/mol of **P6** porphyrin. It is clear that the contribution of the strain elongating the nanotube is dominant over the radial strains by an order of magnitude and, therefore, the total strain is given approximately by the axial strain. Similar calculations were performed for **P2**-SWNT, **P4**-SWNT and **P8**-SWNT composites, giving values in the range ∼2–10 meV/nm NT or ∼1–4 kJ/mol of porphyrin oligomer. The total strain energy is shown as a function of oligomer length in Fig. 8.11 (e) and is largest for **P6**, suggesting the strongest binding for this length, consistent with the lower solubility for the extremes of **P2** and **P*N*** solutions.

The dominant contribution to binding is the van der Waals interaction. For a porphyrin monomer, *meso*-5,10,15,20-tetraphenylporphyrin (TPP), and NTs this has been estimated, using density functional theory, to be ∼80 kJ/mol [283]. For the hexamer, this gives ∼500 kJ/mol and is comparable to values calculated elsewhere for polymers of similar length [284, 285, 286]. This shows that the strain energy measured in this work is only contributing to a reduction of around 1% of the total binding energy. This component cannot be isolated by other means and is an important parameter in determining the nature of the bonding interaction in these complexes. The results demonstrate both the sensitivity and power of optical measurements to determine such physical parameters.

8.7 Binding Constants

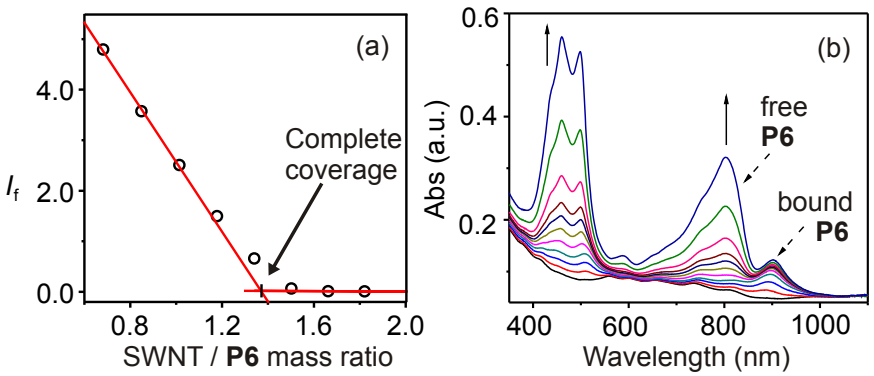

Figure 8.13: (a) Emission from free **P6** oligomer at 930 nm (I_f) with an increasing concentration of HiPCO SWNTs added to a fixed concentration of **P6** (2.1 mgL^{-1}) in THF. The arrow denotes the point at which all the porphyrin is bound to SWNTs. (b) Absorption spectra for a titration of SWNTs with increasing amounts of **P6** oligomer in dichlorobenzene. Figures adapted from Refs [243] and [273].

The quenching of the oligomer emission when bound to NTs can be exploited to determine the stoichiometry of the complexes. Johannes K Sprafke (Chemistry Department, University of Oxford) carried out experiments whereby the free **P6** emission at 920 nm was monitored as increasing amounts of SWNTs were added to a fixed **P6** concentration (2.1 mgL^{-1}) in THF and the results are shown in Fig. 8.13 (a) [243, 273]. The emission intensity was found to decrease linearly with increasing SWNT concentration up until a SWNT/**P6** mass ratio

of 1.35 when the emission is completely quenched by the SWNTs, corresponding to all of the **P6** being bound to the tubes. When isolated complexes were prepared using the preparative scales detailed in Section 8.2, a lower SWNT/**P6** mass ratio of 0.96 was found by comparing the absorption spectra of the isolated complex with that of the complex at the end point of this emission titration. The difference was attributed to a greater tube debundling at higher **P6** concentrations (500 mgL^{-1}). A mass ratio of 0.96 corresponds to 94 SWNT carbon atoms per porphyrin monomer unit such that each **P6** molecule saturates a 4.9 nm segment of an (8,6) nanotube. Johannes K Sprafke also carried out molecular mechanics simulations to show that three **P6** molecules can wrap around a 14.7 nm (3×4.9 nm) length of (8,6) tube to give an almost monolayer coverage. This is shown in the model in Fig. 8.2 (a) and is consistent with the HRTEM image in 8.2 (b).

Fig. 8.13 (b) [243, 273] shows the absorption spectra from a titration experiment carried out by Johannes K Sprafke, in which an increasing amount of **P6** oligomer was added to a fixed SWNT concentration. Dichlorobenzene was used as a solvent due its higher tube solubility than THF [169]. Initially, the oligomers bind to the tubes and a peak corresponding to the bound **P6** appears. Once the binding sites on the tubes are saturated, the peak corresponding to free **P6** rises while the bound oligomer peak remains constant. The difference in absorption values at these two peaks can be plotted and fitted to a 1:1 binding isotherm, assuming that one oligomer binds to one SWNT binding site and the binding sites act independently [243, 273] (data not shown). A binding constant of 4.7×10^7 M^{-1} was obtained for **P2** but the affinities of **P4** and **P6** were too strong to measure using these absorption or fluorescence titrations ($K > 10^9$ M^{-1}) because of sharp titration end points.

Finally, Johannes K Sprafke carried out competition experiments to investigate the relative binding affinities of **P2**–**P6** [243, 273]. Since the Q-bands of the oligomers are red-shifted with respect to each other, absorption measurements could be used to monitor the various bound and free oligomers in each solution. The results showed that an 800-fold excess of **P2** did not displace **P4** from the tube surface and even a 2500-fold excess of **P2** did not displace **P6** from the nanotubes. If **P2** was initially bound to the tubes, **P4** or **P6** displaced **P2**

but equilibirum was only reached after 24 hours. These results are qualitatively similar to those seen in Chapters 6 and 7 for binding competitions between semiconducting polymers. Finally, no displacement occurred in a competition experiment between **P4** and **P6**; the initially bound oligomer remained bound to the tube even with a large excess of the other oligomer. The competition results taken as a whole suggest that the binding of **P4** and **P6** to SWNTs is extremely strong ($K > 10^{11}$ M^{-1}), consistent with the significant interaction between the species leading to the observed mechanical strain on the tubes.

8.8 Conclusion

In conclusion, the binding of porphyrin oligomers to SWNTs was investigated and two remarkable observations were made. Firstly, the binding of porphyrin oligomers to SWNTs is so strong that it induces mechanical strain on the nanotubes, even in solution. Strain values of this magnitude have only been observed previously in the solid state [269, 281]. This effect is not observed for any of the other semiconducting polymers investigated here and appears to be unique to the porphyrin oligomers. These findings are consistent with the large binding constants deduced for these systems [243, 273].

Second, a type-II heterojunction exists between the longer porphyrin oligomers (**P6**, **P8** and **P*N***) and smaller-diameter SWNTs. The type-II interface causes a strong red-shifted absorption and emission of the nanotubes when small-diameter nanotubes are dispersed with porphyrin oligomers. This effect disappears for larger diameter nanotubes or shorter oligomers (*e.g.* **P2**) where no type-II interface is expected. This is attributed to an exciton state where the wavefunction of the SWNT hole extends across the interface due to the band alignment, effectively lowering the energy of the exciton. These results provide a promising avenue for incorporating porphyrin–SWNT composites in efficient OPV devices, utilising the mobilities of both materials and the broad absorption bands of the porphyrin oligomers to capture a wide range of the solar spectrum.

Chapter 9

Conclusions

9.1 Summary of Key Results

In this thesis, nanohybrids consisting of single-walled carbon nanotubes (SWNTs) wrapped with monolayer coatings of various semiconducting polymers were investigated. Steady-state and time-resolved optical measurements, along with high-resolution microscopy, were used to understand why nanotube–polymer blends have shown poor organic photovoltaic (OPV) device performance to date and, in particular, assess the potential of each of these new and/or optimised blends for OPV applications.

Charge photogeneration dynamics at the type-II interface formed between SWNTs and poly(3-hexylthiophene) (P3HT) were investigated using a combination of femtosecond spectroscopic techniques. It was demonstrated that photoexcitation of P3HT forming a single molecular layer around a SWNT leads to an ultrafast (∼430fs) charge transfer between the materials, three orders of magnitude faster than observed previously [201, 214]. The addition of excess P3HT leads to long-term charge separation in which free polarons remain separated at room temperature. The results suggest that SWNT-P3HT blends incorporating only small fractions (1%) of SWNTs allow photon-to-charge conversion with efficiencies comparable to those for conventional (60:40) P3HT:fullerene blends, provided that small-diameter tubes are individually embedded in the P3HT matrix. Previous device studies

showed poor performances because they utilised larger diameter nanotubes, which did not form the required type-II heterojunction with P3HT [5, 152, 153, 154].

A new form of nanostructure consisting of SWNTs wrapped in alternate layers of two different semiconducting polymers, namely P3HT and poly(9,9'-dioctylfluorene-*co*-benzothiadiazole) (F8BT), was nano-engineered. It was shown that, in solution, there is a binding competition between P3HT and F8BT in which P3HT can readily displace F8BT bound to the nanotube surface but not vice versa. By varying the order and timing of the processing steps, the competitive binding processes can be controlled to engineer thin films of dual polymer nanostructures consisting of small-diameter SWNTs coated in either P3HT or F8BT with the entire structure surrounded by an excess of the other polymer. The resulting novel coaxial structures open up a variety of new applications for nanotube blends and are particularly promising for implementation into OPV devices.

The problems of nanotube heterogeneity within distributions and the presence of detrimental metallic nanotubes were also addressed. A method, involving first isolating almost solely (7,5) semiconducting SWNTs using the selectively dispersing polymer poly(9,9-dioctylfluorenyl-2,7-diyl) (PFO), was demonstrated. It was shown that a preferable polymer added to the solution, such as P3HT or F8BT, was then able to displace the bound PFO by dominating a competitive binding process and the remaining, unbound polymers were able to be removed. The method is scalable and the nanohybrid products, containing (7,5) tubes dispersed with the desired polymers, are able to be dissolved in any preferred solvent to any desired concentration, making it highly suitable for use in optoelectronic applications.

Finally, the non-covalent binding of conjugated porphyrin oligomers, nature's light-harvesting systems, to SWNTs was investigated and two remarkable observations were highlighted. First, the binding of the oligomers to SWNTs is so strong that it induces mechanical strain on the nanotubes in solution. The magnitudes of the strains are comparable to those found in solid-state studies. Comparable strains were not observed in any other SWNT–supramolecular complexes. Second, large decreases in polymer band gap with increasing length of the oligomer lead to the formation of a type-II heterojunction between long chain

oligomers and small-diameter nanotubes. Therefore, these complexes also offer considerable promise for photovoltaic devices.

9.2 Outlook and Future Work

The work in this thesis provides scope for promising future work. The long-lived charge separation in P3HT matrices containing small proportions of SWNTs suggests that these blends should be tested by direct implementation into OPV devices. The results taken as a whole show that optimal OPV devices would utilise these nanohybrids in a matrix of P3HT, with hole blocking F8BT monolayer coatings, prepared using the selective dispersion method to eliminate unwanted metallic and larger diameter species. These highly purified and optimised nanostructures, containing (7,5) nanotubes, have the required electronic alignments to allow construction of potentially highly efficient OPV devices.

Recent work by Ren *et al.* [148] used the first of these results to construct OPV devices with [P3HT-NT] nanohybrids in P3HT matrices. The devices showed peak efficiencies of $\sim$0.7 % at a tube weight fraction of 3 %, with V_{OC} values reaching as high as $\sim$1 V. However, the nanotube species used were of intermediate diameters (1.2–1.7 nm), suggesting significant scope for further increasing the photoexcited charge generation yield by utilising the smaller diameter tube distributions used here (0.7–0.9 nm). The presence of the F8BT hole blocking layer preventing recombination may lead to further increased efficiencies.

A compromise between a large charge transfer driving force (deep acceptor LUMO level) and a large V_{OC} (shallow acceptor LUMO level) must be reached in blend systems [126, 130]. For small-diameter nanotubes with P3HT, the driving force ($\sim$1.2 eV) exceeds that for PCBM-P3HT systems ($\sim$0.9 eV), but a lower V_{OC} is predicted. The results of Ren *et al.* suggest that V_{OC} values much larger than predicted by the standard models (theoretical maximum of $\sim$0.8 V) and PCBM systems ($\sim$0.6 V in real devices [136]) can actually be obtained. The higher mobilities and stabilities of nanotubes, combined with the further optimisation steps described above, mean that devices using nanotube-polymer blends have

the potential to exceed efficiencies obtained from benchmark fullerene-polymer blends.

The donor material must also be chosen to maximally harvest the solar spectrum. Many polymers, including P3HT, have peak absorptions in the visible region but much of the near-infrared region of the solar spectrum is lost. This presents a major challenge for increasing OPV device efficiencies, exemplified by the fact that the most efficient OPV devices to date use low bandgap polymers which are able to absorb much of this low energy light [137, 138, 139]. The porphyrin oligomers are particularly good light-harvesting candidates because their peak absorption extends out to >900 nm when planarised on nanotubes. Future device work could even incorporate mixtures of nanohybrids with several complementary bandgap polymers to harvest across the spectrum.

The porphyrin oligomer–nanotube complexes should also be implemented into OPV devices. In addition to their very good light-harvesting ability, porphyrin oligomers exhibit high intra-chain hole mobilities, particularly when planarised as they are on nanotube surfaces [253]. The oligomers may be able to readily stack on one another and further studies may also reveal high inter-chain mobilities through the planarised, π-stacked structures, providing a continous hole transport network away from the nanotube interface. Experiments should be conducted to also integrate an F8BT hole-blocking layer around the nanotube in these systems and to investigate whether the oligomers can displace PFO from the tube surfaces, thereby allowing use of solely (7,5) species.

Using the blend materials investigated in this work for light-harvesting and charge separation, the next pressing challenge is how to maximally transport the generated charges to the electrodes. A randomly aligned distribution of nanotubes would be unlikely to optimise charge collection and alignment may be paramount for efficient charge collection. Concentration gradients of polymers and nanohybrids or novel device geometries could also be used to direct charges in preferential directions.

The ultimate goal would be to produce an 'all-carbon' OPV device. This would consist of a nanotube–polymer blend as the photoactive layer but with the transparent conducting indium tin oxide (ITO) electrode, and perhaps also the metal electrode, replaced by an

electrode composed of carbon nanotubes, or even graphene. ITO has a limited supply, is expensive, fragile and inflexible, whereas graphene sheets can exhibit improved transparencies (>90 %) with much lower sheet resistances [287]. The price of production of both nanotubes and graphene have dropped significantly over the last few years as preparative techniques have improved, paving the way for cheap device components. The development of a truly efficient OPV device using carbon nanotubes and other carbon-based systems would have a huge impact and could make a big contribution towards solving the world's growing energy problems.

Appendix A

Poster Presentations

This appendix includes posters relating to the work described in this thesis that have been presented at Conferences and Workshops.

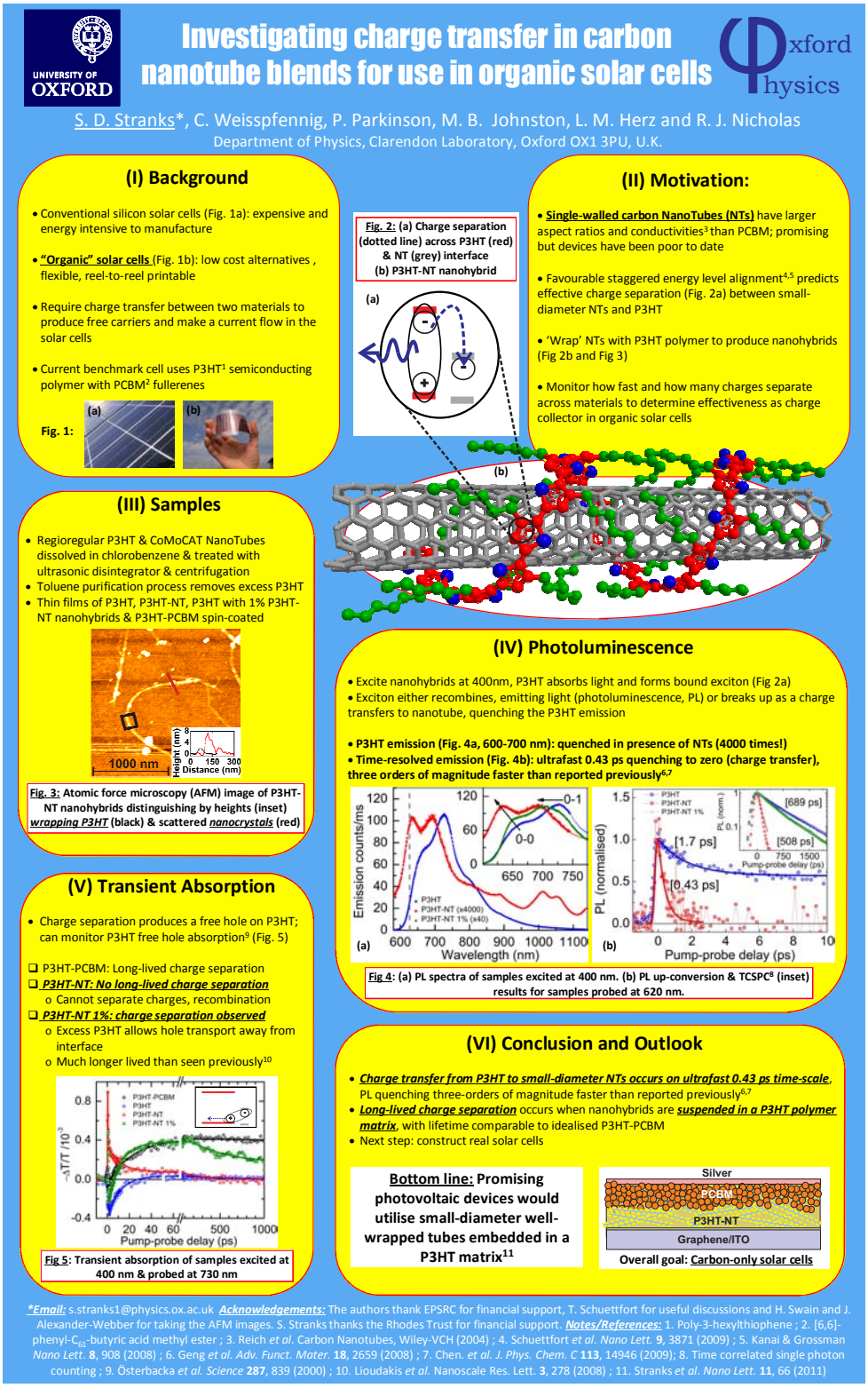

Figure A.1: Poster based on work in Chapter 5. Presented at NT10 International Carbon Nanotube Conference, Montreal, Canada, 2010; SET for Britain Poster Competition, House of Commons, Houses of Parliament, Westminster, London, UK, 2011; Oxford Future Energy Conference, Oxford, UK, 2011; JUDO-PV International Dye-Sensitised and Organic Photovoltaics Workshop, Oxford, UK, 2011; Functional Bulk Nanostructures for Energy Generation and Storage, The Kavli Royal Society International Centre, UK, 2011.

Nano-engineering Coaxial Carbon Nanotube–Dual Polymer Nanostructures

S. D. Stranks*, C-K Yong, J. A. Alexander-Webber, C. Weisspfennig, M. B. Johnston, L. M. Herz, and R. J. Nicholas
Department of Physics, University of Oxford, Clarendon Laboratory, Oxford OX1 3PU, U.K.

(i) Introduction

- Binding semiconducting polymers to single-walled carbon nanotubes (NTs) can give:
  - o Enhanced diameter selectivity[1] or mechanical properties[2]
  - o **Type-II heterojunction** alignments, such as between poly(3-hexylthiophene) (P3HT) and small diameter NTs[3], making blends suitable for charge separation[4] and **use in organic photovoltaics (OPVs)**
- Here, we **nano-engineer dual coated polymer—NT structures** (b,c) by introducing a second polymer layer to further control electronic properties and give specific attributes such as stabilised charge separation

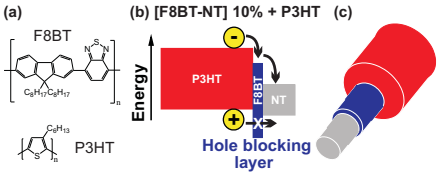

- Immediate dielectric environment of NTs, such as presence of polymers, directly influences Coulomb energies of NT excitons[6]
- Hole of NT exciton delocalised onto polymer due to type-II alignment with P3HT, leading to enhanced red-shift relative to blends with F8BT (of type-I alignment)[3]

→ Determine immediate wrapping polymer using absorption and photoluminescence (PL) measurements

(ii) Solution Binding Competition

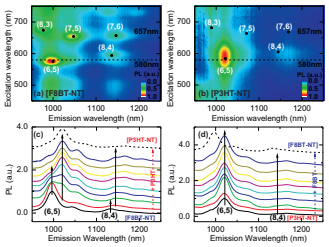

- Nanohybrids in chloroform consisting of CoMoCAT NTs coated with (a) F8BT or (b) P3HT, synthesised using sonication & centrifugation[7]
- (c) Excitation of (6,5) & (8,4) NTs at 580nm as P3HT increasingly added (bottom to top): exchange of intensity from original [F8BT-NT] peaks to [P3HT-NT] peaks

→ **P3HT substitutes F8BT on NT**

- (d) No substitution of P3HT by F8BT

(iii) Isolating Substituted Species

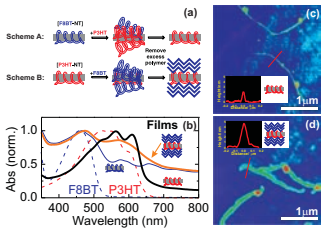

- Allow substitution to occur with 100x polymer excess, then isolate using solvent extraction[7]
- (b) Cannot distinguish F8BT & P3HT in solution but P3HT is red-shifted in films
- AFM images in (c), (d)

→ **Deduce processes & final compositions in (a)**

(iv) Thin Film Substitution Studies

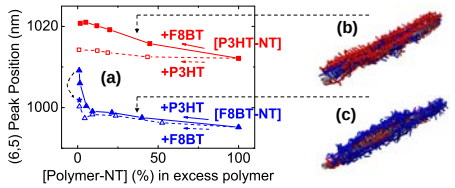

- Thin, uniform films formed by spin-coating [F8BT-NT] & [P3HT-NT] nanohybrid solutions with range of excess F8BT or P3HT concentrations
- (a) As excess polymer added (right to left), (6,5) absorption peak red-shifts due to increasing dielectric; **most significant for thickly coated [P3HT-NT] + F8BT** (AFM)
- **Substitution seen for [F8BT-NT] + P3HT** for nanohybrid concentrations <10%, unless prepared in <10 mins (starred symbol) to 'fix' desired configuration
- Molecular dynamics simulations to represent the (b) [F8BT-NT] + P3HT and (c) [P3HT-NT] + F8BT nanohybrids

(v) Time-Resolved Photoluminescence Studies

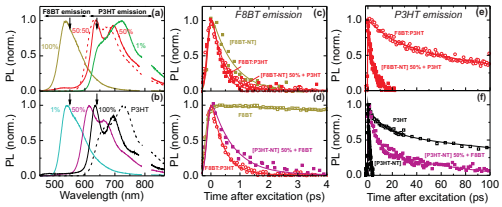

- Time-resolved PL from 50% samples excited at 400nm, monitored at indicated wavelengths by upconversion (~220fs resolution)
- (c,d) F8BT quenched quickly via energy and charge transfer to P3HT and/or NTs
- (e,f) P3HT emission slower because no P3HT → F8BT excitation transfer
- **Insertion of F8BT layer** between P3HT & NTs, [F8BT-NT] + P3HT → **longer-lived P3HT emission** (~20ps) than [P3HT-NT] (~1ps)
- **Addition of excess F8BT**, [P3HT-NT] + F8BT → **long-lived, two-component decay**

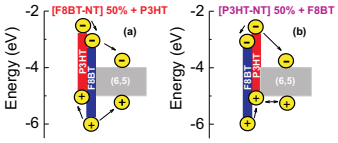

- (a) **Longer-lived decay**: P3HT electrons cascade to NT via F8BT; holes blocked in reverse process
- (b) **Two-component long-lived decay**: alternative pathway for P3HT exciton dissociation by transfer of electrons to F8BT which can tunnel back to P3HT in varied landscape created by polymer wrapping

(vi) Conclusions and Applications

- **Nano-engineered dual polymer nanostructures** consisting of NTs coated in P3HT or F8BT with entire structure surrounded by excess of other polymer
- **OPV applications:**
  - [F8BT-NT] + P3HT: electron cascade, physically separate electrons & holes
  - [P3HT-NT] + F8BT: enhance polymer—polymer blends, NTs as hole collectors

***Email:** s.stranks1@physics.ox.ac.uk ***Acknowledgements:** The authors thank EPSRC and S. Stranks thanks the Rhodes Trust for financial support. ***Notes/References:** 1. Nish *et al. Nat. Nanotech.* **2**, 640 (2007); 2. Carey *et al. ACS Nano* **5**, 2307 (2011); 3. Schuettfort *et al. Nano Lett.* **9**, 3871 (2009).; 4. Stranks *et al. Nano Lett.* **11**, 66 (2011); 5. F8BT – poly(9,9'-dioctylfluorene-*co*-benzothiadiazole); 6. Jiang *et al. Phys. Rev. B* **75**, 035405 (2007); 7. Schuettfort *et al. Nanotechnology* **21**, 025201 (2010)

Figure A.2: Poster based on work in Chapter 6. Presented at NT11 International Carbon Nanotube Conference, Cambridge, UK, 2011; Cambridge Carbon Nanotechnology Symposium, Cambridge, UK, 2012 (winning academic poster prize).

Electronic and Mechanical Modification of Single-Walled Carbon Nanotubes by Binding to Porphyrin Oligomers

S. D. Stranks[1,*], J. K. Sprafke[2], H. L. Anderson[2] and R. J. Nicholas[1]
[1]Department of Physics, University of Oxford, Clarendon Laboratory, Oxford OX1 3PU, U.K.
[2]Department of Chemistry, University of Oxford, Chemistry Research Laboratory, Oxford OX1 3TA, U.K.

(i) Introduction

• **Organic Photovoltaics (OPVs)**: low-cost alternatives to silicon solar cells
• Require efficient charge separation between donor and acceptor exhibiting staggered **type-II heterojunction** (right)

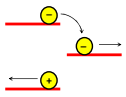

• **Porphyrins**: nature's light harvesting system
• **Single-Walled Carbon Nanotubes** (NTs): high mobilities, large aspect ratios, efficient exciton dissociation centres[1]
→Porphyrin-NT blends promising for OPVs

Stranks *et al. ACS Nano* **5**, 2307 (2011)

(ii) Samples

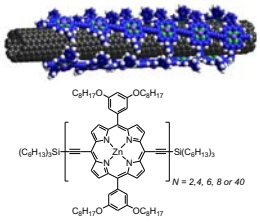

• Porphyrins bind strongly to NTs due to significant π-π stacking

• Functionalised HiPCO & CoMoCAT NTs in THF with porphyrin dimers (**P2**), tetramers (**P4**), hexamers (**P6**), octamers (**P8**), polymers (***PN , N~40***) by sonication & filtration[2]

(iii) Absorption Spectroscopy

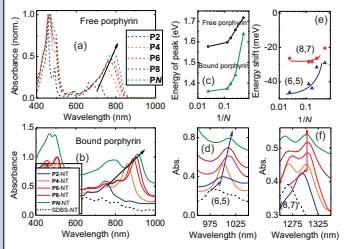

• **Red-shift of ~200 meV in porphyrin Q-band** upon binding (a) free porph. to (b) NTs; summarised in (c) →**planarization on NTs**

• (d) Small diameter (6,5) shows increasing red-shift with oligomer length, (f) unlike larger (8,7) tubes; summarised in (e)

(iv) Photoluminescence Excitation Mapping

• (a) CoMoCAT & (c) HiPCO NTs dispersed in SDBS/D_2O & functionalised in THF by P6 in (b) & (d), respectively.

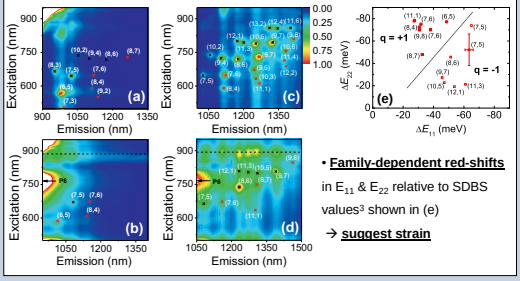

• **Family-dependent red-shifts** in E_{11} & E_{22} relative to SDBS values[3] shown in (e)
→ **suggest strain**

(v) Mechanical Strain (ΔE_{strain})

• Effect of **mechanical strain** on NT optical transitions is opposite for the two families of semiconducting NTs (q = ± 1)

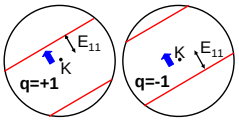

Brillouin Zone around K point showing increase in E_{11} for q = -1, decrease for q = +1 under mechanical strain. Opposite behaviour for E_{22}.

• Split red-shifts into two components:

$$\Delta E_{ii} = \Delta E_{electronic} + \Delta E_{strain}$$

$$\Delta E_{electronic} = (\Delta E_{11} + \Delta E_{22})/2$$
$$\Delta E_{strain} = (\Delta E_{11} - \Delta E_{22})/2$$

• Can fit strain values as a function of chiral angle θ, as shown in (a), to extract $\varepsilon_{\parallel}$ **(axial)** and $\varepsilon_{\perp}$ **(circumferential)** strain components[4]:

$$\Delta E_{strain} = \left(\frac{2t_0 a_{C-C}}{d}\right)(\varepsilon_{\perp} - \nu\varepsilon_{\parallel}) + 3qt_0[(1+\nu)\varepsilon_{\parallel}\cos 3\theta + \varepsilon_{\perp}\sin 3\theta]$$

• **Strain observed in solution** but comparable to solid-state studies[5]

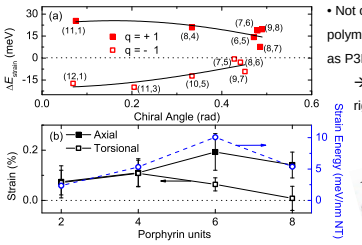

• Not observed in other polymer-NT systems such as P3HT
→ Due to bulkier, more rigid porphyrin units

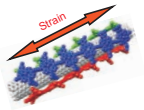

(vi) Type-II Heterojunction ($\Delta E_{electronic}$)

• (a) Valence bands of NTs drop below HOMO of oligomers for **smaller diameter NTs and longer oligomers** → form type-II heterojunctions

• (b) Diameter- and (c) oligomer length-dependent red-shifts observed for type-II blends only, such as P3HT, but not type-I blends such as MEHPPV[6] or P2

• Type-II hole delocalised onto polymer → red-shift[6]

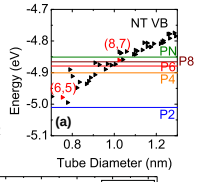

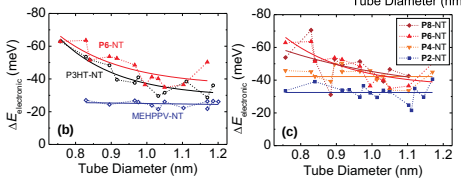

(vii) Conclusions

• Absorption and photoluminescence measurements used to monitor effects of porphyrin oligomers binding to carbon nanotubes (NTs). Show that:
  • **Porphyrin oligomers mechanically strain the NTs** in solution; not observed for other polymer-NT systems
  • A **type-II heterojunction** forms between **longest oligomers and smallest NTs**

Results provide promising avenue for porphyrin-NT organic photovoltaics

Email: s.stranks1@physics.ox.ac.uk ***Acknowledgements:*** The authors thank EPSRC and the European Commission (EU Contract MRTN-CT-2006-036040) for their financial support. S. Stranks thanks the Rhodes Trust for financial support. ***Notes/References:*** 1. Stranks *et al. Nano Lett.* **11**, 66 (2011); 2. Sprafke, Stranks *et al. Angew. Chem. Int. Ed.* **50**, 2313 (2011); 3. Weisman and Bachilo *Nano Lett.* **3**, 1235 (2003); 4 Yang and Han *Phys. Rev. Lett.* **85**, 154 (2000); 5. Li et al. Phys. Rev. Lett. **93**, 156104 (2004); 6. Schuettfort *et al. Nano Lett.* **9**, 3871 (2009).

Figure A.3: Poster based on work in Chapter 8. Presented at NT11 International Carbon Nanotube Conference, Cambridge, UK, 2011.

Bibliography

[1] International Energy Agency (IEA), Key World Energy Statistics (2011).

[2] B. Parida, S. Iniyan, & R. Goic, *Renewable and Sustainable Energy Reviews*, 15 (3) 1625 (2011).

[3] E. Kymakis, I. Alexandrou, & G. A. J. Amaratunga, *J. Appl. Phys.*, 93 1764 (2003).

[4] H. J. Snaith & L. Schmidt-Mende, *Adv. Mater.*, 19 3187 (2007).

[5] J. Arranz-Andrés & W. J. Blau, *Carbon*, 46 2067 (2008).

[6] M. Maghrebi, A. Abbasi, S. Amiri, R. Monsefi, & A. Harati, *Scientometrics*, 86 15 (2011).

[7] M. L. Grieneisen & M. Zhang, *Small*, 7 (20) 2836 (2011).

[8] S. Iijima, *Nature*, 354 56 (1991).

[9] T. C. Dinadayalane & J. Leszczynski, *Struct. Chem.*, 21 1155 (2010).

[10] A. J. Heeger, N. S. Sariciftci, & E. B. Namdas, *Semiconducting and Metallic Polymers*, Oxford University Press, first edn. (2010).

[11] M. S. Dresselhaus, G. Dresselhaus, & P. C. Eklund, *Science of Fullerenes and Carbon Nanotubes*, Academic Print, Inc., first edn. (1996).

[12] S. Reich, C. Thomsen, & J. Maultzsch, *Carbon Nanotubes – Basic Concepts and Physical Properties*, Wiley-VCH, first edn. (2004).

[13] K. S. Novoselov, A. K. Geim, S. V. Morozov, D. Jiang, Y. Zhang *et al.*, *Science*, 306 666 (2004).

[14] M. S. Dresselhaus & G. Dresselhaus, *Annu. Rev. Mater. Sci.*, 25 487 (1995).

[15] L. V. Radushkevich & V. M. Lukyanovich, *Zurn. Fisic. Chim.*, 26 88 (1952).

[16] M. Monthioux & V. L. Kuznetsov, *Carbon*, 44 1621 (2006).

[17] S. Iijima & T. Ichihashi, *Nature*, 363 603 (1993).

[18] D. S. Bethune, C. H. Kiang, M. S. Devries, G. Gorman, R. Savoy *et al.*, *Nature*, 363 605 (1993).

[19] A. Jorio, G. Dresselhaus, & M. S. Dresselhaus (editors), *Carbon Nanotubes*, vol. 111 of *Topics Appl. Physics*, Springer (2008).

[20] E. T. Thostenson, C. Y. Li, & T. W. Chou, *Compos. Sci. Technol.*, 65 491 (2005).

[21] S. Berber, Y. K. Kwon, & D. Tomanek, *Phys. Rev. Lett.*, 84 4613 (2000).

[22] E. Pop, D. Mann, Q. Wang, K. Goodson, & H. J. Dai, *Nano Lett.*, 6 96 (2006).

[23] P. Nikolaev, M. J. Bronikowski, R. K. Bradley, F. Rohmund, D. T. Colbert *et al.*, *Chem. Phys. Lett.*, 313 91 (1999).

[24] B. Kitiyanan, W. E. Alvarez, J. H. Harwell, & D. E. Resasco, *Chem. Phys. Lett.*, 317 497 (2000).

[25] S. M. Bachilo, L. Balzano, J. E. Herrera, F. Pompeo, D. E. Resasco *et al.*, *J. Am. Chem. Soc.*, 125 11186 (2003).

[26] J. E. Herrera, L. Balzano, A. Borgna, W. E. Alvarez, & D. E. Resasco, *J. Catal.*, 204 129 (2001).

[27] T. J. Park, S. Banerjee, T. Hemraj-Benny, & S. S. Wong, *J. Mater. Chem.*, 16 141 (2006).

[28] R. Saito, G. Dresselhaus, & M. S. Dresselhaus, *Phys. Rev. B*, 61 2981 (2000).

[29] P. R. Wallace, *Phys. Rev.*, 71 622 (1947).

[30] N. Hamada, S. Sawada, & A. Oshiyama, *Phys. Rev. Lett.*, 68 1579 (1992).

[31] R. Saito, M. Fujita, G. Dresselhaus, & M. S. Dresselhaus, *Phys. Rev. B*, 46 1804 (1992).

[32] J. W. Mintmire & C. T. White, *Phys. Rev. Lett.*, 81 2506 (1998).

[33] S. Reich & C. Thomsen, *Phys. Rev. B*, 62 4273 (2000).

[34] A. Kleiner & S. Eggert, *Phys. Rev. B*, 64 113402 (2001).

[35] X. Blase, L. X. Benedict, E. L. Shirley, & S. G. Louie, *Phys. Rev. Lett.*, 72 1878 (1994).

[36] L. Yang & J. Han, *Phys. Rev. Lett.*, 85 154 (2000).

[37] Y. N. Gartstein, A. A. Zakhidov, & R. H. Baughman, *Phys. Rev. B*, 68 115415 (2003).

[38] R. B. Capaz, C. D. Spataru, P. Tangney, M. L. Cohen, & S. G. Louie, *Phys. Status Solidi B-Basic Res.*, 241 3352 (2004).

[39] R. S. Deacon, K. C. Chuang, J. Doig, I. B. Mortimer, & R. J. Nicholas, *Phys. Rev. B*, 74 201402 (2006).

[40] L. Yang, M. P. Anantram, J. Han, & J. P. Lu, *Phys. Rev. B*, 60 13874 (1999).

[41] I. Bozovic, N. Bozovic, & M. Damnjanovic, *Phys. Rev. B*, 62 6971 (2000).

[42] H. Ajiki & T. Ando, *Physica B*, 201 349 (1994).

[43] V. N. Popov, *New J. Phys.*, 6 17 (2004).

[44] R. B. Weisman & S. M. Bachilo, *Nano Lett.*, 3 1235 (2003).

[45] J. Jiang, R. Saito, A. Gruneis, G. Dresselhaus, & M. S. Dresselhaus, *Carbon*, 42 3169 (2004).

[46] J. S. Lauret, C. Voisin, G. Cassabois, C. Delalande, P. Roussignol *et al.*, *Phys. Rev. Lett.*, 90 057404 (2003).

[47] C. Manzoni, A. Gambetta, E. Menna, M. Meneghetti, G. Lanzani *et al.*, *Phys. Rev. Lett.*, 94 207401 (2005).

[48] F. Schoppler, C. Mann, T. C. Hain, F. M. Neubauer, G. Privitera *et al.*, *J. Phys. Chem. C*, 115 14682 (2011).

[49] H. Kataura, Y. Kumazawa, Y. Maniwa, I. Umezu, S. Suzuki *et al.*, *Synth. Met.*, 103 2555 (1999).

[50] S. M. Bachilo, M. S. Strano, C. Kittrell, R. H. Hauge, R. E. Smalley *et al.*, *Science*, 298 2361 (2002).

[51] M. Fox, *Optical Properties of Solids*, Oxford University Press, first edn. (2001).

[52] T. Ando, *J. Phys. Soc. Jpn.*, 66 1066 (1997).

[53] C. D. Spataru, S. Ismail-beigi, L. X. Benedict, & S. G. Louie, *Phys. Rev. Lett.*, 92 077402 (2004).

[54] C. D. Spataru, S. Ismail-beigi, L. X. Benedict, & S. G. Louie, *Appl. Phys. A-Mater. Sci. Process.*, 78 1129 (2004).

[55] E. Chang, G. Bussi, A. Ruini, & E. Molinari, *Phys. Rev. Lett.*, 92 196401 (2004).

[56] F. Wang, G. Dukovic, L. E. Brus, & T. F. Heinz, *Science*, 308 838 (2005).

[57] J. Maultzsch, R. Pomraenke, S. Reich, E. Chang, D. Prezzi *et al.*, *Phys. Rev. B*, 72 241402 (2005).

[58] V. Perebeinos, J. Tersoff, & P. Avouris, *Phys. Rev. Lett.*, 92 257402 (2004).

[59] R. B. Capaz, C. D. Spataru, S. Ismail-beigi, & S. G. Louie, *Phys. Rev. B*, 74 121401 (2006).

[60] L. Luer, S. Hoseinkhani, D. Polli, J. Crochet, T. Hertel *et al.*, *Nat. Phys.*, 5 54 (2009).

[61] C. L. Kane & E. J. Mele, *Phys. Rev. Lett.*, 93 197402 (2004).

[62] C. L. Kane & E. J. Mele, *Phys. Rev. Lett.*, 90 207401 (2003).

[63] G. G. Samsonidze, R. Saito, N. Kobayashi, A. Gruneis, J. Jiang *et al.*, *Appl. Phys. Lett.*, 85 5703 (2004).

[64] T. Ando, *J. Phys. Soc. Jpn.*, 73 3351 (2004).

[65] T. Ando, *J. Phys. Soc. Jpn.*, 79 024706 (2010).

[66] Y. Ohno, S. Iwasaki, Y. Murakami, S. Kishimoto, S. Maruyama *et al.*, *Phys. Status Solidi B-Basic Solid State Phys.*, 244 4002 (2007).

[67] J. Lefebvre, J. M. Fraser, Y. Homma, & P. Finnie, *Appl. Phys. A-Mater. Sci. Process.*, 78 1107 (2004).

[68] A. G. Walsh, A. N. Vamivakas, Y. Yin, S. B. Cronin, M. S. Unlu *et al.*, *Nano Lett.*, 7 1485 (2007).

[69] J. Lefebvre & P. Finnie, *Nano Lett.*, 8 1890 (2008).

[70] A. Hagen, M. Steiner, M. B. Raschke, C. Lienau, T. Hertel *et al.*, *Phys. Rev. Lett.*, 95 197401 (2005).

[71] L. B. Huang & T. D. Krauss, *Phys. Rev. Lett.*, 96 057407 (2006).

[72] X. Xu, K. Chuang, R. J. Nicholas, M. B. Johnston, & L. M. Herz, *J. Phys. Chem. C*, 113 18106 (2009).

[73] L. Cognet, D. A. Tsyboulski, J. D. R. Rocha, C. D. Doyle, J. M. Tour *et al.*, *Science*, 316 1465 (2007).

[74] C. Georgi, M. Bohmler, H. H. Qian, L. Novotny, & A. Hartschuh, *Phys. Status Solidi B-Basic Solid State Phys.*, 246 2683 (2009).

[75] K. Yoshikawa, K. Matsuda, & Y. Kanemitsu, *J. Phys. Chem. C*, 114 4353 (2010).

[76] S. Moritsubo, T. Murai, T. Shimada, Y. Murakami, S. Chiashi *et al.*, *Phys. Rev. Lett.*, 104 247402 (2010).

[77] F. Wang, G. Dukovic, E. Knoesel, L. E. Brus, & T. F. Heinz, *Phys. Rev. B*, 70 241403 (2004).

[78] Y. Z. Ma, L. Valkunas, S. L. Dexheimer, S. M. Bachilo, & G. R. Fleming, *Phys. Rev. Lett.*, 94 157402 (2005).

[79] E. B. Barros, R. B. Capaz, A. Jorio, G. G. Samsonidze, A. G. Souza *et al.*, *Phys. Rev. B*, 73 241406 (2006).

[80] C. D. Spataru, S. Ismail-beigi, R. B. Capaz, & S. G. Louie, *Phys. Rev. Lett.*, 95 247402 (2005).

[81] I. B. Mortimer & R. J. Nicholas, *Phys. Rev. Lett.*, 98 027404 (2007).

[82] F. Wang, G. Dukovic, L. E. Brus, & T. F. Heinz, *Phys. Rev. Lett.*, 92 177401 (2004).

[83] M. J. O'Connell, S. M. Bachilo, C. B. Huffman, V. C. Moore, M. S. Strano *et al.*, *Science*, 297 593 (2002).

[84] M. Jones, C. Engtrakul, W. K. Metzger, R. J. Ellingson, A. J. Nozik *et al.*, *Phys. Rev. B*, 71 115426 (2005).

[85] J. Lefebvre, D. G. Austing, J. Bond, & P. Finnie, *Nano Lett.*, 6 1603 (2006).

[86] Y. Oyama, R. Saito, K. Sato, J. Jiang, G. G. Samsonidze *et al.*, *Carbon*, 44 873 (2006).

[87] S. Reich, C. Thomsen, & J. Robertson, *Phys. Rev. Lett.*, 95 077402 (2005).

[88] A. Javey, J. Guo, Q. Wang, M. Lundstrom, & H. J. Dai, *Nature*, 424 654 (2003).

[89] P. L. McEuen, M. Bockrath, D. H. Cobden, Y. G. Yoon, & S. G. Louie, *Phys. Rev. Lett.*, 83 5098 (1999).

[90] X. J. Zhou, J. Y. Park, S. M. Huang, J. Liu, & P. L. McEuen, *Phys. Rev. Lett.*, 95 146805 (2005).

[91] S. J. Kang, C. Kocabas, T. Ozel, M. Shim, N. Pimparkar *et al.*, *Nat. Nanotechnol.*, 2 230 (2007).

[92] Q. Cao & J. A. Rogers, *Nano Res.*, 1 259 (2008).

[93] G. W. C. Kaye & T. H. Laby, *Tables of Physical and Chemical Constants*, Longman, sixteenth edn. (1995).

[94] M. F. Yu, B. S. Files, S. Arepalli, & R. S. Ruoff, *Phys. Rev. Lett.*, 84 5552 (2000).

[95] A. Krishnan, E. Dujardin, T. W. Ebbesen, P. N. Yianilos, & M. M. J. Treacy, *Phys. Rev. B*, 58 14013 (1998).

[96] D. Sánchez-portal, E. Artacho, J. M. Soler, A. Rubio, & P. Ordejón, *Phys. Rev. B*, 59 12678 (1999).

[97] W. P. Su, J. R. Schrieffer, & A. J. Heeger, *Phys. Rev. Lett.*, 42 1698 (1979).

[98] T. W. Hagler, K. Pakbaz, K. F. Voss, & A. J. Heeger, *Phys. Rev. B*, 44 8652 (1991).

[99] G. D. Scholes & G. Rumbles, *Nat. Mater.*, 5 683 (2006).

[100] G. Rumbles, I. D. W. Samuel, L. Magnani, K. A. Murray, A. J. Demello *et al.*, *Synth. Met.*, 76 47 (1996).

[101] M. Kasha, *Radiat. Res.*, 20 55 (1963).

[102] S. Siddiqui & F. C. Spano, *Chem. Phys. Lett.*, 308 99 (1999).

[103] F. C. Spano, *J. Chem. Phys.*, 122 234701 (2005).

[104] J. Clark, C. Silva, R. H. Friend, & F. C. Spano, *Phys. Rev. Lett.*, 98 206406 (2007).

[105] T. A. Chen, X. M. Wu, & R. D. Rieke, *J. Am. Chem. Soc.*, 117 233 (1995).

[106] P. Parkinson, C. Müller, N. Stingelin, M. B. Johnston, & L. M. Herz, *J. Phys. Chem. Lett.*, 1 2788 (2010).

[107] K. Fesser, A. R. Bishop, & D. K. Campbell, *Phys. Rev. B*, 27 4804 (1983).

[108] R. Österbacka, C. P. An, X. M. Jiang, & Z. V. Vardeny, *Science*, 287 839 (2000).

[109] M. Kobashi & H. Takeuchi, *Macromolecules*, 31 7273 (1998).

[110] K. B. Wolfstirn, *J. Phys. Chem. Solids*, 16 279 (1960).

[111] S. Tiwari & N. C. Greenham, *Opt. Quantum Electron.*, 41 69 (2009).

[112] H. Sirringhaus, N. Tessler, & R. H. Friend, *Science*, 280 1741 (1998).

[113] T. Förster, *Discuss. Faraday Soc.*, 27 7 (1959).

[114] A. E. Cohen & S. Mukamel, *J. Phys. Chem. A*, 107 3633 (2003).

[115] D. Beljonne, C. Curutchet, G. D. Scholes, & R. J. Silbey, *J. Phys. Chem. B*, 113 6583 (2009).

[116] D. L. Dexter, *J. Chem. Phys.*, 21 836 (1953).

[117] P. F. Barbara, T. J. Meyer, & M. A. Ratner, *J. Phys. Chem.*, 100 13148 (1996).

[118] J. Jortner, *J. Chem. Phys.*, 64 4860 (1976).

[119] C. Deibel, T. Strobel, & V. Dyakonov, *Adv. Mater.*, 22 4097 (2010).

[120] D. R. Stranks, *Discuss. Faraday Soc.*, 29 73 (1960).

[121] A. C. Morteani, P. Sreearunothai, L. M. Herz, R. H. Friend, & C. Silva, *Phys. Rev. Lett.*, 92 247402 (2004).

[122] S. Gelinas, O. Pare-labrosse, C. N. Brosseau, S. Albert-seifried, C. R. McNeill *et al.*, *J. Phys. Chem. C*, 115 7114 (2011).

[123] A. C. Morteani, A. S. Dhoot, J. S. Kim, C. Silva, N. C. Greenham *et al.*, *Adv. Mater.*, 15 1708 (2003).

[124] I. A. Howard, R. Mauer, M. Meister, & F. Laquai, *J. Am. Chem. Soc.*, 132 14866 (2010).

[125] V. D. Mihailetchi, L. J. A. Koster, J. C. Hummelen, & P. W. M. Blom, *Phys. Rev. Lett.*, 93 216601 (2004).

[126] H. Ohkita, S. Cook, Y. Astuti, W. Duffy, S. Tierney *et al.*, *J. Am. Chem. Soc.*, 130 3030 (2008).

[127] T. Clarke, A. Ballantyne, F. Jamieson, C. Brabec, J. Nelson *et al.*, *Chem. Commun.*, 1 89 (2009).

[128] C. W. Tang, *Appl. Phys. Lett.*, 48 183 (1986).

[129] C. A. Gueymard, *Sol. Energy*, 71 325 (2001).

[130] N. C. Giebink, G. P. Wiederrecht, M. R. Wasielewski, & S. R. Forrest, *Phys. Rev. B*, 82 155305 (2010).

[131] G. Yu, J. Gao, J. C. Hummelen, F. Wudl, & A. J. Heeger, *Science*, 270 1789 (1995).

[132] C. R. McNeill & N. C. Greenham, *Adv. Mater.*, 21 3840 (2009).

[133] C. R. McNeill, A. Abrusci, I. Hwang, M. A. Ruderer, P. Muller-buschbaum *et al.*, *Adv. Funct. Mater.*, 19 3103 (2009).

[134] T. Salim, S. Y. Sun, L. H. Wong, L. F. Xi, Y. L. Foo *et al.*, *J. Phys. Chem. C*, 114 9459 (2010).

[135] S. Swaraj, C. Wang, H. P. Yan, B. Watts, L. N. Jan *et al.*, *Nano Lett.*, 10 2863 (2010).

[136] C. J. Brabec, S. Gowrisanker, J. J. M. Halls, D. Laird, S. J. Jia *et al.*, *Adv. Mater.*, 22 3839 (2010).

[137] Y. Y. Liang, Z. Xu, J. B. Xia, S. T. Tsai, Y. Wu *et al.*, *Adv. Mater.*, 22 E135 (2010).

[138] J. Peet, J. Y. Kim, N. E. Coates, W. L. Ma, D. Moses *et al.*, *Nat. Mater.*, 6 497 (2007).

[139] S. H. Park, A. Roy, S. Beaupre, S. Cho, N. Coates *et al.*, *Nat. Photonics*, 3 297 (2009).

[140] D. Veldman, O. Ipek, S. C. J. Meskers, J. Sweelssen, M. M. Koetse *et al.*, *J. Am. Chem. Soc.*, 130 7721 (2008).

[141] C. Deibel, T. Strobel, & V. Dyakonov, *Phys. Rev. Lett.*, 103 036402 (2009).

[142] S. Chaudhary, H. W. Lu, A. M. Müller, C. J. Bardeen, & M. Ozkan, *Nano Lett.*, 7 1973 (2007).

[143] D. J. Bindl, M. Y. Wu, F. C. Prehn, & M. S. Arnold, *Nano Lett.*, 11 455 (2011).

[144] E. Kymakis, M. M. Stylianakis, G. D. Spyropoulos, E. Stratakis, E. Koudoumas *et al.*, *Solar Energy Materials and Solar Cells*, 96 298 (2012).

[145] S. Kazaoui, N. Minami, B. Nalini, Y. Kim, & K. Hara, *J. Appl. Phys.*, 98 084314 (2005).

[146] E. Kymakis, E. Koudoumas, I. Franghiadakis, & G. A. J. Amaratunga, *J. Phys. D-Appl. Phys.*, 39 1058 (2006).

[147] M. H. Ham, G. L. C. Paulus, C. Y. Lee, C. Song, K. Kalantar-zadeh *et al.*, *ACS Nano*, 4 6251 (2010).

[148] S. Ren, M. Bernardi, R. R. Lunt, V. Bulovic, J. C. Grossman *et al.*, *Nano Letters*, 11 5316 (2011).

[149] N. M. Dissanayake & Z. H. Zhong, *Nano Lett.*, 11 286 (2011).

[150] D. J. Bindl, N. S. Safron, & M. S. Arnold, *ACS Nano*, 4 5657 (2010).

[151] E. Kymakis & G. A. J. Amaratunga, *Appl. Phys. Lett.*, 80 112 (2002).

[152] A. T. Mallajosyula, S. S. K. Iyer, & B. Mazhari, *J. Appl. Phys.*, 108 094902 (2010).

[153] J. X. Geng & T. Y. Zeng, *J. Am. Chem. Soc.*, 128 16827 (2006).

[154] E. Kymakis, P. Servati, P. Tzanetakis, E. Koudoumas, N. Kornilios *et al.*, *Nanotechnology*, 18 435702 (2007).

[155] Y. Kanai & J. C. Grossman, *Nano Lett.*, 8 908 (2008).

[156] T. Schuettfort, A. Nish, & R. J. Nicholas, *Nano Lett.*, 9 3871 (2009).

[157] L. M. Liu, W. E. Stanchina, & G. Y. Li, *Appl. Phys. Lett.*, 94 233309 (2009).

[158] J. M. Holt, A. J. Ferguson, N. Kopidakis, B. A. Larsen, J. Bult *et al.*, *Nano Lett.*, 10 4627 (2010).

[159] A. Nish, *Studies on Optical Characterisation of Carbon Nanotube Suspensions*, Ph.D. thesis, Department of Physics, University of Oxford (2008).

[160] P. Horowitz & H. Winfield, *The Art of Electronics*, Cambridge University Press, first edn. (1980).

[161] S. N. Vainshtein, V. S. Yuferev, & J. I. Kostamovaara, *IEEE Trans. Electron Devices*, 52 2760 (2005).

[162] P. W. Parkinson, *Ultrafast Electronic Processes at Nanoscale Organic-Inorganic Semiconductor Interfaces*, Ph.D. thesis, Department of Physics, University of Oxford (2008).

[163] J. Shah, *Ultrafast Spectroscopy of Semiconductors and Semiconductor Nanostructures*, Springer, first edn. (1996).

[164] D. N. Nikogosyan, *Appl. Phys. A-Mater. Sci. Process.*, 52 359 (1991).

[165] W. Becker, *Advanced Time-Correlated Single Photon Counting Techniques*, Springer (2005).

[166] R. Howland & L. Benatar, *A Practical Guide to Scanning Probe Microscopy*, Thermomicroscopes (2000).

[167] Thermomicroscopes, *User's Guide to Autoprobe M5* (2000).

[168] G. Möbus, in *High-resolution imaging and spectrometry of materials*, Springer, first edn. (2003).

[169] J. L. Bahr, E. T. Mickelson, M. J. Bronikowski, R. E. Smalley, & J. M. Tour, *Chem. Commun.*, 2 193 (2001).

[170] R. C. Weast (editor), *Handbook of Chemistry and Physics*, CRC Press, fifty fifth edn. (1974).

[171] M. S. Arnold, A. A. Green, J. F. Hulvat, S. I. Stupp, & M. C. Hersam, *Nat. Nanotechnol.*, 1 60 (2006).

[172] H. P. Liu, D. Nishide, T. Tanaka, & H. Kataura, *Nat. Commun.*, 2 309 (2011).

[173] M. Zheng, A. Jagota, E. D. Semke, B. A. Diner, R. S. McLean *et al.*, *Nat. Mater.*, 2 338 (2003).

[174] X. M. Tu, S. Manohar, A. Jagota, & M. Zheng, *Nature*, 460 250 (2009).

[175] M. J. O'Connell, P. Boul, L. M. Ericson, C. Huffman, Y. H. Wang *et al.*, *Chem. Phys. Lett.*, 342 265 (2001).

[176] A. Nish, J. Y. Hwang, J. Doig, & R. J. Nicholas, *Nat. Nanotechnol.*, 2 640 (2007).

[177] J. Y. Hwang, A. Nish, J. Doig, S. Douven, C. W. Chen *et al.*, *J. Am. Chem. Soc.*, 130 3543 (2008).

[178] J. Gao, M. Kwak, J. Wildeman, A. Hermann, & M. A. Loi, *Carbon*, 49 333 (2011).

[179] D. Tuncel, *Nanoscale*, 3 3545 (2011).

[180] P. W. Atkins, *Physical Chemistry*, Oxford University Press, second edn. (1984).

[181] N. L. Allinger, Y. H. Yuh, & J. H. Lii, *J. Am. Chem. Soc.*, 111 8551 (1989).

[182] I. Gurevitch & S. Srebnik, *Chem. Phys. Lett.*, 444 96 (2007).

[183] M. Giulianini, E. R. Waclawik, J. M. Bell, P. Castrucci, M. Scarselli *et al.*, *Appl. Phys. Lett.*, 95 013304 (2009).

[184] Y. K. Kang, O. S. Lee, P. Deria, S. H. Kim, T. H. Park *et al.*, *Nano Lett.*, 9 1414 (2009).

[185] M. Bernardi, M. Giulianini, & J. C. Grossman, *ACS Nano*, 4 6599 (2010).

[186] J. Gao, M. A. Loi, E. J. F. Decarvalho, & M. C. Dossantos, *ACS Nano*, 5 3993 (2011).

[187] T. Schuettfort, H. Snaith, A. Nish, & R. Nicholas, *Nanotechnology*, 21 025201 (2010).

[188] Y. Ohno, S. Iwasaki, Y. Murakami, S. Kishimoto, S. Maruyama *et al.*, *Phys. Rev. B*, 73 235427 (2006).

[189] K. C. Chuang, A. Nish, J. Y. Hwang, G. W. Evans, & R. J. Nicholas, *Phys. Rev. B*, 78 085411 (2008).

[190] J. L. Blackburn, T. J. McDonald, W. K. Metzger, C. Engtrakul, G. Rumbles *et al.*, *Nano Lett.*, 8 1047 (2008).

[191] M. F. Islam, E. Rojas, D. M. Bergey, A. T. Johnson, & A. G. Yodh, *Nano Lett.*, 3 269 (2003).

[192] A. V. Naumov, S. Ghosh, D. A. Tsyboulski, S. M. Bachilo, & R. B. Weisman, *ACS Nano*, 5 1639 (2011).

[193] P. H. Tan, A. G. Rozhin, T. Hasan, P. Hu, V. Scardaci *et al.*, *Phys. Rev. Lett.*, 99 137402 (2007).

[194] V. Perebeinos, J. Tersoff, & P. Avouris, *Phys. Rev. Lett.*, 94 027402 (2005).

[195] S. G. Chou, F. Plentz, J. Jiang, R. Saito, D. Nezich *et al.*, *Phys. Rev. Lett.*, 94 127402 (2005).

[196] H. Htoon, M. J. O'Connell, S. K. Doorn, & V. I. Klimov, *Phys. Rev. Lett.*, 94 127403 (2005).

[197] L. L. Chua, J. Zaumseil, J. F. Chang, E. C. W. Ou, P. K. H. Ho *et al.*, *Nature*, 434 194 (2005).

[198] A. J. Cadby, P. A. Lane, H. Mellor, S. J. Martin, M. Grell *et al.*, *Phys. Rev. B*, 62 15604 (2000).

[199] F. B. Dias, J. Morgado, A. L. Macanita, H. D. Burrows, & A. P. Monkman, *Macromolecules*, 39 5854 (2006).

[200] C. C. Kitts & D. A. Vandenbout, *Polymer*, 48 2322 (2007).

[201] F. M. Chen, W. J. Zhang, M. L. Jia, L. Wei, X. F. Fan *et al.*, *J. Phys. Chem. C*, 113 14946 (2009).

[202] V. Barone, J. E. Peralta, J. Uddin, & G. E. Scuseria, *J. Chem. Phys.*, 124 024709 (2006).

[203] T. Umeyama, N. Kadota, N. Tezuka, Y. Matano, & H. Imahori, *Chem. Phys. Lett.*, 444 263 (2007).

[204] D. Garrot, B. Langlois, C. Roquelet, T. Michel, P. Roussignol *et al.*, *J. Phys. Chem. C*, 115 23283 (2011).

[205] R. G. S. Goh, N. Motta, J. M. Bell, & E. R. Waclawik, *Appl. Phys. Lett.*, 88 053101 (2006).

[206] S. D. Stranks, C. Weisspfennig, P. Parkinson, M. B. Johnston, L. M. Herz *et al.*, *Nano Lett.*, 11 66 (2011).

[207] H. W. Lee, Y. Yoon, S. Park, J. H. Oh, S. Hong *et al.*, *Nat. Commun.*, 2 541 (2011).

[208] C. L. Donley, J. Zaumseil, J. W. Andreasen, M. M. Nielsen, H. Sirringhaus *et al.*, *J. Am. Chem. Soc.*, 127 12890 (2005).

[209] J. P. Schmidtke, J. S. Kim, J. Gierschner, C. Silva, & R. H. Friend, *Phys. Rev. Lett.*, 99 167401 (2007).

[210] M. Tange, T. Okazaki, & S. Iijima, *J. Am. Chem. Soc.*, 133 11908 (2011).

[211] T. Offermans, S. C. J. Meskers, M. M. Koetse, & R. A. J. Janssen, *Phys. Rev. B*, 72 045213 (2005).

[212] C. Yin, T. Kietzke, D. Neher, & H. H. Horhold, *Appl. Phys. Lett.*, 90 092117 (2007).

[213] J. J. Benson-Smith, J. Wilson, C. Dyer-smith, K. Mouri, S. Yamaguchi *et al.*, *J. Phys. Chem. B*, 113 7794 (2009).

[214] J. X. Geng, B. S. Kong, S. B. Yang, S. C. Youn, S. Park *et al.*, *Adv. Funct. Mater.*, 18 2659 (2008).

[215] A. Gutierrez-Llorente, G. Horowitz, R. Perez-Casero, J. Perriere, J. L. Fave *et al.*, *Org. Electron.*, 5 29 (2004).

[216] X. M. Jiang, R. Österbacka, C. P. An, & Z. V. Vardeny, *Synth. Met.*, 137 1465 (2003).

[217] F. C. Spano, *Chem. Phys.*, 325 22 (2006).

[218] F. C. Spano, J. Clark, C. Silva, & R. H. Friend, *J. Chem. Phys.*, 130 074904 (2009).

[219] O. J. Korovyanko, R. Österbacka, X. M. Jiang, Z. V. Vardeny, & R. A. J. Janssen, *Phys. Rev. B*, 64 235122 (2001).

[220] C. X. Sheng, M. Tong, S. Singh, & Z. V. Vardeny, *Phys. Rev. B*, 75 085206 (2007).

[221] M. Theander, O. Inganäs, W. Mammo, T. Olinga, M. Svensson *et al.*, *J. Phys. Chem. B*, 103 7771 (1999).

[222] S. Westenhoff, W. J. D. Beenken, R. H. Friend, N. C. Greenham, A. Yartsev *et al.*, *Phys. Rev. Lett.*, 97 166804 (2006).

[223] S. Trotzky, *J. Phys. D-Appl. Phys.*, 42 055105 (2009).

[224] M. H. Chang, M. Hoffmann, H. L. Anderson, & L. M. Herz, *J. Am. Chem. Soc.*, 130 10171 (2008).

[225] T. J. Savenije, J. E. Kroeze, X. N. Yang, & J. Loos, *Adv. Funct. Mater.*, 15 1260 (2005).

[226] I. W. Hwang, D. Moses, & A. J. Heeger, *J. Phys. Chem. C*, 112 4350 (2008).

[227] J. Piris, T. E. Dykstra, A. A. Bakulin, W. Knulst, M. T. Trinh *et al.*, *J. Phys. Chem. C*, 113 14500 (2009).

[228] J. M. Guo, H. Ohkita, H. Benten, & S. Ito, *J. Am. Chem. Soc.*, 131 16869 (2009).

[229] G. Dicker, L. D. A. Siebbeles, & J. M. Warman, *Phys. Rev. B*, 70 045203 (2004).

[230] X. Ai, M. C. Beard, K. P. Knutsen, S. E. Shaheen, G. Rumbles *et al.*, *J. Phys. Chem. B*, 110 25462 (2006).

[231] E. Hendry, M. Koeberg, J. M. Schins, L. D. A. Siebbeles, & M. Bonn, *Chem. Phys. Lett.*, 432 441 (2006).

[232] T. G. Pedersen, *Phys. Rev. B*, 67 073401 (2003).

[233] E. Lioudakis, A. Othonos, & I. Alexandrou, *Nanoscale Res. Lett.*, 3 278 (2008).

[234] A. J. Ferguson, J. L. Blackburn, J. M. Holt, N. Kopidakis, R. C. Tenent *et al.*, *J. Phys. Chem. Lett.*, 1 2406 (2010).

[235] Y. Zhao, A. Liao, & E. Pop, *IEEE Electron Device Lett.*, 30 1078 (2009).

[236] H. Ozawa, T. Fujigaya, Y. Niidome, N. Hotta, M. Fujiki *et al.*, *J. Am. Chem. Soc.*, 133 2651 (2011).

[237] J. N. Coleman, M. Cadek, K. P. Ryan, A. Fonseca, J. B. Nagy *et al.*, *Polymer*, 47 8556 (2006).

[238] B. J. Carey, P. K. Patra, L. Ci, G. G. Silva, & P. M. Ajayan, *ACS Nano*, 5 2715 (2011).

[239] S. D. Stranks, J. K. Sprafke, H. L. Anderson, & R. J. Nicholas, *ACS Nano*, 5 2307 (2011).

[240] Y. Cheng & W. H. Prusoff, *Biochem. Pharmacol.*, 22 3099 (1973).

[241] R. J. Flower, *Nat. Rev. Drug Discov.*, 2 179 (2003).

[242] S. Y. Ju, J. Doll, I. Sharma, & F. Papadimitrakopoulos, *Nat. Nanotechnol.*, 3 356 (2008).

[243] J. K. Sprafke, S. D. Stranks, J. H. Warner, R. J. Nicholas, & H. L. Anderson, *Angew. Chem.-Int. Edit.*, 50 2313 (2011).

[244] Y. Kim, S. Cook, S. A. Choulis, J. Nelson, J. R. Durrant *et al.*, *Chem. Mat.*, 16 4812 (2004).

[245] J. W. Ponder & F. M. Richards, *J. Comput. Chem.*, 8 1016 (1987).

[246] D. Beeman, *J. Comput. Phys.*, 20 130 (1976).

[247] G. Bussi, D. Donadio, & M. Parrinello, *J. Chem. Phys.*, 126 014101 (2007).

[248] M. J. Yang, V. Koutsos, & M. Zaiser, *J. Phys. Chem. B*, 109 10009 (2005).

[249] E. F. Pettersen, T. D. Goddard, C. C. Huang, G. S. Couch, D. M. Greenblatt *et al.*, *J. Comput. Chem.*, 25 1605 (2004).

[250] E. H. Haroz, S. M. Bachilo, R. B. Weisman, & S. K. Doorn, *Phys. Rev. B*, 77 125405 (2008).

[251] A. Nish, J. Y. Hwang, J. Doig, & R. J. Nicholas, *Nanotechnology*, 19 095603 (2008).

[252] T. Pullerits & V. Sundström, *Acc. Chem. Res.*, 29 381 (1996).

[253] F. C. Grozema, C. Houarner-rassin, P. Prins, L. D. A. Siebbeles, & H. L. Anderson, *J. Am. Chem. Soc.*, 129 13370 (2007).

[254] G. Sedghi, K. Sawada, L. J. Esdaile, M. Hoffmann, H. L. Anderson *et al.*, *J. Am. Chem. Soc.*, 130 8582 (2008).

[255] F. Y. Cheng & A. Adronov, *Chem.-Eur. J.*, 12 5053 (2006).

[256] J. P. Casey, S. M. Bachilo, & R. B. Weisman, *J. Mater. Chem.*, 18 1510 (2008).

[257] C. Roquelet, J. S. Lauret, V. Alain-rizzo, C. Voisin, R. Fleurier *et al.*, *ChemPhysChem*, 11 1667 (2010).

[258] G. Magadur, J. S. Lauret, V. Alain-rizzo, C. Voisin, P. Roussignol *et al.*, *ChemPhysChem*, 9 1250 (2008).

[259] C. Roquelet, D. Garrot, J. S. Lauret, C. Voisin, V. Alain-rizzo *et al.*, *Appl. Phys. Lett.*, 97 141918 (2010).

[260] D. M. Guldi, G. M. A. Rahman, N. Jux, N. Tagmatarchis, & M. Prato, *Angew. Chem.-Int. Edit.*, 43 5526 (2004).

[261] D. M. Guldi, G. M. A. Rahman, F. Zerbetto, & M. Prato, *Accounts Chem. Res.*, 38 871 (2005).

[262] J. Bartelmess, B. Ballesteros, D. Kiessling, S. Campidelli, M. Prato *et al.*, *J. Am. Chem. Soc.*, 132 16202 (2010).

[263] E. Maligaspe, A. S. D. Sandanayaka, T. Hasobe, O. Ito, & F. D'souza, *J. Am. Chem. Soc.*, 132 8158 (2010).

[264] H. P. Li, B. Zhou, Y. Lin, L. R. Gu, W. Wang *et al.*, *J. Am. Chem. Soc.*, 126 1014 (2004).

[265] F. Y. Cheng, S. Zhang, A. Adronov, L. Echegoyen, & F. Diederich, *Chem.-Eur. J.*, 12 6062 (2006).

[266] K. Arnold, S. Lebedkin, O. Kiowski, F. Hennrich, & M. M. Kappes, *Nano Lett.*, 4 2349 (2004).

[267] T. K. Leeuw, D. A. Tsyboulski, P. N. Nikolaev, S. M. Bachilo, S. Arepalli *et al.*, *Nano Lett.*, 8 826 (2008).

[268] M. Y. Huang, Y. Wu, B. Chandra, H. Yan, Y. Shan *et al.*, *Phys. Rev. Lett.*, 100 136803 (2008).

[269] L. J. Li, R. J. Nicholas, R. S. Deacon, & P. A. Shields, *Phys. Rev. Lett.*, 93 156104 (2004).

[270] M. U. Winters, E. Dahlstedt, H. E. Blades, C. J. Wilson, M. J. Frampton *et al.*, *J. Am. Chem. Soc.*, 129 4291 (2007).

[271] M. Hoffmann, J. Kärnbratt, M. H. Chang, L. M. Herz, B. Albinsson *et al.*, *Angew. Chem. Int. Edit.*, 120 5071 (2008).

[272] M. Drobizhev, Y. Stepanenko, A. Rebane, C. J. Wilson, T. E. O. Screen *et al.*, *J. Am. Chem. Soc.*, 128 12432 (2006).

[273] J. K. Sprafke, *Supramolecular Control of Synthesis and Electronic Structure of Porphyrin Oligomers*, Ph.D. thesis, Department of Chemistry, University of Oxford (2011).

[274] M. Kasha, H. R. Rawls, & M. Ashraf El Bayoumi, *Pure Appl. Chem.*, 11 371 (1965).

[275] H. L. Anderson, *Inorg. Chem.*, 33 972 (1994).

[276] M. U. Winters, J. Kärnbratt, M. Eng, C. J. Wilson, H. L. Anderson *et al.*, *J. Phys. Chem. C*, 111 7192 (2007).

[277] P. N. Taylor, J. Huuskonen, G. Rumbles, R. T. Aplin, E. Williams *et al.*, *Chem. Commun.*, 8 909 (1998).

[278] D. Beljonne, G. E. O'Keefe, P. J. Hamer, R. H. Friend, H. L. Anderson *et al.*, *J. Chem. Phys.*, 106 9439 (1997).

[279] M. K. Kuimova, M. Hoffmann, M. U. Winters, M. Eng, M. Balaz *et al.*, *Photochem. Photobiol. Sci.*, 6 675 (2007).

[280] B. W. D'Andrade, S. Datta, S. R. Forrest, P. Djurovich, E. Polikarpov *et al.*, *Org. Electron.*, 6 11 (2005).

[281] A. Nish, R. J. Nicholas, C. Faugeras, Z. Bao, & M. Potemski, *Phys. Rev. B*, 78 245413 (2008).

[282] A. Saywell, J. K. Sprafke, L. J. Esdaile, A. J. Britton, A. Rienzo *et al.*, *Angew. Chem.-Int. Edit.*, 49 9136 (2010).

[283] V. A. Karachevtsev, E. S. Zarudnev, S. G. Stepanian, A. Y. Glamazda, M. V. Karachevtsev *et al.*, *J. Phys. Chem. C*, 114 16215 (2010).

[284] S. S. Tallury & M. A. Pasquinelli, *J. Phys. Chem. B*, 114 9349 (2010).

[285] S. S. Tallury & M. A. Pasquinelli, *J. Phys. Chem. B*, 114 4122 (2010).

[286] M. I. H. Panhuis, A. Maiti, A. B. Dalton, J. N. Coleman, B. McCarthy *et al.*, *J. Phys. Chem. B*, 107 478 (2003).

[287] S. Bae, H. Kim, Y. Lee, X. F. Xu, J. S. Park *et al.*, *Nat. Nanotechnol.*, 5 574 (2010).

Abbreviations

FF	Fill Factor
J_{SC}	Short-Circuit Current
V_{OC}	Open-Circuit Voltage
AFM	Atomic Force Microscopy
AM 1.5	Air Mass 1.5
BBO	Barium Borate
CB	Conduction Band
CCD	Charge-Coupled Device
DFT	Density Functional Theory
DGU	Density-Gradient Ultracentrifugation
DOS	Density of States
F8BT	Poly(9,9'-dioctylfluorene-*co*-benzothiadiazole)
F8T2	Poly(9,9'-dioctylfluorene-*co*-bithiophene)
FRET	Förster Resonance Energy Transfer
FWHM	Full Width at Half Maximum
GT	Glan Thompson (polarising prism)
HiPCO	High-Pressure Catalytic Decomposition of Carbon Monoxide
HOMO	Highest Occupied Molecular Orbital
HRTEM	High Resolution Transmission Electron Microscopy
HWP	Half-Wave Plate
LUMO	Lowest Unoccupied Molecular Orbital

MEHPPV	Poly(2-methoxy-5-(2-ethylhexyloxy)-1,4-phenylenevinylene)
MW	Molecular Weight
MWNT	Multi-Walled Carbon Nanotube
NIR	Near-Infrared
OPVs	Organic Photovoltaics
P3HT	Poly(3-hexylthiophene)
P3OT	Poly(3-octylthiophene)
PCBM	Phenyl-C_{61}-butyric acid methyl ester
PEDOT:PSS	Poly(3,4-ethylenedioxythiophene):Poly(styrenesulfonate)
PFB	Poly(9,9'-dioctylfluorene-*co*-bis-*N,N'*-(4-butylphenyl)-bis-*N,N'*-phenyl-1,4-phenylenediamine)
PFO	Poly(9,9-dioctylfluorenyl-2,7-diyl)
PIF	Poly(indenofluorene)
PL	Photoluminescence
PLE	Photoluminescence Excitation (Spectroscopy)
PLUC	Photoluminescence Up-Conversion (Spectroscopy)
PMT	Photon Multiplier Tube
PSPD	Position-Sensitive Photodetector
PZT	Lead Zirconate Titanate
SDBS	Sodium Dodecyl Benzene Sulfonate
SDS	Sodium Dodecyl Sulfate
SWNT	Single-Walled Carbon Nanotube
TA	Transient Absorption (Spectroscopy)
TB	Tight-Binding (Model)
TCSPC	Time-Correlated Single Photon Counting
TPP	*meso*-5,10,15,20-tetraphenylporphyrin
VB	Valence Band